NIST TECHNICAL NOTE **1285**

U.S. DEPARTMENT OF COMMERCE/National Institute of Standards and Technology

NIST Reactor:
Summary of Activities
July 1989 Through June 1990

NIST Reactor:
Summary of Activities
July 1989 Through June 1990

C. O'Connor, Editor

Reactor Radiation Division
Institute for Materials Science and Engineering
National Institute of Standards and Technology
Gaithersburg, MD 20899

December 1990

FOREWORD

This has been a year of great excitement and progress in the Reactor Radiation Division. First and foremost, of course, is the fact that the reactor penetrations for the neutron guides were completed, and the reactor was brought back on line in April 1990. During the shutdown, several important maintenance items were completed, including the cooling tower overhaul, refurbishment of the sealant on the confinement building walls, and the renovation of the thermal shield cooling system. In addition, the Request for Proposals for a new set of main heat exchangers was extremely successful, resulting in a number of proposals currently being evaluated. It is a particular pleasure to note that the Reactor Operations Group received the Silver Medal of the Department of Commerce in recognition of their outstanding performance in the cost effective operation of the NIST reactor as a national resource.

In spite of the very limited operating schedule that resulted from the guide installation, this was a highly productive year for the Neutron Condensed Matter Science group. Both in quality and quantity, the published output of the group continues to increase. Among many possible highlights, I would mention the successful commissioning of the BT-7 neutron reflectometer, and its use to study polymer films on various substrates; the successful development of a new method for the solution of the crystal structures of large molecules of biological significance based on Maximum Entropy techniques; the first observation of rapid hydrogen hopping in rare-earth metals at low temperatures (the result of a Kondo type interaction with the conduction electrons); a wide variety of new results on the physics and chemistry of high-T_c superconductors; and the first results from the study of epilayers and multilayers of magnetic semiconductors which show that these systems display a rich variety of magnetic behaviors.

The Cold Neutron Project continues to progress well, with the first three neutron guides now installed, and several instruments in the final stage of fabrication and installation. In spite of a large number of unforeseen problems arising from funding limitations in the beginning of the fiscal year, scheduling problems with outside vendors, and technical difficulties during the penetration and guide installation, five instruments will be taking data by the end of 1990. In addition, several others are in the fabrication and procurement stage, with installation scheduled for 1991. A new 3.5-KW refrigerator suitable for operation of a second generation cold source will be installed late in 1990, and the conceptual design of this source, which will utilize liquid hydrogen, is now complete and detailed design is under way. The first meeting of the Program Advisory Committee was held in late 1989, and their recommendations are being developed into a user policy for the CNRF. The first two issues of The Neutron Standard, a facility advisory newsletter, were sent out to over 2500 U.S. researchers. As a result of a cooperative project with the Department of Energy,

the performance of neutron supermirrors has been improved to the point at which it is now feasible to consider at least partial coating of some of the remaining four guides, with greatly improved performance as the result. The responses to a Request for Proposals for the actual guide coating are now being evaluated.

As always, the non-RRD programs that rely on the NIST reactor have also had an impressive year, in spite of the long reactor shutdown. As the CNRF comes on line, these programs will also increase their efforts--two of the new instruments will be operated as user facilities by the Nuclear Methods Group of the Center for Analytical Chemistry, and two others will be operated by the Neutron Interactions and Dosimetry Group from the Center for Atomic, Molecular, and Optical Physics.

Finally, it gives me great personal pleasure to thank the entire staff for their performance during this year. As always, change is disruptive, but everyone has joined in the effort to fully develop the NIST reactor and CNRF facilities as a national resource, and have tolerated the disruption to their own research programs due to the reactor shutdown with grace and patience (in the main !). A special word of thanks is due to Carol O'Connor, the editor of this report, which has a new format, and required a major effort to produce. She was ably assisted in this by Linda Clutter, Stephanie Shepperd, Judy Spillman, and Lisa Thomas.
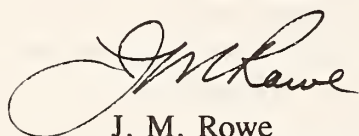
J. M. Rowe
Reactor Radiation Division
National Institute of Standards and Technology

ABSTRACT

This report summarizes all those programs which use the NIST reactor. It covers the period for July 1989 through June 1990. The programs range from the use of neutron beams to study the structure and dynamics of materials through nuclear physics and neutron standards to sample irradiations for activation analysis, isotope production, neutron radiography, and nondestructive evaluation.

KEY WORDS: activation analysis; cold neutrons; crystal structure; diffraction; isotopes; molecular dynamics; neutron; neutron radiography; nondestructive evaluation; nuclear reactor; radiation.

DISCLAIMER

CONTENTS

A. REACTOR RADIATION DIVISION AND COLLABORATIVE PROGRAMS

RAPID LOW TEMPERATURE "HOPPING" OF HYDROGEN
IN A PURE METAL: THE ScH$_x$ SYSTEM

N. F. Berk, J. J. Rush, and T. J. Udovic
and
I. S. Anderson (Paul Scherrer Institut, Villigen, Switzerland)

As part of our continuing effort to study hydrogen dissolved in rare-earth metals, we performed direct neutron quasielastic scattering measurements of the localized motion of hydrogen in scandium [1]. These experiments were carried out between 2 K and 300 K on a single-crystal slab of scandium prepared from high purity Ames laboratory scandium metal and loaded with hydrogen from the gas phase. The measurements were performed at hydrogen concentrations between 5 and 20 atomic percent on the IN-5 Spectrometer at the Institut Laue-Langevin with an energy resolution of 70 µeV in the range of momentum transfer $1.05 < Q < 2.05$ Å^{-1}. Figure 1 shows the quasielastic linewidth Γ as a function of temperature for ScH$_{0.16}$. Data for ScH$_{0.05}$ ScH$_{0.25}$ show behavior consistent with the 0.16 results. All the data show a hopping rate exceeding $\sim 7\times10^{10}$s^{-1} over the entire temperature range, indicative of very rapid motion compared to the bulk diffusion in these systems, even at low T. The remarkable upturn of Γ below the minimum is approximately T^{-1} in the range shown, and is similar in appearance to the observations by Steinbinder et al. [2] of quasielastic scattering from hydrogen trapped by oxygen impurities in Nb, which were explained in terms of Kondo's predictions [3] of nonadiabatic effects of the coupling of the metal conduction electrons to the proton, which in that system is constrained by the trap to hop between a pair of T-sites. We have shown [1] that the scandium-hydrogen system studied here presents an analogous situation--observed for the first time in a pure metal--in which such coupling is also amplified by the effective restriction of the proton to a pair of sites: in this case the nearest neighbor T-sites
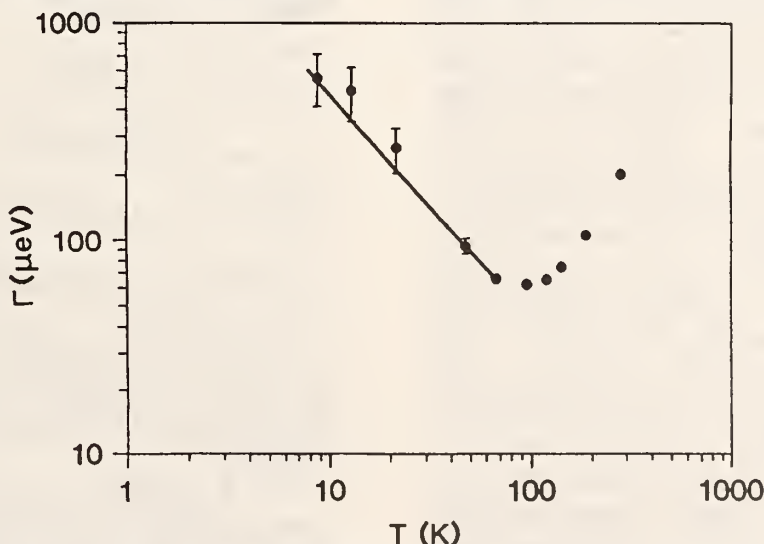
Figure 1. Fitted Lorentzian linewidths (FWHM) for ScH$_{0.16}$. The solid line is the fit to the data below 100 K.

between metal atoms along the c-axis. In this picture the linewidth is the sum of two contributions: the influence of the interaction of the proton with the lattice, which falls monotonically with decreasing T, and the electronically induced broadening which increases with decreasing T.

The low-temperature linewidth was analyzed with the "Kondo" formula

$$\Gamma = K\Delta^3(2\pi k_B T/\Delta)^{2K+1}/[(2\pi k_B TK)^2 + \epsilon^2],$$

where Δ and ϵ are the tunneling matrix element and asymmetry energy, respectively, of a model two-site potential well, and K is the coupling constant of the weak interaction between the proton and conduction electrons. The best fit was obtained for a symmetric model, $\epsilon \approx 0$, K = 0.039, and $\Delta = 0.32$ mev. The values for K and Δ are comparable to those reported for the Nb-O-H system, where the nearest neighbor T-site separation is nearly the same as in the Sc-H system.

References

[1] I. S. Anderson, N. F. Berk, J. J. Rush, T. J. Udovic, R. G. Barnes, A. Magerl, and D. Richter, Phys. Rev. Lett. 65, 1439 (1990).

[2] D. Steinbinder, H. Wipf, A. Magerl, D. Richter, A. J. Dianoux, and K. Neumaier, Europhysics Lett. 6, 535 (1988).

[3] J. Kondo, Physica B125, 279 (1984); ibid. B126, 377 (1984); ibid. 305 (1986).

ELASTIC INCOHERENT NEUTRON SCATTERING FROM THE α-ScH$_x$ SYSTEM

N. F. Berk, J. J. Rush, and T. J. Udovic
and
I. S. Anderson (Paul Scherrer Institut, Villigen, Switzerland)

In the previous report [1] we described new quasielastic neutron scattering results from α-ScH$_x$, showing an upturn of the linewidth at low temperatures, which we associate with nonadiabatic effects of the weak coupling between the protons and the scandium conduction electrons, amplified by the effective restriction of the rapidly moving hydrogens to symmetric near neighbor T-sites between the metal atoms. Our interpretation of the linewidth data is consistent with the simultaneously measured elastic incoherent structure factor (EISF) shown as function of T in figure 1 for x = 0.16. We assume all of the measured hydrogens are in two populations, which we designate as labile (1) and nonlabile (n1), with relative occupations c_1 and c_{n1}, respectively, and with $c_1 + c_{n1} = 1$. We attribute the labile defects to configurations in which H-M-H pairing cannot occur because of the unavailability of nearby protons to form such bridged

parts along the c-axis. The scattering function, $S(\vec{Q},\omega)$, can be written

$$S(\vec{Q},\omega) = eisf(\vec{Q})\delta(\omega)$$
$$+ (1-eisf(\vec{Q}))L_1(\omega), \qquad (1)$$

where $L_1(w)$ is the quasielastic function, and

$$eisf(\vec{Q}) = 1 - c_1 s_1 \sin^2(\vec{Q}\cdot\vec{d}/2), \qquad (2)$$

$s_1 = 1 - \bar{z}$, and with $\epsilon_b = (\epsilon^2 + \Delta^2)^{1/2}$ Reference 1, Δ and ϵ are the parameters of the labile proton double-well, and $\vec{d}$ is the T-site separation.

At T = 300 K, the Q-dependence of the measured EISF is well described by (2) with $c_1 s_1 = 0.89$, indicating that most of the scattering protons at room temperature are labile. With $s_1(T) = 1$ for a symmetric well [1], the measured T-dependence of the EISF is an
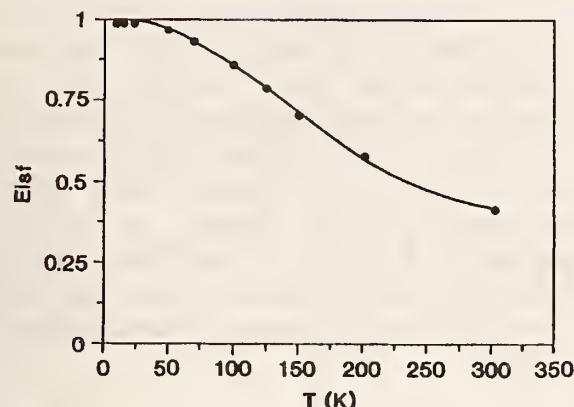
Figure 1. EISF vs. T for $ScH_{0.16}$. The solid line is a fit to the data using (2) with $s_1 = 1$. The T-dependence of c_1 is obtained by assuming Boltzmann occupations of labile and nonlabile configurations and a model density of labile states using two unequally weighted delta functions separated from the nonlabile state by (fitted) energies of 17 meV and 78 meV and with almost all the weight at the higher energy.

empirical measure of $c_{n1}(T)$, the fraction of nonlabile configurations. As figure 1 shows, at low temperatures only a small fraction of the protons are labile, but in our scheme these labile species are responsible for the anomalous hopping [1]. Preliminary analysis indicates that the occupational density of states for the labile protons are separated from the nonlabile configurations by energies in the range of 15-80 meV. The lower end of this broad band may reflect the influence of metastable configurations on the measured EISF at low T, while the upper portion suggests the magnitude of the T-site potential asymmetries due to short ranged order of paired nonlabile protons along the c-axis.

Reference

[1] N. F. Berk, J. J. Rush, T. J. Udovic, and I. S. Anderson, p. 1 of this report.

PROTON HOPPING IN α-YH$_x$ BY QUASIELASTIC NEUTRON SCATTERING

J. J. Rush, T. J. Udovic, and N. F. Berk
and
I. S. Anderson (Paul Scherrer Institut, Villigen, Switzerland)

A recent neutron scattering study of localized hydrogen dynamics in α-ScH$_x$ (described on p. 1) has demonstrated that a fraction of the protons in this system undergo a remarkably fast local "hopping" at low temperature between near neighbor H sites along the c-axis in the hcp structure. The associated quasielastic neutron linewidth shows a minimum at ~100 K and then <u>increases</u> at lower temperatures, leading to an apparent hopping rate of ~10^{12}/s at 10 K. The approximate T^{-1} dependence of the linewidth is consistent with nonadiabatic behavior associated with weak coupling of the quantum two-state system to the conduction electrons, the first such result observed for hydrogen in a pure metal.

Earlier this year we have extended our research on local dynamics of hydrogen in the rare-earth metals to a quasielastic scattering study of the α-YH$_x$ system at H concentrations of 1% and 10%. Previous quasielastic neutron scattering studies of this system have primarily concentrated on very high resolution studies of slow 3-d (long-range) diffusion of H in yttrium and on higher hydrogen concentrations. While the structure of the α-YH$_x$ and α-ScH$_x$ systems are similar, diffuse neutron scattering and neutron vibration spectra suggest a higher degree of proton ordering in the α-YH$_x$ system. In addition, the distance between near-neighbor tetrahedral sites along the c-axis is 30% greater for Y than for Sc, which could significantly affect the details of the potential and local motion and interactions of hydrogen.

Our measurements were performed on the IN-5 cold neutron time-of-flight spectrometer at the Institut Laue-Langevin using a neutron wavelength of 6.5 Å, which provided an energy resolution (FWHM) of 50 μeV. Very high purity single crystal specimens of area 2 x 5 cm and thicknesses of 2 cm and 0.2 cm, respectively, (for 1% and 10% H loading) were

obtained from Ames Laboratory at Iowa State University. Polycrystalline samples of equivalent dimensions were used as "blanks" whose scattering spectra could be subtracted from the H-loaded crystals to yield the H-scattering contribution.

The data from these experiments are currently being analyzed, but the results so far again show a minimum in the quasielastic peak width at ~175 K (compared to ~100 K for α-ScH$_x$) and an apparent turnaround to broader widths (faster "hopping") at lower temperatures.

The quasielastic intensity decreases rapidly with T as observed for α-ScH$_x$, reflecting the diminishing of the "labile" protons, while the widths are in general smaller than those observed for α-ScH$_x$. These observations are consistent with the existence of the considerably larger near-neighbor H-H distance in α-YH$_x$ (suggesting a deeper H potential), which apparently reduces "hopping" rates but still allows coupling of the protons to the conduction electrons.

NEUTRON SPECTROSCOPIC COMPARISON OF HEXAMETHYLDISILOXANE WITH TRIMETHYLSILYL ADSORBATES ON SILICA

T. J. Udovic, D. A. Neumann, and J. J. Rush
L. C. Sander (Organic Analytical Research Division)
and
I. S. Anderson (Paul Scherrer Institut, Villigen, Switzerland)

Incoherent inelastic neutron scattering (IINS) was previously used as a spectroscopic probe of trimethylsilyl (($CH_3)_3$Si-, TMS) adsorbates bonded to silica (SiO_2) via disiloxane-type linkages (i.e., $(CH_3)_3$Si-O-Si<). Above 75 meV, the TMS vibrational spectrum at 4 K (fig. 1a) indicate pronounced features due to Si-C-H and H-C-H bending modes as well as Si-C and Si-O stretching modes. Acceptable spectral fits by normal coordinate analysis required the stiffening of four of the nine Si-C-H bending force constants and six of the nine H-C-H bending force constants, assuming steric interactions between the silica surface and the four H atoms in closest proximity. The inequality of the Si-C-H bending force constants is illustrated by the apparent bending-mode splitting at 86 and 96 meV. This assumption was tested by comparison of the TMS/silica spectrum with the recently measured vibrational spectrum of hexamethyldisiloxane (($CH_3)_3$SiOSi($CH_3)_3$, HMDS) at 10 K (fig. 1b) likewise obtained using the BT-4 triple axis spectrometer. Except for a slight 1-2 meV shift to lower energies, the HMDS spectrum is very similar to the TMS/silica spectrum. Hence, the vibrational splitting in the TMS/silica spectrum appears not to be induced by a steric interaction of the methyl groups with the silica surface, but rather seems to be related to more general intramolecular interactions within the ($CH_3)_3$Si-O- fragment itself.

Future experiments will more closely investigate the origin of this splitting by determining the vibrational spectra of other related compounds containing from one to four bonded methyl groups per Si atom.
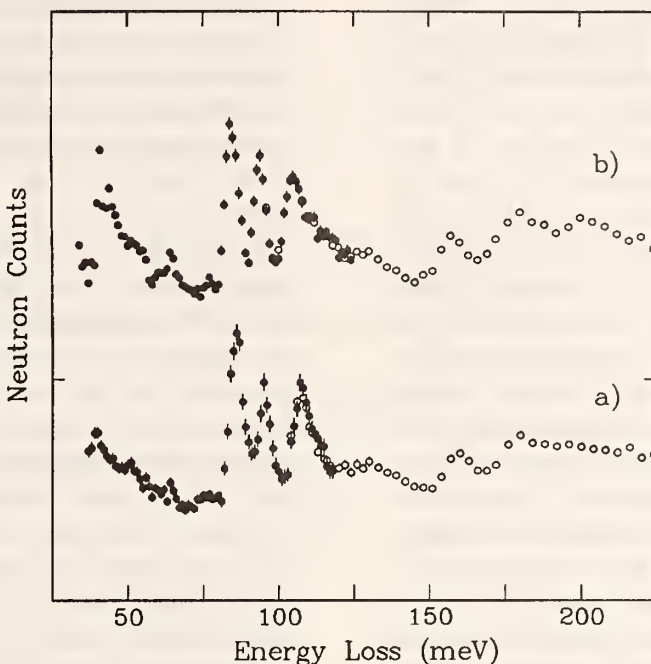
Figure 1. IINS spectra of a) trimethylsilyl/SiO_2 minus the SiO_2 blank at 4 K and b) hexamethyldisiloxane at 10 K. The spectra were obtained on the BT-4 triple-axis spectrometer with Cu($\overline{2}$20) monochromation and 40' pre- and post-collimation, using both the Be-filter (open circles) and the Be-graphite-Be-filter (closed circles) analyzers.

VIBRATIONAL SPECTROSCOPY AND LOCATION OF AMMONIUM IONS IN REAMMONIATED ZEOLITE RHO

J. M. Nicol (Reactor Radiation Division and University of Maryland, College Park, MD)
T. J. Udovic, R. R. Cavanagh, and J. J. Rush
and
G. D. Stucky (University of California, Santa Barbara, CA)

In zeolite rho the high flexibility of the framework and the ability to control the pore size by nonframework cations offers the opportunity of introducing a high degree of catalytic selectivity. This has, for example, been illustrated by the unique selectivity and activity exhibited by H-rho in the synthesis of dimethylamine from methanol and ammonia [1]. Of interest in this reaction is the observation that ion-exchanged ammonium-rho zeolite differs considerably in catalytic activity to ammonium-rho formed by the reammoniation of H-rho. Using inelastic neutron scattering techniques, the vibrational spectroscopy and molecular dynamics of ammonium ions formed during the reammoniation of H-rho have been investigated.

The H-rho zeolite used in the present investigation was generated during a study of the deammoniation of ion-exchanged ammonium-rho, as described previously [2]. The H-rho zeolite was loaded consecutively at 293 K with ammonia to concentrations corresponding to 1, 3, 6, and 11 ammonium ions per unit cell. (During reammoniation bound protons react with the adsorbed ammonia to form ammonium ions.) Inelastic scattering data in the energy range 5-190 meV were obtained using the BT-4 spectrometer at the NBSR in either the Be-filter analyzer or triple-axis mode.

The spectral changes that occur in the energy range 34-190 meV during reammoniation of H-rho as ammonium ions are formed and

5

protons are lost from the framework have previously been described [3]. These observations correlate well with those observed during deammoniation of ammonium-rho [2].

In the energy range below 20 meV, two modes due to the hindered rotations of the ammonium ions are observed at ca. 8 and 16 meV. As the ammonia loading level is increased both modes are seen to increase in intensity. Data collected at 10 and 80 K, however, show very different intensity patterns. In particular, at the highest ammonia loading, additional baseline intensity is seen below 10 meV at 80 K, which subsequently disappears on cooling the sample to 10 K. This intensity appears to result from a very broad quasielastic component. Quasielastic data also indicated the presence of a weakly bound component, as well as a component with a higher reorientation barrier.

The observation of two hindered rotational modes for ammonium ions in reammoniated zeolite rho reflects the location of ammonium ions in two different environments. This result correlates well with recent crystallographic data

for ammonium ion location in partially deammoniated and reammoniated zeolite rho [4]. In both structures the ammonium ions were found in the same framework sites. Two crystallographically different ammonium ion locations were observed, one close to the center of the double 8-rings (D8R) and the other outside the D8R in the α-cage. The ammonium ions located in the center of the D8R, were found to distort the D8R ring and shorten the unit cell constant considerably more than for as-synthesized ammonium-rho. The ammonium ions in the D8R are thus strongly coordinated to the framework oxygens. We suggest that the higher-energy mode observed at 16 meV, associated with a higher rotational barrier, is due to the ammonium ions located in the D8R site. The ammonium ions located in the α-cage are more weakly bound as their coordination to the framework oxygens is much less. We can thus assign the reorientational mode at 8 meV to the more weakly bound ammonium ions located in the α-cage sites.

References

[1] M. Keane, Jr., G. C. Sonnichsen, L. Abrams, D. R. Corbin, T. E. Gier, and R. D. Shannon, Appl. Cat. 32, 361 (1987).

[2] T. J. Udovic, R. R. Cavanagh, J. J. Rush, M. J. Wax, G. D. Stucky, G. A. Jones, and D. R. Corbin, J. Phys. Chem, 91, 5968 (1987).

[3] J. M. Nicol, T. J. Udovic, R. R. Cavanagh, J. J. Rush, and G. D. Stucky, NBS (U.S.) Tech. Note 1240.

[4] R. X. Fisher, W. H. Baur, R. D. Shannon, J. B. Parise, J. Faber, and E. Prince, Acta Cryst. C45, 983 (1989).

INELASTIC NEUTRON SCATTERING STUDIES OF NONLINEAR OPTICAL MATERIALS

J. M. Nicol (Reactor Radiation Division and University of Maryland, College Park, MD)
J. J. Rush
and
G. D. Stucky (University of California, Santa Barbara, CA)

Interest in nonlinear optical materials for second harmonic generation has grown considerably in recent years. The potassium titanyl phosphate and potassium titanyl arsenate family of phases have been shown to have important nonlinear and electro-optical

properties, which may be modified by substitution of potassium ions with other cations, such as ammonium ions, during synthesis.

The vibrational spectroscopy and molecular dynamics of ammonium ions in a series of substituted potassium titanyl phosphates and

studied a mode due to the torsional vibration of the ammonium ion is observed in the energy range 35-50 meV, as well as the symmetric and antisymmetric bending modes at ca. 180 and ca. 210 meV. Further studies and analysis of the data are currently in progress to relate the vibrational spectroscopy and ammonium ion molecular dynamics with structural information obtained from neutron diffraction and the measured nonlinear optical properties of these materials.

NEUTRON SCATTERING STUDY OF Cs-ND$_3$ INTERCALATED GRAPHITE

D. A. Neumann

Ph. Depondt (Universite Pierre et Marie Curie, Paris, France, University of Maryland, College Park, MD, and Reactor Radiation Division)

and

S. F. Trevino (ARDEC Picatinny Arsenal, NJ and Reactor Radiation Division)

Alkali-ammonia intercalated graphite is an ideal system for the study of the structure and dynamics of molecular liquids confined to a single layer. Earlier studies on graphite intercalated with K and ND$_3$ have shown a remarkable coupling of the longitudinal phonons which propagate along the c-axis to a librational mode of the ammonia molecule which occurs at an energy of about 7 meV [1]. In order to obtain additional information on the nature of this librational mode, we have recently begun work on Cs-ND$_3$ intercalated graphite.

The results of this preliminary work show that as in the K compound, the Cs-ammonia layer is a liquid at room temperature, but that the liquid structure factor does not show the prepeak due to clustering of the ammonia molecules about the alkali that was clearly evident for the K-ammonia case. This leads us to conclude that the Cs-ammonia complexes are much less well-defined than are the K-ammonia ones. We have also observed a liquid to solid intercalate transition at 190-195 K in the Cs case. For K-ammonia the same transition occurs at about 180-185 K.

Inelastic scattering results show that the out-of-plane longitudinal acoustic phonons are coupled with a librational mode of the ammonia molecule. As in the K-compound this librational mode occurs at about 7 meV. However, the splitting of the phonon branch is considerably larger in the Cs-ammonia system than that for the corresponding K case indicating that the rotation-translation coupling is much larger. In addition, no pronounced effect was observed in the inelastic scattering data when the sample was cooled through the liquid-solid intercalate transition.

The combination of the less well-defined complexes and the stronger rotation-translation coupling seem to be inconsistent with models of the librational mode which invoke interactions between the alkali ions and the ammonia molecules. It should also be pointed out that previous inelastic neutron scattering results on Cs-NH$_3$ powder taken in the solid intercalate phase show a pronounced peak at about 6 meV which was identified as librations of the ammonia molecule about the C$_3$ symmetry axis [2]. The fact that this energy, in a hydrogenated compound, is still lower than that observed here for the deuterated compound raises questions as to the assignment of this mode or points to other unsuspected interesting effects. Further analysis is currently in progress in order to more fully address these and other outstanding questions concerning the structure and dynamics of alkali-ammonia intercalation compounds.

References

[1] D. A. Neumann, H. Zabel, Y. Fan, S. A. Solin, and J. J. Rush, Phys. Rev. B37, 8424 (1988).

[2] Data taken by J. White et al., from the article by C. C. Wilson, Neutron News, 1(1), 14 (1990).

EVIDENCE OF RANDOM STRAIN FIELDS IN KCN AFTER THERMAL CYCLING

C. Bostoen (University of Antwerp, Wilrijk, Belgium)
and
S. K. Satija

The family of alkali cyanides has attracted a lot of interest due to its ferroelastic properties (e.g., [1]). KCN is known to transform to a low temperature orthorhombic phase. However, recent light transmittance experiments [1], show that the sample transforms after repeated cycling to a monoclinic phase, in agreement with early specific heat and x-ray measurements [2,3]. It was argued that the free energy of both the monoclinic and orthorhombic phase are close to each other and that scars of the low temperature phase are present in the high temperature phase, which after successive cycles force the crystal to transform to a monoclinic phase. Annealing the sample at room temperature removes the memory effect and the cubic phase then transforms again to the orthorhombic phase.

Recently, a Landau theory has been proposed to explain certain aspects of the polymorphism in the alkali cyanides and alkali halide cyanide mixed systems [4]. A competition between the free energy of the interactions and the free energy of the entropy terms exists: for NaCN, the interactions dominate the entropy terms, resulting in a strong first order phase transition to an orthorhombic phase. RbCN is the opposite extreme and closer to a second order phase transition, transforming to a monoclinic phase. KCN, finally, acts as a "bistable borderline case." The scars of the low temperature phase, present in the system at higher temperatures above T_c, act as static imperfections and may lead to random strain fields. These strain fields contribute to the entropy terms, thus favoring the monoclinic phase.

We performed inelastic neutron scattering measurements on KCN and RbCN crystals (purchased from the Crystal Growth Laboratory, University of Utah), in order to probe the possible existence of these random strains. A central peak was observed in earlier studies on mixed crystals of KCN/KBr and interpreted in terms of random strain fields [5,6]. The experiments were done at the BT-4 triple axis spectrometer with fixed incident neutron energy of either 5.0 meV or 5.5 meV. Typical collimations used were 40'-20'-20'-40' giving an energy resolution of the order of 130 μeV. Figure 1 shows the phonon spectrum from KCN at 170 K at Q = (1.9,0,2) before (open circles) the crystal has been subjected to a phase transformation. The solid lines are a fit to the data using a model previously used for KCN [7]. No central peak was observed as reported earlier [7]. First cooling of the crystal below the phase transition resulted in an orthorhombic phase. Upon heating the crystal above the phase transition the phonon spectrum changed dramatically giving rise to a large central peak (fig. 1 (closed circles)). A second cooling of the crystal below the phase transition now gives rise to a monoclinic phase. After annealing the crystal for 16 hrs at T = 340 K, no central peak was found at T = 170 K, and the crystal transformed to the orthorhombic phase. This situation stands in contradistinction with the RbCN crystal. Here no central peak was found, although the low temperature phase is monoclinic. In addition, we measured the LA and TA branches at T = 295 K, 200 K, 150 K, and 135 K. A lineshape analysis has been performed using a model applied earlier to KCN [7].
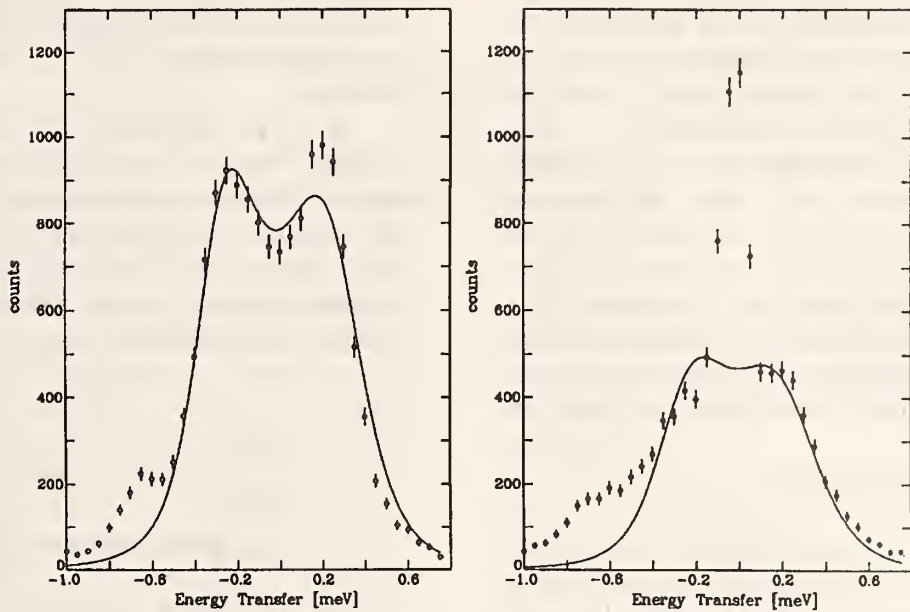
Figure 1. Scans at Q = (1.9,0,2) of KCN at T = 170 K. Open symbols: before cycling through T_c = 168 K; Closed symbols: after cycling through T_c. Solid lines are fits with model used in [7].

References

[1] J. Ortiz-Lopez and F. Lüty, Phys. Rev. B37, 5452 (1988).

[2] H. Suga, T. Matsuo, and S. Seki, Bull. Chem. Soc. Japan 38 1115 (1965).

[3] A. Cimino, G. S. Parry, and A. R. Ubbelohde, Proc. Roy. Soc. A252, 445 (1959).

[4] K. H. Michel and T. Theuns, Phys. Rev. B40, 5761 (1989).

[5] J. M. Rowe, J. J. Rush, D. J. Hinks, and S. Susman, Phys. Rev. Lett. 40, 1158 (1979).

[6] K. H. Michel, Phys. Rev. Lett. 57, 2188 (1986).

[7] J. M. Rowe, J. J. Rush, N. J. Chesser, K. H. Michel, and J. Naudts, Phys. Rev. Lett. 40, 455 (1977).

AN INTERMOLECULAR H-O POTENTIAL FOR NITROMETHANE

B. M. Rice (Ballistics Research Laboratory, Aberdeen MD)
and
S. F. Trevino (ARDEC, Picatinny Arsenal, NJ and Reactor Radiation Division)

In past work [1] the crystal structure of solid nitromethane has been determined by x-ray and neutron diffraction and the methyl group rotational energy levels have been measured at 4 K by inelastic neutron scattering. This work has resulted in a very well determined rotational potential, $V(\theta)$, which is presented in figure 1. In this figure the solid horizontal lines indicate the energy levels corresponding to the CH_3 group and the dashed lines to those for the CD_3 group. The compound shape of the potential is essential for the explanation of the location of these measured levels and their pressure dependence. A simple Lennard-Jones potential describing the H-O pairwise intermolecular interaction had previously been found which well describes $V(\theta)$ as presented in figure 1. In this figure, however, the value of $\theta = 0$ is not

arbitrary but corresponds to the equilibrium orientation of the methyl group about the C-N bond as determined by the diffraction studies. A fact not noted in the previous work is that the minimum of $V(\theta)$ does not occur at $\theta = 0$. The above mentioned H-O potential, which produces a $V(\theta)$ consistent with the spectroscopic observations, is thus not consistent with the crystal structure.

An extensive search for parameters of a Lennard-Jones, Buckingham, and other standard forms of pair potentials failed to obtain the desired $V(\theta)$. In the mean field approximation

$$V(\theta) = \Sigma_j v(r_j) \tag{1}$$

where $v(r_j)$ is the pair potential between the hydrogens and the j oxygen neighbors as a function of r. In order to make the contribution due to the spatial distribution of pairs (the crystal structure) explicit one may rewrite eq. (1) in an approximate form as

$$V(\theta_i) = \Sigma_k \Phi_{ik} v_k \tag{2}$$

where

$$\Phi_{ik} = \Sigma_j \delta[r_k - r_j(\theta_i)] \tag{3}$$

is the pair distribution function which contains the geometry of the problem. In this formulation the v_k are treated as independent parameters thus removing the constraint of a specific form for the pair potential. This is, however, not a problem amenable to least squares refinement. Instead the method of maximum entropy is used to obtain the following relationship.

$$v_k = v^o{}_k exp\{\Sigma_i \Phi_{ik} \times [V(\theta_i) - V^o(\theta_i)]\} \tag{4}$$

where $V(\theta_i)$ is the desired rotational potential and $V^o(\theta_i)$ is that corresponding to the set of values of $v^o{}_k$. This expression used in an iterative manner yields a set of v_k which can be used as a guide for further refinements. Without going into the details, the result of this procedure is the pair potential of figure 2 shown as the solid line and compared with the original Lennard-Jones shown as the dashed line. The solid line potential of this figure produces a $V(\theta)$ indistinguishable from that of figure 1 except

that the minimum is at $\theta = 0$. This is a rather novel form of the pair potential which could not be found without the maximum entropy technique.

Work on H-H and O-O potentials is in progress whose aim is to produce reliable potentials from which simulations of both static and dynamic properties can be made. It is hoped that these simulations will aid in understanding the behavior of nitromethane in both the solid and liquid state.
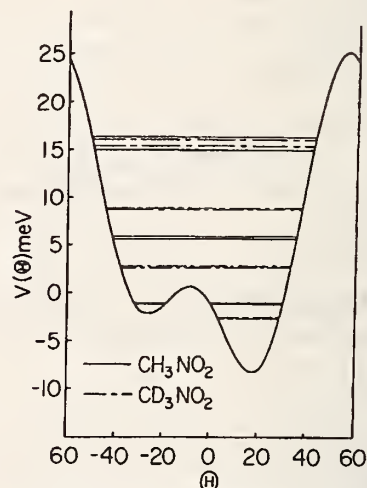
Figure 1. The rotational potential of the methyl groups in solid nitromethane. The horizontal lines represent the energy levels.
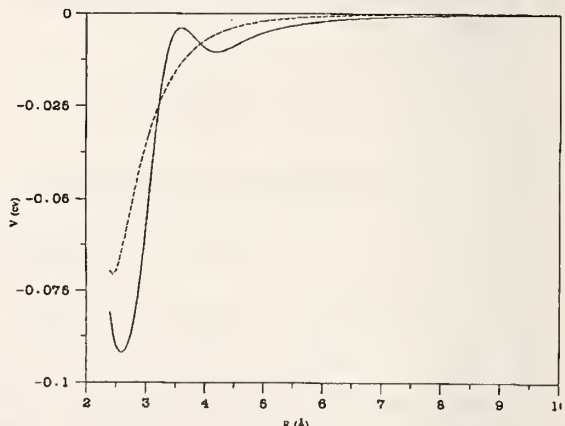
Figure 2. The H-O intermolecular pair potential for nitromethane. The dashed line corresponds to the original Lennard-Jones potential and the solid line to that derived in the present work (see text).

Reference

[1] D. Cavagnat, A. Magerl, C. Vettier, I. S. Anderson, and S. F. Trevino, Phys. Rev. Lett. 54, 193 (1985).

AB INITIO PHASE DETERMINATION IN A PROTEIN BY MAXIMUM ENTROPY

L. Sjölin (Chalmers University of Technology, Göteborg, Sweden)
E. Prince
and
L. A. Svensson and G. L Gilliland (Center for Advanced Research
in Biotechnology, Rockville, MD)

Previous experiments [1] in the use of maximum entropy as a phasing tool in macromolecular crystallography have concentrated on extending phases from a relatively low resolution starting set to higher resolution. From the beginning, however, there was a question whether the starting set could be as small as the two to four reflections whose phases can be chosen arbitrarily in order to specify one of a set of equivalent origins and one of the two enantiomorphs. A preliminary test on a set of x-ray diffraction data collected from bovine heart creatine kinase [2] gave very encouraging results, but it was desirable to determine if the structure of a macromolecule whose structure was known from a high quality refinement could be reproduced using maximum entropy for *ab initio* phase determination.

The data chosen for a test were collected from crystals of recombinant bovine chymosin and used in a recently completed determination and refinement of the structure [3]. The molecule of this protein contains 321 amino acid residues, and it crystallizes in space group I222, with one molecule per asymmetric unit. In this space group there are three sets of reflections hk0, h0l, 0kl, whose structure factors are constrained to be real. The phases of two reflections can be chosen to define a unique origin. There are no reflections whose structure factors are imaginary, so the enantiomorph must be determined by a general hkl reflection. The phases of two strong reflections were assigned the same phase as they had in the refined structure to ensure that they were referred to the same origin. Next, 16 more reflections were chosen, and maximum entropy maps were calculated giving these reflections 32 sets of phases according to a so-called "fractional factorial design," and the entropy of each of these maps was calculated. From this it could be estimated which phase for each reflection produced a higher entropy map. The map with

these phases and its entropy was then calculated, and the 16 others that had one phase different. Of the 49 phase sets tried by this procedure, the one that gave the highest entropy was chosen, and those reflections were then incorporated in the trial map.

This procedure was followed for three more blocks of 16 reflections, giving assigned phases for a total of 66 reflections. This map contained no enantiomorph determination, so the next step was to choose a strong hkl reflection and calculate a maximum entropy map with the phase of this reflection set at each 20° between 0° and 340°. The results of these calculations are illustrated in figure 1a. The entropy is symmetrical about 180°, reflecting the absence of any enantiomorph determining information, and has two sharp peaks at 60° and 300°. Although these calculations contain no information about the crystal structure, the actual phase of this reflection, calculated from the refined structure, is 64°. Therefore, 60° was chosen as the phase of this reflection, and it also was included in the trial map. The same procedure was then followed for the next strongest hkl reflection, with extra points in the vicinity of the peak, with the result shown in figure 1b. The entropy now has a unique maximum at 316°. Using similar procedures, phases were determined for an additional 93 reflections from the hk0, h0l and 0kl sets and 1809 hkl reflections, for a total of 1970 reflections.

Figure 2 illustrates the results of phase determination. Figure 2a compares a four amino acid segment of the refined structure with a density map using 948 reflections, while figure 2b is a map that includes the 1970 reflections whose phases were determined by the maximum entropy procedure. For comparison, the map in figure 2c is calculated using all data and phases calculated from the refined structure. 948 reflections is evidently an insufficient number to

produce connected density, but the similarity between the 1970 reflection map and the refined structure map is remarkable. In all three the molecular diagram is the refined structure, without any fitting to the map density.
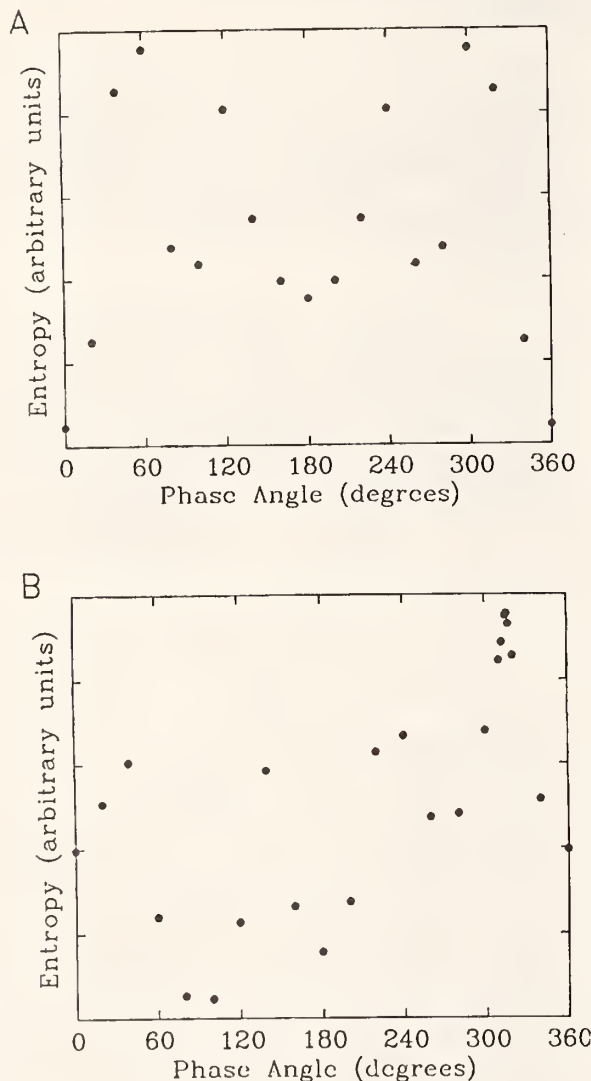
Figure 1. The maximum entropy of a fitted electron density map of recombinant bovine chymosin plotted as a function of the trial phases of the two strongest acentric reflections. (A) The prior map contains only centric reflections, and the strongest acentric reflection has been added. The plot is symmetrical about π, reflecting the two possible enantiomorphs. (B) The prior map contains the strongest acentric reflection, and the second strongest has been added. The plot is no longer symmetrical.

Figure 2. Portions of three electron density maps, compared with a four amino acid residue segment of the molecule of recombinant bovine chymosin. (A) A map computed from 948 reflections, with phases determined by maximum entropy. (B) The map with phases extended by maximum entropy to 1970 reflections. (C) The map computed using all data, with phases calculated from the refined structure.

References

[1] E. Prince and L. Sjölin, NIST Tech. Note 1272, C. O'Connor, ed. p. 18 (1989).

[2] G. L. Gilliland, L. Sjölin, and G. Olsson, J. Mol. Biol. 170, 791-793 (1983).

[3] G. L. Gilliland, E. L. Winborne, J. Nachman, and A. Wlodawer, Proteins (in press).

FAST FOURIER TRANSFORMS FOR MACROMOLECULAR CRYSTALLOGRAPHY

M. An and C. Lu (City University of New York, New York, NY)
and
E. Prince

Crystallographic calculations, including maximum entropy fitting, require repeated Fourier transforms of electron density maps to compute structure factors and of sets of structure factors to compute density maps. The fact that the values of the Fourier transforms can be computed at the points of lattice whose spacing can be chosen to be appropriate to the resolution of the data makes the problem well adapted to solution by fast Fourier transform (FFT) techniques, but it requires that efficient FFT routines be available for a wide range in the number of grid points per period of the crystal. At the same time, the space group symmetry of the crystal can be exploited to reduce still further the computing time and storage requirements for the Fourier transforms of the unit cells of macromolecular crystals [1]. A variety of FFT techniques [2] and newly developed methods for utilizing space group symmetry are being used to create a library of programs for crystallographic computations in the space groups in which biological macromolecules most commonly crystallize.

References

[1] L. F. Ten Eyck, Acta Cryst. A29, 183-191 (1973).
[2] R. Tolimieri, M. An, and C. Lu, Algorithms for Discrete Fourier Transforms and Convolution, (Springer-Verlag, New York, 1989).

ANION AND CATION DISORDER IN THE IONIC CONDUCTING PYROCHLORE SYSTEM $Y_2(Zr_xTi_{1-x})_2O_7$

S. M. Haile and B. J. Wuensch (Massachusetts Institute of Technology, Cambridge, MA)
and
E. Prince

Pyrochlore is a cubic crystal structure with the composition $A_2^{3+}B_2^{4+}O_7$ based on an ordered arrangement of subcells of the fluorite type. If the B ion is much smaller than the A ion, the ordered structure, which has the A ion at $(0,0,0)$, the B ion at $(1/2,1/2,1/2)$, oxygen anions in an eightfold and a forty-eightfold position, and vacancies at another eightfold position of space group Fd3m, forms. If, however, the B ion is too large, the crystal tends to take a disordered defect fluorite structure. In the system $Y_2(Zr_x Ti_{1-x})_2 O_7$ the disordered structure has a very substantial ionic conductivity.

In order to study the nature of the disorder a neutron powder diffraction study was undertaken of samples with $x = 0$ and $x = 0.6$. Because of the negative scattering amplitude of titanium, neutron diffraction is a very sensitive probe for determining its distribution among the different cation sites. It is also a sensitive probe for measuring the extent to which oxygen is redistributed among the sites of the pyrochlore structure. Table 1 is a summary of the results of a Rietveld refinement of the structure of the $x = 0$ composition and of preliminary results of a study of the $x = 0.6$ composition. There is insufficient information in the neutron diffraction data alone for a unique determination of the distribution of the three species of cation between the two sites, so this must include x-ray diffraction data also. The indication is that the disorder of the anion sites is almost entirely due to transfer of oxygen ions from the forty-eightfold positions to the vacant sites.

Table 1. Summary of the results of Rietveld refinement of the pyrochlores $Y_2Ti_2O_7$ and $Y_2(Ti_{0.4}Zr_{0.6})_2O_7$. Space group Fd3m

	$Y_2Ti_2O_7$	$Y_2(Ti_{0.4}Zr_{0.6})_2O_7$
Rwp	9.96%	13.26%
R_E	7.36%	8.45%
R_B	2.17%	11.85%
a_o	10.0947(1) Å	10.2910(4) Å
Y in 16c		
$\beta_{11}=\beta_{22}=\beta_{33}$	0.00160(8)	0.0035(2)
$\beta_{12}=\beta_{13}=\beta_{23}$	-0.00048(11)	0.0007(4)
Ti,Zr in 16d		
$\beta_{11}=\beta_{22}=\beta_{33}$	0.00067(17)	0.0046(5)
$\beta_{12}=\beta_{13}=\beta_{23}$	-0.00023(21)	-0.0001(8)
0(1) in 48f		
x	0.42082(9)	0.4012(4)
β_{11}	0.00157(10)	0.0102(4)
$\beta_{22}=\beta_{33}$	0.00114(9)	0.0065(3)
β_{23}	-0.00051(12)	-0.006(4)
0(2) in 8a		
$\beta_{11}=\beta_{22}=\beta_{33}$	0.00103(12)	0.0060(5)

Reference

[1] P. K. Moon and H. J. Tuller, Solid State Ionics 28-30, 470 (1986).

PROTEIN SYMMETRY

V. L. Himes and A. D. Mighell
and
J. R. Rodgers (National Research Council, Ottawa, Canada)

As part of our review of symmetry in crystalline materials, we have surveyed the proteins in the Brookhaven Protein Databank [1]. Using matrix [2] and reduction techniques, our analyses have revealed that it is not uncommon in these compounds for the metric symmetry to exceed the reported crystal symmetry.

Of particular note are proteins reported in the monoclinic space group $P2_1$. In a number of these cases, the metric symmetry is orthorhombic and the lattice can be defined by a C-centered orthorhombic cell. Potential explanations for this observation include: (1) an incorrect determination of the crystal system and Laue symmetry with subsequent refinement in a space group of too low symmetry, and (2) the overall shape of the molecule is more symmetrical than the internal symmetry or some other factor associated with the shape of the molecule. Because of the intense study devoted to any given protein, it is more likely that the second explanation accounts for our observation.

Regardless of the reason for the observation, our results have important implications for

experimental protein crystallography. Standard laboratory procedure should be modified to always include a direct determination of the metric symmetry as soon as any unit cell defining the lattice has been determined. With full knowledge of the highest possible symmetry, one is then able to determine in a logical and accurate manner the Laue group (2) and the space group. For those proteins in which it has been proved that the metric exceeds the crystal symmetry, the experimentalist must proceed with caution because a given lattice will have metrically similar unit cells that are 'not symmetrically equivalent.' Due to indexing/intensity ambiguities inherent in these cases, great care must be taken in the following situations: a) when comparing intensities on the same protein but taken by different experimentalists; b) when collecting and combining data for the same protein but from different crystals; and c) when measuring data on the same protein with different techniques (e.g., neutron and x-ray diffraction). Finally, in these cases, one should be on guard for such lattice related phenomena as twinning.

References

[1] Brookhaven Protein Databank: J. Mol. Biol. 112, 535-542 (1978).
[2] V. L. Himes and A. D. Mighell, "A Matrix Approach to Symmetry," Acta Cryst. A43, 375-384 (1987).

CRYSTAL STRUCTURE OF $C_{32}H_{46}N_6O_4 \cdot (CH_3)_2CO$

H. L. Ammon (University of Maryland, College Park, MD)
and
C. S. Choi (ARDEC, Picatinny Arsenal, NJ and Reactor Radiation Division)

The crystal structure of the titled compound was determined by x-ray diffraction using the ENRAF-NONIUS CAD-4 diffractometer at the x-ray laboratory of the Department of Chemistry, University of Maryland. The crystals were synthesized and grown by P. R. Dave of Geo-Centers, Inc., Hopatcong, NJ. The compound crystallizes in the orthorhombic Pnma space group with unit cell dimensions of a = 22.782(1), b = 15.950(1), and c = 9.809(1), containing four formula units of the titled compound including the solvent molecules (acetone) per unit cell. The structure was solved with the MITHRIL direct methods link, and was refined to the final R-factors of R = 0.048 and R = 0.064.

The compound is a large cyclic-linkaged molecule consisting of eight smaller molecules; i.e., two butylcyclotrimethyle-trinitramine rings, two benzoxyl rings, and four methylene groups (fig. 1). All the molecules in the crystal are positioned in the mirror plane. The mirror plane passes through the center of the large molecule, through the centers of the two benzene rings, and through the carboxyl atoms as can be seen in
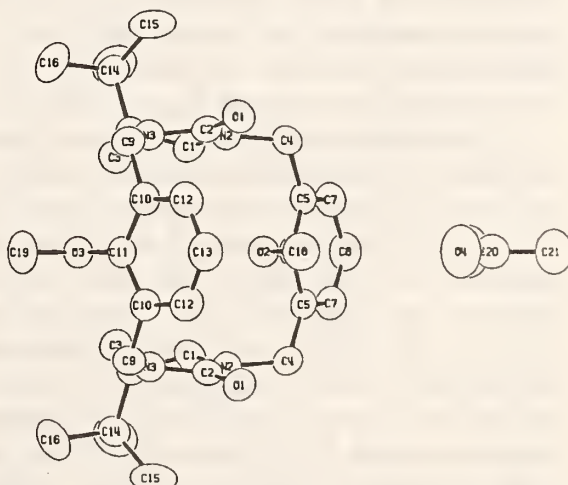
Figure 1. ORTEP drawing of the titled compound, viewed along the b-axis direction. The solvent (acetone) molecule is also included in the figure.

figure 1. The benzene rings are very slightly bent along the intersection line with the mirror plane. The molecules are packed rather loosely. The acetone molecules occupy the space left between the bulky molecules. All the acetone atoms except the H atoms are located on the

mirror plane. The intermolecular distances (nonhydrogeneous) shorter than 3.6 A are C(4) - O(1) = 3.390(3) between the solute molecules, and C(19) - O(4) = 3.597(7) between solute and solvent molecules. There are no evidences of hydrogen-bondings.

CRYSTAL STRUCTURE OF 2,2,4,4-TETRANITROADAMANTANE

H. L. Ammon (University of Maryland, College Park, MD)
and
C. S. Choi (ARDEC, Picatinny Arsenal, NJ and Reactor Radiation Division)

The titled compound is primarily of interest because of the energetic property and high density. The crystals were synthesized and grown by P. R. Dave of Geo-Centers, Inc., Hopatcong, NJ. The crystal structure was determined by x-ray diffraction using the ENRAF-NONIUS CAD-4 diffractometer at the x-ray laboratory of the Department of Chemistry, University of Maryland. The compound crystallizes in the monoclinic $P2_1/m$ with unit cell dimensions of a = 7.074(1), b = 13.395(2), c = 7.304(1), and beta = 112.79(1), containing two formula units per unit cell. The structure was solved with the MITHRIL direct methods link and was refined to the final R-factors of R = 0.047 and R_w = 0.069.

The molecule has mirror symmetry with the C3-C4-C5-C7 unit on the mirror plane as shown in figure 1. The bond lengths and angles are all normal, with the exception of the parameters associated with the dinitromethylene moiety. Here the two C-N bonds are stretched to 1.547 A and 1.551 A, and the N-C-N angle diminished to 98.2. Similarly, small N-C-N angle has been observed in 2,2,dinitro-adamantane with C-N distance of 1.555, and 1.560 A and N1-C2-N2 = 98.7. These distortions may be attributed to the geminal nitrogroups that, because of the strong electron demand place on C2, require an enrichment of the amount of the p character in the exocyclic orbitals at C. Several short intramolecular distances occur between the adjacent nitrogroups; O1...O1' = 2.884(7), O1...O3 = 2.965(4), O2...O4 = 3.394(4), and O2...O2' = 3.498(8). There are no intermolecular H-bonds. The molecules are bound mainly by the Van der
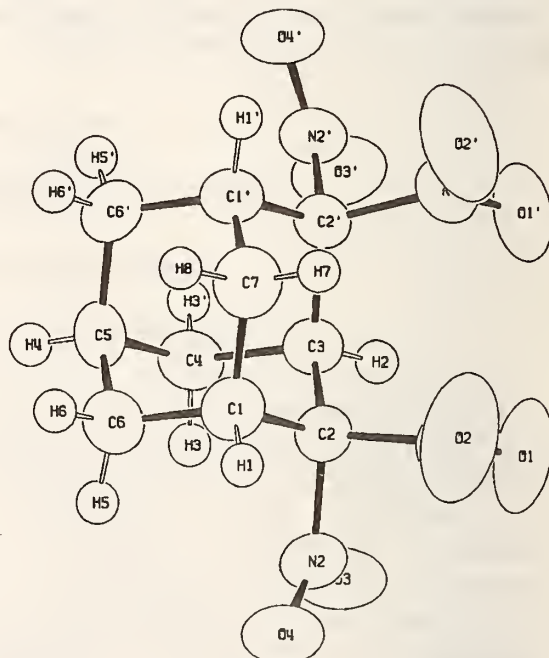
Figure 1. ORTEP drawing of 2,2,4,4-tetranitroadamantane molecule.

Waals' interactions between O and H atoms. The shortest intermolecular distances occur between O atoms with the distances, O1...O4 = 3.093(3) and O3...O4 = 3.153(4), and between O and H atoms with O1...H8 = 2.68(4), O3...H5 = 2.66(4), O3...H6 = 2.75(3), O4...H1 = 2.61(3), and O4...H3 = 2.77(3).

NEUTRON DIFFRACTION TEST OF THE METHOD OF REPRODUCIBLE PREPARATION OF THE AlCuFe ICOSAHEDRAL QUASICRYSTALS

Y. Calvayrac, M. Cornier-Quiquandon, D. Gratias,
and A. Quivy (C.E.C.M./C.N.R.S., Vitry, France)
R. Bellissent (C.E.N., Saclay, France)
J. W. Cahn (Materials Science and Engineering Laboratory)
and
B. Mozer

Isotopic substitutions are used in crystal structure determinations because this technique permits the determination of the contribution to neutron scattering from individual atomic species. Following the original suggestion of Bellissent, we are attempting to determine each individual atomic species' contribution to the neutron diffraction from the AlCuFe icosahedral quasicrystals whose aperiodic structure in 3-d can be described in terms of a 6-d periodic structure. We can determine the 6-d spatial distribution of the pair correlation function for each element in the quasicrystal and thereby deduce the 3-d distribution of all the elements.

To be able to separate each atomic species' contribution, it is necessary to prepare metallurgically identical samples which have different isotopic composition. At Vitry, a method of preparation of excellent icosahedral quasicrystal specimens of the AlCuFe alloy system has been developed. We wanted to determine if the Vitry method of preparation was capable of preparing metallurgically identical samples with different isotopic composition. To test this assumption without using the isotopes, Vitry prepared by their method two samples of the same composition under what was claimed to be identical conditions. Then both x-ray and neutron diffraction patterns were taken of the samples to note any differences. The two samples of $Al_{63}Cu_{24.5}Fe_{12.5}$, of roughly 10 g each, were powdered at Vitry and their x-ray diffraction patterns taken. Neutron diffraction patterns were measured on the BT-1 high resolution powder diffractometer at the NIST reactor on each of the two powder samples. Care was taken to insure that the same amount of powder was illuminated by the incoming neutron beam and that the vanadium sample holder was mounted in the same position in the beam for the two measurements.

The diffraction patterns for each powder sample at casual perusal seem to be identical. We took a difference of the two patterns and examined the resultant carefully with regard to the statistics of the measurement both for the monitor and for the counters. In the smaller q side of many peaks we found a small additional contribution to the intensity from one of the samples. To insure that this difference was a true effect and not a consequence of an error in the multiplicative factor for relative normalization of the two spectra, we varied this multiplicative factor. This adjustment would be expected to produce peaks or dips in the difference pattern in the region of each peak but it was not possible to eliminate the small additional intensity in the short q extreme wings of the lines of one sample. Furthermore, it was not possible to observe differences in the full widths of equivalent peaks for the two samples.

The explanation for the discrepancy in the two spectra might be given from some earlier work at Vitry on samples cooled from different temperatures after an anneal of the pure icosahedral phase. They observed that the shape of the peaks went from almost a pure Gaussian to almost a pure Lorentzian shape at 600 °C. Similar changes result from differences in the rate of cooling following the icosahedral phase anneal at a temperature above 660 °C. It is quite likely that the air cool procedure used in Vitry resulted in unequal cooling rates following the anneal.

We will continue to test preparations until we can say with confidence that the Vitry method of preparation of the AlCuFe icosahedral quasicrystals will yield quasicrystals with identical properties.

NEUTRON POWDER DIFFRACTION STUDY OF THE ORTHORHOMBIC Ti₂AlNb PHASE

L. A. Bendersky and W. J. Boettinger (Metallurgy Division,)
R. G. Rowe (General Electric Corporate Research and Development, Schenectady, NY)
and
B. Mozer

The crystal structure of the orthorhombic phase based on Ti₂AlNb originally discovered by Banerjee et al. [1] has been refined using the Rietveld method on neutron powder diffraction data collected from an extruded and heat treated alloy fabricated at General Electric.

Neutron powder diffraction was performed at room temperature with the high-resolution five detector diffractometer, BT-1, at the NIST reactor [2] using the experimental conditions in table 1. Four 2.5-cm long rods were bundled together with a common axis about which they were rotated during diffraction in order to minimize any effects from texture. The data were analyzed using the code written by Prince [3] which allows processing the intensities from the five detectors simultaneously. The background was represented by a Chebychev polynomial function with up to six coefficients per detector. Six coefficients were used for the first detector and two coefficients were used for the remaining four detectors and were refined for each channel together with the profile and structural parameters. The scattering lengths used for the refinement are b(Ti) = - 0.3438 Fermi (10(-12) cm.), b(Al) = 0.3449 Fermi, and b(Nb) = 0.7054 Fermi.

Rietveld refinement was performed using the structure suggested by Banerjee et al. [1] as an initial guess. First level refinement was performed to establish scale factor, background parameters, lattice parameters, and spectrometer zero. Subsequent refinements were performed to establish the atomic positions and the temperature factor. For the first model, the Wycoff sites were occupied by a unique atomic species having individual densities fixed according to the formula Ti₂AlNb. A correction was allowed for possible texture yielding a slight improvement. This model was not satisfactory in that the temperature factor for titanium was larger than acceptable for a simple alloy and even worse, the temperature factor for aluminum was negative. In order to improve upon this model, we allowed the three sites to be occupied by combinations of the three atoms and refined the occupancies along with all the other parameters. The best refinement obtained was a model where only aluminum occupied the 4cl site and titanium and niobium were distributed on the 8g and 4c2 sites. The total density was fixed according to the chemical formula. Another possible model was used following the suggestion of Banerjee et al. [1] where different Wycoff sites were assumed for the atomic species, their model figure 7(c) of table 4. This model and modifications of it allowing each site to be occupied by a combination of all species gave a much poorer refinement.

Table 1. Experimental conditions used to collect the neutron powder diffraction data

Monochromatic Beam	220 diffraction from Cu with a pyrolytic graphite filter to remove higher order contamination,
Wavelength	0.1553(1) nm
Horizontal Divergences	10, 20, and 10 min of arc for the in-pile, monochromator beam, and diffracted beam collimators, respectively.

The refinement of our powder neutron diffraction data of the orthorhombic phase of Ti_2AlNb was able to fix the model of the structure as one having only aluminum on the 4c1 site and a mixture of titanium and niobium on the 8g and 4c2 sites and eliminate the other two models suggested by Banerjee et al. [1]. The results of our refinement are given in table 2.

Table 2. Results of Rietveld refinement

Space Group Cmcm

| Atom | Wycoff Positions | | | Temperature Factor | Relative Occupancy |
	X	Y	Z		
Ti(8g)	0.2310(12)	-0.0959(6)	1/4	2.02(.14)	0.823(4)
Al(4c1)	0.0	0.1633(3)	1/4	0.48	0.5
Nb(4c2)	0.0	-0.3643(3)	1/4	0.62(.10)	0.323(4)
Nb(8g)	0.2310(12)	-0.0950(6)	1/4	2.02(.14)	0.177(4)
Ti(4c2)	0.0	-0.3643(3)	1/4	0.62(.10)	0.177(4)

Lattice Constants in Angstroms

a = 6.0893(2)   b = 9.5694(4)   c = 4.6666(2)

Statistical Factors

Rn = 10.53   Rp = 11.21   Rw = 14.98   Re = 8.11   Chi = 1.845

Note: Figures in parentheses are standard deviations in the decimal figures. The temperature factor is in Angstroms squared. R factors are defined in A. Santoro, R. S. Roth, and D. Minor. Acta. Cryst. B33, 3945 (1977).

References

[1] A. K. Gogia, T. K. Nandi, and V. A. Joshi, Acta Met. 36, 871.
[2] E. Prince and A. Santoro, Natl. Bur. Stand. (U.S.) Tech Note No. 1117, F. Shorten, ed. p. 11, (1980).
[3] Ibid, p. 8.

K$_{1-x}$(ND$_4$)$_x$I: A CRYSTAL STRUCTURE DETERMINATION

C. Bostoen (University of Antwerp, Wilrijk, Belgium)

and

J. K. Stalick and S. K. Satija

This study was motivated by recent incoherent inelastic neutron scattering experiments [1] and dielectric measurements [2]. These results show that the ammonium ion has a dipole moment; however, its microscopic nature is unknown. In order to elucidate this question, neutron powder diffraction measurements were performed on K$_{1-x}$(ND$_4$)$_x$I mixed crystals. The mixed crystals were prepared from an aqueous solution of D$_2$O (99.7+%) with the appropriate amounts of KI and ND$_4$I. The deuterated ammonium iodide was obtained after successive exchanges with D$_2$O. A Raman scattering analysis showed that six exchanges gave a sufficient degree of deuteration. Assuming Vegard's rule to be valid for this mixed system, the ND$_4^+$ concentration determined from the lattice constant obtained from x-ray data is 41%. The diffraction experiments were performed on the BT-1 high-resolution powder diffractometer with λ = 1.553 Å and collimations 20'-20'-10', before and after monochromator and before the detectors, respectively. Diffraction patterns were recorded for temperatures T = 4.7 K and 43 K.

For this concentration, the structure is cubic, space group Fm3m, with the NaCl structure type. For the Rietveld refinement of the profiles, we applied a model used earlier for NH$_4$I: three of four hydrogens are directed toward the iodide ions, the remaining N-H bond is pointed along the < 111 > direction [3]. The main outcome of the refinement is that the ammonium ion is slightly distorted from its ideal tetrahedral shape. For T = 43 K, the bond angles are 115° for the angles between < 111 > and iodine bonded hydrogens, and 103° for the angles between the iodide bonded hydrogens. For an ideal tetrahedron these angles are all equal to 109.45°. From this deformation one can extract a dipole moment of 1.3 $\pm$ 0.2 D for the 43 K data, in agreement with the dielectric results [2]. The ammonium concentration was also allowed to vary during the refinement and gave x = 0.40, consistent with the x-ray analysis. The obtained U, V, and W linewidth parameters were fairly large and evidence a strain broadening of about 0.3%, comparable to what was obtained in U doped with 0.5% of Ti [4]. There was no indication that the ND$_4^+$ ion was off center and the N-D distances were in agreement with other ammonium compounds [5]. The lattice constants are 7.088 Å and 7.090 Å for T = 4.7 K and 43 K, respectively.

References

[1] C. Bostoen, G. Coddens, and W. Wegener, J. Chem. Phys. 91, 6337 (1989).

[2] I. Fehst, R. Böhmer, W. Ott, A. Loidl, S. Haussühl, and C. Bostoen, Phys. Rev. Lett. 64, 3139 (1990).

[3] H. A. Levy and S. W. Peterson, J. Chem. Phys. 21, 366 (1953).

[4] C.S. Choi and H. J. Prask, J. Appl. Cryst. 18, 141 (1985).

[5] See for example, H. J. Prask, C. S. Choi, N. J. Chesser, and G. J. Rosasco, J. Chem. Phys. 88, 5106 (1988).

$K_{1-x}(NH_4)_xI$: A PHASE DIAGRAM STUDY BY MEANS OF X-RAYS

C. Bostoen (University of Antwerp, Wilrijk, Belgium)

and

S. K. Satija

This study was motivated by recent experimental results. Neutron time-of-flight results show a very broad distribution of tunneling lines, related to the different environments which the ammoniums experience in the alkali halide lattice [1]. Dielectric susceptibility measurements indicate that the ammonium ions have a dipole moment. In addition, a dynamical freezing process similar to other dipolar glass forming materials was reported [2], although no glass like anomalies were found in the specific heat [3]. The nature of the dipole moment was determined by neutron diffraction (see p. 20). However, the phase diagram of this system was unknown.

Polycrystalline mixed crystals were grown from an aqueous solution under nitrogen gas atmosphere in order to reduce the oxidation of the ammonium salt. At room temperature the powders contained the pure mixed crystals, without any Bragg peaks from the pure compounds, KI or NH_4I. From the lattice constants at room temperature and the validity of Vegard's rule, one can determine the ammonium concentration. The concentrations considered are: x = 0.55, 0.72, 0.82, 0.84, 0.88, and 0.97.

A support for a Displex was installed, making it possible to perform x-ray measurements from T = 10 K up to 340 K. Pure NH_4I has a low-temperature CsCl structure, which transforms to a tetragonal structure (slightly distorted from the CsCl structure at low temperatures [1]. The (111) reflection of the NaCl structure and the (100) reflection of the CsCl structure were recorded in subsequent steps of $\Delta T = 10$ K on cooling and heating. All the samples had the following similarities: 1) Part of the sample remained in the NaCl structure down to T = 10 K. 2) A large hysterisis effect was observed: the point where the transition occurred to a low temperature ordered phase, was much lower than the point where the sample was again in the NaCl structure when heated from T = 10 K to

room temperature or higher (fig. 1). It is known that the phase transition in pure NH_4I has a martensitic character, involving a change of a sixfold to an eightfold configuration and a volume change of 17%. As the concentration of spherical impurities is increased, T_c is reduced, similar to the situation in KCN/KBr [4].

The critical concentration, x_c, where the phase transition is suppressed, is between 0.72 and 0.82. It would be interesting to test recent ideas in terms of formations of microdomains each having their own strain order parameter [5], on samples which are close to x_c.
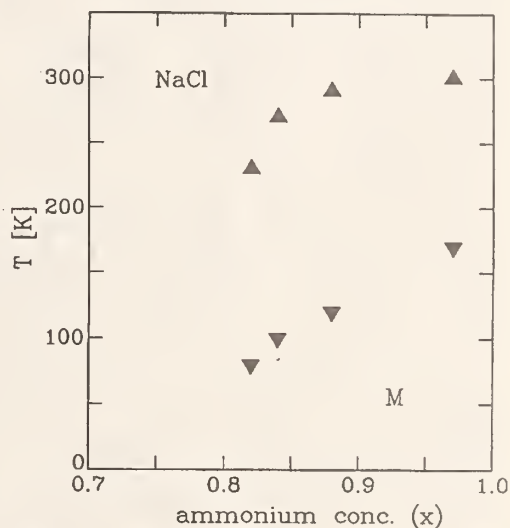
Figure 1. Phase diagram of $K_{1-x}(NH_4)_xI$. NaCl: orientationally disordered rocksalt structure (▼: cooling, ▲: heating). M: mixed phase of NaCl and CsCl structure.

References

[1] C. Bostoen, G. Coddens, and W. Wegener, J. Chem. Phys. **91**, 6337 (1989).

[2] I. Fehst, R. Böhmer, W. Ott, A. Loidl, S. Haussühl, and C. Bostoen, Phys. Rev. Lett. **64**, 3139 (1990).

[3] C. Bostoen, K. H. Michel, B. Vaziri, M. Meissner, and S. Haussühl, PHONONS 89, S. Hunklinger et al., eds. Singapore: World Scientific, 1990, 615 p.

[4] See for example, S. Mertz and A. Loidl, Europhys. Lett. **4**, 583, (1987).

[5] K. Knorr, Phys. Rev. **B41**, 3158 (1990).

STRUCTURAL STUDIES IN THE BaO-Nd$_2$O$_3$-CuO SYSTEM

W. Wong-Ng (Ceramics Division) and J. K. Stalick

The structures of two compounds, BaNd$_2$CuO$_5$ and BaNd$_2$O$_4$, have been determined with the Rietveld method using neutron powder diffraction data collected with the high-resolution five-detector diffractometer at NIST. These studies are in conjunction with phase equilibrium studies in the BaO(BaCO$_3$)-Nd$_2$O$_3$-CuO system [1], which also contains the superconductor NdBa$_2$Cu$_3$O$_7$.

The material BaNd$_2$CuO$_5$ is the stoichiometric end-member of the solid solution Ba$_{2+2x}$Nd$_{4-2x}$Cu$_{2-x}$O$_{10-2x}$, with a narrow solid solution range of $0 \leq x \leq 0.1$. Unlike the smaller lanthanides (R), which form the green phase BaR$_2$CuO$_5$ (tetragonal, space group P$\overline{4}$m2), for R = Nd or La the solid solution is brown, with the tetragonal space group P4/mbm. The La system has been studied by Kilbanow et al. [2] and Michel et al. [3]; the extent of solid solution was found to be $0.15 < x < 0.25$, with the stoichiometric composition BaLa$_2$CuO$_5$ absent. The crystal structure of the La analog has been studied using x-ray diffraction [3], although the Ba and La atoms could not be differentiated owing to the similarity of their scattering factors. The atomic parameters for the La analog were used as starting parameters for the refinement of BaNd$_2$CuO$_5$, and refinement proceeded smoothly to agreement factors of R$_B$ = 2.97, R$_{wp}$ = 5.36, χ = 1.15. Since the scattering lengths for Nd and Ba are significantly different for neutron diffraction, we could confirm that the larger Ba atom exclusively occupies the 2b site, and the smaller Nd atom exclusively occupies the 4g site. The BaNd$_2$CuO$_5$ framework is built from edge- and face-sharing BaO$_{10}$ and NdO$_8$ polyhedra; the square-planar CuO$_4$ groups are isolated in the structure. Our results are in agreement with the atomic distribution suggested by Michel et al. [3] for Ba$_{1.2}$La$_{1.8}$Cu$_{0.9}$O$_{4.8}$, in which some Ba atoms presumably occupy the smaller La site. This seems inconsistent with the inability to prepare the stoichiometric BaLa$_2$CuO$_5$ compound, as this composition would not require such site substitution and should be structurally more stable.

In this same system, phase equilibrium studies [1-2,4] also showed that for the larger lanthanides R = La, Nd only one binary phase BaR$_2$O$_4$ is formed. This is in contrast to the smaller lanthanides, which exhibit additional binary phases as R becomes progressively smaller. For example, when R = Y four binary phases are formed [5], including BaY$_2$O$_4$. X-ray powder diffraction studies of BaY$_2$O$_4$ have suggested that it is orthorhombic with space group Pnab (no. 60) [5], or isostructural with SrY$_2$O$_4$ (CaFe$_2$O$_4$ structure type) with space group Pnam (no. 62) [6]. Recently, intensity calculations by Costa et al. [7] for powder x-ray data indicated that the latter space group is probable, and we have confirmed this for BaNd$_2$O$_4$ using neutron Rietveld refinement. The excellent agreement between the calculated and observed intensities (R$_B$ = 5.12, R$_{wp}$ = 3.59, x = 1.13) indicates that the space group Pnam is correct. In this structure the Ba atom is eight-coordinate, located near the center of a trigonal prism formed by six oxygen atoms; two of the rectangular faces are further capped by oxygen atoms. The two crystallographically independent Nd atoms exhibit the expected octahedral coordination by six oxygen atoms.

References

[1] W. Wong-Ng, B. Paretzkin, and E. R. Fuller, Jr. J. Solid State Chem. 85, 117 (1990).

[2] D. Kilbanow, K. Sujata, and T. O. Mason, J. Amer. Ceram. Soc. 71, C267 (1988).

[3] C. Michel, L. Er-Rakho, and B. Raveau, J. Solid State Chem. 39, 161 (1981).

[4] R. S. Roth, C. J. Rawn, F. Beech, J. D. Whitler, and J. O. Anderson, "Ceramic Superconductors II," M. F. Yan, ed., pp. 13-26, Amer. Ceram. Soc. (1988).

[5] W. Kwestroo, H. A. M. van Hal, and C. Langereis, Mater. Res. Bull. 9, 1623 (1974).

[6] I. M. Maister and L. M. Lopato, Izv. Akad. Nauk SSSR, Neorg. Mater. 9, 64 (1973).

[7] G. A. Costa, M. Ferretti, M. L. Fornasini, E. A. Franceschi, and G. L. Olcese. Powd. Diff. 4, 24 (1989).

POLYTYPIC STRUCTURES OF SODIUM METAL FOLLOWING THE MARTENSITIC TRANSFORMATION

R. Berliner (University of Missouri-Columbia, Columbia, MO)
and
H. G. Smith (Oak Ridge National Laboratory, Oak Ridge TN)
and
J. R. D. Copley
and
J. Trivisonno (John Carroll University, Cleveland, OH)

Neutron diffraction studies of sodium metal performed on the BT-9 spectrometer in 1988 have been the subject of considerable subsequent analysis. Like lithium metal, sodium undergoes a martensitic structural phase transformation as it is cooled [1]. In lithium metal, the transformation is at ~ 78 K to a multivariant nine layer R$\overline{3}$M rhombohedral lattice [2]. Four c-axis crystallization axes are found near each BCC (110) direction. The same 9R lattice and multivariant morphology is observed following the martensitic transformation near 35 K in sodium metal. Evidence that the low temperature structure of sodium is more complicated than lithium is found in the diffraction pattern along a (10ℓ) line in reciprocal space. The most prominent diffraction features are those that can be attributed to peaks of the 9R phase, shifted from their calculated peak positions by the presence of "double-twin" stacking fault type layer defects. The 9R diffraction peaks exhibit shoulders which were initially believed to be the result of stacking-fault-distorted diffraction from an HCP phase, but all attempts to model peak shifting in HCP structures have failed. The asymmetric nature of the diffraction peak shoulders was eventually recognized as evidence that these features were due to another rhombohedral phase, and analysis of the shoulder position suggests that it has between 21 and 27 layer stacking periodicity. There are, for example, 13 different 27R stacking patterns and only one of these produces diffraction patterns sufficiently like the data to be considered at length. This stacking pattern, illustrated in terms of A, B, and C layers,

/ABCBCBCBC/BCACACACA/CABABABAB/

may also be described in terms of hexagonal (H) and cubic (K) layer types.

/HKHHHHHHH/HKHHHHHHH/HKHHHHHHH/

This pattern is easily recognized as a superlattice consisting of an even number of hexagonal layers separated by single layers in a cubic environment. It is possible to show that there is an infinite set of these "almost HCP" rhombohedral stackings. Diffraction from these structures produces better and better approximations to an HCP diffraction pattern as the c-axis lattice parameter becomes longer. This effect is illustrated in figure 1 where the calculated (10ℓ) diffraction patterns for the "almost HCP" structures from 3R (FCC) to 45R are compared to that for HCP. These structures can be transformed, one into another, by the injection of special stacking faults. For instance, the 9R structure is converted to the 15R by the insertion of sufficient "double-twin" stacking faults. In like manner the 15R is converted to the 21R and the 21R to the 27R. The presence of all of these structures is suggested by the analysis of the diffraction patterns of sodium metal as the specimen is warmed to the martensitic reversion temperature. A model which incorporates stacking fault broadened and shifted 9R, 15R, and 21R polytype fractions for the sodium martensite produces a striking resemblance to the major features of the diffraction data. Figure 2 compares the diffraction data to the polytype mixture model calculation.

Analysis of martensite structures and their relative stability in sodium is continuing. In addition, the investigation of alkali metal alloy systems that undergo similar martensitic trans-

formations and the study of the alkali metals
under hydrostatic pressure is also under way.

Rhombohedral Polytype Diffraction Patterns
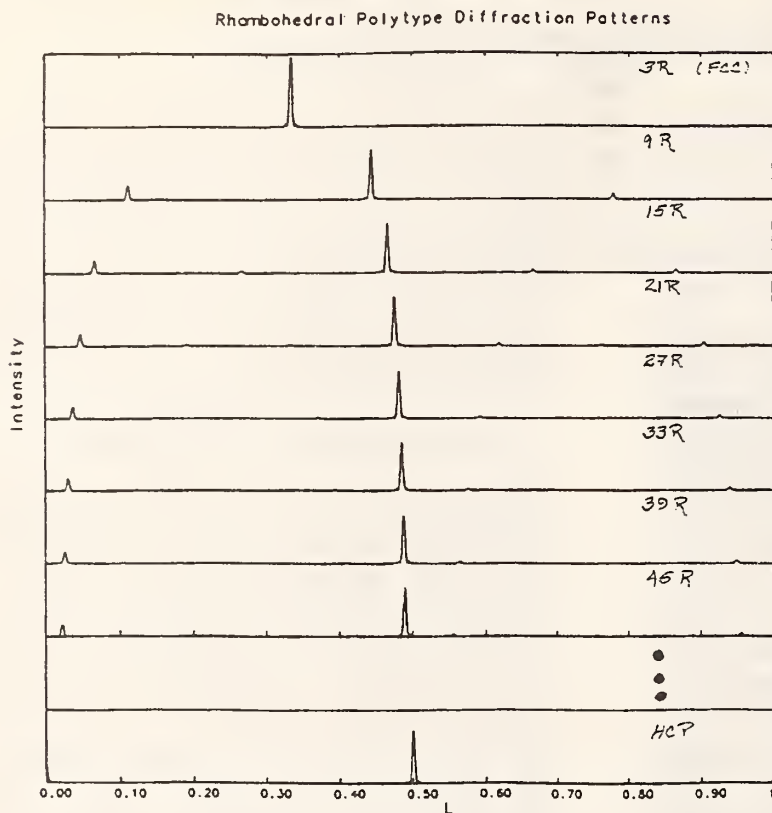
Figure 1. Calculated (10ℓ) diffraction patterns for "almost HCP" rhombohedral stacking polytypes compared to the diffraction pattern for HCP.
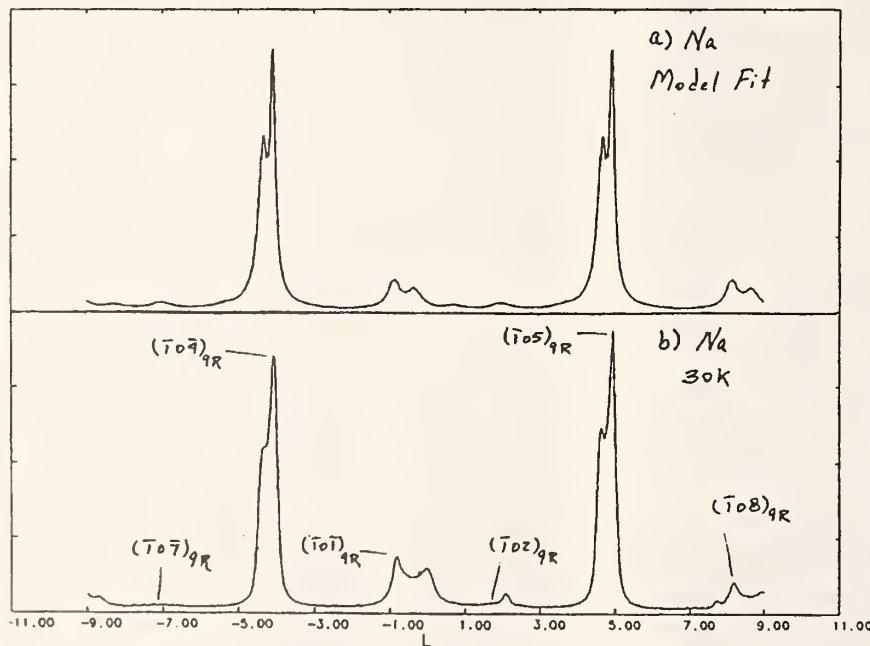
Figure 2. (a) The (10ℓ) diffraction pattern for sodium, calculated for a 9R, 15R, and 21R polytype mixture model. (b) The measured (10ℓ) diffraction pattern for sodium below the martensitic transformation temperature.

References

[1] R. Berliner, O. Fajen, H. G. Smith, and R. L. Hitterman, Phys. Rev. **B40**, 12086 (1989) and references therein.

[2] H. G. Smith, Phys. Rev. Lett **58**, 1228 (1987).

THE CRYSTAL STRUCTURE OF THE 60 K SUPERCONDUCTOR $La_{1.6}Sr_{0.4}CaCu_2O_{6\pm\delta}$

R. J. Cava, J. J. Krajewski, R. M. Fleming, J. V. Waszczak, W. F. Peck, Jr., and P. Marsh
(AT&T Bell Laboratories, Murray Hill, NJ)
and
A. Santoro

All the known copper oxide-based super-conductors contain layers of copper-oxygen squares, pyramids, or octahedra as their electronically active structural components. One structure type (see figure 1) first reported for $La_2SrCu_2O_6$ and $La_2CaCu_2O_6$ [1] has until recently stood as an enigma because it could not be made superconducting even though at its heart are the double copper oxide pyramidal layers common to the highest T_c superconductors. We have recently shown that the structure type can be made superconducting at 60 K at the composition $La_{1.6}Sr_{0.4}CaCu_2O_6$ [2]. This is a uniquely simple double layer superconductor, as it becomes superconducting through the intro-duction of carriers by straightforward atomic substitution, without the intervention of complex charge reservoir layers.

The crystal structure of this superconductor has been determined by neutron diffraction powder profile analysis in this laboratory, using the intensities measured with the high-resolution five-counter diffractometer. The structure was refined with the Rietveld method [3] adapted to the multicounter diffractometer and modified to include background parameters [4]. Peak shapes were described by Gaussian functions. The neutron scattering amplitudes used in the refinements were $b(La) = 0.827$, $b(Ca) = 0.490$, $b(Sr) = 0.702$, $b(Cu) = 0.772$, and $b(O) = 0.581 \times 10^{-12}$ cm.

Initial positional parameters were taken from our structural refinement [5] of the nonsuper-conducting end-member $La_{1.9}Ca_{1.1}Cu_2O_{6-\delta}$, in the tetragonal symmetry spacegroup I4/mmm. All positional parameters, and isotropic temperature factors, as well as metal (with the exclusion of copper) and oxygen site occupancies were allowed to vary simultaneously. The La, Sr, and Ca contents were constrained to sum to their chemically determined values. The refine-ment quickly converged ($\chi = R_W/R_E < 1.5$) for a model where the Sr is in solid solution on the nine coordinated La site, the Ca is ordered as
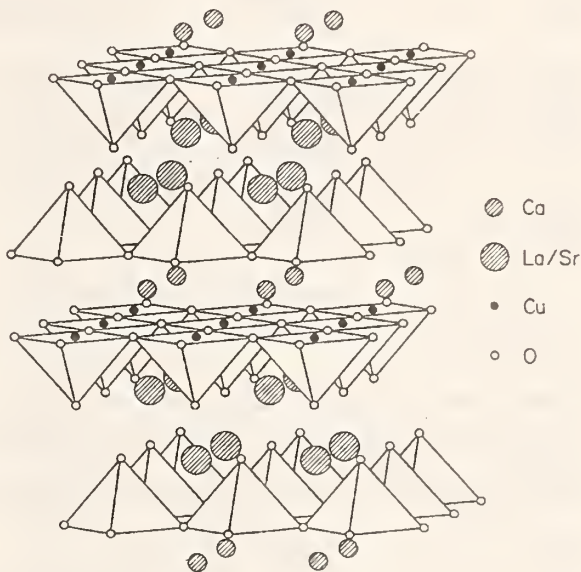
Figure 1. The crystal structure of $La_2CaCu_2O_6$ and $La_{1.6}Sr_{0.4}CaCu_2O_6$. The CuO_5 pyramidal planes are the active electronic components. The large shaded circles are large cations nine coordinated (primarily La and Sr) to oxygen and the small shaded circles are small cations (primarily Ca) eight coordinated to oxygen.

expected in the eight-coordinated site between the bases of the pyramids, with no oxygen in the Ca layer, and a small amount of oxygen deficiency is in the oxygen site at the apices of the copper oxide pyramids. The atomic parameters for the crystal structure are presented in table 1. Also shown for convenience are the results from our earlier refinement of $La_{1.9}Ca_{1.1}Cu_2O_6$. Table 2 presents the metal-oxygen bondlengths for $La_{1.6}Sr_{0.4}CaCu_2O_{5.94}$, again compared to those we found for $La_{1.9}Ca_{1.1}Cu_2O_6$.

Table la. Refined structural parameters of $La_{1.6}Sr_{.4}CaCu_2O_{6-\delta}$

Space Group: I4/mmm a = 3.8208(1), c = 19.5993(7), V = 286.13(2)Å^3

Atom	Position	x	y	z	B(Å^2)	n
La	2a 4/mmm	0	0	0	0.75(16)	0.047(8)
Ca	2a 4/mmm	0	0	0	0.75(16)	0.203(8)
La(l)	4e 4mm	0	0	0.17666(13)	0.79(7)	0.353(8)
Sr(l)	4e 4mm	0	0	0.17666(13)	0.79(7)	0.1
Ca(l)	4e 4mm	0	0	0.17666(13)	0.79(7)	0.047(8)
Cu	4e 4mm	0	0	0.58656(13)	0.76(1)	0.5
O(1)	8g mm	0	0.5	0.08211(11)	1.18(7)	1.02(l)
O(2)	4e 4mm	0	0	0.7036(2)	1.58(10)	0.477(6)
	R_n = 6.27	R_p = 8.41		R_w = 11.36	R_e = 8.60	χ =1.32

Table lb. Refined structural parameters [5] of $La_{1.9}Ca_{1.1}Cu_2O_6$

Space Group: I4/mmm a = 3.8248(1), c = 19.4286(5), V = 284.22(2) Å^3

Atom	Position	x	v	z	B(Å2)	n
La	2a 4/mmm	0	0	0	1.0(1)	0.014(6)
Ca	2 a 4/mmm	0	0	0	1.0(1)	0.236(6)
La(l)	4e 4mm	0	0	0.17578(9)	0.47(5)	0.47(1)
Ca(l)	4e 4mm	0	0	0.17578(9)	0.47(5)	0.03(1)
Cu	4e 4mm	0	0	0.58503(9)	0.32(4)	0.5
O(1)	8g mm	0	0.5	0.08230(9)	0.74(5)	1.005(8)
O(2)	4e 4mm	0	0	0.7046(2)	1.52(8)	0.506(6)
	R_n = 4.58	R_p = 5.96		R_w = 8.54	R_e = 4.34	χ = 1.97

Table 2. Metal-oxygen bondlengths in $La_{1.9}Ca_{1.1}Cu_2O_6$ and $La_{1.6}Sr_{0.4}CaCu_2O_{6-\delta}$

	$La_{1.9}Ca_{1.1}Cu_2O_6$	$La_{1.6}Sr_{0.4}CaCu_2O_{5.94}$
Ca-O(1) x 8	2.493(1)	2.498(1)
La-O(1) x 4	2.638(1)	2.662(2)
La-O(2) x 4	2.762(1)	2.753(1)
La-O(2) x 1	2.324(3)	2.348(7)
Cu-O(1) x 4	1.913(1)	1.912(1)
Cu-O(2) x 1	2.323(3)	2.293(6)

References

[1] N. Nguyen, et al., Mat. Res. Bull. 15, 891 (1980).
[2] R. J. Cava, et al., Nature 345, 602 (1990).
[3] H. M. Rietveld, J. Appl. Cryst. 2, 65 (1969).
[4] E. Prince, Natl. Bur. Stand. (U. S.) Tech. Note 1117, F. Shorten, ed., p. 8-9, (1980).
[5] A. Santoro, et al., Mat. Res. Soc. Symp. Proc. 166, 187 (1990).

CRYSTAL STRUCTURE AND ATOMIC ORDERING IN
$Pb_2Sr_2Y_{1-x}Ca_xCu_3O_{8+\delta}$ ($x = 0$, $\delta = 1.47$)

M. Marezio and R. J. Cava (AT&T Bell Laboratories, Murray Hill, NJ)

J. J. Capponi (Laboratoire de Cristallographie, Grenoble, France)

E. A. Hewat (LETI-CENG, Grenoble, France)

and

A. Santoro and F. Beech

The superconducting series $Pb_2Sr_2Y_{1-x}Ca_xCu_3O_{8+\delta}$ was first reported by Cava et al. [1] and almost simultaneously by Subramanian et al. [2]. The structure for $\delta = 0$ and $x = 0$ was found to be orthorhombic, space group Cmmm, lattice parameters a = 5.393 Å ~ $\sqrt{2}a_p$, b = 5.431 Å ~ $\sqrt{2}a_p$, and c = 15.773 Å (a_p being the simple pervoskite parameter) and two chemical formulate per unit cell. Subsequently, $Pb_2Sr_2 Y_{1-x}Ca_xCu_3O_{8+\delta}$ samples were characterized by electron microscopy by Zandbergen et al. [3].

The structure of the prototype compound $Pb_2Sr_2YCu_3O_8$ can be easily described as built of (AO) and (BO_2) layers arranged as to form either perovskite or NaCℓ blocks in [4]. The sequence of the (AO) and (BO_2) layers for $Pb_2Sr_2YCu_3O_8$ is as follows: $(Y)_o(CuO_2)_c(SrO)_o$ $(PbO)_c(Cu)_o(PbO)_c(SrO)_o(CuO_2)_c(Y)_o$ (see fig. 1.) All oxygen atoms are absent in the (Y) and the (Cu) layers. The subscripts o and c indicate whether the cation is at the origin or at the center of the mesh, respectively.

The structural refinements based on powder neutron data in [5] revealed that the small orthorhombic distortion is due to disordered oxygen displacements in the PbO plane. Electron diffraction patterns perpendicular to [001] showed that the crystallites are twinned by the (110) planes, and that, in agreement with Zandbergen in [3], very weak and well defined (hk0) diffraction spots with h+k odd, which violate the C-centering, are always present. These spots define the unit cell with a = $\sqrt{2}a_p$, b = $\sqrt{2}a_p$, and indicate that the space group is primitive and the small displacements of the oxygen atoms in the PbO layers are actually somewhat ordered [6]. Fu et al. [7] who studied the isostructural compound $Pb_2Ba_2YCu_3O_8$ by electron and neutron diffraction, obtained similar results. By taking into account the reflections violating the C-centering, they determined from the neutron diffraction data that the most probable space group for $Pb_2Ba_2YCu_3O_8$ and isostructural compounds is $P2\bar{2}_12$.

As in the case of $YBa_2Cu_3O_6$, $Pb_2Sr_2YCu_3O_8$ can take up oxygen, too. This property was first discussed by Cava et al. in their original paper [1] and subsequently by Gallagher et al. [8], O'Bryan et al. [9], and Gyory et al. see [10]. No trace of superconductivity has been detected so far in any oxidized $Pb_2Sr_2YCu_3O_{8+\delta}$ samples. In order to understand this unique behavior we have carried out thermogravimetric, x-ray, neutron, and electron diffraction investigations of some oxidized samples.

The neutron powder diffraction measurements were made at room temperature with the high-resolution five-counter diffractometer at the NBSR. Neutrons of wavelength 1.553 Å were used in the experiment with in-pile, monochromatic beam, and diffracted beam collimators having horizontal angular divergencies of 10, 20, and 10 minutes of arc, respectively. The same sample used for the determination by neutron diffraction of the $Pb_2Sr_2YCu_3O_8$ structure [5] was heat-treated at 500 °C in O_2 and then cooled rapidly to room temperature. It was placed in a vanadium can of about 1-cm diam and the data were collected in the angular range 5°-120° in steps of 0.05°.

The structure was refined with the Rietveld method [1] adapted to five-detector geometry and modified to include background parameters [12]. The neutron scattering amplitudes used in the calculation were b(Pb) = 0.94, b(Sr) = 0.702, b(Y) = 0.775, b(Cu) = 0.772, and b(O) = 0.581 x 10^{-12}cm. The peak shape could be described satisfactorily by Gaussian functions. The initial atomic parameters of the structure were those of $Pb_2Sr_2YCu_3O_8$ [5] transformed to

those of the a_p x a_p x c cell. The refined positional and thermal parameters are given in tables 1 and 2. It can be seen that the thermal parameters for the split atoms are reasonable except along the a-axis. The value of the O5 occupancy factor is 0.47(3) which corresponds to a chemical formula $Pb_2Sr_2YCu_3O_{9.47}$, in good agreement with that found by thermo-gravimetry ($O_{9.40}$). One unit cell of the $Pb_2Sr_2YCu_3O_{9.47}$ structure is shown in figure 1.

Table 1. Refined positional, isotropic thermal (Å^2) and occupancy parameters for $Pb_2Sr_2YCu_3O_{9.47}$.

Atom	Position	x	y	z	B	n
Pb	2t mm	1/2	1/2	0.3814(2)	3.5^1	1/2
Sr	2q mm	0	0	0.2204(3)	1.5^1	1/2
Y	1a mmm	0	0	0	0.74(13)	1/4
Cu1	1c mmm	0	0	0.5	3.5^1	1/4
Cu2	2t mm	1/2	1/2	0.1027(2)	0.53(8)	1/2
O1	2t mm	1/2	1/2	0.2499(6)	5.4^1	1/2
$O2^3$	$8\alpha 1$	0	0.165(3)	0.3810(7)	5.1	1/2
O3	2r mm	0	1/2	0.0918(2)	0.96(8)	1/2
O31	2s mm	1/2	0	0.0918^2	0.96^2	1/2
$O4^3$	4x m	0	1/2	0.458(1)	6.5	1/4
O5	2p mm	1/2	0.217(8)	1/2	0.95^4	0.117(3)

[1] The thermal paramters of this atom have been refined anisotropically, the value reported in this column represents the corresponding isotropical B value.

[2] This value has been constrained to the corresponding value of O3.

[3] These positions correspond to the refinements during which these atoms were split over the positions (0yz) for O2 and (0 1/2 z) for O4.

[4] B_{05} was fixed at 0.95, value given by the previous refinement during which the O5 occupancy factor was fixed at the value (0.10) obtained by the thermogravimetric analysis.

Table 2. Anisotropical thermal parameters* (Å^2) of Pb, Sr, Cu1, O1, O2, and O4 on $Pb_2Sr_2YCu_3O_{9.47}$

Atom	B_{11}	B_{22}	B_{33}
Pb	3.0(5)	5.4(7)	2.0(3)
Sr	-0.1(5)	2.9(6)	1.8(3)
Cu1	4.3(7)	3.9(7)	2.3(5)
O1	1.3	11(1)	4.0(5)
O2	5.2(9)	7(1)	2.7(6)
O4	15(2)	2(1)	2(1)

*For all atoms $B_{12} = B_{13} = 0$ by symmetry.

References

[1] R. J. Cava, et al., Nature, 336, 211 (1988).
[2] M. A. Subramanian, et al., Physica C157, 124 (1989).
[3] H. W. Zandbergen, et al., Physica C158, 155 (1989).
[4] A. Santoro, et al., Physica C156 693 (1988).
[5] R. J. Cava, et al., Physica C157, 272 (1989).
[6] E. A. Hewat, et al., Physica C157, 509 (1989).
[7] W. T. Fu, et al., Physica C159, 210 (1989).
[8] P. K. Gallagher, et al., Chem. Matls. 1, 277 (1989).
[9] H. M. O'Bryan and P. K. Gallagher, Chem. Matls. 1, 526 (1989).
[10] E. M. Gyory, et al., Chem. Matls. 1, 571 (1989).
[11] H. M. Rietveld, J. Appl. Crystal. 2, 65 (1969).
[12] E. Prince, Natl. Bur. Stand. (U.S.) Tech. Note 1117, F. Shorten, ed. p. 8 (1980).
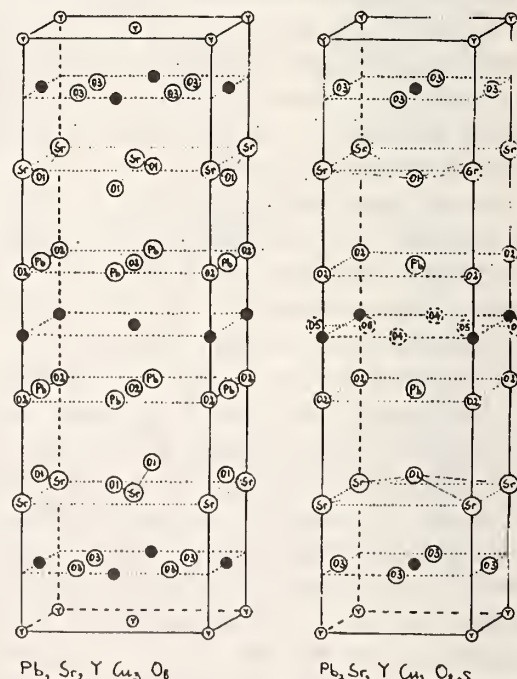
Figure 1. One unit cell of the $Pb_2Sr_2YCu_3O_{9.47}$ structure.

TWINNING AND OXYGEN DISTRIBUTION IN $Pb_2Sr_2YCu_3O_{8+x}$

J. J. Capponi and E. A. Hewat (Laboratoire de Cristallographie, CNRS, Grenoble, France)
R. J. Cava and M. Marezio (AT&T Bell Laboratories, Murray Hill, NJ)
and
A. Santoro

The scheme:

$$...[(CuO_\delta)_o \quad (PbO)_c(SrO)_o \quad (CuO_2)_c(Y)_o(CuO_2)_c \quad (SrO)_o(PbO)_c] \quad (CuO_\delta)_o...$$

$$...[(CuO_\delta)_o \quad\quad (BaO)_c \quad\quad (CuO_2)_o(Y)_c(CuO_2)_o \quad\quad (BaO)_c] \quad\quad (CuO_\delta)_o...$$
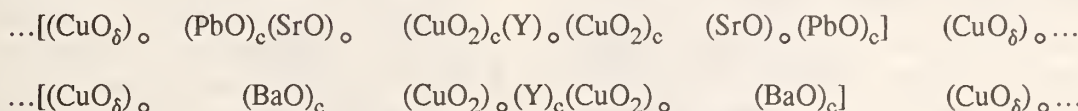
is a comparison of the structure of $Pb_2Sr_2YCu_3O_{8+x}$ (first sequence) and $YBa_2Cu_3O_{6+x}$. The layer (BaO) present in the 1-2-3 compound is replaced by the bilayer (SrO)(PbO) in the lead compound. The other structural elements are the same in the two systems. (In this scheme each layer is represented by a chemical symbol representing the composition of the layer, and by a subscript $\underline{o}$ or $\underline{c}$ indicating if the cation is at the origin or at the center, respectively, of the mesh characteristic of the layer.)

The slice $...(PbO)_c(CuO_x)_o(PbO)_c...$ in the structure of $Pb_2Sr_2YCu_3O_{8+x}$ is represented in figure 1. Atom O2, O4, and O5 are split with respect to their idealized, symmetrical positions. For $x = 0$ the O4 and O5 sites are empty. For $x = 1$, only sites O4 are occupied with an occupancy of 50%. For $x > 1$ the sites O5 become gradually filled and the occupancy reaches a maximum of 50% for $x = 2$. Sites O2 are always half occupied since this oxygen is not involved in the oxidation process.

The approximate bond distances given in figure 1 are for the composition $x \approx 1.5$ (25% occupancy of the O5 sites).

Geometrical constraints impose a correlation between the occupation of sites O4 and O2. More specifically, if an oxygen atom O4 is located on a site above the plane of the copper atoms, then the two sites O2 within the unit cell in the level above will be empty and those in the level below will be full, and vice versa. This situation results in a configuration up-down of the O4 atoms along the b-axis of the structure. No correlation exists, however, along the a-axis.
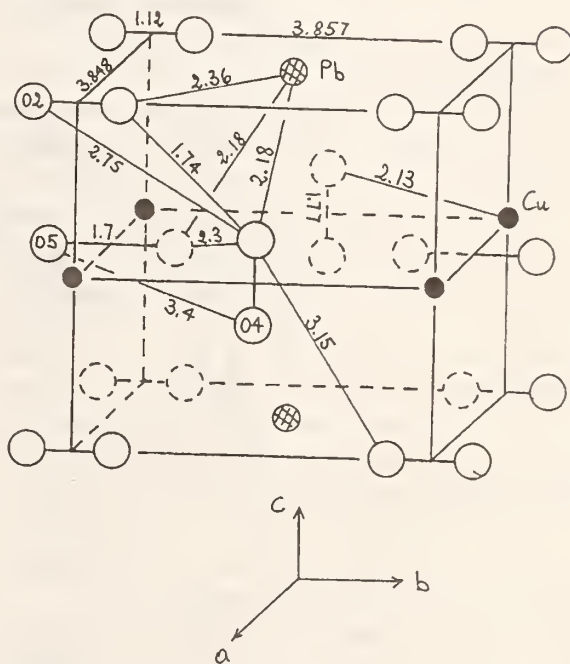
Figure 1. Slice (PbO) (CuO_x) (PbO) in the structure of $Pb_2Sr_2YCu_3O_{8+x}$.

The up-down configuration of the O4 atoms results in a (short-range) doubling of the b-axis and in the formation of square-planar Cu-O$_2$ chains along this axis. The arrangement of the oxygen atoms along the a-axis, however, can be of two types, as indicated in figure 2 for the composition $x = 1$, and does not impose a multiplicity greater than one in this direction (the O5 sites are empty for $x = 1$ and have not been represented for clarity).

Twinning in this system is present at all compositions. The proposed model of the twin boundary structure for the compound $Pb_2Sr_2YCu_3O_{9.0}$ is represented in figure 3. Full circles represent the Cu atoms at $z = 0$, small hatched circles are Pb atoms at $z \approx \pm 1/8$, full large circles are O4 oxygens atoms whose location is represented with a + (above plane of figure) or - (below plane of figure). The circles outlined with broken lines are O2 oxygen atoms located at $z \approx 1/8$ (dotted) or at $z \approx -1/8$ (clear). This configuration is an extension of the model of the twin walls proposed for $YBa_2Cu_3O_{7.0}$.

The lower part of the figure shows the structure of the boundary in three dimensions. Note that the O4 atoms at the wall have an up-down configuration to avoid unrealistically short oxygen-oxygen distances.
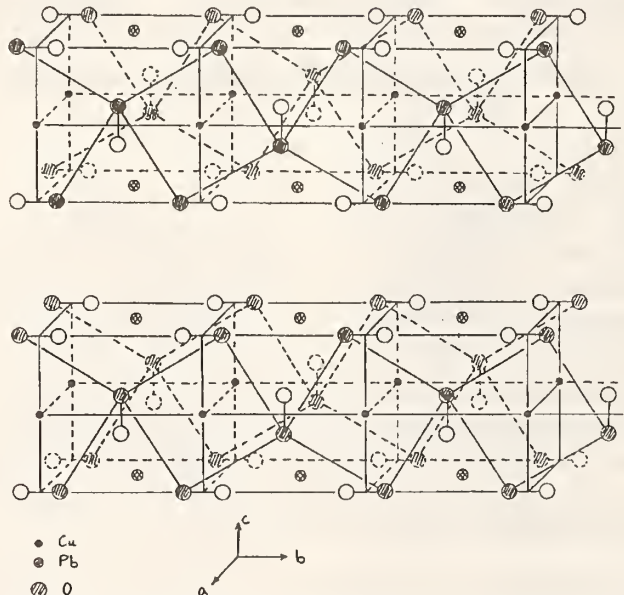
Figure 2. Possible oxygen distributions in $Pb_2Sr_2YCu_3O_9$.
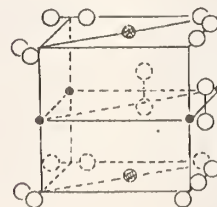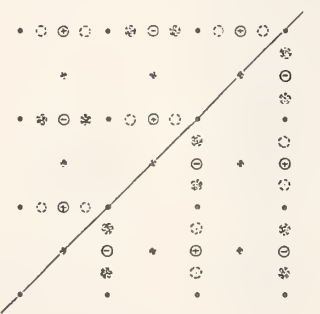
Figure 3. Model of the twin-boundary structure for $x = 1$.

INCORPORATION OF GOLD INTO $YBa_2Cu_3O_7$: STRUCTURE AND T_c ENHANCEMENT

J. K. Stalick and J. J. Rhyne

and

M. Z. Cieplak, G. Xiao, and C. L. Chien (The Johns Hopkins University, Baltimore, MD)

Chemical doping has proven to be a powerful method in unraveling the crucial aspects of high-T_c superconductors [1-3]. However, noble metals, particularly Au, have been widely considered to be inert as far as high-T_c superconductors are concerned. The successful utilization of gold as a buffer layer for high-T_c films, gold-superconductor composites, gold contacts, gold-tunneling barriers, etc., reinforces this belief. Also, gold crucibles have now enjoyed the status of producing some of the best high T_c single crystals to date. Such single crystals have been subjected to intense research in order to capture the fundamental properties intrinsic to $YBa_2Cu_3O_7$.

We have found, however, that Au does in fact substitute for Cu when Au powder is annealed with pure 1:2:3 powder according to the formula $(YBa_2Cu_3O_7)_{1-x}Au_x$. A solubility limit of 10 at.% Au (x = 0.1 in the above formulation) was indicated by gravimetric weight loss measurements, optical microscopy, and x-ray analysis of the lattice parameters. The 1:2:3 material remains orthorhombic upon Au substitution, with a significant increase in the c-lattice parameter. Neutron Rietveld refinement of data on a sample with x = 0.08, collected on the high resolution five-detector powder diffractometer at NIST, showed that the Cu-O plane assembly is not affected by Au doping. However, along the c-axis the bond length between the Cu(1) chain site and the bridging oxygen O(1) increases significantly by 1.36% compared to pure 1:2:3, while the Cu(2)-O(1) distance decreases by 0.3%. Thus the bridging O(1) atom is displaced toward Cu(2) while the Cu(1)-Cu(2) distance increases by 0.4%. Although the above changes in atomic position suggest substitution by Au on the Cu(1) site, the similarities in scattering lengths for Au and Cu preclude direct determination using neutrons. Therefore, since the x-ray scattering factors of Cu and Au are very different, the same sample

was analyzed using x-ray data collected on a Scintag diffractometer with a scattered beam monochromator at NIST. Rietveld refinement of the x-ray data showed conclusively that Au occupies exclusively the Cu(1) site. The refined occupancies of Au(1) = 0.084(4) and Au(2) = - 0.005(3) are consistent with the 8% as-prepared concentration.

It has been established [3] in 1:2:3 that all the divalent dopants (Zn^{2+}, Ni^{2+}) substitute into the Cu(2) plane sites, whereas all the trivalent dopants (Al^{3+}, Co^{3+}, Ga^{3+}) occupy the Cu(1) sites with a concomitant increase in oxygen content. The oxygen content of the Au-substituted 1:2:3 as determined from the neutron refinement was 7.04, consistent with Au^{3+}. For substitution in the Cu(2) planes, T_c is reduced drastically, while for substitution in the Cu(1) chains T_c in general is reduced more gradually and the material becomes tetragonal. Gold substitution is unique, however, in that the orthorhombic distortion increases slightly with increasing Au content, while T_c also systematically increases by about 1.5 K at x = 0.1. This benign effect of Au doping on superconductivity is a very useful feature. The presence of Au will change many other properties such as lattice dynamics and some normal state properties. Studies of the superconducting behavior and the properties affected by Au doping will enable a better understanding of their correlations.

References

[1] J. T. Market, et al., in Physical Properties of High Temperature Superconductors I, D. M. Ginsberg, ed., (World Scientific, Singapore, 1989).

[2] C. L. Chien, G. Xiao, M. Z. Cieplak, Oxygen Disorder Effects in High T_c Superconductors, J. L. Moran-Lopez and I. K. Schuller, eds. (Plenum, New York, 1989).

[3] C. L. Chien, et al., Superconductivity and Its Applications, H. S. Kwok and D. T. Shaw, eds. (Elsevier, New York 1988).

MAGNETIC PHASE TRANSITIONS IN Sm_2CuO_4

S. Skanthakumar, J. W. Lynn, and I. W. Sumarlin
(University of Maryland, College Park, MD and Reactor Radiation Division)
and
J. L. Peng and Z. Y. Li (University of Maryland, College Park, MD)

The magnetic properties of the high-T_c superconducting oxides have attracted considerable interest both because of the intrinsic interest in magnetism and because of the possibility that the magnetic fluctuations are responsible for the Cooper pairing. It is clear now that the 2-d sheets of Cu-O in the $(La_{2-x}Sr_x)CuO_4$ and in $RBa_2Cu_3O_{6+x}$ (R = rare earth) systems are intimately involved in both the magnetism and superconductivity, with magnetic long-range order occurring at small x and fluctuating moments existing in the superconducting regime at larger x. The charge carriers are holes in these systems. Superconductivity has been discovered in a new class of materials, $R_{2-x}Ce_xCuO_{2-y}$ (R = Pr, Nd or Sm), which are known as electron superconductors since the charge carriers are electrons rather than holes. The existence of these materials places important constraints on any theory of the oxide superconductors. In this regard it is of central concern to elucidate the nature of the magnetism in this new class of systems.

The magnetic properties of Nd_2CuO_4 and Pr_2CuO_4, which are parent materials of the electron superconductors, have been studied recently by using neutron diffraction techniques [1-5]. The Cu ions in these compounds order antiferromagnetically at higher temperatures (~ 250 K). Two other spin reorientations of the Cu sublattice occur at 75 K and 30 K in Nd_2CuO_4, and in addition there is a substantial interaction between the Nd and Cu sublattices [2]. However, these spin reorientations do not occur in Pr_2CuO_4 [5]. In the present work we report neutron diffraction measurements on Sm_2CuO_4 which is also a parent material of electron superconductors.

A thin plate-like single crystal weighing 66 mg was grown by mixing SmO_3 and CuO powders. Extra CuO was used as a flux to reduce the melting point of the starting materials. The crystal was mounted in the (hhl) scattering plane and the data were taken between the temperatures of 0.75 and 300 K. The very high neutron absorption for samarium made the measurements quite difficult. Measurements were made at higher temperatures to investigate the ordering of the Cu, and in a ^3He cryostat to search for the Sm ordering.

A series of magnetic Bragg peaks were observed below T_N = 280 K, and can be indexed as $(h/2,k/2,l)$ based on the chemical unit cell, where h and k are odd integers. Since the first two Miller indices are half integers, the Cu magnetic unit cell is double the chemical unit cell along both the a and b directions. This indicates that the magnetic spin configuration of the Cu spins in Sm_2CuO_4 is the same as the configuration found in Nd_2CuO_4 and Pr_2CuO_4 [1-5]. However, the spin directions are different. For example, in Pr_2CuO_4, and Nd_2CuO_4 in the high temperature ordered state, the (1/2,1/2,0) peak is found to have negligible intensity, while in Sm_2CuO_4 a strong (1/2,1/2,0) magnetic Bragg peak is observed. The temperature dependence of that peak is shown in figure 1, and reveals a Néel temperature T_N = 280 ± 1 K. Our measurements do not indicate any spin reorientations, in contrast to the behavior found for the Nd_2CuO_4 material.

Our low-temperature measurements did not show any significant change in the intensities of $(h/2,h/2,l)$ peaks, or development of new peaks down to 0.75 K. Specific heat and magnetic susceptibility measurements show that the Sm orders antiferromagnetically at 5.95 K [6]. If the Sm ions in Sm_2CuO_4 order like the Nd ions in Nd_2CuO_4, then the Sm moment must be less than 0.1 μ_B. However, it is more likely that the Sm ions order in a different configuration than the Nd ions in Nd_2CuO_4, and measurements in other scattering planes will be done to investigate this possibility.

Sm_2CuO_4
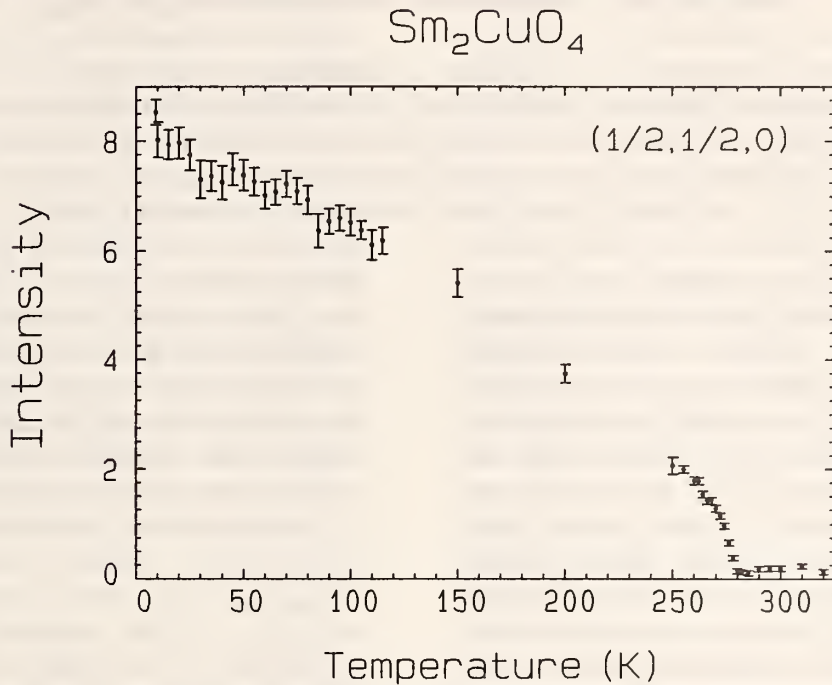
Figure 1. Integrated intensity of the (1/2,1/2,0) magnetic Bragg peak as a function of temperature. The intensity increases with decreasing temperature below the Néel temperature of 280 K.

References

[1] S. Skanthakumar, H. Zhang, T. W. Clinton, W.-H. Li, J. W. Lynn, Z. Fisk, and S.-W. Cheong. Physica C160, 124 (1989). S. Skanthakumar, H. Zhang, T. W. Clinton, I. W. Sumarlin, W.-H. Li and J. W. Lynn, Z. Fisk, S.-W. Cheong, J. Appl. Phys. 67, 4530 (1990).

[2] J. W. Lynn, I. W. Sumarlin, S. Skanthakumar, W.-H. Li, R. N. Shelton, J. L. Peng, Z. Fisk, S.-W. Cheong, Phys. Rev. B41, 2569 (1990).

[3] Y. Endoh, M. Matsuda, K. Yamada, K. Kakurai, Y. Hidaka, G. Shirane, and R. J.Birgeneau, Phys. Rev. B40, 7023 (1989).

[4] D. E. Cox, A. I. Goldman, M. A. Subramanian, J. Gopalakrishnan, and A. W. Sleight, Phys. Rev. B40, 6998 (1989).

[5] P. Allenspach, S.-W. Cheong, A. Dommann, P. Fischer, Z. Fisk, A. Furrer, H. R. Ott, and B. Rupp, Z. Phys. B77, 185 (1989).

[6] See for example, M. F. Hundley, J. D. Thompson, S.-W. Cheong, Z. Fisk, and S. B. Oseroff, Physica C158, 102 (1989). Y. Dalichaouch, B. W. Lee, C. L. Seaman, J. T. Markert, and M. B. Maple, Phys. Rev. Lett. 64, 599 (1990).

MAGNETIC ORDERING OF Nd IN $(Nd-Ce)_2CuO_4$

J. W. Lynn, I. W. Sumarlin, S. Skanthakumar, and W.-H. Li
(University of Maryland, College Park, MD and Reactor Radiation Division)
R. N. Shelton and J. L. Peng (University of California, Davis, CA)
Z. Fisk (Los Alamos National Laboratory, Los Alamos, NM)
S.-W. Cheong (AT&T Bell Laboratories, Murray Hill, NJ)

The microscopic magnetic properties of superconductors have been of interest for many years, first for "magnetic superconductor" systems [1], then in heavy fermion materials [2], and most recently in the oxide superconductors [3]. In magnetic-superconductors such as RMo_6S_8 and RRh_4B_4 (R = heavy rare-earth element), the R ions are physically isolated in the crystal structure from the superconducting electrons. This feature leads to a major role for the dipole-dipole interaction as reflected in the very low magnetic ordering temperatures. The magnetic and superconducting order parameters are coupled via the electromagnetic interaction. The heavy fermion systems, on the other hand, do not have an "isolation" of the magnetic and superconducting subsystems, and in fact the magnetic fluctuations are likely responsible for the superconducting pairing [2]. The oxide superconductors provide the interesting situation of having both heavy rare earths which are often isolated in the lattice and order at low temperatures, and strongly coupled Cu spins which reside in the Cu-O superconducting planes.

We have been investigating the magnetic properties of the recently discovered Nd_2CuO_4 class of electron superconductors, which of course possess both rare earth and Cu spin subsystems. In the insulating phase the Cu spins order at relatively high temperatures (~ 245 K) [4-6]. At low temperatures the Nd ions have also been observed to order magnetically [4,6,7]. We have carried out neutron scattering experiments to characterize the nature of this ordering, and have found a simple antiferromagnetic arrangement of spins. For the superconducting material a sharp Néel transition is observed, but in the parent insulating compound the transition appears "smeared" due to substantial coupling with the ordered Cu sublattice. Hence the rare earth and Cu sublattices cannot be isolated electronically. In the superconducting system, where the Cu spins are disordered, it may be

particularly interesting to determine the effect of the Nd ordering on the superconducting properties such as the critical fields, since this could provide an important clue to the origin of the superconducting pairing depending on whether the magnetic ordering hinders or enhances the superconductivity.

Unpolarized diffraction data were taken on polycrystalline samples of Nd_2CuO_4 and $Nd_{1.85}Ce_{0.15}CuO_4$, and a 20-mg single crystal of Nd_2CuO_4. Figure 1 shows the temperature dependence of the magnetic intensity for the (½½3) Bragg peak. For the superconducting sample (top) a well-defined transition at 1.2 K is observed, which is in good agreement with the specific heat data [7]. Note that there is a small amount of rounding of the intensity in the vicinity of the Néel temperature, which is typical for second order transitions and likely originates from critical scattering. The lower portion of the figure shows the temperature dependence of the same reflection for the Nd_2CuO_4 powder sample. In this case it is difficult to determine the Néel temperature with accuracy since the scattering appears to be "smeared" over several degrees. Such a "smeared" order parameter might be caused by sample inhomogeneities and a consequent distribution of Néel temperatures, but this interpretation is inconsistent with the sharp transition for the superconducting sample, and with the behavior observed for the single crystal sample. We remark that the signal-to-noise ratio for the single crystal data is dramatically improved compared to the data obtained on powders, and we have taken extensive temperature dependent data on a large number of Bragg peaks.

To understand these data it is essential to recall that the Cu spins have already ordered at 245 K in this sample, and that the Cu magnetic Bragg peaks occur at the same positions as for the Nd peaks. Hence the intensities of these peaks represent a coherent addition of the Cu

and Nd order parameters. At high temperatures where only the Cu spins are ordered the intensity is of course directly related to the Cu order parameter, while at low T the Nd contribution dominates since the Nd moment becomes much larger than Cu and there are twice as many Nd as Cu. At 75 K an abrupt spin reorientation of the Cu spins occurs, in which the Cu spins rotate by $\pi/2$. Another spin reorientation occurs at 30 K in which the Cu spins rotate again by $\pi/2$ [4,5]. The single crystal data (not shown) indicate a continuous increase in the intensity of the ($\frac{1}{2}\frac{1}{2}3$) peak below 30 K. Since the ordered Cu moments are essentially saturated at these low temperatures, we believe that the intensity change below 30 K is due to the polarization of the Nd sublattice.

In the present system nearest-neighbor interactions between the Cu and Nd sublattices cancel. Next-nearest-neighbor and third-neighbor interactions, however, do not cancel, but instead produce a staggered field which polarizes the Nd sublattice antiferromagnetically, and this polarization field has the same symmetry as when the Nd ions order. Hence a net sublattice magnetization of the Nd is induced at elevated temperatures. The Nd-Cu interaction may also be the cause of the second spin reorientation observed at 30 K. In the Ce-doped superconducting material the Cu spin system is not magnetically ordered, and hence we do not see any effect on the Nd sublattice. However, when the Nd sublattice orders at low temperatures, we might expect a reverse polarization on the Cu sublattice. If the Cooper pairing is mediated by magnetic interactions, for example, then the induced magnetic order of the Cu spins might quench the superconducting state. We believe it would be particularly interesting to measure the superconducting properties, such as the critical fields, to determine whether such a polarization enhances or hinders the super-conducting pairing.

Figure 1. Magnetic intensity for the ($\frac{1}{2}\frac{1}{2}3$) Bragg peak. The top portion of the figure shows the data obtained on the $Nd_{1.85}Ce_{0.15}CuO_4$ sample, where a well defined Néel temperature of ~ 1.2 K is found. The lower portion of the figure shows the data for the Nd_2CuO_4 sample, where the intensity is seen to be spread over a large range of temperature.

References

[1] For a general review see Topics in Current Physics, Ø. Fischer and M. B. Maple, eds. (Springer, New York, 1982), Vols. 32 and 34.

[2] See, for example, G. R. Stewart, Rev. Mod. Phys. 56, 775 (1984). Z. Fisk, et al., Science 239, 33 (1988).

[3] For a general review see High Temperature Super-conductivity, J. W. Lynn, ed. (Springer, New York, 1990).

[4] S. Skanthakumar, H. Zhang, T. W. Clinton, W-H. Li, J. W. Lynn, Z. Fisk, and S.-W. Cheong, Physica C160, 124 (1989). S. Skanthakumar, H. Zhang, T. W. Clinton, I. W. Sumarlin, W-H. Li, J. W. Lynn, Z. Fisk, and S-W. Cheong, J. Appl. Phys. 67, 4530 (1990).

[5] Y. Endoh, M. Matsuda, K. Yamada, K. Kakurai, Y. Hidaka, G. Shirane, and R. J. Birgeneau, Phys. Rev. B40, 7023 (1989).

[6] J. W. Lynn, et al., Phys. Rev. B41, 2569 (1990).

NEUTRON DIFFRACTION ON ANNEALED $YBa_2Cu_3O_{6.28}$

C. H. Lee, Q. Lin, J. W. Lynn, and S. Green
(University of Maryland, College Park, MD and Reactor Radiation Division)
and
A. Santoro

The $RBa_2Cu_3O_{6+x}$ (R = rare earth) compounds have a layered perovskite-like structure in which there are three copper-oxygen layers stacked along the (unique) tetragonal c-axis. Two of these layers have oxygen ions between the copper in both the a and b crystallographic directions. These are the so-called "plane" layers, and the oxygen in these layers cannot be removed. The third layer has oxygen ions only along the b axis, and is thus called the "chain" layer. The oxygen concentration can be readily varied in this layer from full occupancy ($x = 1$) to complete depletion ($x = 0$), and both the magnetic and superconducting properties are very sensitive to the oxygen concentration x in the "chain" layers. In the small x regime, we have a tetragonal antiferromagnetic insulator; while for $x \geq 0.4$, we have an orthorhombic superconductor with $a \approx b$ and $c \approx 3a$ [1].

The magnetic properties in the small x regime, where the materials are tetragonal and semiconducting, have proved to be very interesting. The Cu "plane" layers order antiferromagnetically with a Néel temperature T_N as high as 500 K. At lower temperatures the spins on the Cu "chain" sites have also been observed to order antiferromagnetically [2]. However, this lower phase transition is not always observed, and clearly depends on more than just the average oxygen concentration. At high x it has been found that the superconducting properties depend on the chemical ordering of the oxygen ions in the chains as well as the average oxygen stoichiometry [3-4], and we suspect that oxygen ordering may be playing an important role in the magnetic properties at small x as well. Consequently we have initiated diffraction experiments to ascertain the effect of oxygen ordering on the Cu magnetic phase transitions.

A fully-oxidized 30-g polycrystalline sample was prepared by the usual solid state reaction technique, and then was partially reduced by heating to 600 °C in pure Ar. Oxygen ordering was promoted by cooling very slowly, as opposed to quenching. Thermogravimetric analysis yielded an average oxygen concentration of 6.24. The neutron powder diffraction patterns were taken at 77 K on the BT-1 high resolution powder diffraction instrument. Profile refinements of the data were made using two different models. Model-1 assumed a tetragonal structure, with random occupancy of the oxygen chain sites. This model gave a reasonable fit to the data, although there were some clear discrepancies between the data and the model. The weighted R-factor (R_w) was 12.0, which was not particularly good, while the thermal factor (B) of the chain-layer oxygen was unreasonably large.

The second model (model-2) allowed for an orthorhombic distortion of the lattice, as well as for an ordering of the oxygen chain ions. The specific order which we assumed was that the occupancy of adjacent chains was unequal. Allowing for the orthorhombic distortion improved the fit substantially, with the weighted R-factor decreasing from 12.0 to 9.0. We also observed a strong tendency to make the oxygen occupancies different, with a occupancy ratio which converged to ~ 4.0. However, the overall improvement in the fit associated with the oxygen ordering was only marginal, and it is not clear whether this oxygen ordering model is appropriate at these smaller values of x. The final value of the oxygen concentration we obtained was $x = 0.28$. The refined structural parameters for the remainder of the atoms were identical within experimental error for the two models.

We have also carried out preliminary experiments to observe the nature of the magnetic ordering in this annealed sample. The plane-ordering peaks were found to be very weak, as expected at the higher x since it has already been observed that the ordered moment decreases rapidly with increasing x [5]. In

addition, no chain-ordering peaks were observed at any temperature. Further work is in progress as a function of x and annealing condition.

References

[1] A review of both theory and experiment that pertains to the oxide superconductors is given in High Temperature Superconductivity, J. W. Lynn, ed. (Springer-Verlag, New York, 1990).

[2] See J. W. Lynn, W-H. Li, H. A. Mook, B. C. Sales and Z. Fisk, Phys. Rev. Lett. 60, 2781 (1988); W.-H. Li, J. W. Lynn, and Z. Fisk. Phys. Rev. B41, 4098 (1990), and references therein.

[3] R. J. Cava, B. Batlogg, C. H. Chen, E. A. Tietman, S. M. Zahurak, and D. Werder, Phys. Rev. B36, 5719 (1987).

[4] For a review, see R. Beyers and T. M. Shaw, Solid State Phys. 42, 135 (1989).

[5] J. M. Tranquada, A. H. Moudden, A. I. Goldman, P. Zolliker, D. E. Cox, G. Shirane, S. K. Sinha, D. Vaknin, , C. Johnston, M. S. Alvarez, and A. J. Jacobson. Phys. Rev. B38, 2477 (1988).

TEMPERATURE DEPENDENCE OF THE TWO-DIMENSIONAL MAGNETIC CORRELATIONS OF Er in $ErBa_2Cu_3O_7$

T. W. Clinton and J. W. Lynn (University of Maryland, College Park, MD and Reactor Radiation Division)
J. Z. Liu and R. N. Shelton (University of California, Davis, CA)

The magnetic ordering of the rare-earth ions in the layered superconducting oxides has been of interest both because of the magnetic-superconductor interactions, and because of the 2-d magnetic behavior these materials display [1-3]. In the $RBa_2Cu_3O_7$ (R = rare earth) materials of direct interest here, the 2-d behavior originates naturally from the crystallography; there is only one rare-earth ion per chemical unit cell, and the c-axis is three times as long as the a- and b- axes. As could be expected, the first neutron experiments on $ErBa_2Cu_3O_7$ observed this 2-d behavior with powder samples [1], and later with a single crystal [2], where excellent quantitative agreement with a 2-d Ising model was obtained. Though the Er magnetic system is 2-d in character, when strong 2-d correlations develop in the a-b plane a weak interaction along the c-axis induces 3-d long-range order at T_N = 0.618 K. Above this 3-d Néel temperature a rod of scattering along $(1/2, 0, \ell)$ characteristic of the 2-d behavior has been observed, showing that the magnetic interactions of the rare-earth ions

are highly anisotropic; below T_N the order parameter follows the exact Onsager solution for a 2-d Ising antiferromagnet.

Recently, we have made additional measurements on a single crystal of $ErBa_2Cu_3O_7$ to determine the temperature dependence of the 2-d rod of scattering. Above the ordering temperature this scattering originates from critical fluctuations, while below T_N it originates from low-energy spin-wave excitations. In the quasielastic approximation this diffuse scattering is proportional to the wave-vector-dependent susceptibility. For a 2-d system in the Ornstein-Zernike approximation

$$I(q)_{diffuse} \propto \chi(q) \propto (\kappa^2 + q_x^2 + q_y^2)^{-1} \quad (1)$$

where κ is the inverse correlation length within the planes. Thus in a 2-d system we expect to see critical scattering about the reciprocal lattice positions as in the 3-d systems, with the important difference that in the 2-d case the critical scattering should be independent of q_z, so one should see a rod of scattering. Therefore by

37

observing the rod of scattering for various temperatures above and below T_N, the temperature dependence of both the susceptibility and the 2-d correlation length can be determined.

We have measured the temperature dependence of the rod intensity at a point on the rod away from where 3-d magnetic Bragg peaks, indexed by (1/2,0,ℓ/2), arise. The temperature dependence of the rod point (1/2,0,0.7) is shown in figure 1. The rod starts to develop below about 1 K, and the intensity steadily increases as the temperature is decreased until T_N is reached. Below T_N the intensity decreases rapidly. The sharp decrease in the rod intensity below T_N is due to the rapid decrease of the spin wave population as anticipated for an Ising system.

The full width at half maximum (FWHM) of the intensity in (1) is equal to twice the inverse

2-d correlation length κ. Therefore to observe the 2-d magnetic correlations in the system we took scans across the rod at various temperatures. In figure 2 the linewidth (FWHM) of the rod is shown as a function of temperature. Because of the Gaussian experimental resolution the scans across the rod are the convolution of a Gaussian function and the intrinsic Lorentzian function in (1). Therefore, the data were deconvoluted using a Gaussian resolution function and a Lorentzian to produce the intrinsic Lorentzian linewidth in figure 2. The graph indicates that as T_N is approached from above, the 2-d correlation length grows until it diverges at T_N, where long-range magnetic order sets in. Below T_N the measurements are resolution limited.

Figure 1. Rod intensity as a function of temperature. The intensity is seen to peak at $T_N \sim 0.62$ K where 3-d long range order sets in.
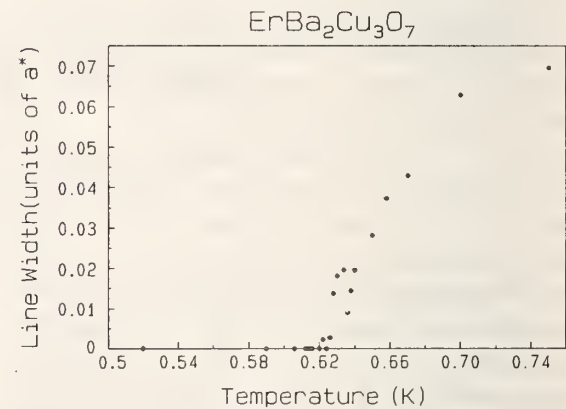
Figure 2. Temperature dependence of the intrinsic linewidth (FWHM). The linewidth decreases from some finite initial value down to T_N, where it reaches a resolution limited minimum as long range order develops.

References

[1] J. W. Lynn, W.-H. Li, Q. Li, H. C. Ku, H. D. Yang, and R. N. Shelton, Phys. Rev. B36, 2374 (1987).

[2] J. W. Lynn, T. W. Clinton, W.-H. Li, R. W. Erwin, J. Z. Liu, K. Vandervoort, and R. N. Shelton, Phys. Rev. Lett. 63, 2606 (1989).

[3] A recent review of the oxide superconductors is given in High Temperature Superconductivity, J. W. Lynn, ed. (New York: Springer-Verlag, 1990).

FIELD DEPENDENCE OF THE MAGNETIC PHASE TRANSITIONS IN Nd_2CuO_4

S. Skanthakumar and J. W. Lynn
(University of Maryland, College Park, MD and Reactor Radiation Division)
and
Z. Fisk (Los Alamos National Laboratory, Los Alamos, NM)

The magnetic properties of the Nd_2CuO_4 class of electron superconductors have been studied recently by neutron diffraction techniques [1-5]. Long range antiferromagnetic order of the Cu moments develops in Nd_2CuO_4 at $T_N = 245$ K, with a simple spin configuration in which nearest-neighbors within the Cu-O planes are antiparallel. The coupling between the layers, on the other hand, cancels to a first approximation, and the delicate balance of interlayer interactions appears to lead to a rich behavior as a function of temperature and field. In particular, there are two spin reorientations which occur at 75 and 30 K in this material. These spin reorientations have not been observed in the sister compounds Pr_2CuO_4 and Sm_2CuO_4 [5]. In addition, there is a substantial interaction between the Cu and Nd sublattices, and the Nd sublattice orders [4] at $T_N = 1.5$ K.

Both noncollinear [1] and collinear [2] magnetic structures have been proposed for this system, and it is not possible to distinguish between them with the present neutron diffraction data. In the noncollinear magnetic structure [1], the spins within the Cu-O layers are collinear and nearest neighbors are antiparallel, but the spin direction between layers is rotated by $\pi/2$, and hence the spins point in different directions (i.e., they are noncollinear). The symmetry of the magnetic system in this case is tetragonal. In the fully collinear spin configuration, the spins within the layers have the same antiparallel arrangement of nearest-neighbor spins, while the spin directions of adjacent layers are collinear rather than noncollinear. The magnetic symmetry in this case is orthorhombic. The two structures are related in that the noncollinear configuration can be thought of as the coherent addition of two separate domains of the collinear structure. The magnetic Bragg intensities calculated for a single domain are different for the two cases, but for a multidomain sample in which the domain populations are equal the domain-averaged intensities

are identical. Indeed the data obtained by us [1,3] and by Endoh et al. [2] are in excellent agreement, and with the present data it is not possible to distinguish the two spin configurations. It may be possible to prepare a sample with unequal domain populations by the application of a magnetic field, or by applying stress. However, even in this case such experiments may not provide an unambiguous answer. For example, a similar situation has occurred for the spin structure of pure Nd [6], and this magnetic structure has been the subject of debate for many years. Here, we report our preliminary field dependent neutron diffraction measurements for Nd_2CuO_4.

The diffraction data were taken with a wavelength of 2.3457 Å and a pyrolytic graphite monochromator and filter at the BT-2 triple-axis spectrometer. A split-coil superconducting magnet with a vertical field capability of 7 Tesla was used for these measurements. The crystal was mounted in the (hhl) scattering plane, with the field applied vertically, that is, in the $[hh0]$ direction.

The temperature dependence of several Bragg peak intensities was observed as a function of magnetic field. The data revealed a small but clear shift in the spin reorientation transition temperatures to higher magnetic fields. The temperature dependence of the $(1/2,1/2,5)$ Bragg peak intensity in a 7 Tesla field is shown in figure 1. Since the magnetic Bragg peak intensities change abruptly at these transitions the small shift in the transition temperature can be easily noticed. Both spin reorientation transition temperatures, which are 75 K and 30 K for zero magnetic field, increase with magnetic field at the rate of about 1.4 and 0.7 Kelvin/Tesla, respectively. These shifts for a 7 Tesla magnetic field can be easily noticed in figure 1. We were unable to map the complete phase diagram due to the inaccessibility of obtaining the very high fields needed. Since the peak intensities at higher temperatures (≥ 200 K) are small and
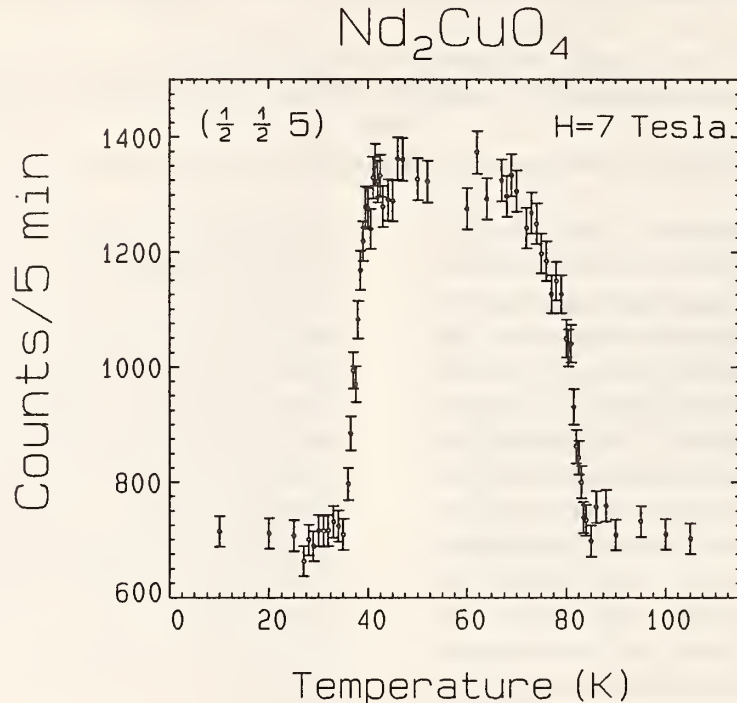
Figure 1. Temperature dependence of the (1/2,1/2,5) Bragg peak intensity with a 7 Tesla applied magnetic field. The data reveal sharp spin reorientations, which are found to increase with increasing applied field.

change slowly with temperature we were not able in these initial studies to observe any significant change in the highest transition temperature (245 K) phase boundary.

The intensities of some nuclear Bragg peaks were also checked as a function of magnetic field at 100 K, and those measurements showed no indication of a measurable induced ferromagnetic component. Measurements at lower magnetic fields showed that the domain populations were strongly affected by modest magnetic fields in the range below 1 Tesla, above which no change was observed in the domain population. Further experiments on this effect and on the field dependence of the higher order transition temperature (245 K) will be done using a larger crystal.

References

[1] S. Skanthakumar, H. Zhang, T. W. Clinton, W.-H. Li, J. W. Lynn, Z. Fisk, and S.-W. Cheong, Physica C160, 124 (1989).

[2] Y. Endoh, M. Matsuda, K. Yamada, K. Kakurai, Y. Hidaka, G. Shirane, and R. J.Birgeneau, Phys. Rev. B40, 7023 (1989).

[3] S. Skanthakumar, H. Zhang, T. W. Clinton, I. W. Sumarlin, W.-H. Li, J. W. Lynn, Z. Fisk, and S.-W. Cheong, J. Appl. Phys. 67, 4530 (1990).

[4] J. W. Lynn, I. W. Sumarlin, S. Skanthakumar, W.-H. Li, R. N. Shelton, J. L. Peng, Z. Fisk, S.-W. Cheong, Phys. Rev. B41, 2569 (1990).

[5] S. Skanthakumar, J. W. Lynn, J. L. Peng, and Z. Y. Li, (to be published).

[6] See, for example, E. M. Forgan, E. P. Gibbons, K. A. McEwen, and D. Fort, Phys. Rev. Lett, 62, 470 (1989), and references therein.

TWO-DIMENSIONAL MAGNETIC ORDER IN SUPERCONDUCTING $DyBa_2Cu_4O_8$

H. Zhang, J. W. Lynn, W.-H. Li, and T. W. Clinton
(University of Maryland, College Park, MD and Reactor Radiation Division)
and
D. E. Morris (Lawrence Berkeley Laboratory, Berkeley, CA)

The magnetic properties of the oxide superconductors have been studied because these materials are ideal systems to investigate the coupling between the rare-earth magnetic and superconducting order parameters. We have been systematically investigating the nature of the rare-earth ordering in the $RBa_2Cu_3O_{6+x}$ systems, and have found [1,2] that they are prototypical 2-d magnetic systems. Recently, we reported our experimental work on the $RBa_2Cu_4O_8$ class of materials, which is similar to the 1-2-3 system except that the (orthorhombic) c-axis is approximately twice as long, with two rare-earth ions in the chemical unit cell [3]. We find unambiguous evidence for 2-d behavior in both the $ErBa_2Cu_4O_8$ and $DyBa_2Cu_4O_8$ systems. Strikingly, in the case of $DyBa_2Cu_4O_8$, the sample did not order 3-d even at temperatures far below T_N as shown in figure 1. Here the solid curves are a least-squares fit to the scattering expected for a 2-d ordered system, with no correlations between

layers, and this is seen to provide an excellent description of the data.

The lack of any 3-d order in the $DyBa_2Cu_4O_8$ material is quite interesting. In the "conventional" 2-d systems such as K_2CoF_4 [5], K_2NiF_4 [6], and more recently $ErBa_2Cu_3O_7$ [2], the 2-d and 3-d ordering occur at (essentially) the same temperature. The reason for the close proximity of the two transitions is that when the system develops a static moment in the layers, then there is an energy $\pm JA^2$ between the layers, where J is the exchange interaction between planes and A is the average size of a domain in the layer. The - sign is for layers that are properly matched (e.g., antiferromagnetic if $J < 0$) and + is for layers that are out of phase. Thus even if the interlayer coupling is very weak, there is an energy difference $2JA^2$ between the "correct" and the "wrong" spin configurations, which can be quite large since A is large. Hence the layers tend to order along the c-axis producing 3-d Bragg peaks.

$DyBa_2Cu_4O_8$
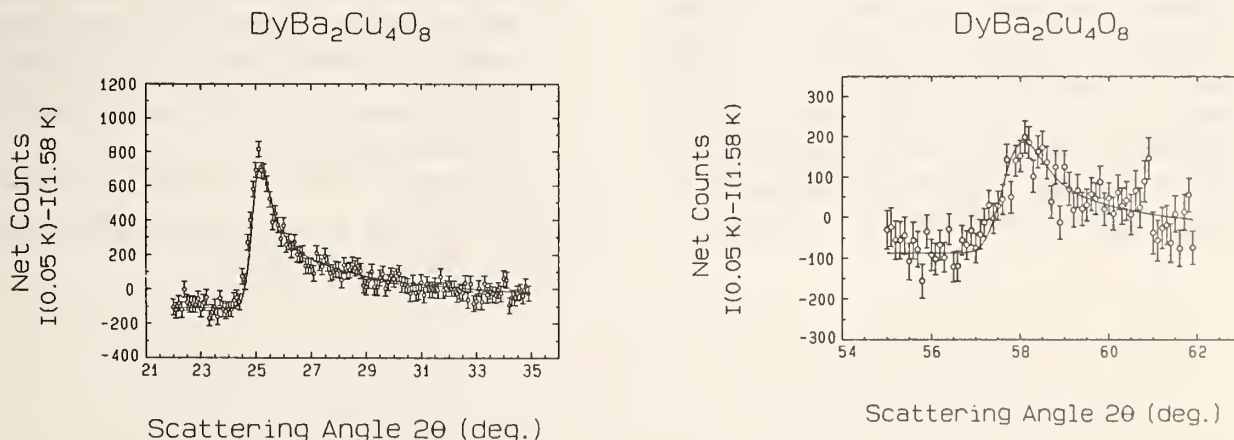
$DyBa_2Cu_4O_8$

Figure 1. Magnetic scattering intensity for $DyBa_2Cu_4O_8$ at T = 0.05 K. The solid curves are the result of a fit to the theoretical scattering expected for a purely 2-d magnetic system; (left) the scattering profile for the (½,½) peak; (right) the scattering profile for the (1/2,3/2) peak.

In the present $DyBa_2Cu_4O_8$ system the nearest neighbor spins within the a-b plane form a simple antiferromagnetic arrangement as shown in figure 2. In the next layer up along the c-axis, all the spins are displaced by b/2. For the closest spins between layers, we will have two + spins, and two - spins, and the net interaction is zero by symmetry [4]. Next neighbor interactions also cancel, and, in fact, all the (point) interactions sum to zero by symmetry. Hence, this is an example of a fully frustrated spin system for the interlayer coupling. In addition, we have an intrinsic interlayer interaction which is very weak, rendering the effective interlayer interaction exceedingly weak; in fact $DyBa_2Cu_4O_8$ is presently the best known example of a 2-d magnet. In the $ErBa_2Cu_4O_8$ system this cancellation does not occur because of the chain-like ordering in the a-b plane, while in the 1-2-3 systems it does not occur because adjacent layers are not displaced b/2. Finally, we note that if the general similarities between the magnetic structures of the 1-2-3 and 2-4-8 systems hold for the remainder of the $RBa_2Cu_4O_8$ materials, then a similar cancellation of the net interactions along the c-axis can be expected since most of the $RBa_2Cu_3O_{6+x}$ compounds which have been investigated so far [1] exhibit the same in-plane nearest-neighbor antiferromagnetic spin configuration. A possible exception to this trend may occur for Gd, where the single-ion anisotropy is small and an Ising model is likely not appropriate. The spin frustration in the 2-4-8 system might then be alleviated by forming a noncollinear structure. Neutron scattering experiments are planned in the near future to investigate this possibility.
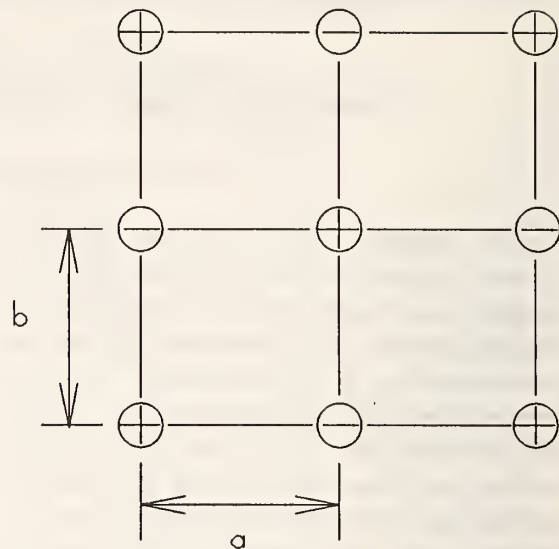
Figure 2. 2-d magnetic spin configuration for the Dy moments within the a-b layers in $DyBa_2Cu_4O_8$. Adjacent layers along the c-axis are uncorrelated even well below the 2-d ordering temperature.

References

[1] J. W. Lynn, W.-H. Li, Q. Li, H. C. Ku, H. D. Yang, and R. N. Shelton, Phys. Rev. B36, 2374 (1987).

[2] J. W. Lynn, T. W. Clinton, W.-H. Li, R. W. Erwin, J. Z. Liu, K. Vandervoort, and R. N. Shelton, Phys. Rev. Lett. 63, 2606 (1989).

[3] H. Zhang, J. W. Lynn, W. H. Li, and T. W. Clinton, Phys. Rev. B41, 11229 (1990).

[4] It is easiest to think of a sum of exchange interactions. The dipole-dipole interactions also cancel if the moments point along the c-axis (which we believe to be appropriate for $DyBa_2Cu_4O_8$), or in fact if they lie anywhere within the a-c plane. They also cancel if they point along the b-axis.

[5] H. Ikeda and K. Hirakawa, Solid State Commun. 14, 529 (1974).

[6] R. J. Birgeneau, H. J. Guggenheim, and G. Shirane, Phys. Rev. B1, 2211 (1970).

$Bi_2Sr_2MnO_{6+y}$: A 2-D MODULATED FERRIMAGNET

P. F. Miceli, J. M. Tarascon, K. Remschnig, and G. W. Hull (Bellcore, Red Bank, NJ)

and

W. R. McKinnon (National Research Council, Ottawa, Canada)

This compound is an isomorph of the high T_c compound containing Cu--both have a structural modulation parallel to the layers, giving a large unit cell. By substituting Mn for Cu, we can use the magnetic ion to directly probe the relationship between structure and magnetism (and therefore the electronic properties as well). Since the magnetic layers are far separated (~12 Å), the magnetic behavior is expected to be two dimensional.

Our preliminary neutron scattering work, using the BT-9 and BT-2 triple-axis spectrometers at NIST, on both powders and single crystals have shown novel magnetic behavior. The powder diffraction suggests that the magnetically ordered state is a simple antiferromagnet with the spins along the c-axis. However, investigation of the crystal shows that a single magnetic domain orders with wave-vector perpendicular to the structural modulation direction when cooled in zero field and a second

magnetic domain, ordered along the structural modulation direction, evolves as a magnetic field is applied. In addition, weak magnetic satellites are observed, indicating that the antiferromagnetic sheets have modulated magnetic moments. These results suggest that the structural modulation induces weak ferromagnetism and that the field induced transition arises from the way in which the magnetic layers stack: antiferromagnetic at zero field and ferrimagnetic at high field.

This work is the first demonstration of a valence modulation of the cations in this general class of compounds and it is important to understand how the relationship between the modulated structure and electronic properties affect the Cu based superconducting isomorphs.

Work in progress is focusing on the detailed nature of the magnetic moment modulation as well as exploring the 2-d aspects of this system.

A THEORETICAL MODEL FOR THE TUNNELING-GAP ANISOTROPY OBSERVED IN LAYERED COPPER-OXIDE HIGH-TEMPERATURE SUPERCONDUCTORS

R. C. Casella

The gap anisotropy and the ratios of these gaps to the critical temperature observed in single-crystal high-T_c superconductors are explained within a model in which double interplanar boson exchange takes place between fermions lying in distinct bands of widths B_c and B_{ab} satisfying $B_c < 2\omega < B_{ab}$, where ω is the cut-off energy of the (unspecified) intermediate boson. For single-crystal $Bi_2Sr_2CaCu_2O_8$ where the observed gap ratio $r \equiv \Delta_{ab}/\Delta_c \approx 2$ and $2\Delta_{ab}/kT_c \approx 6$, I find solutions with $\omega > 0.3$ eV and an extremely narrow width, 60 meV $\leq B_c \leq$ 200 meV for the band associated with overlap along the c-axis, assuming $\omega < 5$ eV. Theoretical constraints on the parameter values allow an experimental test.

Recent tunneling experiments on single-crystal $Bi_2Sr_2CaCu_2O_8$ imply an approximate two-to-one anisotropy of the superconducting gaps, depending upon whether the current is injected into the ab plane or along the c-axis, with $2\Delta_{ab}/kT_c = 6.2 \pm 0.3$ and $2\Delta_c/kT_c = 3.3 \pm 0.5$ [1]. A similar gap anisotropy has been observed in preferentially oriented films of $YBa_2Cu_3O_7$. Tunneling measurements on polycrystals of Tℓ, Bi, and Y-123 layered CuO_2 compounds yield $2\Delta/kT_c = 6.1 \pm 0.5$, quoted as a common result, presumably for the larger gap when one assumes single-crystal gap anisotropy. These data are considered in terms of a two-band model involving interplanar high-energy ($\omega >> \omega_{phonon}$) intermediate bosons (IB) exchanged between carriers in the two bands, labeled C and D, of widths B_C and B_D, respectively. It is further assumed that the maximum energy ω of the exchanged IB satisfies the inequalities $B_C < 2\omega < B_D$. A general two-band, two-gap model of this type, not specifically aimed at producing anisotropy with respect to the crystal c-axis, was considered earlier by this author [2]. Later, in an attempt to understand the dependence of the critical temperature $T_c(n)$ on the number n of closely spaced CuO_2 layers characterizing several of the

high-T_c Tℓ and Bi compounds, an average over possible multiple gaps was taken for each n. This led to a reasonably good accounting of the saturation in the increase of $T_c(n)$ with increasing n [3,4]. In the present analysis the narrow band C is identified in the tight-binding sense with a band whose width results mainly from orbital overlap along the c-axis, while band D is associated with orbitals which overlap mainly in the ab plane. That is, $B_C = B_c$ and $B_D = B_{ab}$. Detailed consideration of the energetics of the IB exchange at the single fermion level leads to an interpretation whereby coherent double IB exchange takes place between the carriers in the two bands. The mechanism involves off-shell propagation of the narrow-band fermion between the emission and absorption of two IBs connecting the narrow-band fermion with each of two fermions in the wide band. This interpretation follows essentially from consideration of energy conservation together with the assumption that interband transitions of the fermions can be neglected. As in the original BCS theory where the phonon coordinates are integrated out leading to an effective fermionic pair interaction, here the coordinates of the two IBs connecting the pair constituents in one band via the intermediary odd fermion in the other band are integrated out along with the coordinates of the third fermion. This unfamiliar pairing mechanism follows ultimately from the assumption that the IB energy ω can exceed the width of the narrower of the two bands. It can be extended to apply reciprocally to both bands. Phenomenologically it allows gap/T_c ratios much larger than 3.5 (e.g., $2\Delta_{ab}/kT_c \gtrsim 6$) *within weak coupling*. Yet it places constraints on the IB energy as well as on the allowed values of the gap anisotropy for a given value of $2\Delta_{ab}/kT_c$. While the IB is yet to be identified either experimentally or by the theory, the model may provide a clue to the experimentalists as to where to look for the elusive boson. The model

already excludes $\omega < 0.3$ eV for the Bi compound measured in reference 1.

Theoretically, I find

$$kT_c = 1.13\Omega\exp\left((-1/g)[1+(\tfrac{g}{2}\ln R)^2]^{1/2}\right) \quad (1)$$

and

$$(1/r)^{1/2}(2\Delta_D/kT_c) = 3.54 \exp \Gamma, \quad (2)$$

where

$$\Gamma = (1/g)\left([1+(\tfrac{g}{2}\ell nR)^2]^{1/2}-[1+(\tfrac{g}{2}\ell nR/r)^2]^{1/2}\right). \quad (3)$$

Here $\Omega = (\omega B_C/2)^{1/2}$ and $R = 2\omega/B_C$. ω and $B_C/2$ are the cut-off energies in BCS-like integrals for the wide and narrow bands, respectively, when $\omega > B_C/2$, as is assumed. (g is the coupling parameter.) Starting with input values of Δ_D, T_c, and r (i.e., of Δ_C), we seek values of g and of R such that $g < 1$, $R > 1$ and such that (2) and (3) are satisfied. One can then test to see whether the inequality, $B_C/4kT_c > 2$, essential to obtain equation (1), is satisfied, rejecting solutions which do not comply. Solutions of these equations, taking as input $\Delta_D = \Delta_{ab} = 22.5$ meV and $T_c = 85.4$ K for the Bi compound measured in reference [1] are given in table 1 for r = 2, 2.1, and 2.2. For each value of r, values of R/2, g, ω, B_C and x_c^C are exhibited. If $2\Delta_{ab}/kT_c > 6.1$ for single-crystal $Bi_2Sr_2CaCu_2O_8$, then a statistically significant upper bound on the gap ratio r of 1.9 would require a revision of the proposed model, at least in the simplest version considered here. Experimentally, $r = 1.9 \pm 0.2$. Subsequent higher statistics experiments should decide the issue.

Table 1. Computed values for the effective coupling g, intermediate boson cut-off energy ω, narrow band width B_C and the parameter $x_c^C \equiv B_C/4kT_c$ for the compound $Bi_2SrCaCu_2O_8$ as a function of the ratio $\omega/B_C \equiv R/2$, given that the critical temperature $T_c = 85.4$ K and that the in-plane superconducting gap $2\Delta_{ab} \equiv 2\Delta_D = 45.0$ meV. Results are presented for three values of the parameter $r \equiv \Delta_D/\Delta_C \equiv \Delta_{ab}/\Delta_c$ where $2\Delta_c$ is the gap along the c axis. (Data from [1].)

ω/B_C	g	ω[eV]	B_C[meV]	x_c^C
		r = 2		
40	0.351	2.12	53.0	1.80
50	0.332	2.88	57.6	1.96
60	0.319	3.69	61.5	2.09
70	0.308	4.56	65.1	2.21
80	0.299	5.47	68.4	2.32
		r = 2.1		
10	0.411	0.51	50.8	1.73
13	0.373	0.77	58.8	2.00
20	0.325	1.50	74.7	2.54
30	0.289	2.81	93,6	3.18
40	0.268	4.40	110	3.73
50	0.254	6.22	124	4.22
		r = 2.2		
6	0.402	0.36	60.6	2.06
7	0.374	0.48	68.5	2.33
10	0.323	0.91	90.9	3.09
15	0.279	1.88	125	4.26
25	0.239	4.71	188	6.39
30	0.227	6.52	217	7.39

References

[1] G. Briceno and A. Zettl, Solid State Comm. **70**, 1055 (1989).

[2] R. C. Casella, Nuovo Cimento **D10**, 1439 (1988).

[3] R. C. Casella, Solid State Comm. **70**, 75 (1989).

[4] R. C. Casella, Appl. Phys. Lett. **55**, 908 (1989).

NEUTRON DIFFRACTION STUDIES OF MAGNETIC SEMICONDUCTORS

P. Klosowski, T. M. Giebultowicz, N. Samarth, H. Luo, and J. K. Furdyna
(University of Notre Dame, Notre Dame, IN)
and
J. J. Rhyne

We investigated new magnetic semiconductor systems fabricated by Molecular Beam Epitaxy (MBE) growth method: ZnSe/MnSe and ZnTe/MnTe superlattices and thick (≈ 1 µm) epitaxial layers of MnTe. In the superlattices, the magnetic layers are sandwiched between non-magnetic spacer layers. Due to differing lattice parameters between the magnetic and non-magnetic components, these structures fall in the category of strained layer superlattices, with the strain being accommodated by elastic deformation. The MnTe epilayers, on the other hand, are not strained. Unlike the case of bulk-grown MnSe and MnTe which crystalize in the NaCl and NiAs structure respectively, all the MBE-grown Mn chalcogenide layers are single crystal zinc-blend (ZB) type-III antiferromagnets (AFM-III). We recall that the only other ZB AFM-III is the classic case of β-MnS, which can only be stabilized in polycrystalline form [1].

We performed a systematic study of the magnetic ordering in ZnSe/MnSe superlattices as a function of both temperature and the magnetic layer thickness [2]. ZB MnSe can be stabilized in such superlattices with good crystalline quality up to thicknesses of around 100 Å (about 33 monolayers). In the samples studied, the magnetic layers contain between 3 and 15 monolayers of MnSe in each superlattice period, hence covering a crossover region between a 3-d- and 2-d-like effects. All the samples are good quality single crystals with well-defined interfaces, and at low temperatures all exhibit long range AFM-III ordering. The magnetic layer thickness determines the order range in the perpendicular direction, with no indication of coupling between the neighboring magnetic layers. Of three possible AFM-III domains, only one orientation is observed, indicating the lifting of a threefold cubic degeneracy usually
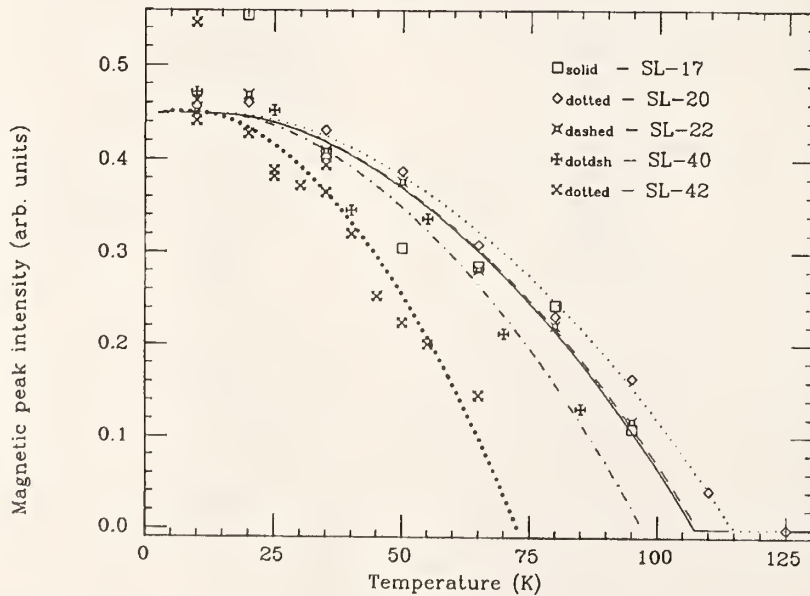
Figure 1. Temperature dependence of the squared sublattice magnetization (measure of the magnetic order) in MnSe/ZnSe superlattices. Samples SL 17, 20, 22, 40, and 42 have MnSe layer thickness 10, 15, 7, 5, and 3 monolayers, respectively. Plotted lines are the squared Brillouin functions for S = 3/2, fitted to the data.

found in isotropic bulk samples. This preferential stabilization of one type of domain is attributed to strain.

The antiferromagnetic-paramagnetic phase transition is continuous, with well defined Néel temperatures (T_N; see fig. 1). Samples with more than 5 monolayers have $T_N = 107 \pm 5$ K. However, T_N decreases slightly for thinner layers. It is not clear at the moment whether this is due to a true dimensional crossover from 3-d to 2-d, or whether it may be an effect of interface disorder. It is worthwhile mentioning that the range of the magnetic order did not change, even for the thinnest 3-monolayer sample. While thick epilayers of ZB MnSe cannot be stabilized with good crystalline quality, MnTe can be easily grown either as thick unstrained epilayers or in strained ZnTe/MnTe superlattices. This allows a direct

study of magnetic ordering as a function of strain. The characteristics of ZnTe/MnTe superlattices are very similar to those of MnSe/ZnSe, except for a lower Néel temperature due to a weaker exchange inter-action. However, the case of MnTe epilayers is remarkably different: they exhibit a first order magnetic phase transition (fig. 2). All three AFM-III domains were populated, indicating absence of anisotropies in this sample.

All these studies show that MBE-grown layered structures involving the Mn-chalco-genides provide a rich variety of systems in which to study fundamental properties of type-III antiferromagnets. Further work involving different strain configurations and systematic studies of possible dimensional crossover effects is now being pursued.
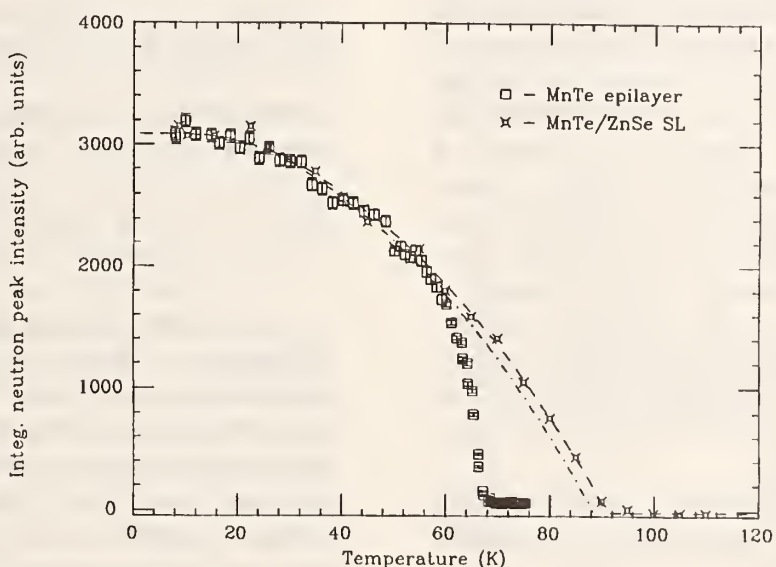
Figure 2. Temperature dependence of the squared sublattice magnetization for MnTe epitaxial layer and the MnTe/ZnTe superlattice. Superlattice data over entire temperature range were fitted by the squared Brillouin function. In the case of MnTe, data points below 60 K have similar temperature dependence. At higher T, however, the first-order discontinuity appears in the data.

References

[1] L. Corliss, N. Elliott, and J. Hastings, Phys. Rev. <u>104</u>, 924 (1956).

[2] T. M. Giebultowicz, P. Klosowski, N. Samarth, H. Luo, J. J. Rhyne, and J. K. Furdyna, Phys. Rev. B, August 1990 (in print).

MAGNETOELASTICITY IN RARE-EARTH SUPERLATTICES AND FILMS

R. W. Erwin, J. A. Borchers, and J. J. Rhyne
and
R. R. Du, C. P. Flynn, and M. B. Salamon (University of Illinois, Urbana, IL)

The magnetic structure has been measured with neutron scattering and SQUID magnetometry for a number of epitaxial multilayers and films of the magnetic rare-earths dysprosium and erbium grown with nonmagnetic yttrium. We have recently been able to calculate the new magnetic structures produced by epitaxial strains in these materials. In particular, we show that the first order ferromagnetic phase transitions are suppressed, although the Néel temperatures are within 5% of the bulk values. The calculations of the resulting critical fields are in reasonable agreement with the observed values.

A. Magnetoelasticity and Structure in the Bulk. The bulk magnetic structures for Dy and Er have been previously measured using neutron and x-ray scattering. The spins are aligned within each basal plane sheet of the hcp structure, and the magnitude or direction is modulated along the c-axis direction with an effective temperature dependent turn angle, w.

Both Dy and Er have a first order phase transition to a ferromagnetic state, which is primarily driven by magnetoelastic energetics. For example, in Dy this transition is accompanied by a 0.5% orthorhombic distortion of the basal plane and a 0.25% expansion of the c-axis as the moments align.

The bulk magnetoelastic coefficients of Dy and Er are known from measured aanomalous strains.

Here $\tan\Theta = <S^x>/<S^z> = 0.51$ at the ferromagnetic transition and $\beta \approx 1 - 2\omega/\pi$ is the averaged nearest neighbor correlation function of the z spin components.

B. Modifications to Magnetoelasticity in Films and Multilayers. When a magnetic material is grown with a nonmagnetic material in a film or multilayer, additional elastic terms are added to the free energy. In the case that the strains in the growth plane are coherent the additional elastic energy from the nonmagnetic material can be written as

$$\frac{1}{2}r_\alpha \sum_{\mu,\upsilon \neq \alpha} \{ (\tilde{c}_{\mu\upsilon} - \tilde{c}_{\mu\alpha}\tilde{c}_{\upsilon\alpha}/\tilde{c}_{\alpha\alpha})$$

$$(\epsilon_{\mu\mu} - \tilde{e}_{o\mu})(\epsilon_{\upsilon\upsilon} - \tilde{e}_{o\upsilon}\} \qquad (1)$$

The relative amount of nonmagnetic material is represented by r_a. The $\tilde{e}_{o\mu}$ are the strains in the free nonmagnetic material measured with respect to the nonmagnetic strains in the free magnetic material. In other words they represent the nonmagnetic lattice mismatch. This additional elastic energy has both quadratic and linear strain terms, so that the effective elastic coefficients for $\mu, \upsilon \neq \alpha$ are

$$\hat{c}_{\mu\upsilon} = c_{\mu\upsilon} + r_\alpha(\tilde{c}_{\mu\upsilon} - \tilde{c}_{\mu\alpha}\tilde{c}_{\upsilon\alpha}/\tilde{c}_{\alpha\alpha}) \qquad (2)$$

and the effective magnetoelastic coefficients for $\mu \neq \alpha$ are

$$\hat{K}_\mu = K_\mu + r_\alpha \sum_{\upsilon \neq \alpha} \tilde{e}_{o\upsilon}(\tilde{c}_{\mu\upsilon} - \tilde{c}_{\mu\alpha}\tilde{c}_{\upsilon\alpha}/\tilde{c}_{\alpha\alpha}). \qquad (3)$$

C. Critical Fields in Rare-Earth Films and Multilayers. Here we shall calculate the magnitude of the critical field necessary to induce the ferromagnetic state. In the case that the layered rare-earth material is grown along the hcp c-axis, the magnetic structure is sufficiently close to the bulk magnetic structure that the exchange energy can be transferred directly. If we assume that the elastic constants are equal in the magnetic and nonmagnetic materials then the magnetoelastic driving energy for the ferromagnetic transition, $\Delta = f(\omega = 0) - f(\omega)$, can be calculated based on the above equations for the coefficients. For example, if the low-temperature state of the Dy in the layered material has $\omega = 30°$, then in K/atom

$$\Delta = -1.25 - (3.95 - 91.0 r_z \tilde{e}_{ox,y})/(1 + r_z). \qquad (4)$$

This magnetoelastic driving energy is plotted in figure 1a in terms of an equivalent magnetic field acting on the magnetic moments

of Dy, for values of the parameter r_z ranging from zero to infinity as a function of the lattice mismatch ϵ. The conversion of the driving energy to a magnetic field is based on the assumption that its value at a spontaneous ferromagnetic transition would correspond to zero field.

A similar calculation of the driving energy for Er c-axis growth materials is based on $\omega = 2\pi/7$ in the low temperature state. Thus the magnetoelastic driving energy in K/atom

$$\Delta = -1.56 - (0.86 - 553 r_z \tilde{e}_{ox,y})/(1 + r_z). \quad (5)$$

This expression is plotted in figure 1b in terms of an equivalent field on the c-axis moments of Er. The dependence of the driving energy on the lattice mismatch is strong compared to the Dy case. This explains the large difference in the magnitudes of the critical fields in Dy and Er materials as shown in figure 2. This also explains why critical field data suggest that a several micron thick film of Er on yttrium is required before a low-temperature ferromagnetic transition is obtained. Note also that for slightly negative values of ϵ, as might be obtained by growing Er on Lu, the ferromagnetic transition is expected to occur at a higher temperature than in the bulk.

Presently we are extending this work by studying Er and Dy rare-earths grown with Lu. Preliminary results support our calculations for Er on Lu. However, a DyLu superlattice has been observed to be ferromagnetic near the Néel temperature of bulk Dy. It is clearly important that this new result be incorporated into the theory outlined here.
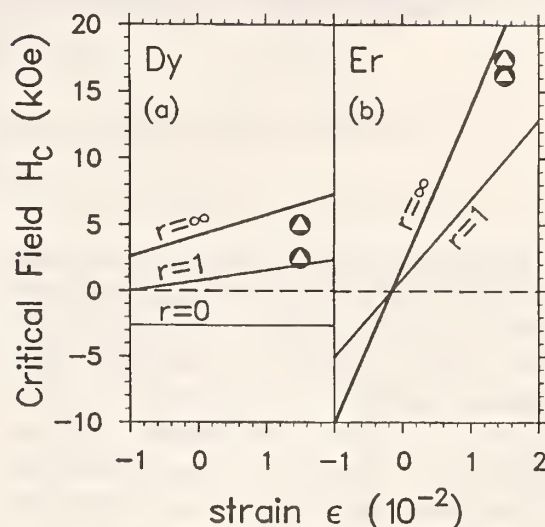
Figure 1. Calculated critical fields for (a)Dy and (b)Er c-axis growth layered materials as a function of the lattice mismatch with a nonmagnetic material. The calculation is shown for small and large values of the parameter rz, which represents the ratio of nonmagnetic to magnetic material. The critical fields in Er materials are suggested to be a much stronger function of the lattice mismatch than in Dy materials. This result in supported by the critical field data shown in figure 2.
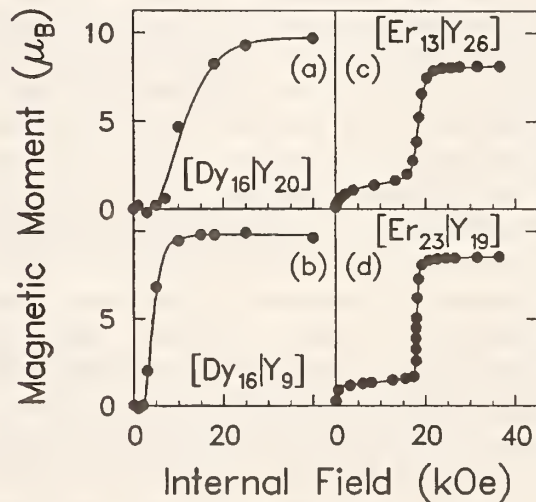
Figure 2. Measured critical fields for Dy(a,b) and Er(c,d) c-axis growth layered materials. The critical fields in Er materials are measured to be larger than the critical fields in Dy extrapolated to the same lattice mismatch.

References

[1] B. R. Cooper, in Magnetic Properties of Rare-Earth Metals, R. J. Elliot, ed. (Plenum, New York, 1972), p. 17.

[2] W. E. Evenson and S. H. Liu, Phys. Rev. 178, 783

ANTIFERROMAGNETIC ORDERING OF ErAs THIN EPITAXIAL LAYERS ON GaAs

P. F. Miceli, C. J. Palmstrøm, S. J. Allen, and G. W. Hull (Bellcore, Red Bank, NJ)

and

R. W. Erwin, D. A. Neumann, and J. J. Rhyne

Rare-earth arsenides have been recognized recently for their ability to be epitaxially lattice matched to GaAs, providing a new way to make buried layer contacts for integrated semiconductor devices. Furthermore, ErAs is expected to order magnetically at low temperature. Given the recent interest in magnetic thin films which are sensitive to the microstructural quality, ErAs provides an excellent system for studying thin film magnetism since the crystalline perfection can be rigorously controlled.

A recent transport study [1] has shown that ErAs/GaAs is a semimetal and that spin-disorder scattering gives rise to a resistivity anomaly at the antiferromagnetic transition. However, they report a transition temperature of 4.5 K which is significantly higher than the 3.5 K expected from early neutron scattering [2] as well as specific heat [3] measurements on bulk ErN and ErSb powders (ErAs had not been measured but is expected to fall between the nitride and antimonide).

We have investigated a 1000 Å ErAs film on GaAs using the BT-9 triple-axis spectrometer. Antiferromagnetic ordering with a (111) wavevector was observed and the temperature dependence is shown in figure 1 where the transition occurs at 4.3 ± 0.2 K. This direct measurement of antiferromagnetic ordering, therefore, confirms the enhanced transition temperature in the film. For this "thick" film, the lattice parameters of the ErAs have completely relaxed to their bulk values, thus, one expects that strain effects may not be an issue. However, differential thermal expansion between the film and substrate as well as magnetoelastic effects [3] may be crucial in understanding the magnetic properties of the film. Future work will focus on the role of strain by looking at thinner films.
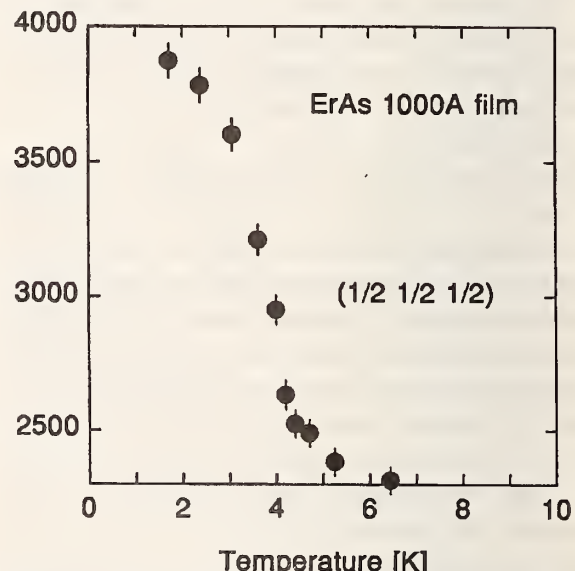
Figure 1. Temperature dependence of the intensity of the (1/2, 1/2, 1/2) antiferromagnetic reflection for a 1000 Å ErAs film.

References

[1] S. J. Allen et al., Phys. Rev. Lett. 62, 2309 (1989).
[2] H. R. Child et al., Phys. Rev. 131, 922 (1963).
[3] M. E. Mullen et al., Phys. Rev. B10, 186 (1974).

ORIENTATION DEPENDENCE OF THE SPIN COUPLING IN Gd/Y SUPERLATTICES

R. W. Erwin, J. A. Borchers, J. J. Rhyne and C. F. Majkrzak
and
T. F. Tsui and C. P. Flynn (University of Illinois, Urbana, IL)

To determine the symmetry of spin-coupling through nonmagnetic yttrium interlayers, b-axis Gd/Y superlattices were grown by Molecular Beam Epitaxy on $(10\bar{1}0)$ Y substrates and examined by neutron techniques. For c-axis Gd/Y superlattices [1], the Gd layer moments align or anti-align across the intervening layers depending in an oscillatory manner on the Y thickness. The spin interaction is associated with RKKY coupling mediated by the Y conduction band. Studies of b-axis Dy/Y superlattices [2] suggest that this spin coupling is not isotropic. In contrast to c-axis Dy/Y system [3], the helical Dy spin order is confined to a single magnetic layer. Because bulk gadolinium is ferromagnetic, the b-axis Gd/Y samples provide a simpler probe of the orientational dependence of the RKKY interaction.

In figure 1 the scan through the $(10\bar{1}0)$ reflection for the sample b-$[Gd_{43\text{Å}}/Y_{52\text{Å}}]_{85}$ demonstrates that the Gd moments anti-align across the yttrium. Preliminary measurements at 150 K for a sample with thinner Y interlayers, b-$[Gd_{60\text{Å}}/Y_{26\text{Å}}]_{80}$, give similar results. The saturation fields for this sample obtained from bulk magnetization measurements, however, are significantly smaller than the fields for b-$[Gd_{43\text{Å}}/Y_{52\text{Å}}]_{85}$ (i.e. at 50 K, 5 Oe in comparison to 150 Oe respectively). Judging by these two measurements, it is unlikely that the antiferromagnetic alignment follows from simple dipolar coupling between the Gd spins. Instead the sign of the interaction seems to oscillate suggesting an RKKY-like interaction, in sharp disagreement with observations from b-axis Dy/Y superlattices [2]. Field dependent diffraction measurements are in progress to determine the relative strength of the spin coupling in the two Gd/Y samples.
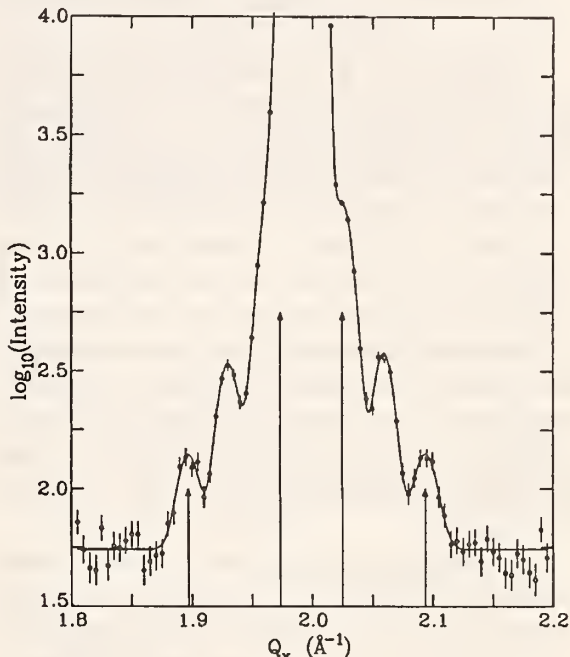
Figure 1. Neutron diffraction scans along the b* direction for b-$[Gd_{43\text{Å}}/Y_{52\text{Å}}]_{85}$ at 80 K. The reflections designated by arrows result from the antiferromagnetic arrangement of the Gd layer moments across the Y. The unmarked superlattice satellites are separated from each other by $\Delta Q = 2n\pi/\Lambda$ where Λ is the periodicity of the superlattice. The central peak is the $(10\bar{1}0)$ lattice reflection of the large yttrium substrate.

References

[1] C. F. Majkrzak, J. W. Cable, J. Kwo, M. Hong, D. B. McWhan, Y. Yafet, J. V. Waszczak, and C. Vettier, Phys. Rev. Lett. 56, 2700 (1986).

[2] C. P. Flynn, F. Tsui, M. B. Salamon, R. W. Erwin, and J. J. Rhyne, J. Phys. Condens. Matter 1, 5997 (1989).

[3] R. W. Erwin, J. J. Rhyne, M. B. Salamon, J. A. Borchers, Shantanu Sinha, R. Du, J. E. Cunningham, and C. P. Flynn, Phys. Rev. B35, 6808 (1987); M. B. Salamon, Shantanu Sinha, J. J. Rhyne, J. E. Cunningham, R. W. Erwin, J. A. Borchers, and C. P. Flynn. Phys. Rev. Lett. 56, 259 (1986).

PROPAGATION OF MAGNETIC ORDER THROUGH NONMAGNETIC INTERLAYERS IN RARE-EARTH SUPERLATTICES

J. A. Borchers, R. W. Erwin, and J. J. Rhyne
and
R. S. Beach, T. Matheny, M. B. Salamon, and C. P. Flynn (University of Illinois, Urbana, Il.)

Advances in the controlled deposition of metals have sparked interest in a new class of materials with tailored structural, magnetic and electronic properties. Previous studies of c-axis rare-earth superlattices (i.e., Dy/Y [1], Er/Y [2], and Gd/Y [3]) have demonstrated that the complex spin structure in the magnetic rare earths is propagated through yttrium interlayers. To determine if nonmagnetic rare earths other than yttrium can sustain long-range exchange interactions, we have performed neutron diffraction experiments on Dy/Lu and Dy/Y/Sc/Y superlattices grown by Molecular Beam Epitaxy.

A. Dysprosium/Lutecium. In bulk form dysprosium exhibits a basal-plane helical spin structure with a propagation vector along the c^* axis. At T_c the Dy spins align parallel to the a^* direction. Diffraction studies of c-axis Dy/Y superlattices [1] indicate that the Dy spiral is coherent across intervening layers of yttrium. The mechanism behind this coupling is a spin density wave stabilized in the Y conduction band via the RKKY interaction. The effective wavevector of the "magnetic order" in the yttrium is close to Q that maximizes the generalized susceptibility calculated from the band structure [4]. In addition the low temperature ferromagnetic state does not develop in the Dy/Y superlattices. It was suggested [5] that the epitaxy modifies the magneto-elastic energy and inhibits the orthorhombic distortion that accompanies the ferromagnetic transition in bulk Dy.

Because the generalized susceptibility [4] for lutecium has a peak similar to Y, the Dy spiral should again be coherent through the non-magnetic Lu layers in Dy/Lu superlattices. Preliminary studies of the sample [6] $[Dy_{15.5}/Lu_{22}]_{75}$ show that the spiral state never develops. At all temperatures below T_N, the spins ferromagnetically align within each Dy layer contrary to predictions from magneto-
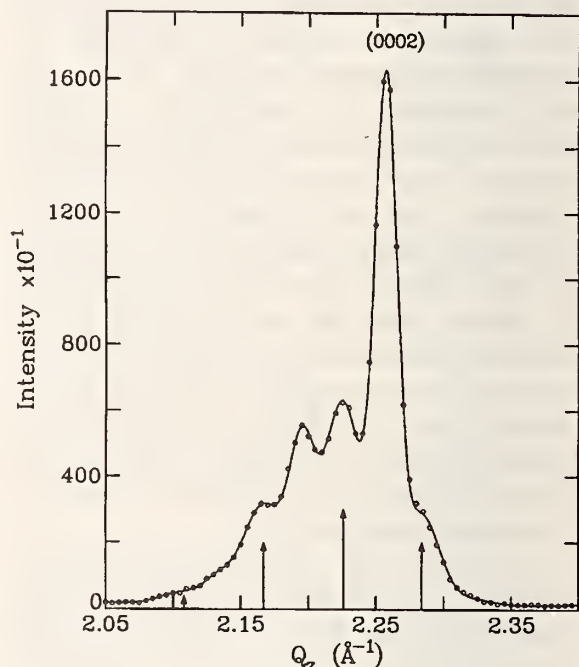
Figure 1. Neutron diffraction scans along the [0001] direction for $[Dy_{15.5}/Lu_{22}]_{75}$ at 10 K. The central (0002) lattice reflection is surrounded by superlattice satellites separated from it by $\Delta Q = 2n\pi/\Lambda$, where Λ is the superlattice periodicity. The peaks designated by arrows are magnetic reflections that result from the anti-alignment of the ferromagnetic Dy layer moments across the Lu interlayers.

elastic energy arguments [5]. These Dy layer moments anti-align across the intervening Lu, as demonstrated in figure 1. Bulk magnetization measurements suggest that a field of less than 1 kOe is required to induce ferromagnetic order. The weak antiferromagnetic coupling could thus result from dipolar coupling of the Dy layer moments or from the oscillatory RKKY interaction responsible for the spin order in c-axis Gd/Y superlattices [3]. Measurements of samples with varying Lu and Dy thicknesses are in progress to determine the origin of the antiferromagnetic alignment and the mechanism responsible for the suppression of the helical spin phase.

B. Dysprosium/Scandium. Similar to lutecium and yttrium, the generalized susceptibility of the rare-earth scandium is expected to have a distinct peak [7], which suggests that the conduction band can sustain long-range exchange interactions. In rare-earth/Sc alloys, however, the magnetic order becomes spin-glass like in samples with greater than 75% Sc [8] (Magnetic order persists in RE/Y alloys with as much as 95% Y [9]).

To resolve this discrepancy, the sample $[Dy_{3.5}/Y_{3.5}/Sc_{1.5}/Y_{3.5}]_{200}$ was examined using zero field diffraction techniques. It is noted that the Y-spacer layers in this sample are required for coherent growth due to the 6.8% mismatch between the Dy and Sc lattice. Unlike the Dy/Lu sample, the Dy spiral does persist in this sample at temperatures as low as 10 K and is coherent through the Y/Sc/Y interlayers. Because the nominal Sc thickness of 1.5 atomic layers is comparable to the usual number of interface layers (3 - 4), it is possible that interdiffused Y is responsible for the Dy spin coupling. Growth of superlattices with larger Sc layers is currently under way.

References

[1] R. W. Erwin, J. J. Rhyne, M. B. Salamon, J. A. Borchers, Shantanu Sinha, R. Du, J. E. Cunningham, and C. P. Flynn, Phys. Rev. B35, 6808 (1987); M. B. Salamon, Shantanu Sinha, J. J. Rhyne, J. E. Cunningham, R. W. Erwin, J. A. Borchers, and C. P. Flynn, Phys. Rev. Lett. 56, 259 (1986).

[2] R. W. Erwin, J. J. Rhyne, J. A. Borchers, M. B. Salamon, R. Du, and C. P. Flynn, J. Appl. Phys. 63, 3458 (1988); J. A. Borchers, Ph.D. thesis, University of Illinois, 1990.

[3] C. F. Majkrzak, J. W. Cable, J. Kwo, M. Hong, D. B. McWhan, Y. Yafet, J. V. Waszczak, and C. Vettier, Phys. Rev. Lett. 56, 2700 (1986).

[4] S. H. Liu, R. P. Gupta, and S. K. Sinha, Phys. Rev. B4, 1100 (1971).

[5] R. W. Erwin, J. J. Rhyne, J. A. Borchers, M. B. Salamon, R. Du, and C. P. Flynn, Mat. Soc. Symp. Proc. 166, 133 (1990).

[6] In the sample designation $[Dy_n/Lu_m]_l$, n refers to the number of Dy layers per bilayer, m is the number of Lu layers per bilayer, and one is the total number of bilayers in the sample.

[7] R. P. Gupta and A. J. Freeman, Phys. Rev. B13, 4376 (1976).

[8] H. R. Child and W. C. Koehler, Phys. Rev. 174, 562 (1968).

[9] H. R. Child, W. C. Koehler, E. O. Wollan, and J. W. Cable, Phys. Rev. 138, A1655 (1965).

DIFFUSE X-RAY SCATTERING FROM A GaAs/AlAs SUPERLATTICE

D. A. Neumann, C. F. Majkrzak, and S. K. Satija
A. Salvador and H. Morkoç (University of Illinois, Urbana, IL)
H. Homma (Brooklyn College, CUNY, Brooklyn, NY)
and
M. Sanyal and S. Sinha (Brookhaven National Laboratory, Upton, NY)

Neutron and x-ray reflectivity are becoming standard techniques for measuring the scattering density profile of many different types of films and multilayers. These techniques, however, only yield information perpendicular to the basal plane of the film thereby making it impossible to ascertain whether the interfacial width determined from these measurements is due to interdiffusion or roughness. In order to obtain a complete description of the interface, scans having a component of the scattering vector ∥ to the interface must be performed. We have, therefore, begun to measure the diffuse in-plane scattering from a variety of films including GaAs/AlAs superlattices.

The sample used in this study was grown by molecular beam epitaxy at the University of Illinois and has a superlattice period of 120 Å. The data was taken on a standard 2 axis x-ray diffractometer using CuK_α radiation. Scans were performed by fixing the scattering angle at various satellite reflections and scanning the sample angle θ. This very closely approximates an in-plane scan along the 110 direction. The results of one of these rocking curves is shown in figure 1. The solid line is the sum of a Gaussian peak and a Lorentzian peak which yielded the best fit to the data. The Gaussian lineshape represents the specular scattering while the Lorentzian peak represents the diffuse scattering presumably from interfacial roughness, since pure interdiffusion should give monotonic diffuse scattering. Several features of the scattering should be noted. At lower values of Q (i.e., for the first few satellites) the sum of a Gaussian and a Lorentzian was not a good model for the scattering, presumably due to dynamical effects. Second, the width of both peaks was found to be constant in angle, not Q. While this is not surprising for the Gaussian peak which reflects the instrumental resolution, one would expect that the width of the diffuse scattering should be constant in Q-space. We have no
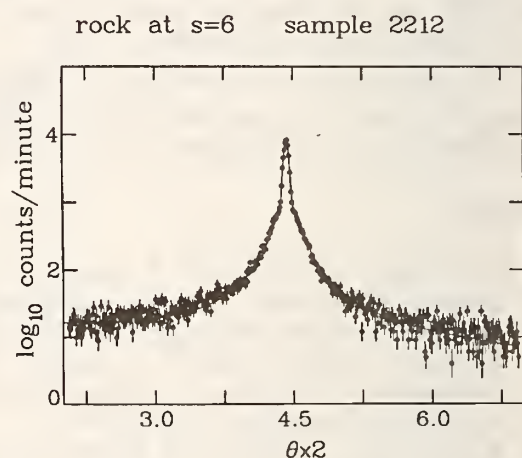
Figure 1. Rocking scan of the 6th satellite of a GaAs/AlAs superlattice. The solid line is the sum of a Gaussian peak and a Lorentzian peak which yielded the best fit to the data.

good explanation for why it is not. Third, the ratio of the diffuse intensity to the specular intensity is consistent with the Q^2 law typical for diffuse scattering. Further measurements on this and on other systems are in progress. It is hoped that these measurements will give a more complete understanding of the microstructure of the interfaces in a variety of thin-film systems.

POLARIZED NEUTRON REFLECTOMETER AND GRAZING ANGLE DIFFRACTOMETER

C. F. Majkrzak, S. Satija, D. A. Neumann, and J. F. Ankner

A neutron reflectometer, in which the incident beam can be polarized and the spin state of the reflected beam analyzed, has recently been constructed on beam tube BT-7 at the NBSR. In addition to obtaining reflectivity data, from which chemical and magnetic density profiles normal to a surface can be deduced, surface- or near-surface-sensitive diffracted intensities can be measured from properly oriented single crystal samples. In this report we briefly describe the reflectometer itself, i.e., how the incident beam is polarized and the neutron spin state selected, what the instrumental resolution and flux at the sample are, etc.

In figure 1 is shown a schematic of the reflectometer. The polychromatic beam first passes through a pyrolytic graphite (PG) filter to suppress the higher-order wavelengths which would also be reflected by the vertically focussing PG monochromator set for a principal wavelength λ of 2.35 Å. For collimations of the order of one degree and one minute of arc preceding and following the monochromator, respectively, the wavelength resolution $\Delta\lambda/\lambda \sim$ 0.01. Associated with a given wavevector transfer $\vec{Q}(|\vec{Q}| = |\vec{k}_f - \vec{k}_i|$ where $\vec{k}_i$ and $\vec{k}_f$ are the initial and final neutron wavevectors, respectively) is an instrumental resolution ΔQ given by

$$\Delta Q = \frac{\Delta\lambda}{\lambda}Q + \sqrt{(\frac{4\pi}{\lambda})^2 - Q^2}\ \Delta\theta \quad (1)$$

where $\Delta\theta$ is the angular divergence of the beam incident on the sample. The first term on the right-hand-side of Equation (1) ranges, for $\Delta\lambda/\lambda$ = 0.01, from 0.0001 Å^{-1} at Q = 0.01 Å^{-1} to 0.001 Å^{-1} at Q = 0.1 Å^{-1} whereas, for $\Delta\theta$ = 1 min. or $\sim$0.0003 rads, the second term is $\sim$0.0015 Å^{-1} up to a Q of 0.1 Å^{-1}. Thus, at Q = 0.01 Å^{-1}, $\Delta Q \sim$ 0.0016 Å^{-1} and at Q = 0.1 Å^{-1}, $\Delta Q \sim$ 0.0025 Å^{-1}. This resolution is adequate in most cases and, at higher values of Q, can often be further relaxed. Without a cold source, it is more advantageous to work at 2.35 Å rather than, say, 4.0 Å since, for a given Q-resolution, the neutron flux is substantially higher. For $\Delta\lambda/\lambda \sim$ 0.01, λ = 2.35 Å, and $\Delta\theta \sim$ 1 min, the actual flux on the sample is $\sim$5. x 10^5 neutrons/cm^2-s.

Between the pair of slits which define the angular divergence of the incident beam is a fast neutron mask consisting of two 4-in long slabs of borated polyethylene spaced $\sim$0.040" apart. The apertures of the incident beam-defining slits can each be opened from about 0.003" to 0.040" (the distance between slits is of the order of a meter). An adjustable aperture following the sample more accurately defines the scattering angle. The ^{3}He detector (1/2" diam, 4" high), is surrounded by boron-carbide and borated polyethylene shielding material. Room background with the reactor running is about 0.1 counts/minute. An identical detector is located overhead (not shown in fig. 1) for grazing angle diffraction experiments.

Polarization of the incident beam is accomplished in transmission by one or more polarizing Fe-Si supermirrors deposited on single crystal Si substrates. The supermirrors are aligned to reflect out (of the incident beam direction) neutrons in one spin state. The deflected neutrons are then captured in the absorbing material of the masks which define the slit before the sample. Because the reflectivities of the polarizing supermirrors are not unity for the unwanted spin state, two or more supermirrors are used in series. For example, for a reflectivity of 80%, two supermirrors in series give a polarizing efficiency of $\sim$96% or a flipping ratio of 25. Using three or more plates results in a higher flipping ratio, but the transmission of the desired spin state is reduced to about 50% due to losses which can be primarily attributed to attenuation of the beam as it passes through the Si substrates (with path lengths of several inches at such low angles). Better supermirror coatings such as Fe-Ag and Co-Ti exist [1] but cannot be used in

transmission because of the absorption losses which would occur in the Ag or Co layers. Nonetheless, by polarizing the beam in transmission, the undeviated beam of the desired spin state is not appreciably broadened, which is an important advantage. A secondary benefit is that the spectrometer is of simpler design. A second (or third) transmission polarizing device can be placed in the reflected (or grazing angle diffracted) beam. To flip from one neutron spin state to the other, simple flat solenoids, in which a field is applied orthogonally to both the vertical guide field and beam propagation directions, are used (see, e.g., [2]).

In figure 2 is plotted neutron (unpolarized) reflectivity vs. Q for a diblock copolymer film as obtained using the reflectometer described above. Data for two different collimations or instrumental resolutions are shown. Reflectivities down to about 2. x 10^{-7} with a signal-to-noise ratio of about 1 can be measured. A number of reflectometry measurements on magnetic and polymer films and multilayers have already been performed on this machine, as has the first polarized beam, grazing angle diffraction experiment [3]. Its success is due in large part to the efforts of the expert technical staff of the Reactor Radiation Division.

Figure 2. Example of the (unpolarized) neutron reflectivity profiles which can be obtained with this reflectometer. The sample is a multilayer of a diblock copolymer of polystyrene and polyisoprene made by T. Russell et al. at IBM. Data are plotted for two separate collimations.

Figure 1. Schematic of the polarized beam reflectometer at the NBSR as described in the text.

References

[1] R. Pynn, in Thin-Film Neutron Optical Devices, C. F. Majkrzak, ed., SPIE Vol. 983 (SPIE, Bellingham, WA, 1989) p. 18.

[2] W. G. Williams, Polarized Neutrons, (Oxford University Press, Oxford, 1988).

[3] J. F. Ankner, C. F. Majkrzak, D. A. Neumann, A. Matheny, and C. P. Flynn, Physica B (to be published).

NEUTRON REFLECTIVITY OF Y/Gd

J. F. Ankner and H. Zabel (University of Illinois, Urbana, IL)
Y. Y. Huang and G. P. Felcher (Argonne National Laboratory, Argonne, IL)
D. A. Neumann and C. F. Majkrzak
and
A. Matheny, J. A. Dura, and C. P. Flynn (University of Illinois, Urbana, IL)

Neutron reflectivity is an important tool in the study of surface and interfacial magnetism. Using polarized-neutron techniques, we have begun to study the magnetic moment distribution in the interfacial region of Y/Gd films grown by molecular beam epitaxy. These experiments, carried out at the Intense Pulsed Neutron Source at Argonne National Laboratory, continue work begun at NIST [1].

The interfacial magnetism of gadolinium has been a subject of intensive study over the past several years. These experiments fall into two categories: work on Gd/vacuum interfaces (free Gd surfaces) [2] and studies of synthetic Y/Gd superlattices [3]. Our experiments represent something of a hybrid of these two fields, since we use neutron reflectivity to measure the depth-dependence of the layer- averaged magnetic structure at one Y/Gd interface.

By measuring the reflectivity of neutrons polarized parallel and anti-parallel to an applied magnetic field, one can determine the depth profile of the magnetization in a sample. A useful measure of the magnetization is the neutron spin asymmetry,

$$ A = \frac{I_\uparrow - I_\downarrow}{I_\uparrow + I_\downarrow} $$

where $I_\uparrow$ is the reflected intensity of neutrons polarized parallel to the field applied at the sample and $I_\downarrow$ the intensity for those polarized anti-parallel. Figure 1 shows the spin asymmetry as a function of temperature for a film consisting of 97 Å Y(0001) on 1000 Å Gd(0001) near the bulk Curie temperature with a 20 G applied field. Within the uncertainty of the measurement, all in-plane magnetization in the sample disappears at T = 293 K. Studies of Gd using electron diffraction and photo-emission showed that the surface remains ordered for up to 20 K above the bulk Curie temperature
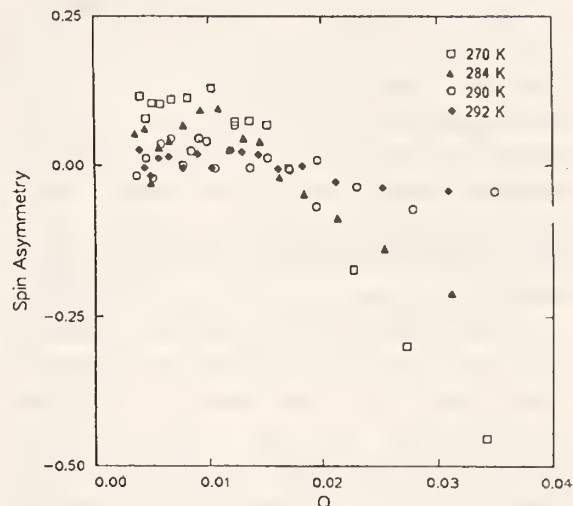
Figure 1. Spin asymmetry for 97 Å Y(0001) on 1000 Å Gd(0001).

($T_C^{Gd} = 293$ K). Our results on Y/Gd indicate that, in this system, any in-plane moment must be quite small, if it exists at all. We plan, in further work, to perform a more detailed study of the temperature region around T_C^{Gd} and to investigate the depth-dependence of the interfacial magnetism using both reflectivity and grazing-angle diffraction.

References

[1] J. F. Ankner, H. Zabel, D. A. Neumann, C. F. Majkrzak, A. Matheny, J. A. Dura, and C. P. Flynn, in Neutron Scattering for Materials Science, S. M. Shapiro, S. C. Moss, and J. D. Jorgensen, eds. Matls. Res. Soc. Sym. Proceedings, Vol. 166, (Matls. Res. Soc., Pittsburgh, 1990).

[2] D. Weller, S. F. Alvarado, W. Gudat, K. Schröder, and M. Campagna, Phys. Rev. Lett. 54, 1555 (1985).

[3] C. F. Majkrzak, J. W. Cable, J. Kwo, M. Hong, D. B. McWhan, Y. Yafet, J. V. Waszczak, and C. Vettier, Phys. Rev. Lett. 56, 2700 (1986).

INTERFACIAL WIDTHS IN HOMOPOLYMER/DIBLOCK COPOLYMER SYSTEMS

T. P. Russell, A. Menelle and S. H. Anastasiadis (IBM Research Division, San Jose, CA)

S. K. Satija

and

W. Hamilton and G. Smith (Los Alamos National Laboratory, Los Alamos, NM)

The interface formed between poly(styrene), PS and polymethyl methacrylate, PMMA, homopolymers was found to be 50 Å[1,2]. Symmetric, diblock copolymers of PS and PMMA, denoted P (S-b-MMA) form a lamellar microphase separated morphology where the interface between the PS and PMMA micro-domains is also 50 Å. Yet, placing P(S-b-MMA) between the PS and PMMA yielded an interfacial thickness of 75 Å [3]. The quantity of P(S-b-MMA) placed at the interface corresponded to a film thickness of L/2 where L is the repeat period of the lamellar microdomain morphology in the bulk. This poses two separate questions which are the subject of this report. First, is the broadening of the interfacial width as a function of the amount of P(S-b-MMA) present. Secondly, is there a broadening of the interface between the PS and PMMA microdomains of the copolymer as PS and PMMA homopolymer is added.

The latter question was addressed by investigating mixtures of P(S-b-MMA) and P(S-b-d-MMA) with PS and PMMA homopolymers where the homopolymers have the same labeling as the blocks of the copolymer. Each block of the copolymer had a molecular weight of ~5x10^4 whereas the homopolymer molecular weights were ~ 1x10^5. Mixtures having 4.5% of PS and PMMA with P(S-b-MMA) were prepared in toluene, cast onto silicon substrates and annealed for 240 h under vacuum. Reflectivity profiles displayed interferences arising from the multilayered morphology. As expected, the period of the lamellar morphology increased with increasing concentration of the homopolymer. In addition, as the homopolymer concentration increased the width of the interfaces between the PS and PMMA microdomains was found to increase from the 50 Å of the pure copolymer to ~ 55 Å for the 4.5% mixture to ~ 70 Å for the 8.3% mixture. The gradual increase in the interfacial width clearly shows that the homopolymer molecules penetrate deeply within the interfacial region. These data also show that the interfacial broadening is a function of the ratio of the number of copolymer to homopolymer molecules at the interface.

On the opposite end of the composition scale experiments were performed on trilayer specimens of PS/P (S-b-MMA)/PMMA where the MMA segments were perdeuterated (homopolymer and copolymer). Specimens were prepared by casting a film of PMMA from toluene onto a silicon substrate. On a separate substrate a film of P(S-b-MMA) was prepared with the desires thickness. This film was then floated off into a pool of deionized water and retrieved with the PMMA coated substrate. Similarly, PS film was prepared on a separate substrate, floated off onto deionized water and retrieved with the P(S-b-MMA)/PMMA, bilayer forming a trilayer. This was annealed at 170 °C for 240 h under vacuum.

The reflectivity profiles could be described using a bilayer model comprised of a PS and d-PMMA layer. The interface formed between the two layers is given by an error function or hyperbolic tangent whose width increased with increasing P (S-b-MMA) concentration. At a P(S-b-MMA) thickness of 255 Å, i.e., L/2, the interfacial with was 75 Å in agreement with previous results [3]. However, increasing the thickness of the P(S-b-MMA) layer above L/2 yielded an interfacial width excess of 250 Å. Measurement of the off-specular scattering, i.e., where the diffraction vector is not normal to the film surface, indicated a substantial amount of in-plane correlations in the scattering length density which can be attributed to the information of ordered structures at the interface. Consequently, a saturation in the number of copolymers molecules that could be located at the interface was achieved.

The combination of these two sets of measurements showed conclusively that, at the molecular weights studied, there is significant

penetration of the homopolymer into the interfacial region and that there is a maximum number of copolymer molecules that can align themselves at the interface.

References

[1] S. H. Anastasiadis, T. P. Russell, S. K. Satija, and C. F. Majkrzak, J. Chem. Phys. 92, 5677 (1990).
[2] M. L. Fernandez, J. S. Higgins, J. Penfold, R. C. Ward, C. Shackleton, and D. J. Walsh, Poly. 29, 1923 (1988).
[3] T. P. Russell, S. H. Anastasiadis, A. Menelle, G. P. Felcher, and S. K. Satija, Macromol. (submitted for publication).

FILM THICKNESS CONSTRAINTS ON DIBLOCK COPOLYMER MORPHOLOGIES

T. P. Russell, A. Menelle, and S. H. Anastasiadis (IBM Research Division, San Jose, CA)
and
S. K. Satija and C. F. Majkrzak

Secondary ion mass spectrometry studies [1,2], optical microscopy [3], and neutron reflectivity studies [4,5] performed on symmetric diblock copolymers of poly(styrene) and poly(methylmethacrylate), denoted P(S-b-MMA), have shown that thin films of the copolymers on silicon substrates form a multilayered morphology. It has been shown that the lamellar microdomain morphology of the P(S-b-MMA) orients parallel to the surface of the substrate with PMMA layer adjacent to the silicon substrate and a PS layer at the air surface. The widths of the layers adjacent to the air and silicon interfaces are one-half that seen in the bulk of the multilayer and, consequently, the thickness of the specimen at any point in the specimen is given by $(N + 0.5) L$ where L is the period of the lamellar microdomain morphology and N is an integer.

This report concerns the effect of film thickness on the copolymer morphology where the total thickness of the specimen is less than or equal to 3L/2, i.e., where N = 1. A series of neutron reflectively studies were performed on a P(S-b-MMA) copolymer films, where the PS block is perdueterated, such that the film thicknesses were L/4, L/2, 3L/4, L, and 3L/2. The molecular weight of the PS block was 1.6×10^5 and that of the PMMA block was 1.3×10^5. In the bulk the lamellar repeat period is 762 Å.

Copolymer films with thickness of 209 Å (L/4), 381 Å (L/2), 555 Å (3L/4, 726 Å (L), and 1299 Å (3L/2) were prepared by casting solutions of the copolymer from toluene onto silicon substrate and annealed for 240 h at 170 °C under vacuum. In all but one of the specimens x-ray photoelectron spectroscopy showed that, over the first 70 Å from the air surface, the specimens consisted of pure PS. In the L thick specimen, the surface was comprised of 54% PS.

Neutron reflectivity measurements on the L/2 and 3L/2 specimen yielded scattering length density profiles characteristic of a layered morphology with PMMA at the silicon interfaced and PS at the air interface. In the L/2 case a 345 Å layer of PS on top of a 210 Å layer of PMMA was found with an interface of 50 Å separating the two layers. In the 3L/2 case four layers, alternating PS and PMMA from the air surfaces, were found separated by interfacial widths of 50 Å. Thus, in these two cases the morphologies conformed to the expected layered morphology.

Decreasing the film thickness to L/4 yielded a reflectivity profile that was well described by a bilayer of PS and PMMA with thicknesses of 122 and 87 Å. Each of these is much less than that seen for the L/2 specimen. However, the width of the interfaced between the lamellar

microdomains was maintained at 50 Å. These results showed clearly that the microphase separation was maintained and that the copolymer chains were compressed normal to the film surface. However, the characteristics of the interface between the PS and PMMA layers are vastly different.

Increasing the film thickness to 3L/4 yielded a reflectivity profile that could be described by a bilayer of PS and PMMA with layer thicknesses of 345 and 210 Å, respectively. In comparison to the thicknesses of the lamellar microdomains in the bulk, these are much thicker. In addition, the width of the interface between the PS and PMMA layers was found to be 100 Å, again larger than the bulk values. These results show that the PS and PMMA chains of the copolymer are markedly stretched and cause a broadening of the interface between the PS and PMMA layers.

For the L thick specimen the reflectivity results could be well described with a trilayer model comprised of a 250 Å layer of a 54%PS/46%PMMA mixture on top of a 313 Å layer of PS on a 163 Å layer of PMMA. The width of the interface between the lower PS and PMMA layer was 50 Å and that between the mixed layer and the PS layer was 150 Å. The chain stretching observed in the 3L/4 case could not be extended to the L case since this would

require too much elastic energy. Thus, the copolymer chains are forced to mix despite the fact that the copolymer is well below the order-disorder transition temperature. The thickness constraint has caused a suppression of the microphase separation.

In summary, these studies have shown that the film thickness can cause rather dramatic alterations in the morphology of the diblock copolymers and, consequently, perturb the thermodynamics of the copolymer molecules.

References

[1] G. Coulon, T. P. Russell, V. R. Deline, and P. F. Green, Macromol. 22, 2581 (1989).

[2] T. P. Russell, G. Coulon, V. R. Deline, and D. C. Miller, Macromol. 23, 4600 (1990).

[3] G. Coulon, D. Ausserre, and T. P. Russell, J. Phys. France. 51, 777 (1990).

[4] S. H. Anastasiadis, T. P. Russell, S. K. Satija, and C. F. Majkrzak, Phys. Rev. Lett. 62, 1852 (1989)

[5] S. H. Anastasiadis, T. P. Russell, S. K. Satija, and C. F. Majkrazak, J. Chem. Phys. 92, 5677 (1990).

SEGMENT DENSITY DISTRIBUTION OF SYMMETRIC DIBLOCK COPOLYMERS AT THE INTERFACE BETWEEN TWO HOMOPOLYMERS AS REVEALED BY NEUTRON REFLECTIVITY

T. P. Russell, S. H. Anastasiadis, A. Menelle (IBM Research Division, San Jose, CA)

G. P. Felcher (Argonne National Laboratory, Argonne, IL)

and

S. K. Satija

The segment density distribution of symmetric, diblock copolymers of poly(styrene), PS, and poly(methylmethacrylate), PMMA, denoted P(S-b-MMA), at the interface between two homopolymers PS and PMMA were investigated by neutron reflectivity measurements. Selective labelling of either block of the P(S-b-MMA) or of the homopolymers PS or PMMA with deuterium provided the contrast necessary to isolate the distribution of the segments of the components of block copolymer at the interface. Results from a series of experiments were used to solve a simultaneous set of linear equations that yielded the segment density profiles of the PS and PMMA segments of the homopolymers and copolymers at the interface.

Typical reflectivity profiles for two (out of a total of six different combinations) of the specimens studied are shown in figures 1 and 2 along with scattering density profiles which were used to calculate the reflectivities shown by solid lines. Neutron reflectivity experiments were performed on POSY-II at the IPNS at Argonne National Laboratory.

The following conclusion could be drawn from this study [1].

It was found that the addition of the copolymer to the interface between the homopolymers significantly broadened the interface between the PS and PMMA homopolymers over that seen for the pure copolymer or that between the PS and PMMA homopolymers. It has been
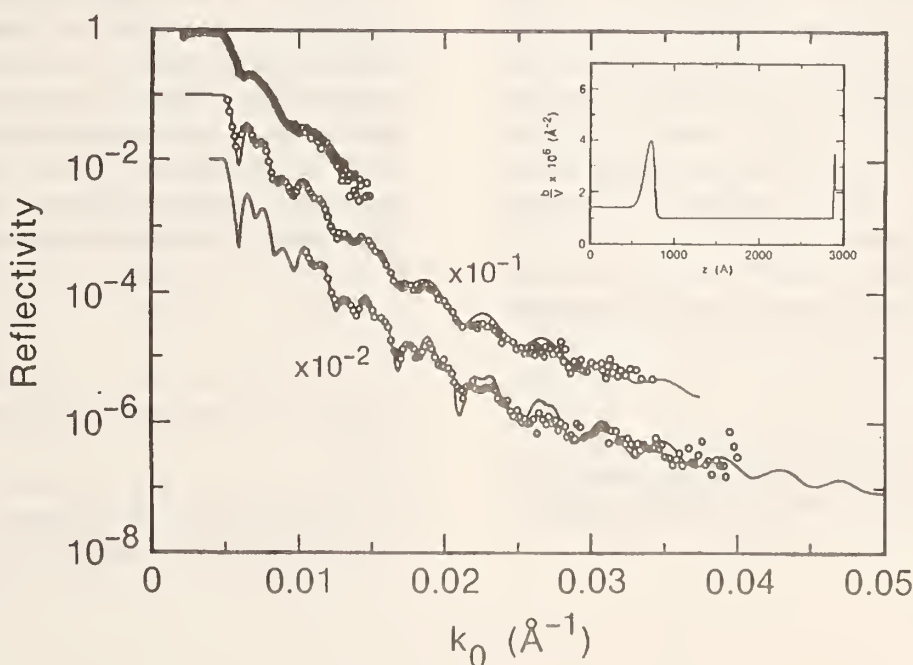
Figure 1. Experimental neutron reflectivity profile (O) for a trilayer on a silicon substrate. The trilayer is comprised of PS homopolymer at the air surface, a dPS/PMMA diblock copolymer and a PMMA layer adjacent to the substrate. Three different reflectivity results obtained at 0.27°, 0.78°, and 1.46°, angles of incidence are shown. These have been offset for clarity by factors of 1, 0.1, and 0.01, respectively. The solid line represents the calculated reflectivity profile using the segment density profile shown in the inset.
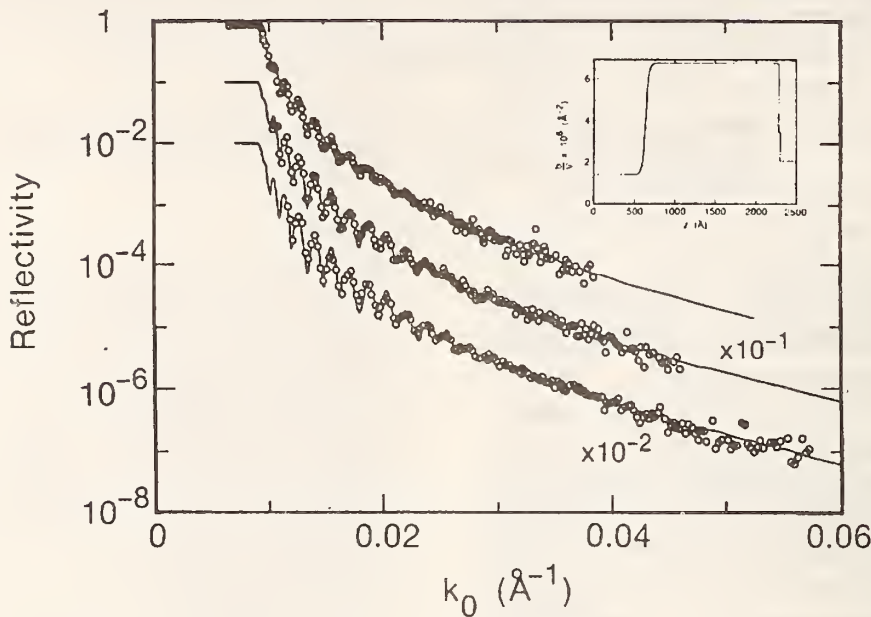
Figure 2. The same as in figure 1 but now the trilayer is comprised of a layer of PS at the air surface, a PS/d-PMMA copolymer at the homopolymer interface and a layer of d-PMMA adjacent to the substrate.

shown that the diblock copolymers are located at the interface between the homopolymers and that the PS segments of the copolymer were located in the PS phase and the PMMA segments of the copolymer in the PMMA phase. It was also found that the junction points of the copolymer were localized to a region around the midpoint of the interface over a distance comparable to the interfacial width observed for the neat diblock copolymers.

Furthermore, results from a series of experiments were used to solve a simultaneous

set of linear equation that yielded the segment density profiles of the two homopolymers, of each block of the copolymer and of the total copolymer at the interface. Results from this analysis were shown to be consistent with independent experimental results. This treatment showed that the homopolymers penetrated well into the interfacial region in contrast to theoretical arguments which would place the copolymer in the dry brush regime.

Reference

[1] T. P. Russell, S. H. Anastasiadis, A. Menelle, G. P. Felcher, and S. K. Satija, Macromol. (in print).

X-RAY REFLECTIVITY STUDIES OF THIN DIBLOCK COPOLYMER FILMS

S. K. Satija

E. B. Sirota and G. J. Hughes (Exxon Research & Engineering Co., Annadale, NJ))

S. K. Sinha (Brookhaven National Laboratory, Upton, NY)

and

T. P. Russell (IBM Research Division, San Jose, CA)

The technique of choice for studies of bulk polymer and polymer surfaces is neutron scattering because of the large contrasts one can obtain by substituting hydrogen and deuterium. Neutron reflectivity has been widely used to polymer surfaces and interfaces [1,2]. Recently, we have shown by neutron reflectivity measurements that annealed thin films of diblock copolymers of polystyrene and polymethyl-methacrylate P(S-b-MMA) form a very highly oriented multilayer morphology parallel to the film surface [3]. In neutron measurements a high degree of scattering contrast between different blocks of copolymers was achieved by deuterating one of the blocks while leaving the other block hydrogenated. This enabled us to study details of the interfacial profiles between PS and PMMA blocks [4].

In this report we show x-ray reflectivity measurements on films of same PS and PMMA block copolymers. The type of scattering contrast achievable with neutrons is not possible with x-rays. However, extremely high Q resolution and high intensity in x-ray measurements makes it possible to get unique information about polymer films which is complementary to neutron reflectivity measurements.

Figure 1(a) show x-ray reflectivity from a film of P(s-b-dMMA) (molecular wt. 30 K) annealed at 170 °C for 24 h. Neutron reflectivity studies on this and other similar systems have already been reported [3,4]. X-ray reflectivity measurements were done at beam X-10A at the National Synchrotron Light source at Brookhaven National Laboratory. Neutron reflectivity from the same sample, which was reported earlier [3], is shown in figure 1(b). Figure 1(b) shows three Bragg reflections from the ordered multilayer morphology of the two block copolymers. The inset in that figure gives the scattering density profile perpendicular to the surface which was used to calculate the solid line through the data points. However, the x-ray data in figure 1(a) shows a hint of one Bragg peak near $Q \simeq .045$ Å^{-1} and other rich structure. The x-ray scattering contrast between the two polymer blocks is not strong enough to give Bragg peaks in the x-ray data. The "high frequency" oscillations in figure 1(a) arise from the total thickness of the diblock copolymer film (1450 Å). The resolution in the neutron data was not sufficient to resolve these oscillations. A further modulation in the "high frequency" oscillations is also evident in figure 1(a). These arise due to the fact that the top bilayer of the polymer film is incomplete giving rise to islands at the top of the film. These x-ray data can be well fitted by assuming that scattering density of the top bilayer is 75% of scattering density of the rest of the bilayers. This means that the island size at the top is smaller than the transverse coherence length of the x-ray beam, which is of the order of 10-15 microns. Both specular and off-specular data are being used to get detailed information on interfacial structures in such films.
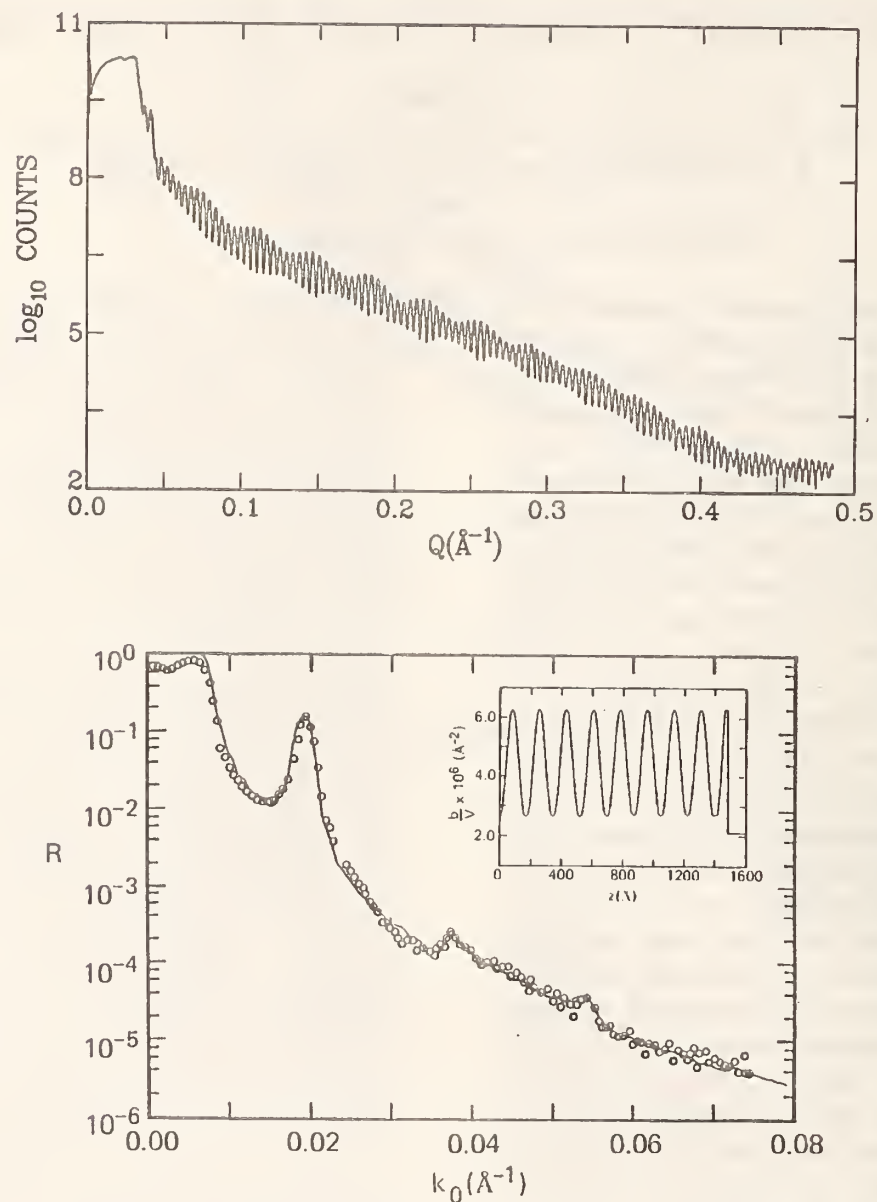
Figure 1. (top) a) X-ray reflectivity as a function Q from 1450 Å thick film of P(S-b-d-MMA) diblock copolymer. (bottom) b) Neutron reflectivity data from the same film. Note that $k_0 = 2Q$ in figure 1(b).

References

[1] E. Bouchard, B. Farnoux, X.Sun, M. Daoud, and G. Janink, Europhysics Lett. 2, 315 (1988).

[2] M. L. Fernandez, J. S. Higgins, J. Penfold, R. C. Ward, C. Shackleton, and D. J. Walsh, Poly. 29, 1923 (1988).

[3] S. H. Anastasiadis, T. P. Russell, S. K. Satija, and C. F. Majkrzak, Phys. Rev. Lett. 62, 1852 (1989).

[4] S. H. Anastasiadis, T. P. Russell, S. K. Satija, and C. F. Majkrzak, J. Chem. Phys. 92, 5677 (1990).

NEUTRON REFLECTIVITY FIT PROGRAM

J. F. Ankner

Neutron reflectivity continues to be important in the study of the interfacial structure of thin films and multilayers of polymer and both magnetic and nonmagnetic metal and semiconductor systems. We have developed several least-squares fitting programs to aid in the extraction of the depth profile of a sample from its reflectivity.

The reflection and refraction of a neutron plane wave are described by the Schrödinger equation and can be solved exactly. We have adapted the x-ray formalism of Parratt [1] to describe the reflectivity of an arbitrary number of layers deposited on a flat substrate. This reflectivity depends on the refractive indices, thicknesses, and interfacial roughnesses of the constituent layers, which we can selectively vary as parameters in a nonlinear least-squares Levenberg-Marquardt [2] fit routine.

We calculate the effect of interfacial roughness in two different ways. The program REFFIT employs the static Debye-Waller factor described by Nevot and Croce [3] to model the roughness at each interface and folds these individual reflectivities into the Parratt recursion formula (see [4] for a FORTRAN source code listing and description). This static Debye-Waller approach only remains valid as long as the individual layer thicknesses are much greater than the interfacial roughnesses. Natural oxide layers at metal and semiconductor surfaces often violate this condition. The program BLOCKS explicitly generates interfacial layers and can therefore be used to model such cases of extreme interdiffusion.

Figure 1 shows the reflectivity of a nickel film used to determine the resolution of the BT-7 instrument for a particular slit configuration, with the data fitted using REFFIT. The best-fit parameters show that a 1043 Å Ni film sits atop a float glass substrate with a surface roughness of σ_{0Ni} = 13.0 Å and roughness at the interface of σ_{NiG} = 2.9 Å, as measured by a neutron beam with $\delta\theta$ = 0.28 mradian and $\delta\lambda/\lambda$ = 0.009 (λ = 2.35 Å).
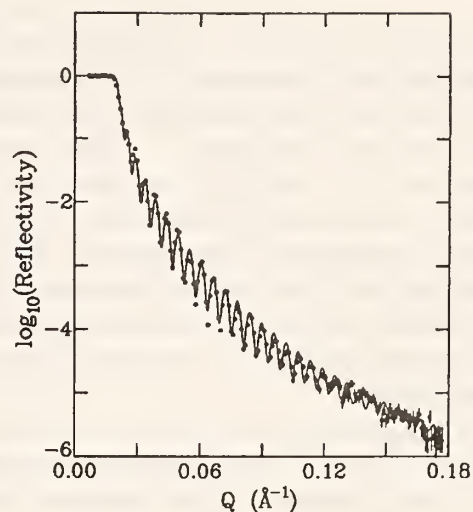
Figure 1. Neutron reflectivity of nickel film sputtered on float glass substrate. The fitted parameters are: film thickness d = 1043 Å, nickel/vacuum roughness σ_{0Ni} = 13.0 Å, and nickel/glass roughness σ_{NiG} = 2.9 Å.

These programs should make the determination of layer profiles more accurate and less time-consuming. We have nearly completed a program (MLAYER) to fit the reflectivity of artificial superlattices and plan to model supermirrors in the near future.

References

[1] L. G. Parratt, Phys. Rev. 95, 359 (1954).

[2] W. H. Press, B. P. Flannery, S. Teukolsky, and W. T. Vetterling, Numerical Recipes, Cambridge: Cambridge University Press. 1986.

[3] L. Nevot and P. Croce, Rev. Phys. Appl. 15, 761 1980).

[4] J. F. Ankner, Ph. D. Thesis, University of Illinois at Urbana-Champaign, 1990 (unpublished).

SANS FROM HOT STRETCHED PARTIALLY DEUTERATED POLYSTYRENE

B. Hammouda

and

J. Schroeder and R. A. Bubeck (Dow Chemical, Midland, MI)

The small angle neutron scattering technique is applied to hot stretched 5% perdeuterated polystyrene in order to investigate the residual macromolecular orientation. The observed orientation is left over after fast quenching (in ice water) of the hot stretched sample. Previous similar investigations [1] focused on the effect of higher external draw ratios (EDR) on the radius of gyration. The present measurements [2] also included varying the hot stretching temperature and strain rate.

Perdeuterated macromolecules are found to follow the external draw ratio affinely for low EDR's as expected. The extent of chain anisotropy is found to increase with increasing EDR, with increasing strain rate, and with decreasing hot stretching temperature. Local macromolecular relaxation was observed for short chain segments. This is shown as an increase of the eccentricity with the momentum transfer Q in figure 1.
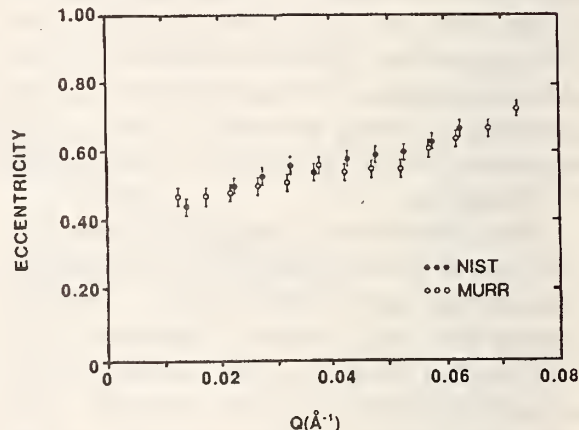
Figure 1. Variation of the ellipticity of the isointensity contour plots with momentum transfer Q. Data shown were taken on the MURR-SANS and the NIST-SANS 8-m instruments. This sample corresponds to an EDR = 1.6.

Most of this work was performed before B. Hammouda joined NIST.

References

[1] B. Hammouda, R. A. Bubeck, and D. F. R. Mildner, Polymer 27, 393-397, (1986).

[2] D. Bradford, B. Hammouda, R. Bubeck, J. Schroeder, C. Glinka, and P. Thiyagarajan, J. Appl. Cryst. 23, 1-5 (1990).

SHEAR DEPENDENCE OF CRITICAL FLUCTUATIONS IN BINARY POLYMER MIXTURES BY SMALL ANGLE NEUTRON SCATTERING

A. I. Nakatani and C. C. Han (Polymers Division)

Two different polymer blends were used to examine the effect of shear on the critical behavior by small angle neutron scattering. The two different blends were polystyrene/poly(vinylmethylether) (PSD/PVME) and polystyrene/polybutadiene (PSD/PB). The data was analyzed based on simple rotatory diffusion model and mode-mode coupling theory to relate a critical dimension for concentration fluctuations to shear rate. Both model predictions are in good agreement with our results.

PSD of $M_w = 4.4 \times 10^5$ and $M_w/M_n = 1.28$ was blended with PVME ($M_w = 1.8 \times 10^5$ and $M_w/M_n = 1.76$). The PSD/PVME blend composition was 20:80 by weight and represents the critical composition based on the data of Han et al. [1]. The PSD/PVME blend exhibits LCST behavior. A second PSD ($M_w = 1.0 \times 10^3$ and $M_w/M_n = 1.04$) was blended with PB with a nominal $M_w = 4.5 \times 10^3$. The sample composition was 77:23 PSD/PB by weight and is off-critical. The PSD/PB blend displays UCST behavior.

The shear apparatus and methods used for data acquisition have been described in detail elsewhere [2]. Sector averages of the scattered intensity parallel and perpendicular to the flow (horizontal and vertical) were obtained in $\pm 10°$ sectors. The PSD/PVME blend was studied between 100 °C and 142.5 °C at shear rates between $0.02 \, s^{-1}$ and $1.30 \, s^{-1}$. The optical cloud point at zero shear was 140 °C. The scattering profiles for the PSD/PB blend were obtained between 35 °C and 80 °C and at shear rates ranging between 50 and 200 s^{-1}. The zero shear cloud point was determined to be approximately 40 °C by optical methods. For each system in the one phase region at constant temperature, a decrease in scattering intensity at low q was observed which implies the suppression of large fluctuations. A cutoff value, q_s, was determined as the value of q where the zero shear and sheared structure factors diverge. As the shear rate increases, q_s also increases. Perpendicular

to flow, no changes in the scattering behavior were observed.

For rotatory diffusion of a sphere in solution the following relation holds [3]:

$$\tau = \Theta^{-1} = 8\pi\eta R^3/k_B T \qquad (1)$$

where τ is a rotational relaxation time, Θ is the rotational diffusion coefficient, η is the solution viscosity, R is the radius of the sphere, k_B is Boltzmann's constant and T is the temperature. For the case of concentration fluctuations under the influence of shear, at a given shear rate $\dot{\gamma}$, concentration fluctuations with $\tau > 1/\Theta$ (large R), will be suppressed. The suppression of these large fluctuations below q_s is related to Θ as follows:

$$\tau = \Theta^{-1} = (8\pi\eta/k_B T q_s^3) \qquad (2)$$

The viscosity and temperature dependence of the experimental q_s values may be analyzed by plotting $[\log q_s - (1/3)\log \eta + (1/3)\log T]$ versus $\log \dot{\gamma}$. From equation 2, a plot of this form should give a slope of 1/3 and an intercept value of $(1/3)\log(8\pi/k_B) = 5.753$.

From the mode-mode coupling analysis of Ferrell [4] and Kawasaki [5], the decay rate, Γ_q, of fluctuations with wavenumber q may be written as a sum of molecular and hydrodynamic contributions. If we first neglect the molecular contribution to the relaxation process, the hydrodynamic term is defined as $(k_B T q^2/6\pi\eta\xi)$ for $q\xi < 1$ and $(k_B T q^3/16\eta)$ for $q\xi > 1$. The shear rate dependence of the longest wavelength, q_c^{-1}, not affected by shear rate is therefore given as:

$$q_c = (6\pi\eta\xi/k_B T)^{1/2}\dot{\gamma}^{1/2} \qquad \text{for } q_c\xi < 1 \quad (3a)$$

$$= (16\eta/k_B T)^{1/3}\dot{\gamma}^{1/3} \qquad \text{for } q_c\xi > 1 \quad (3b)$$

Equating the experimentally determined q_s to q_c, we would expect in the strong shear limit ($q_c\xi > 1$), a slope of 1/3 and an intercept of

$(1/3)\log(16/k_B) = 5.688$ for the types of plots discussed in the preceding paragraph.

Data for both the PSD/PVME and PSD/PB blends were combined in the [log q_s - $(1/3)$log η + $(1/3)$log T] versus log $\dot{\gamma}$ plot shown in figure 1. The experimentally determined viscosity values for both blends were utilized in the analysis. The slope was determined by linear regression analysis to be 0.332 with a standard deviation of 0.006. The intercept value was 5.71 with a standard deviation of 0.01. These values are entirely consistent with the rotatory diffusion analysis as well as the mode-mode coupling analysis with the hydrodynamic term dominating the molecular term. Hashimoto [6] and Onuki [7] have argued that the molecular contribution to the relaxation should be the dominant process and predict that in the strong shear limit, q_c should vary with a $\dot{\gamma}^{1/4}$ power dependence. Our data does not support this prediction; however, Hashimoto and Onuki have argued from the standpoint of a blend in the two phase region while our data is taken in the one phase region of the phase diagram.
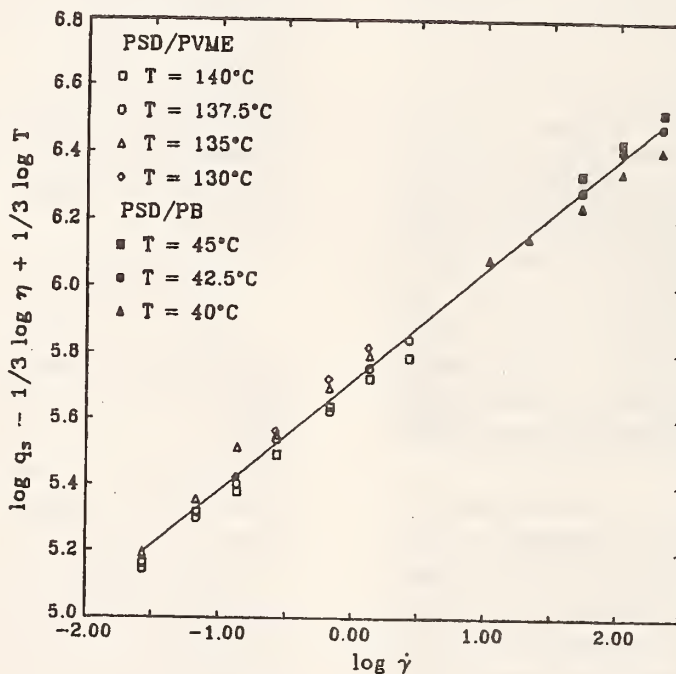
Figure 1. Log q_s - $(1/3)$log η + $(1/3)$log T vs log $\dot{\gamma}$ Open symbols are data for the PSD/PVME blend. Closed symbols are data for the PSD/PB blend.

References

[1] C. C. Han, B. J. Bauer, J. C. Clark, Y. Muroga, Y. Matsushita, M. Okada, Q. Tran-Cong, T. Chang, and I. C. Sanchez, Poly. 29, 2002 (1988).

[2] A. I. Nakatani, H. Kim, and C. C. Han, J. Res. Natl. Inst. Stand. Technol. 95, 7 (1990).

[3] See, for example, C. Tanford, Physical Chemistry of Macromolecules, (John Wiley and Sons, NY, 1961), 432-451 pp.

[4] R. Ferrell, Phys. Rev. Lett. 24, 1122 (1970).

[5] K. Kawasaki, Phase Transitions and Critical Phenomena, C. Domb and M. S. Green, eds. 5a, New York: Academic Press; 1976).

[6] T. Hashimoto, T. Takebe, and S. J. Suehiro, J.Chem. Phys. 88, 5874 (1988).

[7] A. Onuki, J. Chem. Phys. 85, 1122 (1986).

MICROSTRUCTURE EFFECTS ON LCST PHASE BEHAVIOR OF POLYBUTADIENE AND POLYISOPRENE BLENDS STUDIED BY SANS AND LS

S. Sakurai, H. Jinnai, H. Hasegawa, and T. Hashimoto (Kyoto University, Kyoto, Japan)
and
C. C. Han (Polymers Division)

It is extremely important to control the state of mixing and the phase-separated structure of polymer blends if it is expected for the blends to have superior properties than those of the individual constituent polymers. For this purpose, it is necessary to clarify the fundamental relationships between the molecular parameters of constituent polymers and the static and dynamic phase behaviors of polymer mixtures; e.g., miscibility, phase diagrams, and mechanism and dynamics of phase transition. The molecular parameters to be considered are the molecular weight (M), polydispersity (M_w/M_n) of polymers, molar volume of monomeric units (v), statistical segment length (b) related to the flexibility of the polymers, and the thermodynamic interaction parameter (χ) between two monomers. The other parameters such as copolymer composition, microstructure of polydienes, tacticity of vinyl polymers and isotope effects can be taken into consideration in terms of χ-parameter. Our aim is to clarify these relationships by a systematic scattering study using well-defined polymer systems.

Polydiene samples were synthesized by living anionic polymerization initiated by sec-butyllithium, and have narrow molecular weight distributions. Three HPI samples (sample code: VIRH) were synthesized and have the microstructures with the content of 3,4-unit in the range of 7% to 15%. Four DPB samples (sample code: VBRD) were synthesized and have the microstructures with the content of 1,2-unit in the range of 12% to 28%. SANS profiles for all HPI/DPB blends studied show increase in intensity at all q's with increasing in temperature. These phenomena are typical for LCST-type of phase behavior. Data were fitted, using nonlinear regression fitting routine, with the scattering theory of deGennes based on the random phase approximation (RPA). The effective interaction parameter, χ_{eff}, the correlation length, ξ and the zero-wavenumber structure factor, $S(q = o)$ obtained are used to

establish phase diagram of different blends. In order to discuss the microstructure effects on the blend miscibility, χ_{eff} for each HPI/DPB blend at the same composition was compared and plotted against T^{-1} in figure 1 (for $\phi_{DPB} = 0.48$). There are 10 sets of data on χ_{eff} which are shown in two figures; figure 1a shows the effect of the DPB microstructure on χ_{eff} for three given HPI's and figure 1b shows the effect of the HPI microstructure on χ_{eff} for three given DPB's. χ_{eff} shows a linear relationship with T^{-1} ($\chi_{eff} = A + B/T$) with a negative slope (B < 0) for each blend, indicating that all the HPI/DPB blends studied here show the LCST-type phase behavior, irrespective of the microstructure. Moreover, it can be seen that as the content of 1,2-unit in DPB increases and/or the content of 3,4-unit in HPI decreases, the χ_{eff} value decreases, and therefore the blend becomes more miscible for given molecular weights and a composition of the blends.

By neglecting a difference between cis-1,4 and trans-1,4, it can be assumed that HPI is a random copolymer of 3,4-unit (Iv) and 1,4-unit (I) and that DPB is that of 1,2-unit (Bv) and 1,4-unit (B). Then χ_{eff} is given by six sets of fundamental χ's according to copolymer theory.

By solving these equations with minimizing the square residuals, the fundamental χ was obtained as a function of temperature, as shown in figure 2. All the fundamental χ's exhibit the temperature dependence giving rise to the UCST-type phase behavior excepting $\chi_{Iv.Bv}$ and $\chi_{I.B}$ which are likely to be independent of the temperature. To confirm validity of these solutions, the predicted χ_{eff}'s for all ten systems was compared with the experimental data on χ_{eff}'s in figure 3. The predicted χ_{eff} is found to be in good agreement with the experimental χ_{eff}.

Although the fundamental χ's have the temperature dependence relevant to the UCST-type, a subtle balance among the various fundamental χ's gives rise to a temperature

dependence of χ_{eff} relevant to the LCST-type for the blends studied in this work.

(a)

(b)
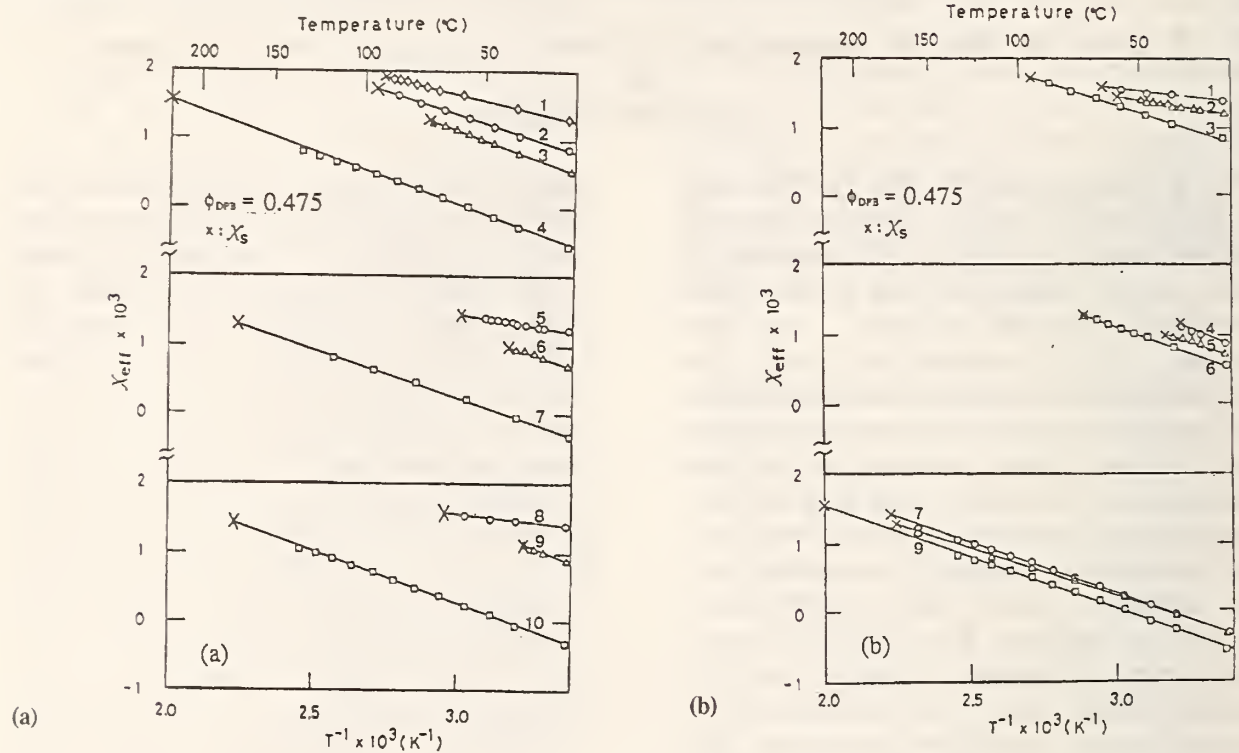
Figure 1 (a). χ_{eff} plotted as a function of T^{-1} for the blends of VIRH-7-101 with (1) VBRD-12-52, (2) VBRD-16-61, (3) VBRD-20-103, and (4) VBRD-28-71, for the blends of VIRH-12-192 with (5) VBRD-16-61, (6) VBRD-20-103, and for (7) VBRD-28-71, and for the blends of VIRH-15-136 with (8) VBRD-16-61, (9) VBRD-20-103, and (10) VBRD-28-71. The composition of each blend is fixed at $\phi_{DPB}=0.475$. The first suffix number indicates the vinyl content of the sample and the second suffix number indicates the molecular weight in 10^3 for the sample. (b). χ_{eff} plotted as a function of T^{-1} for the blends of VBRD-16-61 with (1) VIRH-15-136, (2) VIRH-12-192, and (3) VIRH-7-101, for the blends of VBRD-20-103 with (4) VIRH-15-136, (5) VIRH-12-192, and (6) VIRH-7-101, and for the blends of VBRD-28-71 with (7) VIRH-15-136, (8) VIRH-12-192, and (9) VIRH-7-101. The composition of each blend is fixed at $\phi_{DPB}=0.475$.
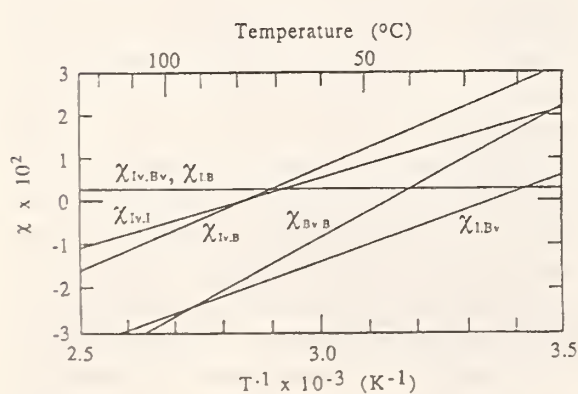
Figure 2. Fundamental χ's as a function of T^{-1}.
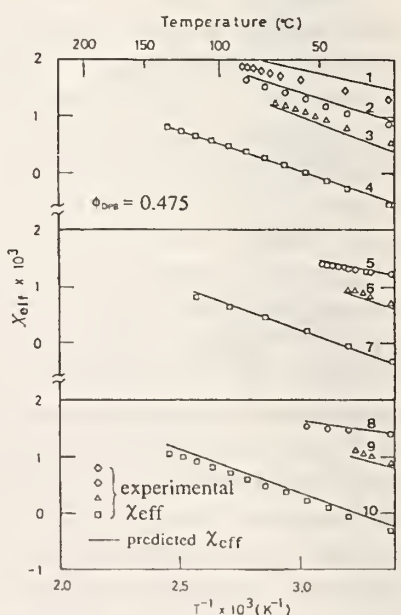
Figure 3. Measured (data points) and predicted values of χ_{eff} (solid lines) plotted against T^{-1}.

TIME-RESOLVED SMALL-ANGLE NEUTRON SCATTERING STUDY
ON LATE STAGE SPINODAL DECOMPOSITION OF POLYMER BLENDS

H. Jinnai, H. Hasegawa, and T. Hashimoto (Kyoto University, Kyoto, Japan)
and
C. C. Han (Polymers Division)

Recently there have been a number of studies on the kinetics of phase separation of polymer blends in early stage spinodal decomposition (SD) and on self-assembling processes, dynamics, and pattern formation (morphology) in the late stage SD as a problem of non-equilibrium statistical mechanics of long chain molecules. Most of the experimental studies utilized time-resolved light scattering (LS) methods, and only a limited number of studies utilized time-resolved small-angle neutron scattering (SANS) and small-angle x-ray scattering (SAXS) methods. It has been shown, efficiently, by time resolved LS, that the growing global structure can be scaled with a single time-dependent length parameter $\Lambda_m(t)$. There still remains an important question on whether the local structure; e.g., interfacial structures including waviness of the interface and interfacial width, can also be scaled with $\Lambda_m(t)$. The time-resolved SANS is a powerful method to investigate this problem as it can approach much shorter length scale than LS. In this series of study we investigated the time evolution of the interfacial structure using time-resolved SANS and LS on the same blend specimens. In this report we discuss general trends on the time-change of SANS profiles in detail and the result on the time-evolution of the composition difference, $\Delta\Phi(t)$, between two coexisting domains in the late stage SD.

Deuterated polybutadiene (DPB) ($M_w = 10.3 \times 10^4$, $M_w/M_n = 1.0_3$) and protonated polyisoprene (HPI) ($M_w = 13.6 \times 10^4$, $M_w/M_n = 1.0_4$) samples are used in this study. The volume fraction of DPB of this mixture is very close to that of the critical mixture, $\phi_{C,DPB} = 0.52$, according to Flory-Huggins theory. This mixture exhibited the LCST behavior and had the spinodal temperature $T_S = 36.1$ °C by the SANS analysis of single-phase state.

Figure 1 shows the time-evolution of the structure factor during early-to-late stage SD. The left and the right half of the figure correspond to the structure factors obtained by LS and SANS, respectively. Two sets of structure factors are vertically shifted for convenience but are plotted on the common logarithmic scales to compare the time-evolution of SANS profile with that of LS. It is quite obvious that the change of the structure factor at small q's observed by LS is quite large compared with that at large q's observed by SANS. The vertical broken line at $qR_g = 1$ indicates the q value corresponding to $1/R_g$ where R_g is an average radius of gyration of DPB and HPI. Thus our SANS experiments are concerned with the time-change of the composition fluctuations at a length scale of R_g or at even much shorter sale in early-to-late stage SD.

SANS profiles $I_T^e(q)$ due to the local composition fluctuations in single-phase state could be quantitatively described by the Random Phase Approximation. This provides a guiding principle to determine the time-evolution of the composition difference $\Delta\Phi(t)$ for two phases in the later stage SD. The time-resolved SANS profiles $S(q,t)$ at the early-stage SD ($t < 30$ min) show a crossover behavior in $\partial S(q,t)/\partial t$; the derivative is positive, nearly zero, and negative, respectively, at $q < q^*$ (regime I), $q \approx q^*$ (regime II) and $q > q^*$ (regime III) but the crossover q^* was much larger than the q_c predicted by the linearized theory of SD. $S(q,t)$ at a given t showed the crossover from the domain scattering $I_d(q,t)$ to the internal scattering $I_T(q,t)$ with increasing q through a time-dependent crossover wavenumber $q_s(t)$. The wavenumber $q_s(t)$ primarily reflects the growth of the global domain structure $\Lambda_m(t) = 2\pi/q_m(t)$, and hence its time-change occurs as a result of the shift of the large q-tail of the domain scattering $I_d(q,t)$ toward the smaller q region with t. $I_T(q,t)$, which depends on the time-change of the local composition $\phi_{A1}(t)$ and $\phi_{A2}(t)$ in domains 1 and 2, allows us to determine $\Delta\Phi(t)$. Both $q_s(t)$ and $\Delta\Phi(t)$

underwent a characteristic change at the crossover time $t_{cr}(\simeq 270$ min) from the intermediate to the late-stage SD as shown in figure 2.
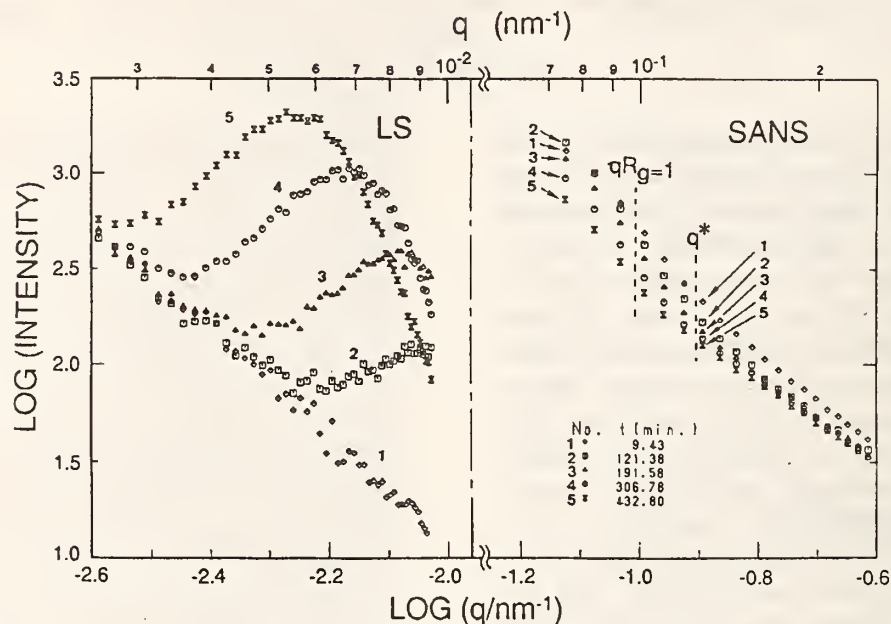
Figure 1. Time-evolution of LS and SANS profiles after the onset of the phase separation.
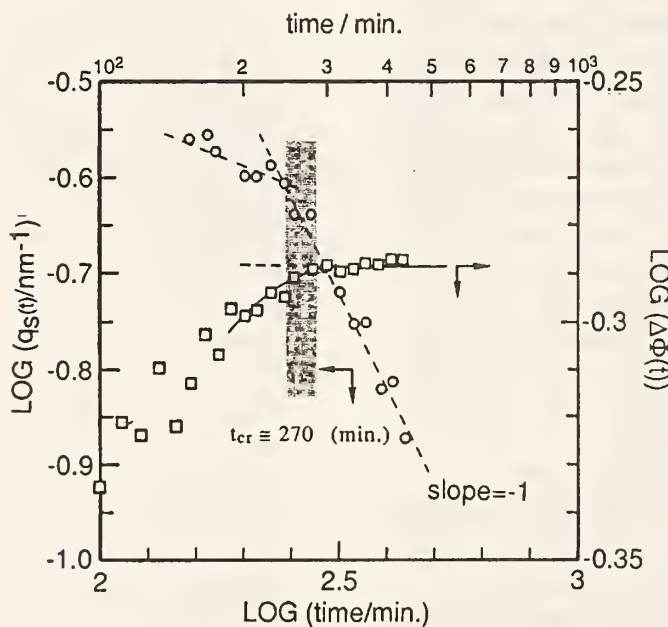
Figure 2. Time-change of the crossover wavenumber q_s and the composition difference between the two coexisting phase $\Delta\Phi(t)$ plotted in double logarithmic scale for a HPI/DPB (50/50) blend after T-jump from 23 to 40°C.

SMALL-ANGLE NEUTRON SCATTERING CHARACTERIZATION OF PROCESSING/MICROSTRUCTURE RELATIONSHIPS IN THE SINTERING OF CRYSTALLINE AND GLASSY CERAMICS

G. G. Long (Ceramics Division) and S. Krueger
R. A. Gerhardt (Rutgers University, Piscataway, NJ)
and
R. A. Page (Southwest Research Institute, San Antonio, TX)

Knowledge of the microstructure evolution as a function of thermal processing is important for the development of process models in ceramics. In particular, such techniques as liquid phase sintering have received renewed interest, and it will be important to achieve a detailed understanding of the mechanisms involved to take full advantage of the possible benefits of the technique. Since both viscous flow and diffusion, as well as reactivity, are generally involved, it is useful to first investigate the porous microstructure evolution as a function of sintering in two relatively well understood model systems, crystalline alpha-alumina, in which diffusion mechanisms dominate, and porous glassy silica, in which viscous flow mechanisms are dominant.

One important consideration is the surface free energy, which is the driving force for sintering. For a glass, the minimum free energy surface is a sphere. For a crystalline material, the surface tension is anisotropic, and there are facets, well-defined flat edges, and sharp corners. During sintering, the elevated temperature causes the surfaces to become rounded because the surface energy is reduced. Another important consideration is the grain boundary. In the densification of a crystalline compact, there is a general tendency to eradicate both free surfaces and grain boundaries. The grain boundaries are thought to act as vacancy sinks, permitting the removal of pores. In the glassy body, there is no grain boundary, and this is expected to have consequences on the microstructure evolution during sintering.

The present study was undertaken to examine processing/microstructure relationships in a crystalline and in a glassy system in order to gain a quantitative measure of the structural evolution that takes place when different sintering mechanisms dominate.

In the experiments that form the subject of this work, samples of pure alumina were prepared by slip casting, and samples of microporous silica were prepared by a sol-gel process. For each system, a collection of nearly identical samples were prepared and partially sintered. During sintering, samples were removed one by one from the furnace as they achieved intermediate densities representative of sintered microstructure from the early part of intermediate stage sintering to the late part of final stage sintering. Microstructure parameters of these samples were derived from small angle neutron scattering measurements and multiple small angle neutron scattering measurements, as required by the sizes and volume fractions of the pores.

Both the low-Q and the large-Q portions of the scattering curves were analyzed for the two scattering systems. The low-Q part of the data was analyzed using SANS or multiple-SANS (MSANS) theory, and the large-Q part of the curve was studied via Porod analysis. For silica, the two analyses were qualitatively different. This was taken as evidence of the existence of two populations of pores in the silica system, consistent with a model [1] proposed by Cao, Gerhardt and Wachtman. In this model, there is a population of small pores between fine silica particles which exist in clusters or domains. There is also a population of larger pores between domains, and it is this population which dominates the MSANS [2] data. Results from the low-Q portion of the scattering curves for silica are shown in figure 1, where it can be seen that the interdomain pores first coarsen, presumably while the domains densify, and then shrink when domain densification is complete.

Comparing MSANS results and Porod results for the alumina indicates that there is
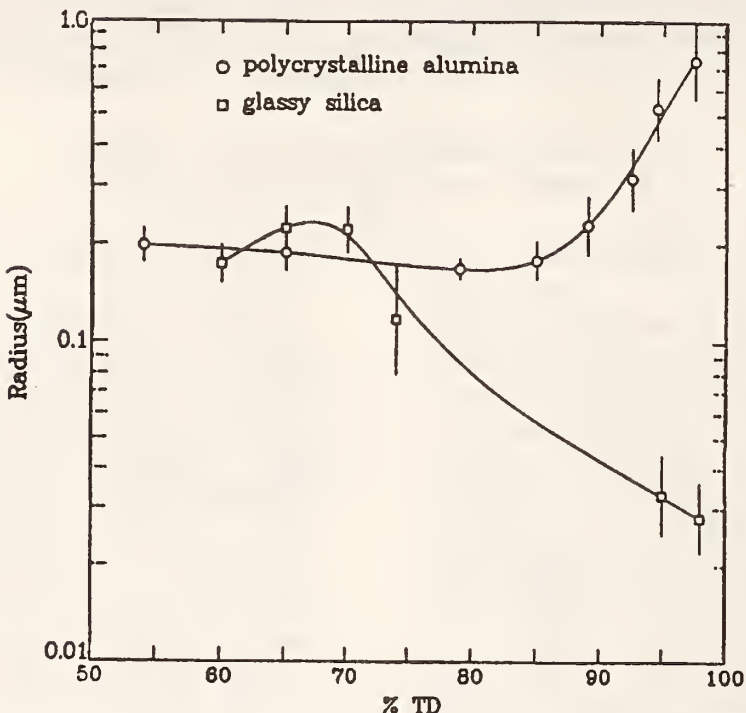
Figure 1. Pore radius as a function of the percent theoretical density for silica and alumina.

only one population of pores in this system. The SANS results are volume-weighted and the Porod results are surface-area weighted, but both results are qualitatively the same. Each set of results indicates a constant pore radius during the intermediate stage of sintering, unlike silica for which coarsening and subsequent shrinkage were seen, and a rapidly increasing pore radius during the final stage of sintering. These large sizes were recently confirmed [3] using high-resolution SAXS measurements on the same samples. The SANS results on alumina, also shown in figure 1, lend support to a topological decay model of Rhines and DeHoff [4] in which the interconnected channel network of pores decays in a stable manner. The pore channels become fewer, although of the same diameter, as densification proceeds. At the onset of the final stage, the pore radius coarsens abruptly as the stable decay breaks down.

Taken together, the silica and alumina results shown in figure 1 highlight the different microstructure evolution signatures that exist for the viscous flow and the diffusion mechanisms of sintering.

References

[1] W. Cao, R. A. Gerhardt, and J. B. Wachtman, Jr., J. Am. Ceram. Soc. 71, 1103-1113 (1988).
[2] N. F. Berk and K. A. Hardman-Rhyne, J. Appl. Cryst. 18, 467-472 (1985).
[3] S. Krueger, G. G. Long, D. R. Black, D. Minor, P. R. Jemian, W. Nieman, and R. A. Page (in preparation).
[4] F. N. Rhines and R. T. DeHoff, Sintering and Heterogeneous Catalysis, Mater. Sci. Res., 16, G. C. Kuczynski, A. E. Miller, and G. A. Sargent, eds. (Plenum Press, NY, 1984).

SMALL-ANGLE NEUTRON SCATTERING MEASUREMENT OF THE EFFECT OF GREEN DENSITY AND THE ROLE OF MgO ADDITIVE ON THE DENSIFICATION OF ALUMINA

S. Krueger, and G. G. Long (Ceramics Division)
and
R. A. Page (Southwest Research Institute, San Antonio, TX)

Numerous sintering models have been developed over the years in attempts to reliably predict the kinetics of sintering and to estimate sintering rates. Although it has been difficult to find a consensus of opinion regarding many aspects of sintering mechanisms, there is general agreement that the driving force for sintering is the surface free energy, and that the microstructure characteristics are determinative of the specific mechanisms by which the pore and the solid phases evolve during densification. The present investigation was undertaken to examine the microstructure evolution during sintering with the goal being to gain insight into the mechanisms operative during thermal processing.

In the experiments that form the subject of this research, samples of pure alumina and of alumina with 0.25 wt.% MgO added were prepared by slip casting, or alternatively by cold pressing. For each green state density, a collection of nearly identical samples were conventionally sintered. During sintering, these samples were removed one by one from the furnace as they achieved intermediate densities, yielding examples of microstructure from the early part of the intermediate stage of sintering out to the latter part of final stage sintering. The microstructure parameters of these samples were derived from multiple small angle neutron scattering measurements [1,2].

Figure 1 shows the evolution of the pore size as a function of densification, or percent of theoretical density (%TD), for four suites of samples: slipcast alumina, cold pressed alumina,
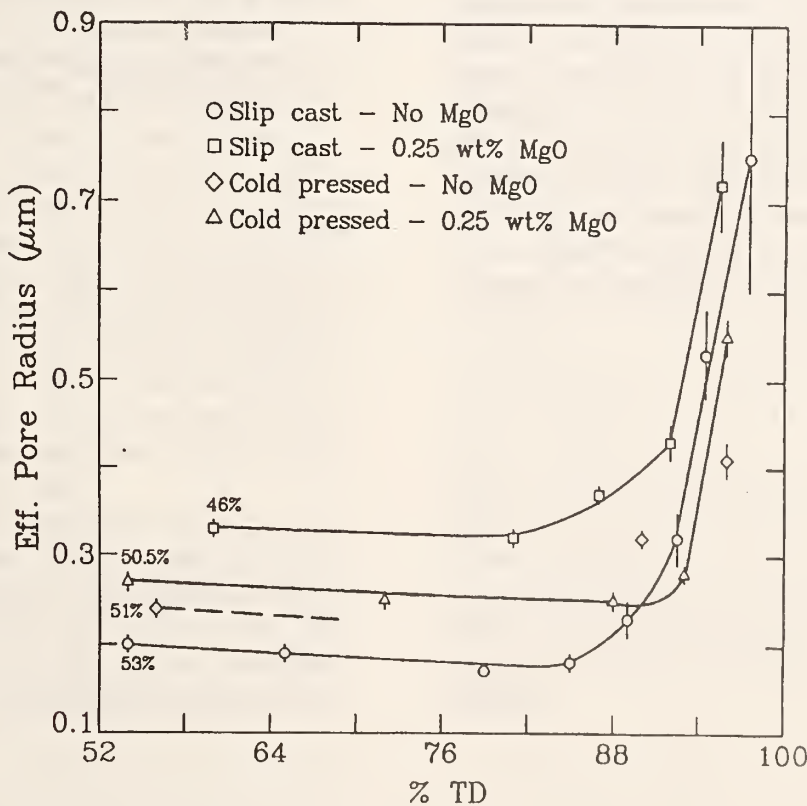
Figure 1. Effective pore radii as a function of %TD for the four series of samples.

slipcast alumina doped with MgO, and cold pressed alumina doped with MgO. The numbers associated with the left-most symbols in figure 1 indicate the average green density of each suite of samples. It can clearly be seen that the effective pore radius was constant during the intermediate stage of sintering for each of the suites of samples, independent of doping and green density, and consistent with a stable topological decay model [3] of porosity during intermediate stage sintering. However, the actual value of the effective pore radius depends inversely on the green density. These results indicate that the connectivity that is established in the alumina green body determines the pore size throughout the stable intermediate sintering stage, and once this size is determined, it is unvarying as long as isolated porosity has not yet begun to form. At the onset of final stage sintering, the pore radius apparently coarsens abruptly. Part of this apparent coarsening may be due to the pinching- off of pore channels such that the larger dimension of the newly isolated pores comes increasingly within the range of sizes visible to the MSANS technique.

Figure 1 also indicates that for the samples with 0.25 wt.% MgO, the intermediate sintering stage remains stable out to significantly higher density (93%TD) than the pure alumina, which remains stable out to 87%TD. Consequently, the pores in the doped sample begin to coarsen later and thus the grains do not suffer the same degree of exaggerated growth evident in the thermal processing of the pure alumina, even though the average green density was lower in the doped sample.

In summary, it was found that the initial connectivity in the green state plays a dominant role in establishing the channel diameters during the intermediate stage of sintering, and contributes also to determining the onset density at which the final stage of sintering begins. The role of MgO as a sintering aid lies, at least in part, in prolonging the stability of intermediate stage sintering such that the body achieves greater density before the transition to final stage sintering after which isolated pores are formed.

References

[1] N. F. Berk and K. A. Hardman-Rhyne, J. Appl. Cryst. 18, 467-472 (1985) and J. Appl. Cryst. 21, 645-651 (1988).

[2] G. G. Long and S. Krueger, J. Appl. Cryst. 22, 539-545 (1989).

[3] F. N. Rhines and R. T. DeHoff in Sintering and Heterogeneous Catalysis, Mater. Sci. Res. 16, G. C. Kuczynski, A. E. Miller, and G. A. Sargent, eds. (Plenum Press, NY, 1984).

MICROSTRESSES IN CERAMIC COMPOSITES

H. J. Prask

C. Choi (ARDEC, Picatinny Arsenal, NJ and Reactor Radiation Division)
E. Fuller and R. Krause (Ceramics Division)
A. Krawitz (University of Missouri, Columbia, MO)
and
J. Richardson (Argonne National Laboratory, Argonne, IL)

Micro residual stresses occurring between constituents of a composite, e.g. between particles or fibers and matrix, are indicators of the strength of bonding between these components. X-ray diffraction provides the best-established method for determination of residual stresses and has been used for the study of ceramic composites. In the x-ray case, however, surface macro-stresses contribute to peak shifts and complicate the analysis. Neutron diffraction parallels x-ray diffraction for residual stress determination but because neutrons in the diffraction-wavelength regime penetrate, typically, three orders of magnitude deeper than x-rays, either depth-profiling or total-sample averaging of stresses is possible. When a sample is totally immersed in the neutron beam the macro-stress contribution to peak shifts averages to zero.

In the present measurements, Al_2O_3 reinforced with SiC(whisker) was studied. Two different types of whiskers at two different concentrations were used: TWS 100 (~ 0.4 μm diam, ~ 10 μm long) and TWS 400 (~ 1.1 μm diam, ~ 50 μm long), each at 20 and 30 vol%.

With each whisker type, processing into the composite was the same: hot-pressing into a disk 5 cm in diam and ~ 0.25 cm thick, at 6000 psi at 1700 °C for 30 min. The samples for neutron study were cut from the center of the pressed disks, stacked and glued, and ground to cubes ~ 0.9 cm on a side.

The general purpose powder diffractometer at the IPNS/Argonne National Laboratory was used to collect data for all reflections in the range 0.767 < d(hkl) < 2.972 A for four different directions in the sample coordinate system. Of the many reflections observed the (113), (024), (116), and (300) of alumina and (111), (220), and (311) of the cubic SiC were selected for analysis based on intensity and freedom from overlap. Unstressed d-spacings, d_o's, were obtained from the starting materials. Stresses were calculated from the strains in the standard way, using the elastic isotropic diffraction elastic constants for both materials. Representative results are shown in table 1 for one sample.

For each reflection for each constituent it is clear that the pressing direction is unique, with less average stress than is observed in the orthogonal directions, which are essentially equivalent. As one would expect from the difference in thermal expansion coefficients, and as has been observed elsewhere, the whiskers are in a state of high compression, the matrix in tension. The marked variation in stress magnitude for the same stress component for different reflections indicates that the use of "bulk" elastic constants is not justified. In table 2 the stress values averaged for the reflections of each constituent are listed.

It is interesting that in the matrix the volume fraction seems to be the critical quantity in that the two 30 vol% samples show stress magnitudes in the alumina that are very similar. In the whiskers, no such clear correlations are seen although the TWS 400 composites look similar. This correspondence between sample types is also exhibited in the measured total peak breadths. One puzzling feature of these results is that it appears that no reasonable adjustment of the diffraction elastic constants can be made which would lead to balancing of microstresses between the two constituents for all four samples.

Table 1. Average microstresses in the 20 vol%/TWS 400 sample

	σ_{xx}	σ_{yy}	σ_{zz} *
Al_2O_3(113)	296(5)MPa	299(18)	221(6)**
(024)	314(9)	325(34)	239(12)
(116)	412(4)	416(14)	345(4)
(300)	214(2)	228(8)	141(3)
SiC(111)	-1126(14)	-1148(60)	-933(17)
(220)	-1066(4)	-1030(19)	-894(6)
(311)	-1180(4)	-1120(15)	-1094(5)

* The pressing direction.
** Standard deviations due to counting statistics only.

Table 2. Averaged residual stress values

	σ_{xx}	σ_{yy}	σ_{zz}
$\underline{Al_2O_3}$			
TWS 100, 20vol%	200MPa	197	103
TWS 100, 30vol%	461	460	324
TWS 400, 20vol%	309	317	237
TWS 400, 30vol%	403	464	319
$\underline{SiC}$			
TWS 100, 20vol%	-1330MPa	-1334	-1244
TWS 100, 30vol%	-1148	-1117	-1127
TWS 400, 20vol%	-1124	-1099	- 974
TWS 400, 30vol%	-1056	-1037	- 937

A CHORD DISTRIBUTION DESCRIPTION OF MICROPOROUS GLASS

M. Y. Lin (Exxon Research and Engineering, Annandale, NJ)

S. K. Sinha (Brookhaven National Laboratory, Upton, NY and Exxon, Annandale, NJ)

and

C. J. Glinka

We have used a chord distribution model for the microstructure of Vycor glass, a widely used model system for microporous media, to analyze small angle neutron scattering (SANS) measurements on this material. The chord distribution derived from the analysis is in good qualitative agreement with that determined by other techniques. In addition, we have used the model to study the process of capillary condensation, and show how the structure probed by SANS evolves as liquid condenses in the pores.

A chord (length) distribution of a random isotropic two-phase structure is defined as the distribution of the distance between two adjacent interfaces along a line at an arbitrary direction. Depending on the substance between the two interfaces, it can be either a pore chord distribution, or a solid chord distribution. These are denoted as $F_p(l)$ and $F_s(l)$, where the subscript p stands for pore and s stands for solid. The two functions are therefore a description of the porous structure. Levitz et al. have measured the actual chord distributions for Vycor glass similar to those we use [1].

Neutron scattering data were obtained at NIST's 8-m SANS spectrometer [2]. The scattering structure factor $S(Q)$ was measured as a function of the momentum transfer Q. It can be expressed in terms of the chord distribution as

$$S(Q) \sim \left[\frac{2 - f_p(Q) - f_s(Q)}{1 - f_p(Q)f_s(Q)} + C.C. - 2\right]$$

$$(1 + Q^2\xi^2)^{-\mu} \qquad (1)$$

where C.C. is the complex conjugate of the previous term, and $f_{p,s}(Q)$ are the complex Fourier transforms of the chord length distributions $F_{p,s}(l)$ over the range $l = 0$ to $l = \infty$. The factor $(1 + Q^2\xi^2)^{-\mu}$ will dominate when $Q > 2\mu/\xi$, where ξ is about 10 Å. It describes the surface roughness of the solid-pore interfaces. When the surface is describable by

fractals, $\mu = (6 - D_s)/2$ where $D_s > 2$ is the surface fractal dimension. For a smooth surface, $\mu = 2$.

Equation 1 was used in analyzing the SANS data. The exponent $\mu = 2.4$ is predetermined using data at large Q in order to minimize the number of the free parameters. For the chord distribution we assume a form as

$$F(l) = l^a(Ae^{-bl} + Be^{-cl}) \qquad (2)$$

The result using equation 1 to fit the scattering data is shown in figure 1. The fitted parameters give the average pore size $l_p = 84.6$ Å, the average solid size $l_p = 177.6$ Å, and the porosity is $l_p/(l_p + l_s) = 0.32$. These values are in good agreement with the results obtained by other measurements [2]. Using the fitted parameters, both pore and solid chord distributions can be constructed and the pore chord distribution is shown in figure 3. The pore chord distribution is peaked at $l = 71.4$ Å. A comparison of the pore chord distribution with that measured directly with TEM pictures shows a qualitatively good agreement of the two forms, although the one shown here decays faster at large chord distances.

We have also studied the process of capillary condensation inside Vycor's porous structure. The condensing liquid used was a mixture of C_6H_{14} and C_6D_{14} which acts as a simple liquid in condensation, and which has the same scattering density as the solid part of Vycor glass (silica). This ensures that when condensation takes place inside the pores, the microstructure seen by the neutrons is still two phases: the condensing liquid and the solid are one phase, and the remaining space in the pores occupied by the much-lower density gaseous molecules is the other phase. Thus, the chord distribution model discussed above should still be applicable.

The scattering data were obtained in the same experiment described above. In this case, the molecular pressure of the C_6H_{14}/C_6D_{14}

mixture is increased from zero (vacuum) to p_s, the saturated vapor pressure of the mixture in bulk, in several steps. For each p, a set of scattering data was taken. The data are shown in figure 2. At $p = p_s$, the entire pore space of the glass is filled with the liquid, and the sample becomes one homogeneous phase. This is evident in the scattering data, as it is almost flat, and is more than two orders of magnitude less in peak intensity than the data at $p = 0$.

We were able to analyze the first few data curves using the chord distribution model. Fitting results similar to that shown in figure 1 are obtained, for p up to a value of 0.57 p_s. The next S(Q) curve at $p = 0.71$ p_s starts to

show noticeable difference in its shape, and the model can hardly fit the data. This is about when, presumably, massive condensation starts to take place, as suggested by isotherm absorption measurements [2].

The fact that for small p the scattering data are well described by the model used for dry Vycor indicates, that the condensing "liquid" forms a thin wetting layer on the solid surface. This changes the chord distributions, but does not change the overall micromorphology as probed by the neutrons. As the pressure increases to a certain value, capillary condensation starts to take place, as the liquid completely fills some small pore areas.
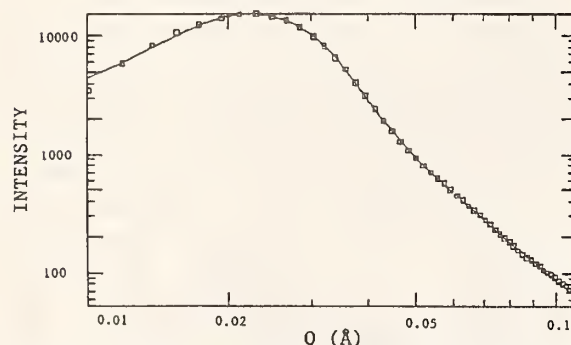
Figure 1. SANS intensity data (squares) taken with dry Vycor and the fit using the chord distribution model.
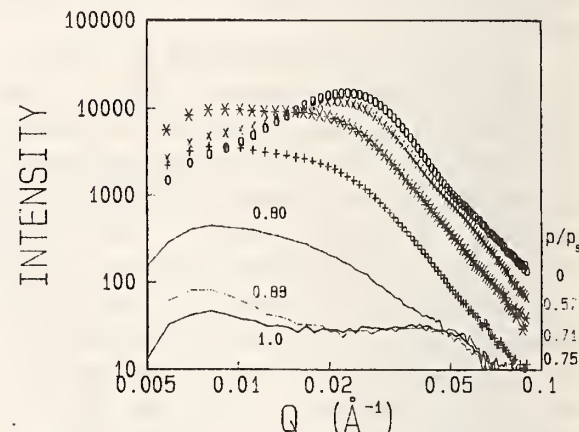
Figure 2. SANS data from Vycor as condensation takes place in it. Data were taken at several different pressures as marked (p = 0) is for dry Vycor).

References

[1] P. E. Levitz, G. Ehret, and J. M. Drake, J. Chem. Phys. (submitted for publication).
[2] M. Y. Lin, S. K. Sinha, J. S. Huang, B. Abeles, J. W. Johnson, J. M. Drake, and C. J. Glinka, in Neutron Scattering for Materials Science, S. M. Shapiro, S. C. Moss, and J. D. Jorgensen, eds. (MRS Symp. Proc. 166, Pittsburgh, PA 1990), pp. 449-454.

SMALL-ANGLE NEUTRON SCATTERING OF POLY(VINYLALCOHOL) GELS

W.-L. Wu (Polymers Division)

M. Shibayama, H. Kurokawa, and S. Nomura (Kyoto Institute of Technology Kyoto, Japan)

M. Muthukuma and R. S. Stein (University of Massachusetts, Amherst, MA)

and

S. Roy (Polaroid Corporation, Norwood, MA)

Structure of aqueous poly(vinylalcohol) (PVA) gels with and without adding borate ions, hereafter referred as alkaline gels and hydrogel, respectively, were investigated using small angle neutron scattering (SANS). The correlation length ξ, a measure of the wavelength of concentration fluctuation, was estimated from SANS results. The value of ξ showed a modest temperature dependence; it decreased with increasing temperature. The scattering intensity within the range of $0.3 < q\xi < 10$ for the alkaline gel over a wide temperature range could be superimposed into one master curve by employing these reduced variables, $I(q)/\xi^3$ and ξq, where q is the magnitude of the scattering vector (fig. 1). This indicates that the PVA clusters can be described adequately by a single characteristic length over a broad temperature range embracing the sol-gel transition

temperature, and the internal structure of the cluster is homogeneous down to a size scale of 0.1ξ. For the hydrogel, the superposition was valid only in the region of $0.3 < q\xi < 2.0$ (fig. 2). In the high q region of $2 < q\xi < 10$, an increase in the mass fractal dimension with lower temperatures is evident; this can be explained by the local consolidation of the polymer chains in hydrogels. Such a consolidation is absent in alkaline gels due to the presence of interchain didiol-borate complexes. The presence of interchain crosslinks in alkaline gels while not in hydrogels manifests itself in many other aspects, for example, the temperature dependence of both the correlation length ξ and the aggregation index. The details of this work will be presented in a future publication.
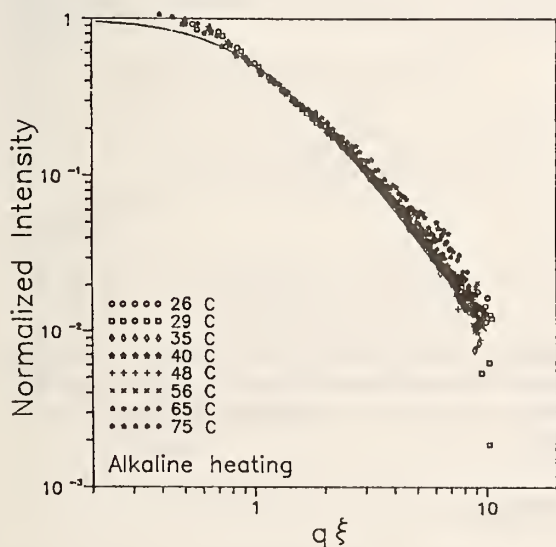
Figure 1. A mater curve of normalized excess scattering intensity versus $q\xi$ of an alkaline PVA solution. SANS data of eight different temperatures (26 °C - 75 °C) in a heating cycle were superimposed. The solid line is the Lorentzian form $(1 + \xi^2 q^2)^{-1}$.
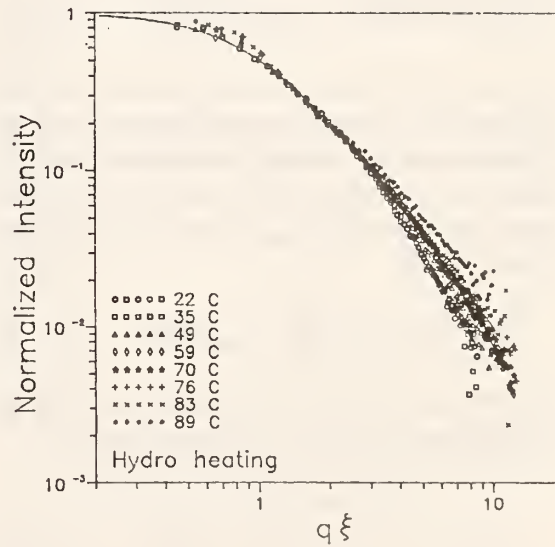
Figure 2. A mater curve of normalized excess scattering intensity versus $q\xi$ of an aqueous PVA solution. SANS data of eight different temperatures (22 °C - 89 °C) in a heating cycle were superimposed. The solid line is the Lorentzian form $(1 + \xi^2 q^2)^{-1}$.

SANS FROM TPB BASED MICROEMULSIONS

B. Hammouda

and

P. L. Lindemuth and R. L. Venable (University of Missouri, Rolla, MO)

Small angle neutron scattering has been used to investigate tetradecylpyridinium bromide/pentanol/heptane/heavy water microemulsions in the water-in-oil microemulsion phase diagram region [1,2]. Heavy water content was increased while the other components (surfactant, cosurfactant, hydrocarbon) were kept constant. Using a simple model assuming spherical micelles interacting with a hard sphere potential (Percus-Yevick model), aggregate sizes and packing fractions have been extracted and found to agree with values determined from the mixing conditions. These experiments clearly show the transition from the single particle (heavy water + Stern layer droplet) scattering regime at low water concentration to the mixed single/interdroplet scattering regime when the intermicellar distance becomes comparable to the size of the micelles.

The scattered intensity for a droplet system of arbitrary concentration is given by:

$$I(Q) = P(Q) + n P(Q) h_{cm}(Q)$$

in terms of the single droplet structure factor $P(Q)$, number of particles per droplet n, and the interdroplet total correlation function $h_{cm}(Q)$ which can be expressed in terms of the direct correlation function $C_{cm}(Q)$ by the Ornstein-Zernicke form:

$$h_{cm}(Q) = C_{cm}(Q)/[1-nC_{cm}(Q)]$$

The Percus-Yevick form (with hard sphere potential) for $C_{cm}(Q)$ is used in figure 2.

Most of this work was performed before B. Hammouda joined NIST.
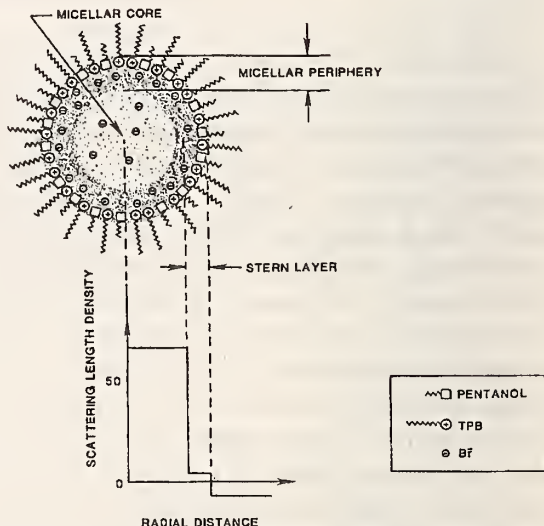
Figure 1. Scattering length densities in the micellar core, the Stern layer, and the outside hydrocarbon continuum.
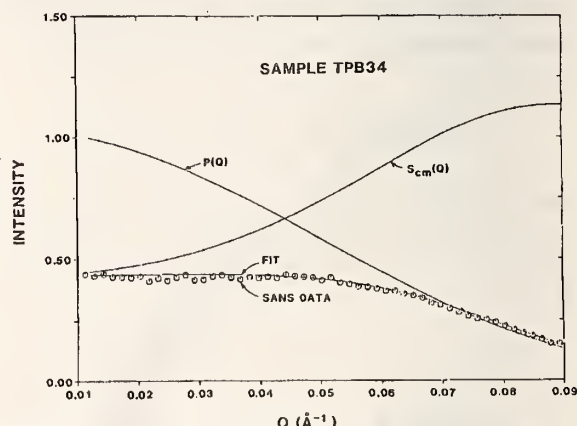
Figure 2. Result of the nonlinear least squares fit to the Ornstein-Zernicke form with Percus-Yevick approximation (hard sphere potential) for a sample with 12% water volume fraction.

References

[1] B. Lindemuth, B. Hammouda, F. D. Blum, J. R. Duke, and R. L. Venable, PGSE-NMR and SANS from TPB based Microemulsions. Proceedings of the MRS Fall Meeting in Boston (Dec. 1989).

[2] P. Lindemuth, B. Hammouda, and R. Venable, SANS from TPB based Microemulsions. J. Phys. Chem. <u>94</u>, 8247 (1990).

QUASIELASTIC GAMMA-RAY SCATTERING FROM PENTADECANE AND FROM POLYDIMETHYLSILOXANE SOLUTIONS

B. Hammouda

and

G. Schupp (University of Missouri, Columbia, MO)

A Mossbauer instrument was used to study the dynamics of liquid pentadecane [l] and of polydimethylsiloxane in benzene solutions [2]. Quasielastic scattering (fig. 1) of gamma-rays (QEGS) is a purely coherent scattering process yielding the coherent dynamic structure factor directly. The instrument used is a gamma-ray diffractometer which uses an intense Mossbauer source (Ta-183) cooled to 77 K in which the energy analyses of the scattered photons are performed by Doppler shifting a Mossbauer absorber (W foil).

In the case of molecular liquid pentadecane, quasielastic widths ranged from 64 μeV (at 12 °C) to 192 μeV (at 74 °C) at a scattering vector which corresponds to the first maximum of the structure factor (1.15 A^{-1}). Similar measurements at five different scattering angles (at 12 °C) were also taken to investigate the wavevector dependence of the quasielastic width. The results observed were in good agreement with known theories giving the quasielastic width as:

$$\Gamma(Q,T) = [Q^2/S(Q,T)]k_bT/M$$

where Q is the scattering vector, $S(Q,T)$ is the structure factor, k_bT the temperature in energy units and M an effective mass of the scattering unit. The de Gennes narrowing of the quasielastic peak at the maximum value of Q for the structure factor has been observed for liquid pentadecane.

In the case of macromolecular liquid polydimethylsiloxane in benzene solutions, variation of the quasielastic width has been observed as a function of polymer concentration. The high energy resolution of the QEGS technique (8 μeV) allows the separation of the scattering signal (see fig. 2) into a narrow component associated with stiff motions along the polymer chain backbone and a quasielastic component associated with softer side group motions. The narrow component disappears upon dilution in benzene while the intensity of the quasielastic component grows proportionately. This observation is interpreted as a softening of the backbone normal modes upon dilution.

Figure 1. Diagnostic methods used to investigate the dynamics of liquids: quasielastic light Rayleigh scattering (QELRS), quasielastic light correlation spectroscopy (QELCS), quasielastric neutron scattering (QENS) and quasielastic gamma-ray scattering (QEGS). The computer simulation region (molecular or Brownian dynamics) overlaps with QENS and QEGS.
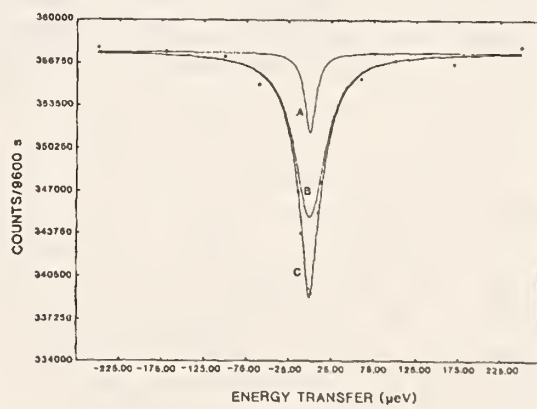
Figure 2. QEGS spectrum from undiluted polydimethyle siloxane taken at room temperature with Q = 0.9 A^{-1}. Curves A and B give the individual Lorentzian fits for the narrow width and quasielastic scattering components respectively. Curve C gives the overall fit to the data points indicated by circles.

Most of this work was performed before B. Hammouda joined NIST.

References

[1] G. Schupp, B. Hammouda, and C. M. Hsueh, Phys. Rev. A41, 5610-5615 (1990).

[2] B. Hammouda, G. Schupp, and S. Maglic, J. Chem. Phys. 93, 5473 (1990).

TEXTURE STUDY ON TANTALUM METAL SHEET BY NEUTRON DIFFRACTION

C. S. Choi (ARDEC, Picatinny Arsenal, NJ),
and
H. J. Prask

Tantalum is a high-density metal with a high melting point; it has a high ductility and moderate tensile properties. Recently, this material has attracted considerable attention among the defense-related, research community as a prime candidate for shaped-charge liners and explosively-formed projectiles. The texture measurements are conducted commonly by x-ray diffraction methods because of the easy availability and the faster measurement time compared to neutron diffraction. However, the penetration power of the x-ray is so weak (approximately 1/10000 of that of neutron) that it is essentially impossible to see the subsurface texture below a few microns depth in the heavy metals, and the surface texture is often different from that of the interior. Therefore, neutron diffraction was used in this study. A sample specimen with approximate dimensions of 0.64 x 1.0 x 1.9 cm^3, was cut from a long strip, 0.64 x 1.9 x 20 cm^3, of Ta metal for a texture study. The sample was mounted on the four-circle neutron diffractometer with the long axis oriented approximately parallel to the sample rotation axis. The intensity distributions of five reflections, 200, 211, 220, 310, and 222, were measured over an entire orientation hemisphere ranging from 0 to 360° in phi-angle and 90° to 0 in chi-angle, each with 5° step intervals.

The raw data were corrected for background neutrons and converted to the pole densities in the multiples of random distribution (mrd) units. The observed pole density data were smoothed by the Gaussian-filtering method with a 5° width. The experimental pole figures are shown in figure 1. The "12 o'clock

direction" of the pole figures correspond approximately to the normal direction of the sample, the "3 o'clock direction" to the rolling direction, and the center to the transverse direction. The contour levels are shown in mrd units in the legend of each figure. The textures are clearly the sheet-type, but have no clear mirror symmetry about the RD or TD. This suggests that the sample has been either annealed after the rolling or processed with multidirectional rolling or forges.
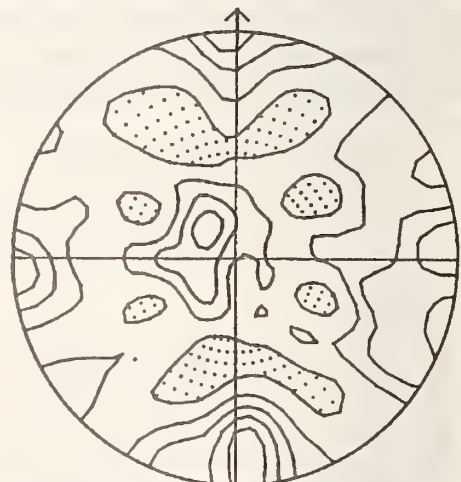
100 Stereographic Projection
Contours at .50 1.00 1.50 2.00 2.50

Figure 1. Observed pole figures.

The Orientation Distribution Function (ODF) analysis, based on the harmonic method, was performed using the program LATEX developed at Los Alamos National Laboratory. The coefficients of the series were determined up to l = 22, using the five experimental pole figures with diad symmetry. The recalculated pole

figures from the resultant ODF are shown in figure 2. The calculated pole figure is quite similar to the corresponding experimental one, which indicates that the ODF represents the true texture reasonably well. The inverse pole figures of the two sample directions, SOP1 (rolling direction) and SOP2 (normal direction), were calculated from the ODF, and are shown in figure 3. The rolling direction is dominated by {100} poles. It also contains two smaller peaks of {110} and {112} poles. There are only two maxima in the normal direction, one centered at {100} and the other at {111}, with approximately equal intensity. This study suggests that the texture of the Ta sheet has three-slip systems: the cube texture (010)[100] with the volume ratio of 50% or more, and (111)[110] and (111)[112] with equally less volume ratio. The occurrence of (001)[110] is possible but probably less significant because of the small amount of [110] aligned toward the RD. The cube texture found in the sample is considered to be quite important because of the fact that it produces extremely anisotropic physical properties. The cube texture has been observed mostly in many FCC metals and alloys after primary recrystallization annealing in certain temperature ranges. Recently, the cube texture has been found also in BCC metals; i.e., laminated steels.
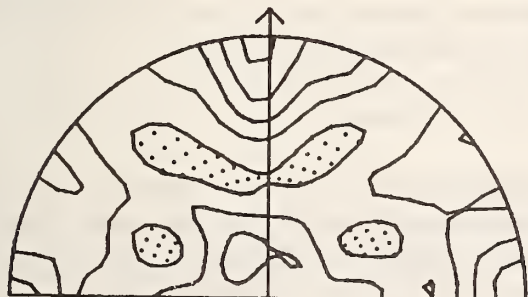
(100) Stereographic Projection
Contours at .50 1.00 1.50 2.00 2.50

Figure 2. Recalculated pole figures from ODF.
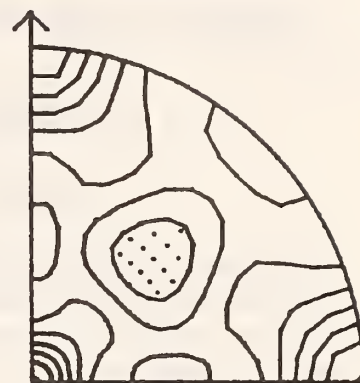
SOP1 Stereographic Projection
Contours at .50 .75 1.00 1.25 1.50 1.75 2.00 2.25
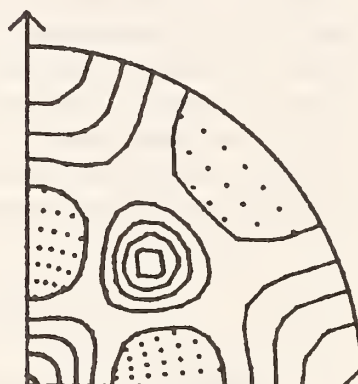
SOP2 Stereographic Projection
Contours at .50 1.00 1.50 2.00 2.50

Figure 3. Inverse pole figures calculated from ODF, where SOP1 and SOP2 corresponds to the rolling direction and the normal direction, respectively.

RESIDUAL STRESS MEASUREMENTS IN METALLURGICAL SAMPLES

H. J. Prask

C. S. Choi (ARDEC, Picatinny Arsenal, NJ and Reactor Radiation Division)

and

T. Cordes (John Deere Product Engineering Center, Waterloo, IA)

Last year a feasibility study was made for the SAE Fatigue Design and Evaluation (FD&E) Committee to determine the applicability of the neutron diffraction technique to residual stress determination as part of a fatigue lifetime prediction project. Specifically, the project is an integrated engineering approach for design analysis and validation of components for vehicles in which test spindles will be tested for fatigue life, characterized for materials properties--including residual stress, and modeled by finite element techniques. Depth-profiling of residual stresses had been done by x-ray diffraction with layer removal, about which the FD&E Committee felt some uncertainty.

The nondestructive neutron diffraction residual stress determination, in which $(\sigma_{rr} - \sigma_{\theta\theta})$ was measured as a function of depth at two positions on a test spindle, showed the applicability of the technique.

This year these measurements have been continued. Values of d-spacings have been obtained as a function of depth for two positions on the original spindle and three positions on a fatigued spindle. In progress is the determination of d_o-values for the fully induction-hardened outer 3 mm, and the unaffected 10-mm radius core region of the 20-mm radius spindle. On completion, the full triaxial residual stress distributions will be determined.

ANALYTICAL CALCULATIONS USING ACCEPTANCE DIAGRAMS

J. R. D. Copley

This year we have used the acceptance diagram technique [1,2] to perform calculations which have been of direct benefit to group members charged with the design of neutron scattering instruments. Acceptance diagrams show the y-β distribution of neutrons in a beam, where y is one of the neutron's spatial coordinates normal to the beam direction and β is the corresponding angle between the neutron's direction and the beam direction. Using these diagrams we can compute integrated intensities and related properties.

Vertically curved monochromators. We have investigated the performance of vertically curved monochromators, both at beam tubes and guide tubes. Our work complements the analytical treatment of Currat [3], in some cases offering important additional insights. In figure 1 we show an example of a calculation of the integrated intensity per unit height of sample, for

samples of various heights, as a function of the effective monochromator radius

$$R^* = R/\sin \theta_B, \qquad (1)$$

where R is the radius of curvature of the monochromator and θ_B is the mean Bragg reflection angle. For small samples the intensity is not only constant but spatially uniform, over a range of R^* which decreases with increasing sample height.

We have also performed calculations of the behavior of vertically curved monochromators at the BT-4 spectrometer, taking account of structural components which limit the height of the beam. The results, shown in figure 2, are in good agreement both with independent Monte Carlo calculations [4] and with an extensive set of neutron measurements [5].
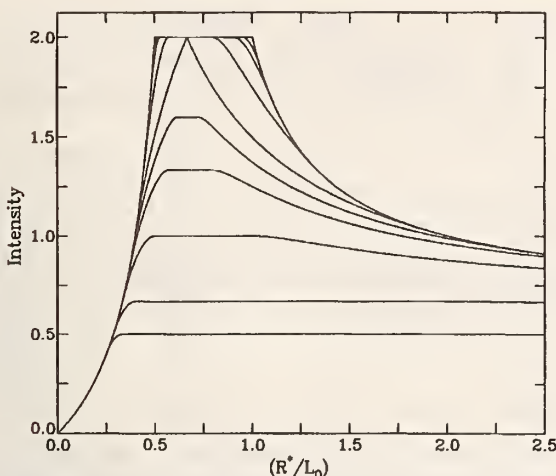
Figure 1. Dimensionless intensities per unit height of sample, as a function of the ratio (R^*/L_0), where R^* is explained in the text and L_0 is the distance from the source to the monochromator. The distance from monochromator to sample is $L_0/2$. The heights of the source and monochromator are identical, and the ten curves, starting from the top, are for ratios of sample height to source height of 0.0, 0.05, 0.1, 0.25, 0.5, 0.625, 0.75, 1.0, 1.5, and 2.0 .
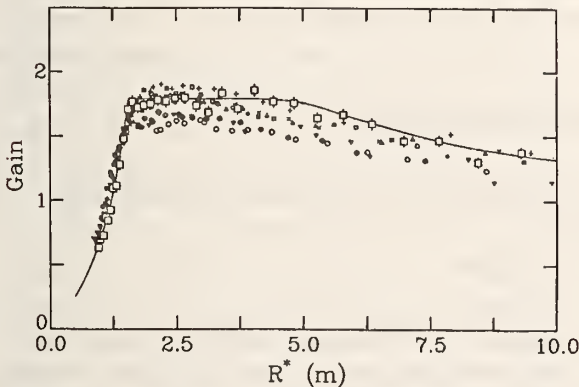
Figure 2. Gain, i.e., the ratio of intensity on a 1 cm sample using a curved monochromator of effective radius R^* to intensity on the same sample using a flat monochromator, plotted as a function of the quantity R^*. The solid line is the analytical calculation, the large open squares are the Monte Carlo results, and the small symbols are the neutron measurements with a copper monochromator; each type of symbol corresponds to a different value of θ_B, in equal steps from 30° to 75°.

<u>Design of the CNRF time-of-flight spectro-meter</u>. The acceptance diagram technique has recently proved invaluable in two important aspects of the design of the chopper system for the CNRF time-of-flight spectrometer.

(1) We have calculated 2-d phase space volumes transmitted by a separated counter-rotating pair of choppers, as a function of time and wavelength. The setup is illustrated in figure 3, and typical results are described elsewhere in this report [6].
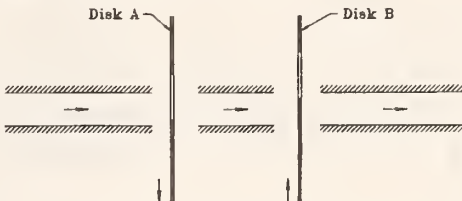
Figure 3. A scale drawing of the setup for one of the calculations of the transmission properties of a separated pair of choppers embedded in a guide. The separation between the disks is 54.6 mm.

(2) A simple system of two choppers or chopper pairs, phased to transmit neutrons of wavelength λ_0, will also transmit neutrons of wavelength

$$\lambda_j = \lambda_0 + j \, (h/m) \, (T_R/L_{14}), \qquad (2)$$

where the order number j is an integer, T_R is the time between chopper bursts, L_{14} is the distance between the mid-planes of the choppers or chopper pairs, h is Planck's constant and m is the mass of the neutron. To suppress these unwanted bursts, one or more additional choppers must be included in the design of the spectrometer. The problem of deciding where to place these intermediate order removal choppers has been tackled using the acceptance diagram technique. For given intermediate chopper positions, and a given order number j, the task is equivalent to the problem of determining the intensity transmitted by a set of four noncollinear apertures, given their separations, widths and lateral displacements, illustrated in figure 4. This problem appears to be very simple, but in fact it is not easy to write an algorithm for its general solution without recourse to the concept of acceptance diagrams.
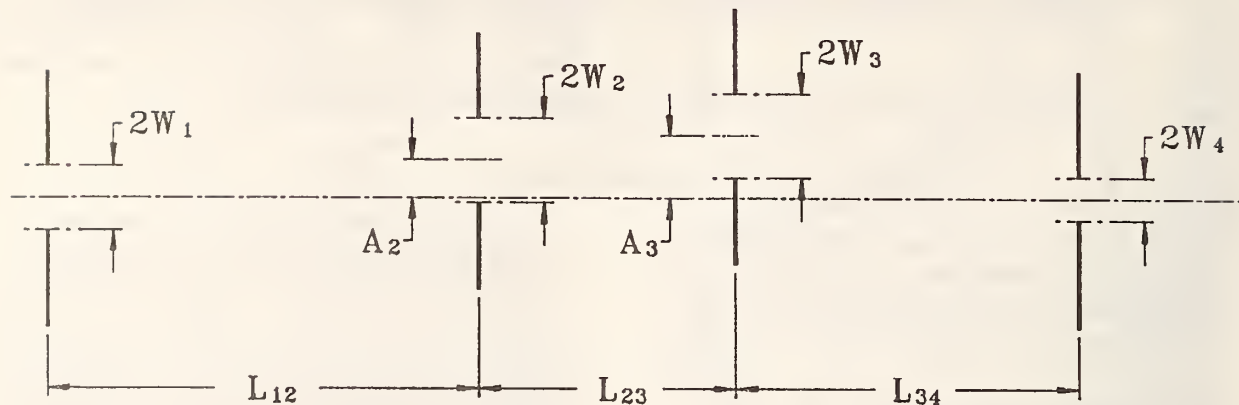
Figure 4. A set of four noncollinear apertures. The parameters of the problem are indicated. Without loss of generality the first and fourth apertures are placed on a common axis.

References

[1] J. R. D. Copley, NIST Tech. Note 1272, C. O'Connor, ed. p. 202 (1989).

[2] J. R. D. Copley, Nucl. Instr. Meth. A287, 363 (1990).

[3] R. Currat, Nucl. Instr. Meth. 107, 21 (1973).

[4] The Monte Carlo calculations were performed by D. A. Neumann.

[5] The neutron measurements were made by S. F. Trevino.

[6] J. R. D. Copley, "Aspects of the design of the counter-rotating chopper pairs for the high resolution time-of-flight spectrometer," p. 103 in this report.

NEW DATA ACQUISITION SYSTEM

B. R. Schmid (Reactor Radiation Division and University Of Maryland, College Park, MD)
and
G. Greene and J. J. Rhyne

The shutdown of the NIST research reactor during the neutron guide installation was used to update the instrument control system in the reactor hall by replacing the old PDP 11/44 computer with a pair of μVAXes and a new operating system. This afforded the opportunity to develop a new data-acquisition system using many of the enhancements of VMS version 5. We completely redesigned the system around CAMAC modules and intelligent motor controllers. We run four instruments from one CAMAC crate without interfering with each other. CAMAC communication is achieved through a Q-bus interface. The stepping motor controllers come with a nonvolatile memory for the motion control variables and a seven digit LED position display. The internal controller logic in combination with the incremental

encoders on the motor shafts make the motors move very precisely. One RS232 line is used to communicate with up to 5 units each housing two controllers.

The new instrument control program (ICP) has a significantly improved user interface and combines several of the old programs into one. The entire code (including the CAMAC, temperature and motor controller routines) is written in VAX-Fortran. All instrument specific parameters are concentrated in an ASCII configuration file, unique to each instrument, so that only one software version for all six instruments is needed. ICP makes extensive use of the VMS screen management utilities and is menu driven to a degree. Its features include two scanning modes; e.g., constant increment and constant Q/E with predefined buffers, an

enhanced temperature control with sample feedback as well as the possibility to scan magnetic fields. The data files are in pure ASCII format and, therefore, easily transferable from one computer to the other using various devices and protocols.

THEORY OF THE AHARONOV-CASHER EFFECT AS OBSERVED BY NEUTRON INTERFEROMETRY

R. C. Casella

Recently, Cimmino et al. [1] have measured the Aharonov-Casher [2] (AC) phase shift ϕ_{AC} via neutron interferometry. Derived originally on the basis of a duality principle [2], the AC effect has also been discussed in terms of a spatially extended model of the neutron. Physically, however, at the low momentum transfers inherent in such experiments [1], the neutron can clearly be treated as a point particle with a dipole moment μ proportional to its intrinsic spin. Moreover, I show that to obtain ϕ_{AC} one needs only the minimal prescription of electromagnetism, according to which the non-relativistic (NR) Hamiltonian $H(P,x)$ follows from the NR classical energy functional $E(p,x)$ by replacing the kinematic momentum p by $P - eA/c$ where $P_k = \partial L/\partial \dot{x}_k$ is the canonical momentum. ϕ_{AC} then follows directly from the Lorentz-invariant stationary-phase Feynman path integral over the classical action, *assuming* a unique axis of spin quantization exists over the *entire* spatial trajectory (classical orbit) in the absence of ambient magnetic fields. Moreover, the electric field $\underline{E}$ produces no acceleration of the neutron if one neglects terms $O(\underline{E}^2)$. To $O(\underline{E})$, the *local* aspects (*dynamics*) are shown to be *effectively 1 dimensional (1-d)*--again assuming the full 3-d Hamiltonian depends upon only one component of the neutron spin every-where on the loop--while, in the conventional geometric arrangement [1,2], ϕ_{AC} depends *only* on the linear charge density contained in a *2-d loop*. By arriving at the AC result in such a direct fashion, the present analysis makes especially clear the *nonlocal* nature of the effect as well as its associated *topological invariance* in a 2-d sense. Further experimental tests of topological invariance in more general situations are under consideration. A detailed analysis of the conventional arrangement follows.

I consider a neutron with instantaneous velocity $v = (v_x,O,O)$ traveling in an electric field $\underline{E}(x,y) = (\underline{E}_x,\underline{E}_y,O)$. In its instantaneous inertial rest frame, the four-momentum (E',p') is given by ($c = 1$, $\mu = -1.913 \mu_N$)

$$E' = m - \mu \cdot B' = m + \mu \sinh u \, \sigma_z \, \underline{E}_y,$$

$p' = O$, with $\tanh u = v_x$. In the original frame (where $B = O$), neglecting gravity and putting back c, $p = (mv_x,O,O)$ and

$$E = mc^2 + \tfrac{1}{2} mv_x^2 + \mu(v_x/c)\sigma_z \, \underline{E}_y,$$

to lowest order in v/c. Replacing the kinematic momentum p in the NR energy

$$E_{NR} = p_x^2/2m + \mu p_x \, \sigma_z \, \underline{E}_y/mc$$

by letting $p \rightarrow P - eA/c$, one obtains the NR (1-d) Hamiltonian ($e = O$),

$$H = P_x^2/2m + \mu P_x \, \sigma_z \, \underline{E}_y/mc$$

where $P_x = \partial L/\partial \dot{x}$ is the canonical momentum, L is the 1-d Lagrangian and

$$\underline{E}_y = \underline{E}_y(x,y)\big|_{y = \text{const.}}.$$

By Hamilton's equation,

$$\dot{x} = \partial H/\partial P_x = (1/m)(P_x + \mu \, \sigma_z \underline{E}_y/c).$$

Taking the inverse Legendre transform, $L = \dot{x}P_x - H$, it follows that

$$L = \tfrac{1}{2} m \, \dot{x}^2 - \mu \sigma_z \underline{E}_y \, \dot{x}/c + (\mu \underline{E}_y)^2/2mc^2.$$

From the Euler-Lagrange equation $\ddot{x} = \tfrac{1}{2} \, \partial/\partial x \, (\mu \underline{E}_y/mc)^2$. For uniform fields $\ddot{x}$ and $\ddot{y}$ vanish identically. In any event they are of second order in $\underline{E}$ and can be neglected in experiments such as that of Cimmino et al. [1]. Letting ℓ_i be the length of a straight-line segment of path (which, neglecting gravity, is the distance between reflections in the experiment of Ref. 1), x_i, the distance along the path, and ϕ_i, the path-integral phase change due to the electric field, then to $O(\underline{E}^1)$,

$$\phi_i = 1/\hbar \int_o^{\ell_i} L_{i,EM} \, dt$$

$$= 1/\hbar \int_o^{\ell_i} (-\mu \sigma_z \underline{E}_{yi} \dot{x}_i/c) \, dt$$

$$= 1/\hbar \int_o^{\ell_i} (-\mu \sigma_z \underline{E}_{yi}/c) dx_i \, .$$

At each reflection, we may rotate the coordinate frame about z (axis of quantization) such that the new x-axis lies along the path. Then, in a circuit

$$\sum_i \phi_i = 1/\hbar \oint L_{EM} \, dt$$

$$= - \mu \sigma_z/\hbar c \oint (\vec{ds} \times \underline{\vec{E}}) \cdot \hat{z}$$

$$= - 4\pi \Lambda \mu \sigma_z/\hbar c,$$

where Λ is the path-enclosed charge per unit length along $\hat{z}$ and the sense of the contours is left-handed along $\hat{z}$. Defining ϕ_{AC} right-handedly, $\phi_{AC} = 4\pi \Lambda \mu \sigma_z/\hbar c$.

Thus, the AC phase shift depends only on the enclosed linear charge density Λ and is therefore *topological in a 2-d sense*. As noted above, the phase shift produced by static electric fields in neutron interferometers under more general conditions is currently being investigated with a view towards suggesting new experiments to test for topological invariance.

References

[1] A. Cimmino, G. Opat, A. Klein, H. Kaiser, S. Werner, M. Arif, and R. Clothier, Phys. Rev. Lett. 63, 380 (1989) and S. A. Werner (private communication).

[2] Y. Aharonov and A. Casher, Phys. Rev. Lett. 53, 319 (1984).

NEUTRON ACTIVATION AUTORADIOGRAPHY PROGRAM

Y.-T. Cheng and J. Olin
(Smithsonian Institution, Washington, DC and the Reactor Radiation Division)

The technique of neutron activation autoradiography to obtain images of under-painting, brushstroke, and changes in the composition of paintings has been demonstrated to be a highly valuable complement to x-ray radiography and other techniques of painting examination. Gamma-ray spectroscopy can also be conducted and provides the general composition information of the painting. It is desirable, however, to identify the specific element or elements that comprise the different features in the painting. Localized gamma-ray spectroscopy has been found useful for this purpose [1].

An alternative method of identifying what elements are present employs changes in the film density resulting from the radioactive decay. The autoradiography films used in a painting study act as area detectors and register the radioactive decay characteristics of all the activated elements in the painting that emit charged particles. Therefore, a careful study of the changes in density at a given area by digitizing the series of autoradiography films should yield information for the composition of the corresponding area on the painting. Certain anticipated difficulties are imprecision in the

density measurements, mixtures of multiple elements with similar half-lives and inconsistency in film handling and processing. A feasibility study was initiated by establishing a procedure that compares the local density changes in an autoradiography series to reference film responses for individual elements and combination of elements. Reference film responses were obtained using a set of selected metal foils. The intrinsic characteristic of the film used was deduced from the analysis of the above results. This information was then applied in calculating the film responses for aluminium and nonmetallic elements antimony, arsenic, barium, manganese and sodium.

The first application of this procedure is shown in figure 1. The autoradiographic responses of an edge area on the painting "Pastoral Study" (R. A. Ryder, National Museum of American Art) is compared to that of gold. (There is no corresponding exposure 6 for the paintings.) The gold was likely transferred to the painting from the gilded painting frame. Figure 2 compares the film responses of another area on the painting to the combined responses of antimony and barium and shows that these two elements do account for the densities of the films in this area. However, as there is no obvious opaque white pigment containing only barium, it is likely that further refining of the density relationships will be needed. Figure 3 shows the comparison of the responses from a blue-white sky area on the painting "Lord Ullin's Daughter" (R. A. Ryder, National Museum of American Art) to that of iron and zinc. As iron could be present as the blue pigment, Prussian blue which has been identified in Ryder's paintings, and zinc as zinc white, this identification can be considered complete.

A data bank is being collected with these reference film responses. Other selected elements will be added in the future. With the anticipated increased use of image processing for the study of autoradiographs of paintings, this information can help in distinguishing areas of restoration in a painting and identifying the pigments the artist used. The locations of specific elements in a painting can be mapped and shown visually.

The Smithsonian Institution's Conservation Analytical Laboratory (CAL) has received grants

from the Samuel H. Kress Foundation and the Smithson Society to extend the present auto-radiography facility to handle larger paintings and to increase the number of paintings which can be studied. New shielding will be constructed to accommodate paintings larger than 4 ft by 4 ft and up to 7 ft by 8 ft in size. Figure 4 shows the shielding layout. This design replaces one reported earlier which would have been a permanent installation. The shielding will be removed after its use and painting activation will be carried out during reactor start up. In order to accommodate a larger number of paintings NIST has provided a second laboratory which CAL will equip with environmental control and security devices.
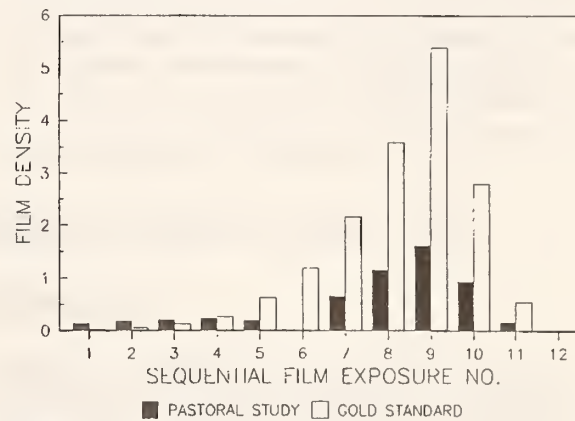
Figure 1. Pastoral study (edge area).
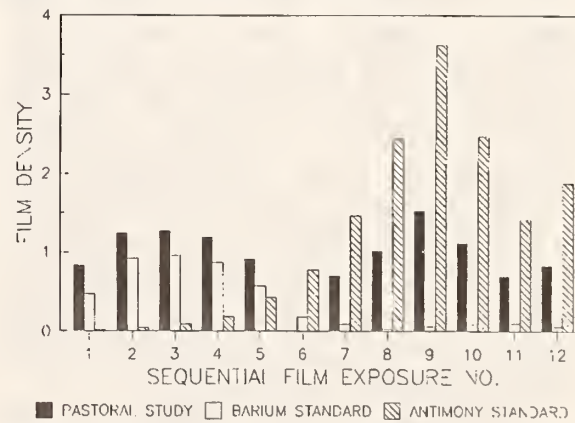
Figure 2. Pastoral study (yellow-white area).
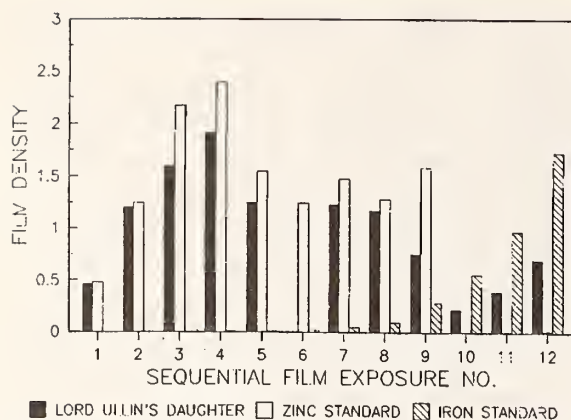
Figure 3. Lord Ullin's daughter (sky area).
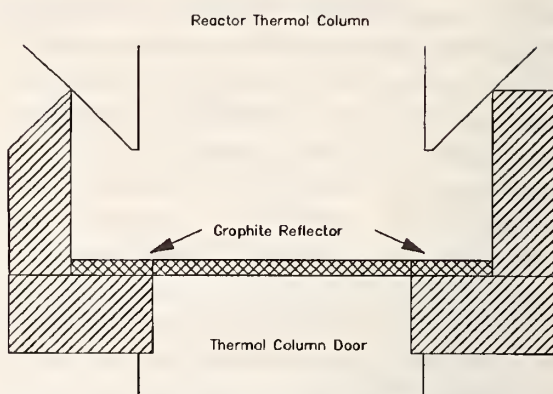
Figure 4. Proposed shielding layout for large painting activation.

Reference

[1] C. Fischer, C. Laurenze, W. Leuther, and K. Slusallek, "Neutronenautoradiographie," in <u>Der Mann With Goldhelm</u>.

NIST CRYSTAL AND ELECTRON DIFFRACTION DATA CENTER

A. D. Mighell and V. L. Himes

The NIST Crystal Data Center is concerned with the collection, evaluation and dissemination of data on solid-state materials. The Data Center maintains a central database with chemical, physical, and crystallographic information on all types of well-characterized substances. These materials fall into the following categories: inorganics, organics, organometallics, metals, intermetallics, and minerals. During the year, the master database has been updated and now contains greater than 150,000 entries. From this central database, two distribution databases are produced: NIST CRYSTAL DATA [1] and the NIST/Sandia/ICDD Electron Diffraction Database [2].

These data are made available to the scientific community through computer modes of dissemination. A new CD-ROM product with documentation has been produced that contains three related databases on the same disc: NIST CRYSTAL DATA, the Electron Diffraction Database, and the ICDD Powder Diffraction File. With this product, many types of searches can be carried out at one's desk using a PC computer. A second, and highly versatile method of

dissemination, is the on-line mode. This method is discussed separately below as it has been significantly enhanced during the year.

<u>On-line Search System</u>. The on-line system for NIST CRYSTAL DATA is known as CRYSTDAT [3]. This system consists of the database along with search and analysis software. CRYSTDAT is built and maintained via a long-term cooperative agreement between the National Research Council of Canada and NIST.

Recently, we have upgraded CRYSTDAT to include all 150,000 entries in the master database. Other data oriented improvements include: (1) cross-references to other databases; (2) all key data items directly searchable (indexed); (3) additional derived data.

Two important new search tools have been recently created--a generic chemical formula search and an interplanar spacing search. These tools, designed in response to requests from industrial users, will be applicable to research in analysis and materials design.

The new formula search permits one to search on generic classes and types of formulas. Both the elements present and subscripts in the

formula are subject to algebraic manipulation in the search 'find' command. Thus, for example, all formulas with atoms in specified ratios can be found regardless of element type. The inter-planar search permits one to find all materials having any specified combination of d-spacings and will be used in research in such areas as thin films. This command, especially when used with the lattice matching search function, will permit one to establish many types of inter- and intralattice relationships. As all data parameters are indexed, the system can rapidly execute the searches. Resultant answer sets from individual searches can be intersected using Boolean logic.

The CRYSTDAT System has many industrial applications in the materials sciences. Thus it can be used in the following: 1) in research in materials design (e.g., super conductors, lasers, thin films, optical materials); 2) in materials characterization and analysis (e.g., in neutron profile analysis, it can be used to identify the presence of minor impurities); 3) and in phase identification by neutron, x-ray and electron diffraction (e.g., from a few elements and d-spacings, most materials can be uniquely identified).

References

[1] NIST CRYSTAL DATA (1990). A Database of chemical, physical and crystallographic data ($\sim$ 150,000 entries). Compiled and evaluated by the NIST Crystal Data Center, NIST, Gaithersburg, MD 20899.

[2] NIST/Sandia/ICDD Electron Diffraction Database (1988). A Database designed for phase characterization by electron diffraction. Prepared by the NIST Crystal Data Center in collaboration with Sandia National Laboratories and the International Centre for Diffraction Data, NIST, Gaithersburg, MD 20899.

[3] CRYSTDAT (1990). An International On-line Search System for NIST CRYSTAL DATA. Developed jointly by the Canada Institute of Scientific and Technical Information and the NIST Crystal Data Center, NIST, Gaithersburg, MD 20899.

COLD NEUTRON PROJECT

G. Baltic, J. R. D. Copley, D. H. Fravel, C. J. Glinka, J. A. Gotaas, G. Greene, W. C. Knill, J. G. LaRock, H. P. Layer, C. F. Majkrzak, C. O'Connor, D. Pierce, H. J. Prask, M. J. Rinehart, J. M. Rowe, S. K. Satija, I. G. Schröder, T. J. Udovic, R. E. Williams, and R. H. Williams

On June 5, 1989, the NBSR was shutdown to begin guide installation. As planned, the guides, fabricated by Cilas-Alcatel of France, were in-hand for the first three beam-lines (NG 5, 6, 7). The initial phase of installation entailed the very difficult job of drilling 0.50-m diam holes through 7.5 m of reinforced concrete in the reactor-building wall that had stored hot plugs. This and the placing and grouting of 0.50 m diam stainless steel liners were completed in August, 1989.

With technicians from Cilas-Alcatel, installation of guide segments then began. As of January 1990, the special isolation shutters and neutron guides through the reactor-building wall were in place and leak-checked. By late March, installation of the three guide segments and associated shielding from reactor-building wall to cold source was completed, along with shielding associated with the NG-0 port which ends in the reactor hall. Follow-on leak and surveillance tests of the reactor-hall confinement were completed, after which the reactor was restarted on April 8, 1990.

Following reactor startup and resumption of "thermal" neutron research, installation of the remaining sections of neutron guides NG 5-7 in the guide hall continued. It is worth noting that these initial three guides will be ^{58}Ni-coated over their entire lengths to maximize intensity. Major new developments in Ni-based supermirrors--described on p. 116 in this report--will be incorporated in neutron guides NG 1, 2 and 4, installation of which is planned for 1991-2.

Neutron instruments are being developed as quickly as possible, and are described in some detail in other sections of this report. Overall, it is planned that at least six instruments will be operational by early 1991. These will include an 8-m SANS to be installed and operated by the

NIST Polymers Division; a diffuse scattering time-of-flight spectrometer; the 30-m NIST/ Exxon/U. Minn. SANS, which will be among the world's best in resolution, intensity, and versatility; the cold neutron depth-profiling facility, which is expected to increase measurement sensitivity by a factor of twenty over the existing thermal instrument; the new cold neutron prompt-gamma activation analysis station, which is expected to be the world's best full-time instrument of this type; and the neutron-lifetime experiment which will be installed at the fundamental neutron physics station. The planned layout for all guides is shown in figure 1.

The CNRF, which is a response to a critical national need for a cold neutron measurement capability, will be a National User Facility; to this end, the experimental stations installed will be available to the scientific and engineering community on the basis of scientific merit of proposals or in Participating Research Teams. A Program Advisory Committee (PAC) will play a critical role in advising NIST on the utilization of the facility.

On October 24, 1989, the PAC for the CNRF met for its first session. The PAC members are Chairman S. K. Sinha, Brookhaven National Laboratory and Exxon Research and Development Corp.; D. L. Price, Argonne National Laboratory; E. A. Schweikert, Texas A&M University; and H. Yu, University of

Wisconsin. In the first meeting the committee made the following principal recommendations:
-- Utilize calendar 1990 for "shake-down" and development.
-- Send out the first call for proposals toward the end of 1990, with two (possibly three) submission periods a year thereafter.
-- Have several external reviewers evaluate the proposals by mail with the PAC allotting instrument time based on the reviews.
-- Expand the PAC.
-- Form a CNRF User Committee in 1990.

Action is being taken to develop the details of all aspects of the user program with the recommendations of the PAC as the starting framework. Bill Kamitakahara, who is newly added to the staff, will be the scientific coodinator for the program.

Relating to instrument development, the following major collaborations have been initiated in this period. The University of Minnesota has agreed to participate in the development and use of two high resolution instruments: the 30-m NIST/Exxon/U. Minn. SANS and the cold neutron reflectometer. Their utilization is expected to focus on the elucidation of the structure and microstructure of polymers and other materials as well as surface and interfacial structure and interactions. According to the agreement, the University of Minnesota will provide a share of the development costs of the instruments, and will continue contributions
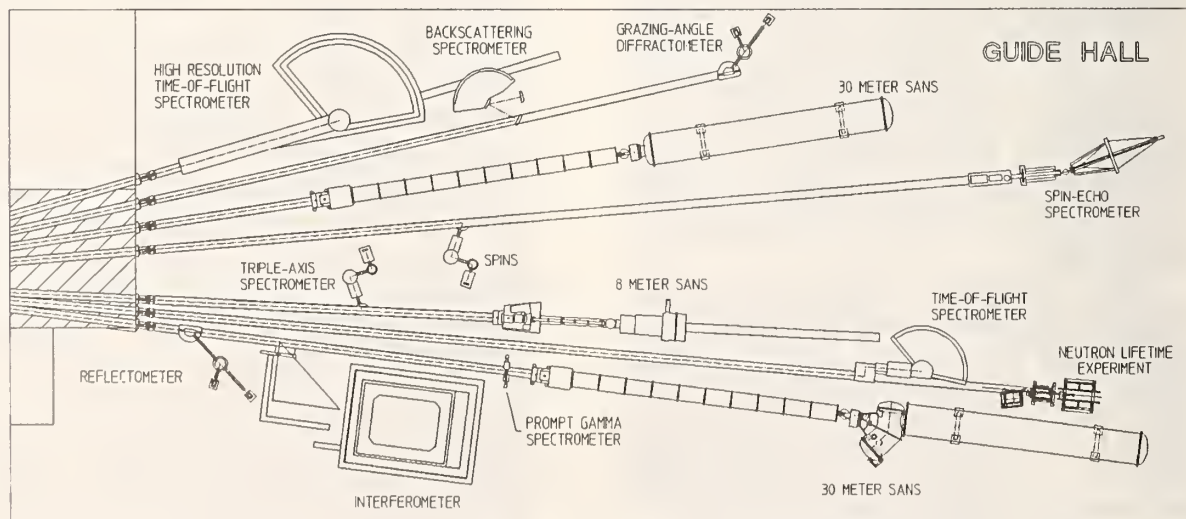
Figure 1. Cold Neutron Research Facility layout showing instrumentation complex.

to maintain state-of-the-art capabilities following instrument installation. IBM, through its Almaden Research Center, has entered into a similar agreement for development and utilization of the cold neutron reflectometer. Their interests are also expected to focus on polymers and surface interactions.

In March, the second issue of our newsletter, the **Neutron Standard**, was sent to approximately 2500 scientists and engineers.

This issue highlighted the installation of the guides and the development of the instruments. In the next issue we will include a detailed description of instruments and a request for proposals.

Detailed planning for a workshop on condensed matter spectroscopy with cold neutrons, tentatively scheduled for mid-1991, has begun.

LIQUID HYDROGEN COLD NEUTRON SOURCE

J. Gotaas, P. Kopetka, J. M. Rowe, and R. E. Williams

The flux of long-wavelength (> 4A) neutrons at the CNRF can be increased by replacing the D_2O ice moderator with a liquid hydrogen (LH_2) moderator. Although deuterium has a lower absorption cross section than hydrogen, H_2 has a larger scattering cross section, and is more efficient at slowing neutrons. Therefore, LH_2 will be used both to minimize the inventory of liquid hydrogen in the reactor (deuterium and hydrogen are chemically equivalent), and to avoid generating gaseous radioactive tritium.

Monte Carlo calculations are being performed to predict the cold-neutron flux as a function of source geometry using the MCNP code developed at the Los Alamos National Laboratory [LANL]. MCNP allows accurate representations of complex volumes and surfaces. We have obtained neutron scattering kernels for LH_2, developed at LANL in support of calculations on LANSCE moderators. In addition, we have developed cold-neutron scattering cross sections for D_2O ice and bismuth to compare MCNP results with previous NBSR flux measurements (see "Cold Source Spectrum and Flux Measurements" [1]).

We are planning to install a hydrogen source fabricated from 6061-T6 aluminum, with triple containment of the hydrogen for all parts of the system. Cooling will be provided by a new 3.5 KW helium gas refrigerator providing 14 K gas at up to 150 g/s. This refrigerator is currently being fabricated, and installation will begin late in 1990. Based on current calculations, the new source should provide an increase in intensity of long wavelength neutrons of at least two.

A safety analysis report is being prepared for submission to the Nuclear Regulatory Commission this fall, as the design is finalized. It is expected the LH_2 source will be approved and ready for installation when the second set of neutron guides is installed.

Reference

[1] C. J. Glinka, T. J. Udovic, J. M. Rowe, and J. J. Rush. NBS Tech. Note 1257, C. O'Connor, ed. p. 134 (1989).

CENTER FOR HIGH RESOLUTION NEUTRON SCATTERING

J. J. Rhyne, B. Hammouda, and S. Krueger

The National Science Foundation (NSF) has provided funding for a national user facility, the Center for High Resolution Neutron Scattering (CHRNS), as part of the NIST Cold Neutron Research Facility. Two instruments are under development for CHRNS--a 30-m SANS (see fig. 1) and a Spin Polarized INelastic Spectrometer (SPINS, to be jointed developed by NIST and NSF). These instruments will be operated as a user facility open to qualified research workers from universities, national laboratories, and industry. Proposals for beam time will be evaluated by the CNRF program committee.

The 30-m SANS is to occupy an end-guide position in the Guide Hall and will provide the highest resolution available in the United States (minimum Q of 0.0005 $Å^{-1}$ with a sample flux of approximately 10^6 n/sec for a $Q_{min} = 0.01$ $Å^{-1}$ on a 2 cm diam sample) and will incorporate a high counting rate 2-d detector. The detector will move inside a 15-m evacuated flight path to within 1.5 m of the sample permitting a maximum Q of O.6 $Å^{-1}$ without the use of a second area detector. It is also planned to provide a polarized neutron capability using a polarizing filter or multilayer reflection crystals.

The neutron monochromator is to be a variable pitch velocity selector providing wavelength tunability over the range 4 to 25 Å with a variable wavelength spread, $\Delta\lambda/\lambda$, from about 5% to 25%.

Two sample tables will be incorporated-- one with a multiple sample changer and a second independent table for cryostats, magnets, furnaces, etc.

As of July 1990 the CHRNS SANS instrument is over 90% designed with more than 30% of the parts and fabrication complete. It is expected to be operational in the summer of 1991. Preliminary design work is complete on the SPINS instrument with detailed design work and major parts procurement to occur in the last quarter of calendar 1990.
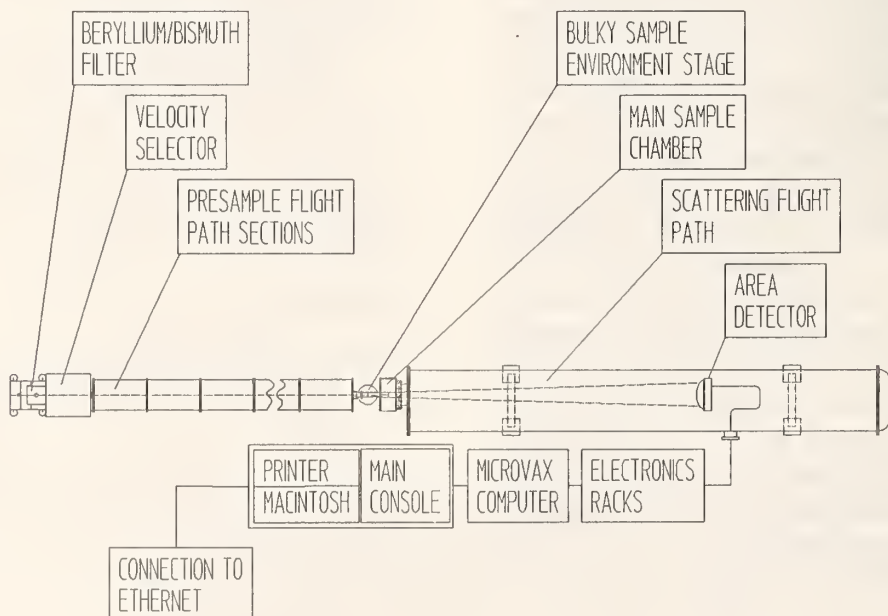
Figure 1. The 30-m NSF-SANS instrument.

HIGH RESOLUTION SMALL ANGLE SCATTERING SPECTROMETER

C. J. Glinka, J. J. Moyer, A. E. Heald, C. H. Chen, S. T. Krueger, and B. Hammouda
S. K. Sinha (Brookhaven National Laboratory, Upton, NY
and Exxon Research and Engineering Co., Annandale, NJ)
and
M. Lin (Exxon Research and Engineering Company, Annandale, NJ)

Construction of the 30-m long, high-resolution SANS spectrometer developed by the participating research team of the Exxon Research and Engineering Co., the University of Minnesota, and NIST is now essentially complete. Operational testing will take place in the Fall (1990) with the first scheduled experiments expected to begin in early 1991.

A line drawing of the instrument is shown in figure 1. The 15-m long, post-sample flight path is designed to house two large position-sensitive area detectors; one that can be positioned within the main cylindrical section of the flight path at any distance from 4 m to 15 m from the sample, and a second detector that moves along a circular arc at a fixed distance of 2 m from the sample. Together the two detectors will span a Q-range from roughly 0.001 to 1.0 A^{-1}. The carriage for the primary detector includes a motor driven mechanism for

selecting and positioning any of four beam stops in front of the detector to match the size of the incident beam.

As indicated in the cross-sectional view (A-A) in figure 1, the instrument's 15-m long pre-sample flight path has provision for the insertion of 1.5-m long neutron guide sections to allow the effective source to-sample distance to be varied from 5 m to 15 m to match the beam collimation to the sample-to-detector distance. The beam collimation and number of guide elements can be easily changed externally while the flight path is under vacuum.

The section of the incident flight path closest to the sample will house a doubly curved, grazing incidence mirror, 2.4-m long, to focus the beam onto the detector. The mirror consists of eight, 30-cm long x 5-cm high, concave cylindrical segments that will be aligned tangent to an arc 1700 m in radius. Each segment will
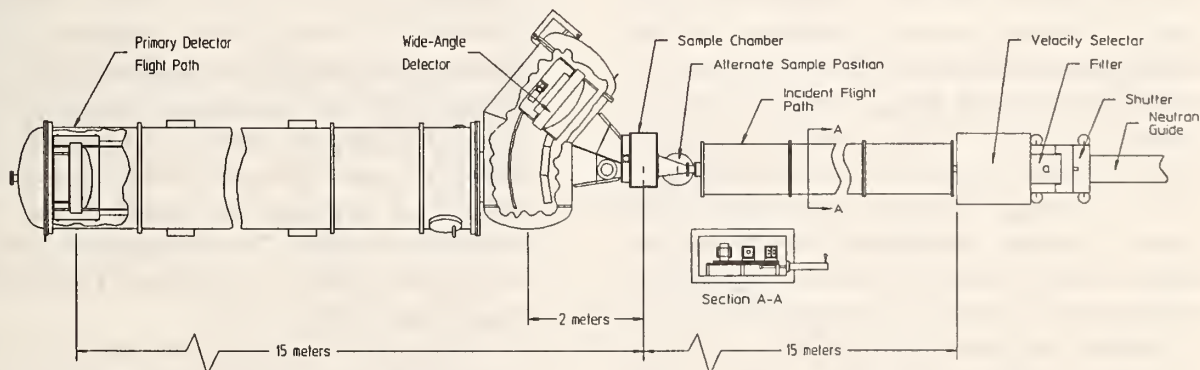
Figure 1. NIST/Exxon/University of Minnesota SANS spectrometer.

be slightly bent to conform approximately to this 1700-m arc to achieve focusing in the horizontal plane. In principle, such a mirror can provide up to a fourfold increase in flux on the sample, for a given minimum Q-value, over what can be obtained with pinhole collimation. The cylindrical quartz mirror segments have been obtained and tested both optically and with neutrons and do meet their design specifications for figure and finish. These elements will be coated with ^{58}Ni and then assembled and aligned for actual performance testing.

Proceeding in parallel with the construction of the instrument has been the development of the data acquisition system and software. Data will initially be stored in CAMAC-based histogramming memory modules under the control of a μVAX 3400 computer. This scheme provides both the capability to perform time resolved measurements, by switching among a set of memory modules, and the capability to carry out on-line data reduction and analysis since the main cpu is essentially freed from the task of acquiring data. The data currently being collected, as well as previously acquired data, can be displayed in a variety of ways on a color Macintosh computer to the μVAX using image processing software that has been customized for use with SANS data from a 2-d detector. A menu driven user interface has been written for the μVAX to aid users in both acquiring and displaying data.

Once in operation, the members of the PRT will control 75% of the available beam time with the remaining 25% to be allocated by the Program Advisory Committee for the CNRF. The first call for experimental proposals is planned for early 1991.

TIME-OF-FLIGHT SPECTROMETER MODIFICATIONS FOR GUIDE-HALL INSTALLATION

T. J. Udovic, I. G. Schröder, and J. G. LaRock

The NBSR Time-of-Flight (TOF) spectrometer is most-suited for quasielastic and low-energy inelastic neutron scattering studies. Monochromated neutrons (λ = 2.3-6.1 Å) are produced by double Bragg reflection from two pyrolytic graphite (002) crystals. Using the (004) reflection extends the wavelength range to 1.15 Å. Double reflection allows for a fixed sample position independent of the incident neutron energy and reduces the fast-neutron background contributions from the primary beam by shifting the monochromated beam axis away from the primary beam axis. After monochromation, fast-neutron and higher-order contamination is removed using either a pyrolytic graphite filter (typically for λ = 2.43, 2.35, and 1.71 Å) or a liquid-nitrogen-cooled Be filter (for λ > 4.08 Å). The beam is subsequently pulsed with a curved-slit Fermi chopper before scattering off the sample. The 98 ^{3}He detectors are radially located 2.286 m (i.e., 90 in) from the sample encompassing an angular scattering range of -20° < 2θ < 120°. The spectrometer is controlled with a dedicated CAMAC-interfaced μVAX computer. A TOF interface encodes the time and position of each detected neutron for subsequent recording by the CAMAC histogram memory. Contents of the histogram memory are periodically transferred to the μVAX computer and added to data from previous transfers. This updated data can then be analyzed with the appropriate TOF software routines available.

The TOF spectrometer was previously situated at the CTW-beam position in the Reactor Hall and is being relocated in the Guide Hall in a non-end position on the NG-6 guide tube. Installation is scheduled for the end of this year. Necessary modifications have been made to the spectrometer design in order to reutilize the instrument at its new location. Among other things, because of the non-end guide position, the first monochromator will now be held translationally stationary within a 15-cm guide

cut. Wavelength selection will then occur by the linear motion of the second monochromator using the first monochromator as a pivot point. The distance between the second monochromator and the sample position has been minimized. The flight path has been rotated from right-side scattering angles to left-side scattering angles and the angular scattering range has been altered to $0° < 2\theta < 140°$.

Additional upgrade modifications are also being made at this time to (i) increase the neutron flux at the sample position for all wavelengths, (ii) mitigate the effects of parasitic scattering (from cryostat shielding, etc.) on the sample spectrum, and (iii) upgrade the data acquisition instrumentation. The double monochromators will be increased in size to match the large 15 x 6-cm guide cross section. In addition, unlike the previous arrangement, the second monochromator will be vertically focussing onto the sample position. Vertical focussing is optimized when the vertical mosaic spread is minimized. Yet, for an isotropic mosaic spread, this minimized fwhm in the horizontal direction leads to an unnecessarily small wavelength spread and a subsequent decreased intensity on the sample. Hence, to gain maximum benefit from vertical focussing while still maintaining a desirably broad horizontal mosaic spread, both monochromators will possess an anisotropic mosaic distribution, 25' FWHM in the vertical direction and 40'-50' FWHM in the horizontal direction. This is being accomplished by using two layers of PG(002) crystals, each layer possessing a 25' mosaic, but staggered horizontally with 20'-25' angular offset. Parasitic scattering will be mitigated by the installation of an oscillating radial collimator centered on the sample position and located between the sample and the detectors. New data acquisition systems are currently being investigated for the new high-resolution TOF spectrometer. If an acceptable one is found or developed, it will be tested on the existing TOF spectrometer to ascertain its potential use for both TOF spectrometers.

COLD NEUTRON DEPTH PROFILING

G. P. Lamaze, R. G. Downing, J. K. Langland, and K. C. Littrell
(Inorganic Analytical Research Division)

The Cold Neutron Depth Profiling (CNDP) facility at Cold Tube West (CTW) is nearly ready for routine operation. The sapphire filter (13.5-cm thick) and the collimation have been installed. Figure 1 shows the expected neutron energy profile.
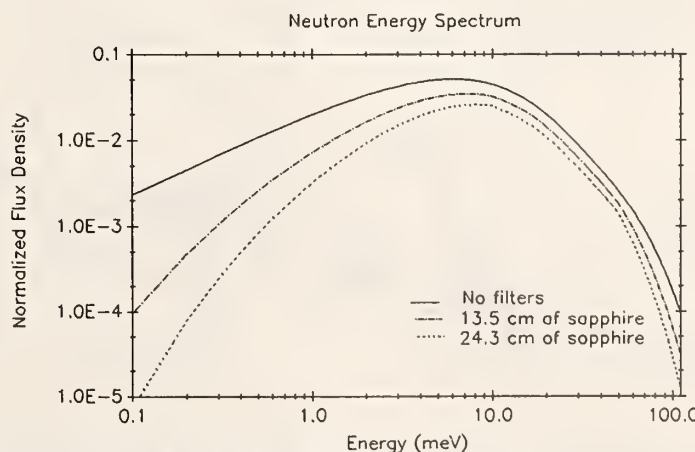
Figure 1. The neutron energy profile for the unfiltered beam and two different sapphire thicknesses. The 13.5-cm thickness has been selected for CTW.

A rotating shutter external to the reactor has been installed, aligned, and tested. Pancake type uranium fission chambers have been installed for monitoring the neutron fluence. A new 60-cm diam chamber has been installed. This chamber is capable of ultra high vacuum (UHV) at pressures of 5×10^{-8} Torr, which have been achieved without baking the chamber. The chamber has been designed to be adaptable to many different types of experiments by changing the component configuration. The main configuration provides for remote controlled scanning of 15 cm x 15 cm samples while varying both sample and detector angle with respect to the neutron beam. The scanner and rotator are undergoing final tests prior to installation in the chamber. They are controlled by a PC compatible computer. The software for the instrument control has been written. All of the necessary electronics for signal processing are now in place. The analog-to-digital (ADC) converters have been installed in a Vax based Genie system. The Genie work station is in place at CTW and is connected to the main Genie at the thermal NDP facility at BT-3.

HIGH RESOLUTION TIME-OF-FLIGHT SPECTROMETER

J. R. D. Copley

A schematic layout of the high resolution time-of-flight spectrometer is shown in figure 1. The instrument will be located on guide NG-1, which will have supermirror-coated top and bottom inside surfaces in order to increase intensity at the sample, by a factor of at least two as compared with ^{58}Ni-coated surfaces.

A total of seven disk choppers, in four evacuated housings, will be used to produce pulses of monochromatic neutrons at the sample. The maximum speed of the choppers will be 20,000 rpm, and the outside diameter of the disks will be 580 mm. The disks for the pulsing and monochromating choppers will each be fitted with three slots of different widths, allowing a choice of three distinct energy resolution widths at a given wavelength and chopper speed.

Downstream from the fast neutron filter the inside dimensions of the guide will be 30-mm wide, 100-mm high. The guide will be partitioned into five channels in order to improve intensity in the medium- and high-resolution modes of operation [1,2].
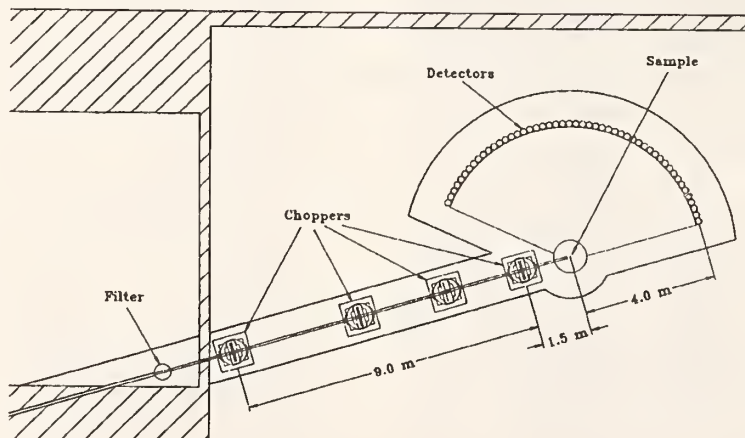
Figure 1. A schematic view of the layout of the proposed high resolution time-of-flight spectrometer. The fast neutron filter will be located in a separate room through which the guide passes on its way to the guide hall.

The distance from sample to detectors will be 4 m, and the total active area of the detectors will be of the order of 10 m^2. Furthermore, the detectors will be relatively thin in the direction traveled by neutrons from the sample ($\sim$ 12 mm or less) to achieve the required timing resolution.

We anticipate that the full width at half maximum of the energy resolution, at 20,000 rpm with 6 Å neutrons, will be $\sim$ 12, $\sim$25, and $\sim$50 µeV in the high, medium and low resolution modes, respectively.

Specific aspects of the design of the chopper system are discussed in this report [3,4].

References

[1] J. R. D. Copley, Nucl. Instr. Meth. A291, 519 1990).

[2] J. R. D. Copley, "Optimized design of the chopper disks and the neutron guide in a disk chopper neutron time-of-flight spectrometer," p. 101 in this report.

[3] J. R. D. Copley, "Aspects of the design of the counter-rotating chopper pairs for the high resolution time-of-flight spectrometer," p. 103 in this report.

[4] J. R. D. Copley, "Analytical calculations using acceptance diagrams," p. 86 in this report.

OPTIMIZED DESIGN OF THE CHOPPER DISKS AND THE NEUTRON GUIDE IN A DISK CHOPPER NEUTRON TIME-OF-FLIGHT SPECTROMETER

J. R. D. Copley

In last year's Summary of Activities [1] we discussed the possibility of using a channeled guide to increase the intensity on the sample in a counter-rotating disk chopper spectrometer. Since that time we have thoroughly investigated this problem and our principal findings are presented in the following paragraphs. Full details of most aspects of this work may be found in [2].

Consider the arrangement illustrated in figure 1. The first pair of counter-rotating choppers pulses the beam and the second pair (subscript 4) selects a narrow range of wavelengths from the pulsed beam. A neutron guide is placed before, between, and after the chopper pairs in order to increase intensity at the sample. In the present context we may (and shall) ignore the additional intermediate choppers which are found in a real instrument.
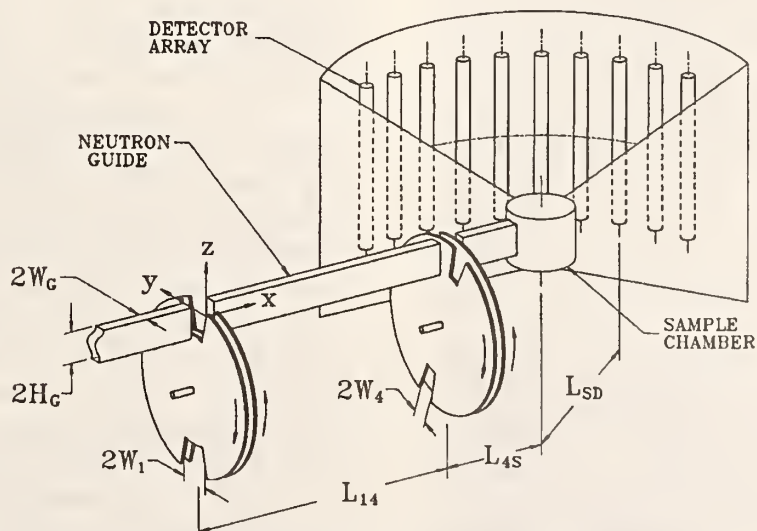
Figure 1. Schematic diagram showing the principal components of a counter-rotating disk chopper spectrometer; the intermediate choppers have been omitted for clarity. The disks of the CNRF spectrometer will each be fitted with three single slots rather than with a pair of slots as shown in the figure.

The intensity per pulse at the sample position, I_S, for the setup illustrated in figure 1, may be written as follows [2]:

$$I_S = A_0(W_1{}^2W_4{}^2/W_G)\rho_1(2-\rho_1)\rho_4(2-\rho_4), \quad (1)$$

where

$$A_0 = \Phi_0(\lambda)\,(2\theta_C)^2\,(2H_G)\,(2/v^2)\,(h/mL_{14}), \quad (2)$$

W_1 and W_4 are the half-widths of the slots in the choppers (fig. 1), W_G is the half-width of the guide, and ρ_k ($k = 1$ or 4) is the ratio (W_G/W_k) or unity, whichever is the smaller. In equation 2, $\Phi_0(\lambda)$ is the differential current density of neutrons of wavelength λ in the incident beam, θ_C is the (wavelength-dependent) critical angle of the guide material (assumed identical for all surfaces), H_G is the half-height of the guide (and of the slots in the choppers), v is the tangential velocity of the choppers, L_{14} is the distance between the chopper pairs, h is Planck's constant, and m is the mass of the neutron.

The resolution of the chopper system, measured by its contribution to the standard deviation of the time distribution at the detector bank, is given by [2]

$$\sigma_D{}^2 = \alpha^2\,\sigma_1{}^2 + \beta^2\,\sigma_4{}^2, \quad (3)$$

where σ_k ($k = 1$ or 4) is obtained from

$$\sigma_k{}^2 = (1/6)\,(W_k/v)^2\,(2 - 2\rho_k + \rho_k{}^2), \quad (4)$$

the dimensionless parameter

$$\alpha = [L_{4S} + L_{SD}\,(\lambda_S/\lambda_I)^3]\,/\,L_{14} \quad (5)$$

and

$$\beta = 1 + \alpha. \quad (6)$$

In eq. (5), L_{4S} is the distance from the second chopper pair to the sample (fig. 1), L_{SD} is the distance from the sample to the detectors, and λ_I and λ_S are the neutron's wavelengths before and after scattering, respectively.

The intensity I_S is maximized at constant resolution σ_D when [2]

$$(W_G/W_1) = \frac{2\alpha}{(\alpha + \gamma)} \quad (7)$$

and

$$(W_4/W_1) = \frac{\alpha(\beta + \gamma)}{\beta(\alpha + \gamma)}, \quad (8)$$

where

$$\gamma^2 = \alpha^2 + \beta^2. \quad (9)$$

This is illustrated in figure 2, which is a plot of the reduced intensity

$$J_S = I_S/[A_0(\sigma_D v)^3] \quad (10)$$

for the case that $\alpha = 0.5$.

For a given value of (λ_S/λ_I), such as unity, the optimum width ratios (W_G/W_1) and (W_4/W_1) only depend on the distance ratios (L_{4S}/L_{14}) and (L_{SD}/L_{14}). This implies that the optimum values of the width ratios, for an instrument of the type shown in figure 1, are independent of λ and v. A second implication is that if $2W_1$ and $2W_4$ are changed, as is possible with a counter-rotating disk chopper spectrometer, the guide width $2W_G$ should also be changed. This is most practically achieved using a channeled guide, which is not unlike a very long reflecting Soller collimator,
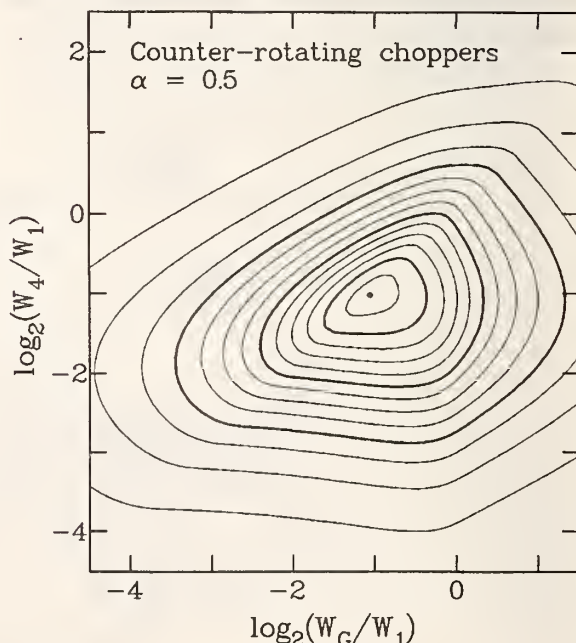
Figure 2. Contours of constant reduced intensity J_S for $\alpha = 0.5$. The interval between contours is 0.5 and the value of J_S at the peak is 6.746

102

except that the widths of the channels are not identical.

We have shown that a heavy price can be paid in lost intensity if a simple guide of fixed width, as opposed to a channeled guide, is used in conjunction with counter-rotating chopper pairs fitted with slots of different widths [2]. In order to avoid such losses we shall use a channeled guide in the CNRF high resolution time-of-flight spectrometer [3].

The optimization of slot widths and guide widths in a real instrument is more complicated than the analysis presented above and in reference 2. One reason is that the half-widths W_1 and W_4 vary with z, whereas W_G is a fixed quantity. The channeled nature of the guide also implies behavior which cannot be ignored. Both of these effects were included in the calculations which were used to determine final dimensions for the slots and the channeled guide in the CNRF time-of-flight spectrometer.

References

[1] J. R. D. Copley, NIST Tech. Note 1272, C. O'Connor, ed. p. 207 (1989).
[2] J. R. D. Copley, Nucl. Instr. Meth. A291, 519 (1990).
[3] J. R. D. Copley, "High resolution time-of-flight spectrometer," p. 100 in this report.

ASPECTS OF THE DESIGN OF THE COUNTER-ROTATING CHOPPER PAIRS FOR THE HIGH RESOLUTION TIME-OF-FLIGHT SPECTROMETER

J. R. D. Copley

The CNRF high resolution time-of-flight spectrometer [1] will use seven disk choppers to provide a pulsed, monochromatic beam of neutrons at the sample position. The conventional description of this type of instrument (e.g., Ref. 2) states that the first pair of counter-rotating choppers pulses the beam, the final pair selects a narrow band of wavelengths from the pulsed beam, and the intermediate choppers remove unwanted orders and reduce the burst repetition frequency in order to alleviate problems of "frame overlap". In what follows we shall see that this type of statement oversimplifies the behavior of the first and final chopper pairs in a real instrument.

One of the advantages of using counter-rotating pairs of choppers, rather than single choppers, is that the effective chopping speed is doubled; it follows that the transmitted intensity is doubled for a given choice of burst time [3,4]. A second advantage is that each disk can be fitted with a small number of slots of different widths in such a way that different slot widths can be selected by suitably changing the relative phase of the choppers; this in turn implies a choice of resolution widths without changing the chopper speed or incident wavelength [4].

The disks in the first and final chopper pairs of the CNRF high resolution time-of-flight spectrometer will each have slots of three different widths. One of the challenges in designing these disks has been to determine where to place the slots in order to eliminate unwanted bursts of neutrons. *If the separation between the disks can be neglected*, the problem becomes that of finding a solution to a set of inequalities of the form $|a| > b$, where a and b only involve angular slot positions and the dimensions of the slots and the guide. This problem is by no means trivial because the inequalities are nonlinear. We have nevertheless devised a procedure to search for solutions (if they exist), as well as a convenient method to evaluate their stability to engineering and electronic phasing tolerances.

In the course of a more detailed analysis it has became clear that we cannot neglect the separation between the members of a counter-rotating chopper pair in the new CNRF time-of-flight spectrometer. Though small (~ 55 mm), this separation drastically modifies the transmission properties of the chopper pair, and a different approach is required to the problem of where to place the various slots on a disk. An additional consequence is that we have had to abandon the idea of using two closely spaced slots in each disk in order to increase intensity at constant resolution [3].

The transmission function T, for a separated pair of counter-rotating chopper disks, is a

function not only of the time t that neutrons cross the mid-plane between the disks, but of their wavelength λ. This is most easily understood by thinking about two disks, each of which is fitted with a single very narrow slot, spinning in opposite directions with angular velocity ω, separated by a distance 2s, and illuminated by a very narrow highly collimated beam of neutrons. Such a system transmits neutrons of a single wavelength λ_0, which depends on the relative phasing of the disks, at times $(t_0 + mT_R)$, where m is any integer and the chopper period $T_R = 2\pi/\omega$. [Its transmission is also non-zero for wavelengths $(\lambda_0 + n\lambda_R)$ at times $(t_0 + nT_R/2 + mT_R)$, where n is any integer and λ_R is the wavelength of neutrons which take one complete chopper period to travel the distance between the disks, but we shall ignore this periodicity in λ since λ_R is typically of order 200 Å or more.] The transmission function for this simplest of systems may therefore be represented in a "transmission diagram", which is a plot of t vs. λ, by a series of points at wavelength λ_0 and times separated by T_R.

If each disk has N very narrow slots there will be N^2 distinct paths for neutrons to pass through the system. In (t, λ) space the situation is represented by a set of N^2 points within a "unit cell" which has dimensions (T_R, λ_R). These points are the basis of a centered rectangular lattice (plane group $p1$); if the disks are identical an additional mirror symmetry operation is introduced and the plane group
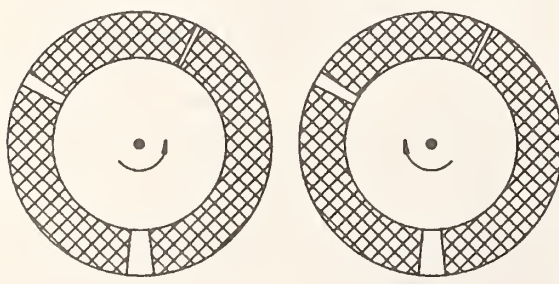
becomes cm. Negative wavelengths correspond to neutrons which travel in the opposite direction through the system. A change in the phasing of the disks corresponds to a shift of the pattern of points with respect to the origin of the transmission diagram.

In a realistic situation both the slots and the channel between the disks have significant width, and the incident beam has considerable divergence; the transmission function is a set of peaks of finite width in both t and λ, each of which is in part represented by a closed loop such that T is only non-zero within these loops. This concept is illustrated in figure 1, which shows (a) the arrangement of the slots in the first two disks of the CNRF time-of-flight spectrometer and (b) a portion of the corresponding transmission diagram, calculated using the acceptance diagram technique [5], for the low resolution mode of operation.

We have made exhaustive use of this type of diagram in order to select positions for the slots in the first and final chopper pairs of the new spectrometer. The basic idea is to ensure that all neutrons transmitted by the first chopper pair, other than those in the intended bursts, cannot get through the final chopper pair because they have wavelengths for which the final chopper pair's transmission function is zero at all times. The inverse condition, which may or may not impose additional constraints, must also be met. Our choice of slot positions satisfies both criteria, in all three resolution modes, for $\lambda_0 \leq$ 12 Å and $(\lambda - \lambda_0) \leq 66$ Å.
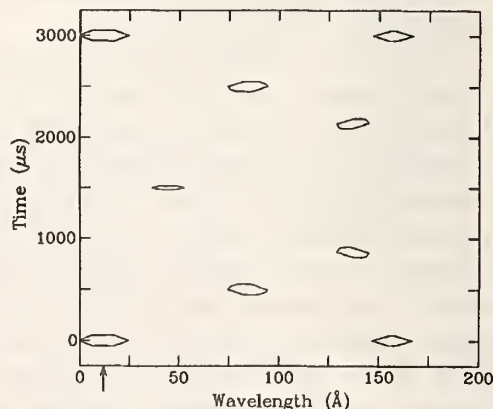
Figure 1. (a) The arrangement of slots in the first pair of disks of the CNRF high resolution time-of-flight spectrometer, as "viewed" by the incident neutrons. The disk nearer the source rotates clockwise. (b) A portion of the transmission diagram for this pair of disks. The incident wavelength λ_0 is 12 Å, indicated by the arrow. The period T_R is 3000 μs and the separation is 54.6 mm: λ_R is therefore $\sim$ 217 Å.

104

References

[1] J. R. D. Copley, "High resolution time-of-flight spectrometer," p. 100 in this report.

[2] J. R. D. Copley, NIST Tech. Note 1272, C. O'Connor, ed. pp. 201, 207 (1989).

[3] J. R. D. Copley, Nucl. Instr. Meth. <u>A273</u>, 67 (1988).

[4] J. R. D. Copley, Nucl. Instr. Meth. <u>A291</u>, 519 (1990).

[5] J. R. D. Copley, "Analytical calculations using acceptance diagrams," p. 86 in this report.

COLD NEUTRON CRYSTAL SPECTROMETERS

J. Ankner, C. Majkrzak, D. Neumann, S. Satija, and S. Trevino

Five cold neutron crystal spectrometers-- some of which share common design components--are currently under development at the CNRF. Two of these, a reflectometer and a triple-axis spectrometer, will be installed on the first three guides in 1991. The spin-polarized inelastic neutron scattering spectrometer (SPINS), the backscattering spectrometer, and the spin-echo instrument will be installed on the final four guides. Progress in the last year includes the following.

The cold neutron triple-axis spectrometer and the reflectometer are each in the final detailed design stage. Many components of each instrument have been fabricated or purchased.

For the backscattering spectrometer, preparations are under way for tests of the phase-space transform of neutrons using mosaic graphite crystals mounted on a rapidly moving chopper. Computer simulations indicate that success with this device could increase the intensity of neutrons on the sample by a factor of five or more.

Progress on the SPINS spectrometer includes the development of neutron supermirrors discussed on p. 108 in this report. Development of the wavelength-dependent spin-flipper is continuing in a NIST/Brookhaven National Laboratory collaboration.

ACCORDION SUPERMIRROR POLARIZER FOR NEUTRONS

C. F. Majkrzak

and

L. Passell (Brookhaven National Laboratory, Upton, NY)

Various polarizing mirror and supermirror Soller arrays and benders for neutrons have been proposed and constructed [1-3]. These devices effectively produce polarized neutron beams with large cross sections via reflection of one of the two neutron spin states. Nonetheless, all of these devices, in one way or another, broaden the angular divergence of the beam. In a transmission polarizing device, wherein the undeviated or nonreflected beam of neutrons of one spin state is utilized, this broadening is avoided. Furthermore, if a transmission device is used to polarize, the beam which is utilized is not deviated so that the overall instrumental design can often be simplified. Mezei [4] has proposed placing a polarizing supermirror within a guide tube section at the proper angle to function as a transmission polarizer. Another, similar, transmission geometry which we have been developing consists of trans- parent, single crystal plates of Si, on which polarizing supermirrors have been deposited, arranged in an antiparallel or accordion array as shown in figure 1(a). The problem with a conventional parallel or Soller array, depicted schematically in figure 1(b), is that multiple reflections of neutrons of the unwanted spin state cannot be entirely avoided for a beam with a finite angular divergence. Consequently, in the parallel arrangement, neutrons in the unwanted spin state are in effect deviated from the incident or transmitted beam direction only if they make an odd number of reflections from the super-mirror coatings. That fraction of the neutron beam of the undesired spin state which makes an even number of reflections emerges parallel to the transmitted or undeviated beam of the desired spin state, thereby reducing the polarizing efficiency. One way the multiple reflections could be eliminated would be to properly stagger the parallel plates along the beam direction. Unfortunately, for the relatively small angles usually involved, the required overlap is negligible and the resultant configuration is nearly the same length as a single long plate which, for large beam cross sections, can be impractical.

Another solution is the accordion arrangement of figure 1(a) in which it is possible to insure, for a given wavelength spread and angular divergence, that neutrons of the wrong spin state undergo a single reflection if the angle of inclination and critical angles of the polarizing supermirror are properly selected. In many cases it is, of course, necessary to subsequently absorb the neutrons of the wrong spin state, which were intentionally deviated by the polarizer, in a nonreflecting Soller collimator.
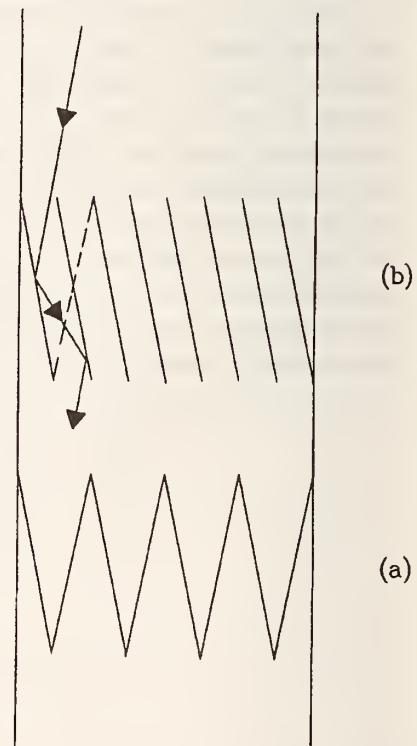
Figure 1. (a) antiparallel or accordion transmission polarizer array for neutrons consisting of polarizing supermirror films deposited on transparent single crystal Si plates as described in the text; (b) conventional parallel or Soller array of supermirror polarizers illustrating detrimental double reflection.

Now in transmission, the polarizing efficiency is determined by the reflectivity of the supermirror for the neutrons of the spin state being eliminated. Thus, if that reflectivity is only, say, 80%, then the polarizing efficiency cannot be better than ~80%. However, even if the reflectivity were only 80%, for example, placing two such transmission polarizers in series would result in a polarizing efficiency of about 96%. Currently we are using Fe-Si supermirrors which are not yet as good as the Fe-Ag or Co-Ti supermirrors made by O. Scharpf and coworkers [1,5]. This is necessary because the absorption losses in the latter supermirror materials are prohibitively high in transmission (the transmission losses in the Si single-crystal substrate plates, on the other hand, amount to at most ~20% for practical thicknesses and critical angles and neutron wavelengths as short as 2 Å passing through two plates in series). Fe-W supermirrors are also being tried, but, due to rougher interfaces, their reflectivities are, so far, lower than those of the Fe-Si.

In figure 2 is shown a more detailed schematic of the accordion transmission polarizer, which we intend to construct, where each pleat of the accordion is composed of a pair of partially overlapping Si plates with the supermirror coating deposited on opposite sides. This particular topology allows the supermirror films on adjacent substrates to make direct contact at each apex, thereby preventing passage of the beam through the edges of the Si plates without being incident on the supermirror film at some point (refraction of the beam in the Si substrate has a negligible effect on the performance of the device). It may in fact be possible to continuously adjust the angle of inclination of the plates relative to the incident beam accurately by sliding spacers (located above and below the beam) between plates along the beam direction. Because the spacing between 100-mm long plates would actually be only about 1 mm, there is a substantial geometrical advantage in that a small change in angle requires a relatively large translation of the shim along the beam direction. The transmission polarizer could then be adjusted for a specific neutron wavelength mechanically.

Figure 2. Accordion transmission polarizer detail showing pairs of Si plates with supermirror coatings on opposite sides forming individual pleats as described in the text.

References

[1] O. Schärpf, Physica B 156 &157, 639 (1989).

[2] W. H. Kraan, J. B. van Tricht, and M. Th. Rekveldt, Physica B 156 & 157, 657 (1989).

[3] H. Mook, private communication.

[4] F. Mezei, in Thin-Film Neutron Optical Devices, SPIE Proc. Vol. 983, C. F. Majkrzak, ed. (SPIE, Bellingham, WA, 1989) p. 10.

[5] R. Pynn, in Thin-Film Neutron Optical Devices, SPIE Proc. Vol. 983, C. F. Majkrzak, ed. (SPIE, Bellingham, WA, 1989) p. 18.

SUPERMIRROR COATINGS FOR NEUTRON GUIDES

C. F. Majkrzak, D. A. Neumann, J. R. D. Copley
and
D. F. R. Mildner (Analytical Chemistry Division)

During the past 2 years significant progress has been made in the development of nonpolarizing, supermirror guide coatings for neutrons. Reflectivities of the order of 95% or better at glancing angles up to three times the critical cutoff for total reflection from an ordinary Ni surface have been achieved. The implications of this advance go beyond the factor of nine enhancement in flux which would be obtained by coating the surfaces of a guide installed on a cold source with such a multi-layered thin-film structure. It is also now possible that thermal neutron guides; i.e., guides for shorter wavelength neutrons, can be constructed more advantageously given the increased angular acceptance afforded by these supermirrors.

Although high reflectivities for Fe-Ag polarizing supermirrors up to a critical angle twice that of Ni have been achieved by O. Schärpf and coworkers some time ago [1], the nonpolarizing supermirrors composed of Ni and Ti layers (the combination of which gives one of the highest scattering powers for elements consisting of naturally occurring isotopic mixtures) possess a relatively large amount of interfacial roughness as has been clearly revealed by electron microscopy [2]. Not only does the interfacial roughness reduce the specular scattering power of each bilayer, but the diffuse scattering arising directly from the roughness makes possible additional nonspecular scattering through simultaneous or multiple scattering processes as illustrated schematically in figure 1. In this figure the points along the x^* axis in reciprocal space correspond to the fundamental and higher harmonic reflections for a multilayer with a single periodicity of about 63 Å or reciprocal lattice vector of 0.1 Å^{-1}. In this picture the incident and primary diffracted wavevectors have a length of 2.67 Å^{-1} and define an Ewald sphere (circle) as indicated by the dashed curve. Superimposed on the multilayer specular reflection points are bars parallel to the y^* axis which qualitatively represent diffuse scattering due to roughness along the boundaries between layers of dissimilar materials. The intersection of a diffuse scattering ridge with the Ewald sphere means that simultaneous or multiple scattering events can occur when the multilayer is oriented to reflect from, for example, the first order reflection as shown in the figure.

The larger the interfacial roughness, the greater the direct and indirect diffuse scattering losses. In certain cases it is therefore necessary to consider whether the superposition of additional bilayers to compensate a reduction in bilayer reflecting power caused by interfacial roughness is counterproductive. The possibility of multiple and simultaneous scattering occurring increases with decreasing wavelength since the radius of the Ewald sphere becomes larger and the arc of the circle approaches the multilayer growth axis more closely.

Well-defined peaks due to the secondary scattering mechanism described above can be observed by fixing the incident wavevector relative to the sample and Q, as shown in figure 1, and rotating the scattered wavevector to a position such as indicated by the primed final wavevector. In practice this can be accomplished simply by scanning the spectrometer detector which is equivalent to following the trajectory defined by the Ewald circle in reciprocal space. Alternatively, scans can be performed transverse to the longitudinal or growth axis along the diffuse ridge until the perimeter of the circle is intersected at which point a peak will occur (such a scan is very nearly a sample rocking curve sufficiently close to the x^* axis and can be performed by rotating the sample relative to a fixed incident beam direction and detector or scattering angle).

For relatively rough interfaces these multiple scattering effects can be pronounced in transverse scans as is shown in figure 2 for a Ni-Ti supermirror in which a cusp shaped interface had been observed by transmission electron microscopy [2]. In the case of a supermirror,

multiple periodicities are present, so that a continuous ridge of scattering extends from the origin out to a cutoff along the longitudinal or growth axis. As for a simple multilayer, however, if diffuse scattering is present, similar multiple scattering peaks should appear. Interference effects due to the nonspecular scattering of x-rays from Si-Ge multilayers have also been observed and analyzed [3] by generalizing the treatment discussed by Sinha et al. [4] of scattering from single roughened surfaces. The problems pertaining to surface and interfacial roughness, steps, terraces, conformal and nonconformal in-plane cor-relations, and interdiffusion are of interest not only for technological reasons such as the one presently described, but are of importance in the understanding of fundamental physical phenomena in lower dimensional systems. Efforts to understand the diffuse scattering from interfaces in a more general, quantitative way are in progress (see, for example, "Diffuse X-ray Scattering from a GaAs/AlAs Super-lattice," by D. A. Neumann et al., p. 55 in this report).

Two commercial enterprises with experience in thin film coatings, the Ovonics Co. of Troy, MI and the Optoline Co. of Andover, MA, were awarded Small Business Innovation Research (SBIR) Phase I contracts with the Department of Energy (DOE) to develop supermirrors and solve the interfacial roughness problem. This support supplemented funds initially invested by NIST through the Department of Commerce. J. Wood and his colleagues at Ovonics have been experimenting with a carbon buffer layer in-between the alternating polycrystalline Ni and Ti layers to minimize the roughness, whereas J. Bradshaw et al. at Optoline have been attempting to make amorphous $Ni(x)C(1-x)$-$Ti(y)Mn(1-y)$ alloy layers based on predictions of molecular dynamics simulations of sputtered film growth [5]. Neutron reflectivity and diffuse scattering measurements are performed at the NBSR on these new products in order to determine what progress is actually being made.

For example, a reduction in the interfacial roughness is clearly evident by making a simple qualitative comparison of the transverse scans shown in figures 3 and 4 for Ni-C-Ti and $Ni(x)$ $C(1-x)$-$Ti(y)Mn(1-y)$ supermirrors, respectively, with that shown in figure 2 above. In figure 5 is shown the reflectivity profile for a Ni-C-Ti supermirror from Ovonics as measured at the NBSR. Superimposed on this plot of the supermirror reflectivity is the profile for an ordinary 1000-A Ni film. In both cases the substrate material is ordinary float glass and the neutron wavelength is 4 Å. The reflectivity is at least 95% out to about three times the critical cutoff for Ni. Similar reflectivity results were obtained on this particular supermirror by W. Yelon who generously agreed to perform measurements at the University of Missouri Research Reactor during the period of time when the NBSR was temporarily shut down for guide tube installation [6].

In a separate but parallel development, J. Hayter and H. Mook have derived an optimal algorithm for generating a supermirror layer thickness sequence [7] which enhances the performance of the improved supermirrors even further. This can be seen by comparing figures 6 and 7 which show neutron reflectivity profiles for a Ni-C-Ti supermirror composed of discrete sets of bilayers of different thicknesses (where in this case Ni-C is considered one layer and Ti-C the other layer of a bilayer) [8] (fig. 6) and one made up of layers whose thicknesses were determined according to the algorithm derived by Hayter (fig. 7).

Recently both Ovonics and Optoline were awarded Phase II SBIR DOE Contracts to develop high-quality neutron supermirror coatings on a larger scale. J. Hayter has also been instrumental in securing additional funding from the DOE through ORNL to support the corresponding research at the NBSR. We are hoping that it will now be possible to coat several of the guide tubes at the new NIST Cold Neutron Research Facility (CNRF) with these improved, high-performance supermirrors.

Q=0.1 K=2.67 Å⁻¹
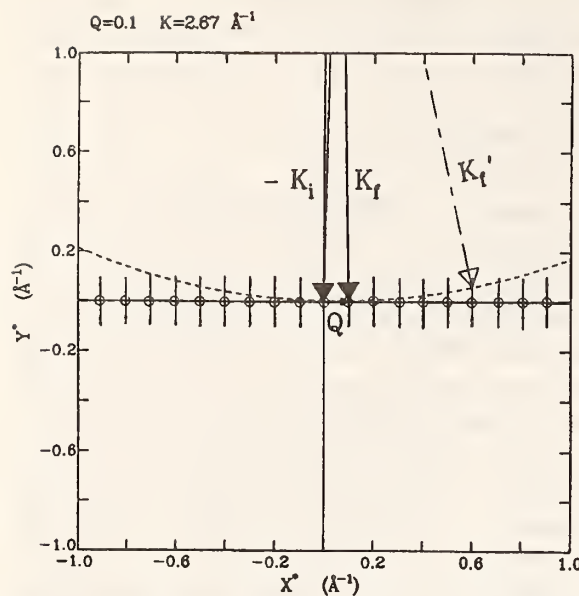
Figure 1. Reciprocal space schematic for multiple or simultaneous scattering effects arising from diffuse scattering ridges in multilayered structures with rough interfaces intersecting the Ewald sphere as described in the text.
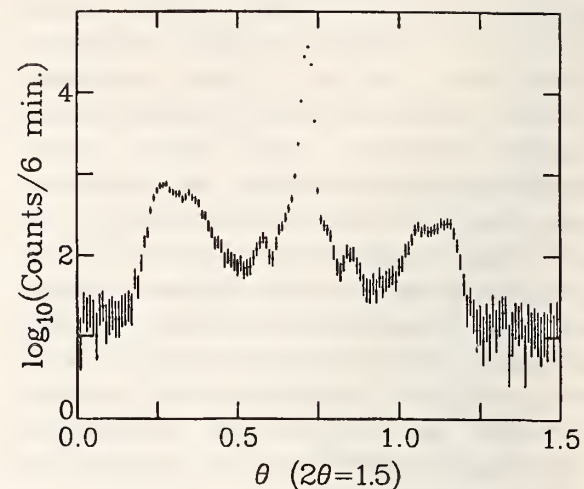
Figure 2. Transverse scan intensity versus sample angle with fixed detector or scattering angle for a Ni-Ti supermirror with rough interfaces.
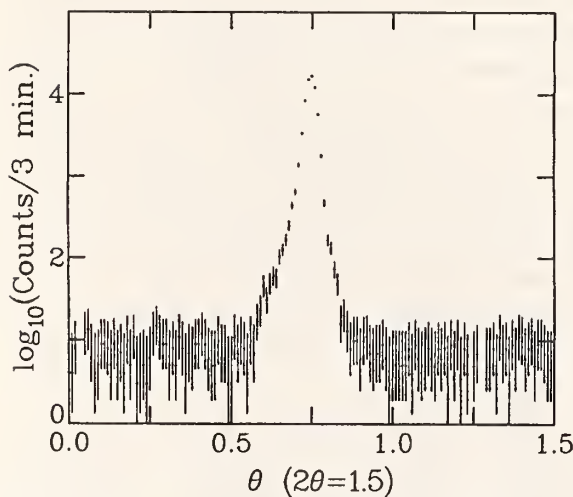
Figure 3. Transverse scan for a Ni-C-Ti supermirror.
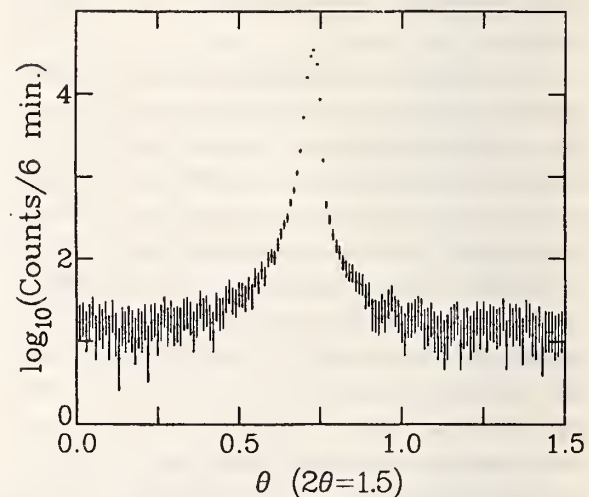
Figure 4. Transverse scan for a Ni(x)C(1-x)-Ti(y)Mn(1-y) supermirror.

110
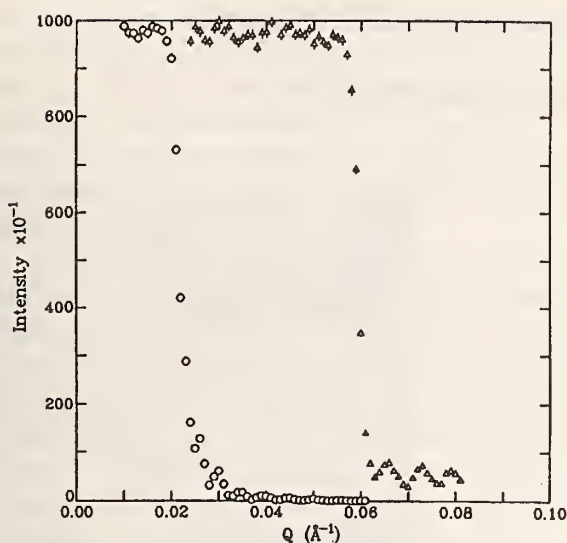
Figure 5. Neutron reflectivity as a function of wavevector transfer for a Ni-C-Ti supermirror superimposed on the reflectivity profile of a 1000-A thick Ni film. This supermirror has an effective critical angle about three times that of the Ni film and a nearly uniform reflectivity of better than 95%. This supermirror is composed of discrete sets of bilayers of different thicknesses as described in the text.

Figure 7. Reflectivity profile for a Ni-C-Ti supermirror composed of layers with thicknesses determined according to the optimized algorithm derived by Hayter as described in the text.

Figure 6. Reflectivity profile for a Ni-C-Ti supermirror composed of discrete sets of bilayers with different thicknesses.

References

[1] R. Pynn, in Thin-Film Neutron Optical Devices, C. F. Majkrzak, ed. SPIE Proc. Vol. 983, (SPIE, Bellingham, WA, 1989) p. 18.

[2] J. E. Keem, J. Wood, N. Grupido, K. Hart, S. Nutt, D. G. Reichel, and W. B. Yelon, in Thin-Film Neutron Optical Devices, C. F. Majkrzak, ed. SPIE Proc. Vol. 983, (SPIE, Bellingham, WA, 1989) p. 38.

[3] A. Bruson, C. Dufour, B. George, M. Vergnat, G. Marchal, and Ph. Mangin, Solid State Comm. 71, 1045(1989).

[4] S. K. Sinha, E. B. Sirota, S. Garoff, and H. B. Stanley, Phys. Rev. B38, 2297 (1988).

[5] I. K. Schuller, MRS Bulletin XlII, 23 (Nov. 1988).

[6] W. B. Yelon and J. Wood, private communication.

[7] J. Hayter and H. Mook, J. Appl. Cryst. 22, 35 (1989).

[8] C. F. Majkrzak and L. Passell, Brookhaven National Laboratory, Report No. 34343 (Upton, NY, 1984) and Acta Cryst. A41, 41 (1985).

NEUTRON FOCUSING USING CONVERGING GUIDES

D. F. R. Mildner (Inorganic Analytical Research Division)

The neutron current density can be increased by using a converging guide; this can be particularly useful as the last section of a long straight guide [1]. This increased density is obtained at the expense of increased divergence of the beam, which is unimportant in neutron absorption techniques. A diagrammatic representation of neutron trajectories within the guide in each of the two transverse directions of the guide is useful for deriving analytical expressions in the small angle approximation which describe the transmission properties of the guide.

We define a 1-d gain G for the converging focusing guide as the ratio of the current density of neutrons (transmitted acceptance per unit dimension) leaving the converging guide system to the current density of neutrons (acceptance area per unit dimension) incident on the system. Using the acceptance technique, Anderson [2] has indicated that the converging guide gain as a function of wavelength shows discontinuities in the first derivative. Analytic expressions for the functional form of the gain for the focusing guide with limited acceptance have been derived [3] as a function of the converging guide dimensions, the incoming beam divergence, and the critical angle of the converging guide surface material. The results can be reduced to a set of nine basic formulae (some of which have a reflection index n) with three independent parameters: 1) the convergence factor H/H', 2) the ratio m of the critical angles θ_c and θ of the converging and straight guides, and 3) the neutron wavelengh λ which effectively links the other two parameters. These expressions are in agreement with measurements on straight-converging guide systems [4]. This method can also be applied to a reflectivity which is describable by a series of step functions.

A graphical method has been found for determining the appropriate equation for the current density gain for the particular guide configuration and relative surface coatings, as a function of wavelength. Shown in figure 1 is a diagram giving the various regions in (θ, θ_c) space for the most convergent geometric configurations of the measurements of Copley
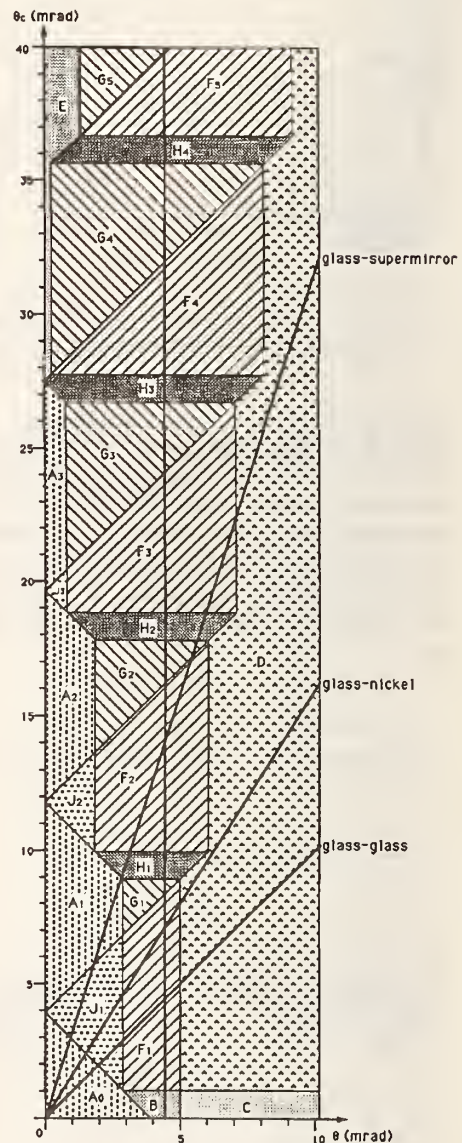
Figure 1. A schematic diagram in (θ, θ_c) space showing the regions for the configuration of the converging guide measurements of Copley and Majkrzak [4]. The line $\theta = 4.43$ mrad corresponds to $\lambda = 4.1$ Å for float glass.

and Majkrzak [4]. This is determined solely by the geometry of the converging guide (the length L, and the entrance and exit heights, H and H'), and at this point the figure is independent of the coatings of the guide. The abscissae are normalized to the particular reflecting material of the straight guide, so that a given wavelength

corresponds to a particular value of θ. Straight lines through the origin, $\theta_c = m\theta$, indicate the loci of the different combinations of guide coatings. The intersection of this line with the wavelength line determines the region and hence the equation for the current density gain of the guide combination.

We have calculated the expected gain for the cold neutron flux at the exit of a 50 x 50 mm^2 guide on the cold source at the NIST reactor using a 2-d converging guide with supermirror coating having a critical angle three times that of natural nickel. The 2-d gains G^2 are shown in figure 2. At short wavelengths the gain is unity. It then rises at longer wavelengths, until the divergence angle becomes too great to be reflected within the converging guide, at which point the gain levels off or even drops. Except for certain cases, the distribution of neutron trajectories at the exit is neither uniform in position nor in angle.
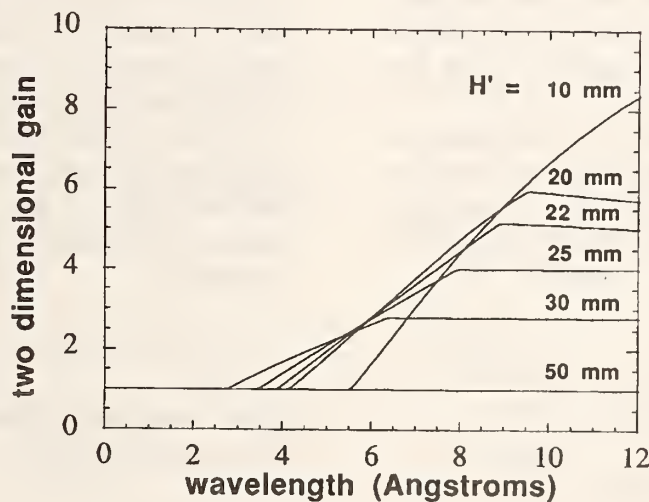
Figure 2. Two-dimensional current density gains obtained on a 50 x 50 mm^2 straight guide of ^{58}Ni using a 500 mm long converging guide with exit dimension H' and with a coating of critical angle three times that of natural nickel.

References

[1] M. Rossbach, O. Schärpf, W. Kaiser, W. Graf, A. Schirmer, W. Faber, J. Duppich, and R. Zeisler, Nucl. Instrum. & Meth. B35, 181-190 (1988).
[2] I. S. Anderson, SPIE Proc. 983, 84-92 (1989).
[3] D. F. R. Mildner, Nucl. Instrum. & Meth. (accepted for publication).
[4] J. R. D. Copley and C. F. Majkrzak, SPIE Proc. 983, 93-104 (1989).

MULTIPLE REFLECTIONS IN CURVED NEUTRON GUIDES

D. F. R. Mildner (Nuclear Methods Group)

There is increased use of neutron optical elements which depend on the principle of total external reflection of cold neutrons. For example, curved devices in neutron optics are used quite extensively as beam benders, particularly for filtering a beam of cold neutrons from the fast neutron component, in lieu of a crystal filter. In particular, our concept for focusing cold neutrons is to use stacked curved microguides which superimpose their outputs at the focal point. The method of acceptance diagrams is used to obtain analytic expressions for the intensity and spatial and angular distributions of the neutrons which are transmitted along a curved guide [1], provided that the length of the guide is greater than the minimum length necessary to eliminate direct radiation. The diagram describes the path traversed in position-angle space in the plane of curvature as the neutron proceeds along the curved guide.

The acceptance area for curved guides is parabolic in shape, and shows the asymmetry in the spatial distribution of the transmitted neutrons. The transmitted intensity curve as a function of wavelength λ is given by

$$I(\lambda) \sim 4/3 H \lambda_c (\lambda/\lambda_c)^3 \qquad \text{for } \lambda \leq \lambda_c$$

$$\sim 4/3 H \lambda_c [(\lambda/\lambda_c)^3 - \{(\lambda/\lambda_c)^2 - 1\}^{3/2}],$$
$$\text{for } \lambda \geq \lambda_c$$

where λ_c is the wavelength characteristic for the curved guide and depends both on the dimensions of the guide and on the surface coating of the guide. H is the width of the curved guide with a radius of curvature R. Then the characteristic wavelength λ_c is given by $\sqrt{(2H/R)}/\gamma_c$, where γ_c is the critical angle per unit wavelength for the guide surface material. These equations are valid only if the guide is longer than the line of direct sight, $\sqrt{(8HR)}$.

The effect of less than perfect reflectivity appears as a factor of the nth power of the reflectivity of the neutron density in the phase-space regions corresponding to trajectories which undergo n reflections. Provided that the reflectivity is close to unity, the reflectivity for all neutrons averaged over all regions in phase space is given by the average reflectivity to the power n, where n is the number of reflections averaged over all possible reflections.

For the curved guide, the mean number of reflections depends on the neutron wavelength and the length of the guide [2]. The mean number of reflections per length of direct sight is given by

$$\bar{n} = 3/2 \ (\lambda_c/\lambda) \qquad \text{for } \lambda \leq \lambda_c$$

which make only garland reflections from the outer surface, and by

$$\bar{n} = 3\lambda_c \ (2\lambda^2 - \lambda_c^2)/2[\lambda^3 - (\lambda^2 - \lambda_c^2)^{3/2}] \qquad \text{for } \lambda > \lambda_c$$

which make both garland and zig-zag reflections. The mean number of each type of reflection in this case is given by

$$\bar{n}_{gar} = 3\lambda_c^3/2[\lambda^3 - (\lambda^2 - \lambda_c^2)^{3/2}] \qquad \lambda > \lambda_c, \text{ and}$$

$$\bar{n}_{zz} = 3\lambda_c \ (\lambda^2 - \lambda_c^2)/[\lambda^3 - (\lambda^2 - \lambda_c^2)^{3/2}] \qquad \lambda > \lambda_c.$$

For $\lambda > \lambda_c$, $\bar{n}$ approaches $2\lambda/\lambda_c$, which is the value of the straight guide of length $\sqrt{(8HR)}$. Of course, the total number of reflections is the addition of the number in the plane of the curve, and the number in the plane perpendicular to the curve, which is given by the straight guide of the same length.
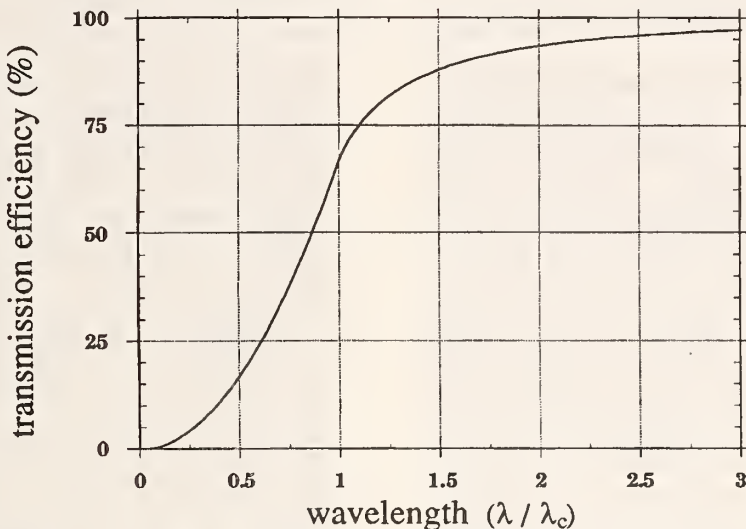
Figure 1. The relative transmission efficiency of the curved guide in units of the characteristic wavelength.
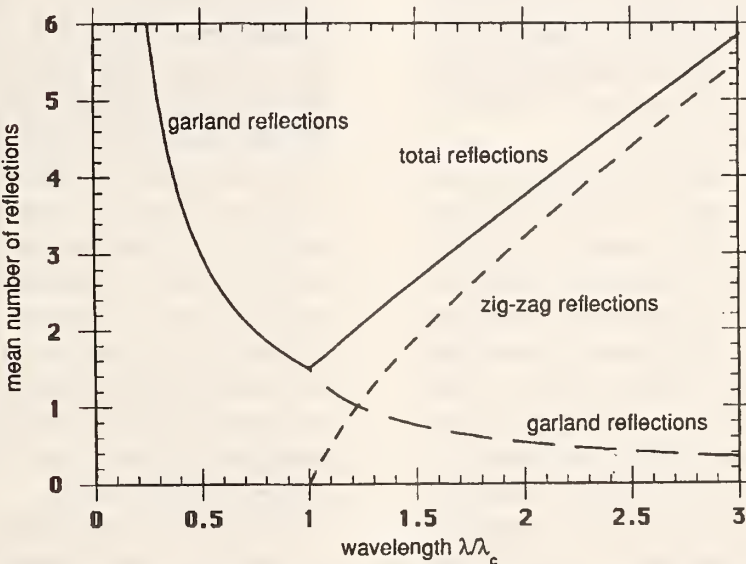
Figure 2. The mean number of reflections $\bar{n}$ for a curved guide of characteristic wavelength λ_c, having only garland reflections for $\lambda \lesssim \lambda_c$, and both garland and zig-zag reflections for $\lambda > \lambda_c$.

References

[1] D. F. R. Mildner, Nucl. Instrum. & Meth. <u>A290</u>, 189-196 (1990).
[2] D. F. R. Mildner, Nucl. Instrum. & Meth. <u>A292</u>, 693-699 (1990).

^{6}Li-DOPED SILICATE GLASS FOR THERMAL NEUTRON SHIELDING

C. A. Stone and R. Zeisler (Center for Analytical Chemistry)
and
D. H. Blackburn, D. A. Kauffman, and D. C. Cranmer (Ceramics Division)

Choosing a thermal neutron shielding material for neutron scattering instruments or prompt gamma-ray activation analysis (PGAA) instruments is often difficult. The ideal neutron shield is one which attenuates the neutron beam rapidly without creating additional background. But the materials which are most attractive for attenuating the thermal neutrons, such as boron and cadmium, produce gamma-rays in the neutron capture process. Although this gamma-ray background might be tolerated near some neutron scattering instruments, it quickly degrades the quality of a PGAA instrument.

The nuclide ^{6}Li is more attractive than other nuclides as a thermal neutron shield because it has a large absorption cross section, 941 barns, and the primary reaction is the (n, α) charged particle reaction. There is only a small prompt gamma-ray branch (0.0004% of the total). Enriched ^{6}Li can thus provide rapid attenuation of the neutron beam without producing significant background problems.

A disadvantage of using ^{6}Li has been the lack of a suitable host matrix. Fused ^{6}Li$_2$CO$_3$ is one common form but it is prone to attack by moisture and has poor structural properties. Sintered ^{6}LiF is a better material for shielding since fluorine has a low absorption cross section and will not contribute substantially to the gamma-ray background. Structural properties of sintered ^{6}LiF are also better than those of lithium carbonate, as it is not prone to attack by moisture and is less brittle. This material, though, is not easily formed into irregular shapes and cannot be easily machined.

We have developed a ^{6}Li silicate glass for use as a thermal neutron shield. There are only two components to the glass: SiO$_2$ and ^{6}Li$_2$O. Lithium silicate glasses tend to be susceptible to crystallization at higher Li$_2$O concentrations. Glasses have been successfully prepared with ^{6}Li$_2$O concentrations of up to 18% wt with no evidence of crystallization. This glass provides a thermal neutron attenuation of 76% per mm of glass. To further increase the concentration of Li$_2$O in the glass, alkaline earth or other divalent oxides can be added to the melt. We have been successful in creating a ^{6}Li glass containing as much as 22% wt percent by adding 8% wt Al$_2$O$_3$. The thermal neutron attenuation for this alumina-doped lithium silicate glass is 82% per mm.

Long-term irradiation tests have been performed on the ^{6}Li silicate glass. A one by one cm piece of glass, with a thickness of one mm, was cut from a larger sample of glass and then polished. This glass was irradiated in the 1PH1 pneumatic beam tube of the MITR-2 reactor at the Massachusetts Institute of Technology. The neutron current density in this beam tube is 8 x 10^{12} neutrons/cm^{2}s and the cadmium ratio is 400. To irradiate the sample, the glass was wrapped in Al foil and placed in a polyethylene rabbit that was packed with polystyrene packing material. Short irradiations, lasting from a few seconds to 15 min, showed that the temperature of the rabbit was stable after 15 min and thus heating by the glass was not a problem. Following these short irradiations, the sample was irradiated for 10 hrs. Two weeks after the end of irradiation, the glass was unpacked and inspected. Some localized charring of the polystyrene was observed within ca. 2 mm of the glass sample. The glass showed no detectable change in appearance other than a discoloration from color centers produced by charged particle recoil.

Much of the usefulness of this glass is in external beam environments, where the neutron current densities are lower, on the order of 10^9 neutrons/cm^{2}s, and the beams have much lower gamma-ray and fast neutron components. The irradiation studies described above were equivalent to an external beam irradiation of at least seven years. This lithium glass is more applicable as a thermal neutron shield than other shielding materials: it can be cast into a variety of shapes and sizes, and it can be machined using ordinary glass machining techniques into shapes with close tolerances.

FUNDAMENTAL NEUTRON PHYSICS

G. L. Greene (Quantum Metrology Division)

Two instrumental positions at the CNRF have been designated as experimental stations for investigations in an area of research which has come to be known as "Fundamental Neutron Physics." This work includes measurements of basic neutron properties, tests of fundamental symmetries of nature as well as investigations involving advanced methods in neutron optics. An additional program in advanced methods for neutron flux determination will have implications in neutron dosimetry, analytical chemistry, and nuclear physics. One instrumental position (on NG-7) will be on a monochromated beam, devoted to neutron interferometry. The other position (on NG-6) will be a full flux end position. It will initially be devoted to studies of weak interaction physics.

Design and construction work on the neutron interferometer position has been focussed primarily on the implementation of a sophisticated seismic and vibrational isolation system. Neutron interferometers are exceptionally sensitive to external noise sources. The seismic isolation will consist of a cascaded series of passive isolation elements which will allow the use of an entirely new class of neutron interferometers employing separated perfect crystals as optical elements. This work is a collaboration with the University of Missouri, the University of Vienna (Austria), and the University of Melbourne (Australia).

The end position will initially be employed for an experiment to determine the neutron lifetime. This quantity has important implications for the study of the theory of weak interactions, for astrophysics and cosmology. The neutron life apparatus has already been used in a initial measurement at the Institut Laue Langevin in Grenoble. It will be installed at NG-6 in October 1990. This work is a collaboration between NIST, the University of Sussex (England), the Central Bureau for Nuclear Measurements (Belgium), and the Scottish Universities Research Reactor. It is supported in part by the Department of Energy and the Science and Engineering Research Council (U.K.).

B. NON-RRD PROGRAMS

NEUTRON INTERACTIONS AND DOSIMETRY GROUP

J. A. Grundl (Ionizing Radiation Division)

The Neutron Interactions and Dosimetry Group develops and applies well-characterized neutron fields and related capabilities for neutron dosimetry methods evaluation and standardization, for detector development and calibration, and for reactor cross-section measurements. Involvement with outside organizations, both in the Federal and private sectors includes many types of research and technology assistance programs as well as leadership roles on national and international standards and radiation policy making bodies.

A selection of accomplishments for FY90 with emphasis on NIST reactor related activities are outlined below in titled paragraphs grouped under four projects.

DOSIMETRY FOR MATERIAL PERFORMANCE ASSESSMENT

E. D. McGarry, C. M. Eisenhauer, J. A. Grundl, and D. M. Gilliam

Dosimetry methods for monitoring the degradation of materials in high fluence neutron exposures are diverse. This project provides some form of measurement assurance, standardization, or methods development for nearly every approach to materials dosimetry employed in the United States. Interlaboratory measurement cooperation with substantial international participation are an important feature of this project.

NIST/Nuclear Regulatory Commission (NRC) Contract. By law, Title 10 of the Code of Federal Regulations, Appendix G and H require that a program, involving irradiation of metallurgy test specimens and dosimeters, be carried out for the surveillance of pressure vessel embrittlement damage. NIST continues to participate in Pressure Vessel Surveillance Dosimetry to benchmark dosimetry measurements and calculations and continues as general dosimetry consultant to the NRC.

Whereas the contract of former years has concerned itself with materials dosimetry tasks related to pressure vessel exposures to fluence greater than 1 Mev [ϕt(E > 1 MeV)], current dosimetry concerns have expanded to include damage in steel by neutrons in the energy range 0.01-to- 1 MeV and, for different reasons, by thermal and epithermal neutrons. Concern for this energy range comes about because of the gas-cooled advance reactor design and growing discontent with either the ϕt(E > 1 MeV) or the DPA Model (Displacement Per Atom) of embrittlement in ferritic steels. New Heavy Section Steel irradiation programs are under way to compare pressure vessel steel damage in spectra with enhanced neutrons in the high-epithermal and "just below 1 MeV" ranges to damage in conventional light-water reactor spectra. Because the test efforts represent design and startup of new irradiation experiments, NIST is involved in various test reactors. Separate concern for the very low-energy neutrons comes from a realization that experimental data exist to suggest that more damage is observed at lower fluence when the thermal-to-fast neutron ratios are a factor of 50 higher than in PWR reactors.

NRC Regulatory Guide Preparation. Major involvement continues in the development of a draft regulatory guide "Status of a New

Regulatory Guide on Methods and Assumptions for Determining Pressure Vessel Fluence," to provide guidance for improving and benchmarking neutron transport calculations. A near-final version is now being reviewed by the Nuclear Regulatory Commission prior to its issuance as a Draft Regulatory Guide for review by the nuclear industry. The primary object of the guide is to achieve better consistency in determining and reporting neutron fluences and associated uncertainties.

The guide contains up-to-date methodology for carrying out absolute transport calculations, assuming a widespread use of two-dimensional discrete-ordinates Sn transport codes. The mechanism for validating calculation is comparison with accurate measurements. Discussion of neutron fluence measurement methods emphasizes more measurements, quality assurance of dosimetry materials, and better reporting. There is also emphasis on validating transport calculations against experimental benchmarks and confirming power cycle calculations against in-situ surveillance dosimetry.

ASTM Benchmark Standard. A draft of this ASTM Standard Guide for Benchmark Referencing of Neutron Dosimetry for Reactor Pressure Vessel Surveillance was prepared by NIST and was proposed for ballot at the June 1989 E10.05 meeting in Scottsdale, Arizona. A revised draft was then sent to ASTM in January 1990 in preparation for an E10.05 ballot at ASTM and Radiation Effects Symposium meeting in Nashville.

NIST/Westinghouse Cooperative Agreement. Dosimetry Measurement Assurance Program: Measurement assurance activities for Westinghouse radiometric (activation foil) and Solid State Track Recorder (SSTR) dosimetry continues. NIST is especially interested in problems associated with obtaining reliable masses for SSTR fissionable deposits in the nano-gram to pico-gram range.

SSTR Ultralight Mass Determination: The trend in the nuclear power industry to implement SSTR dosimetry in ex-vessel cavities is increasing. The bulk of the interest is in work taking place in Westinghouse PWRs and in the B&W Owner's Group's Davis Besse Dosimetry Benchmark Experiment. NIST provides known fluences for mass determinations of the ultra-lightweight SSTRs. The irradiations are carried out in the ^{235}U Cavity Fission Source in the reactor thermal column, to an accuracy of about 2.5% (1σ).

Cooperative Research on a New Dosimeter: The dosimeter consists of a fissile layer placed adjacent to a polymer material that becomes conducting as a result of implantation of energetic heavy ions such as those from neutron-induced fission. The results of preliminary calibration experiments carried out on a prototype detector in the Cavity Fission Source were reported at the 7th ASTM/Euratom Symposium, Strasbourg, France, August 1990.

Dosimetry Methods Development for Reactor Support Structures. A priority effort in the Heavy Section Steel Technology (HSST) Program is evaluation of low-temperature, low-fluence-rate embrittlement on reactor vessel support structures. This issue arose from findings of higher than expected embrittlement in the High Flux Isotope Reactor (HFIR), at Oak Ridge, as compared with the reactor shield tank from the Shippingport Reactor. The HFIR and Shippingport reactors have different fast fluences (E > 1 MeV) but HFIR has a factor of 50 more thermal fluence. The physics of interest here is that there is thought to be a thermal damage mechanism tied up with the excitation energy required to displace iron atoms after the thermal capture of a neutron by any nearby nucleus (iron or impurity atom). This process is similar to the Szilard-Chalmers reaction.

Materials-damage interests in reactor support structures have not been of concern in the past because of their low exposure to fast neutrons. Now, there is emphasis to obtain dosimetry measurements and neutron transport calculations for the total neutron spectrum near these critical support structures. NIST is responsible for consultation and contracting for the dosimetry measurements, and for benchmarking the measurements against NIST standard neutron fields in two operating reactors. The benchmarked dosimetry will be used to make necessary adjustments to the calculations at the dosimeter locations near the support structures. Calculations will be used to extrapolate the radiation (damage) exposure into the support structures.

The two plants selected for specific-plant evaluation of support structures are the TROJAN Reactor (Oregon) and the Turkey Point Reactor (Florida). Current experimental efforts focus on the TROJAN plant where, under NIST advisement, dosimetry will be installed in the ex-vessel cavity. The purpose is to make measurements as close as possible to the cantilever-beam type support structure buried in the concrete of the biological shield. These measurements will normalize neutron transport calculations used to predict cumulative exposures at critical flaw depths in the support structure.

A contract for the dosimetry has been let with the Westinghouse Center for Science and Technology (formerly Westinghouse Research) and the irradiation (to last about 1 year) are under way.

Dosimetry Development for Test Reactors Metallurgy Irradiations. NIST has assumed a dosimetry consultants role for the new, combined Materials Engineering Associates and Oak Ridge National Laboratory run Heavy Section Steel Technology (HSST) Program at the University of Michigan Research Reactor. The current interest in this particular reactor comes about because of the near absence of available test reactors with sufficient fluence rate (5×10^{11} n/sec) to carry out HSST steel experiments. The 2-MW Reactor has room in its pool for several rather large experiments and there is interest in looking at tailored spectrum experiments where the epithermal fluence is enhanced by several orders of magnitude over the fluence greater than 1 MeV.

Energy Response of Innovative Electronic-Hardware Dosimetry. The Nuclear Effects Directorate (NED) at the Aberdeen Proving Ground has been evaluating a new personnel dosimetry system for battlefield use by the Army. Special NIST neutron-field facilities were used to establish the neutron energy sensitivity of this semiconductor device. Multiple irradiations were performed for NED in a thermal neutron beam, in the 2-keV scandium filtered beam, in the 24-keV iron filtered beam, and at the 144-kev silicon filtered beam, all at the NIST Reactor, and at several Van de Graaff beams, and finally at the NIST ^{252}Cf Fission Neutron Irradiation Facility.

^{7}LiF Gamma Dosimeter for Oconee Reactor Cavity Dosimetry. The results of a test of "LiF Chips" as gamma dosimeters in the cavity surrounding a reactor pressure were analyzed and reported. The results appear to contradict previously reported neutron sensitivity data and suggest that the dosimeter package may be better than expected as a gamma monitor for mixed gamma and neutron radiation fields. However, the ratio of gamma dose to neutron fluence was found to be too low in the Oconee reactor cavity for accurate gamma determination of gamma dose, until better neutron sensitivity data is obtained and until the possibility of fading of the color center development at temperatures in the range of 50 °C is ruled out.

PERSONNEL DOSIMETRY

R. B. Schwartz, E. Boswell, and C. M. Eisenhauer

Standard neutron fields are used to calibrate radiation protection instrumentation and to investigate and test new types of dose measuring techniques. Responsibilities in national and international dosimetry methods research focuses on tissue dose modeling, and tissue equivalent proportional counter (TEPC) measurements, and the development of written standards.

Characterization of Neutron Exposure Fields. As a result of TEPC measurements, the Armed forces Radiobiology Research Institute (AFRRI) recently obtained very surprising results in experiments which examined the relative biological efficiency (RBE) for lethality in mice exposed to reactor radiations. In brief, the experiments indicated that a slight (5%)

addition of neutron dose, into a pure gamma-ray field, decreased the lethal dose for the mice by almost 40%. The neutron and gamma-ray dose components were determined by conventional AFRRI ion chamber dosimetry and fission chamber measurements made this year; it now appears that the neutron kermas measured with ionization chambers are too low. In the most extreme case the neutron kerma inferred from both TEPC and fission chamber measurements is seven to nine times greater than that measured with ionization chambers. The larger neutron doses combined with the observed lethality of mice imply a neutron RBE fairly constant with neutron energy, as expected.

Summary of Threshold Neutron Detector Measurements at AFRRI. A summary of threshold neutron detector chamber measurements made over a period of about 6 years are complete. In addition to discussion of measurements in two of AFRRI's conventional fields, the summary documents measurements with a ^{237}Np fission chamber, which is now used as a neutron monitor in AFRRI exposure rooms.

Instrument Calibration Service. Approximately 40 neutron radiation protection instruments were calibrated this year. As usual, the majority of the calibrations were done for commercial nuclear power plants, but our customers also included institutions as diverse as Redstone Arsenal and Baylor College of Medicine.

Performance Tests of "Bubble Dosimeters." We are continuing our measurements of the properties of "bubble", or superheated drop, neutron detectors.

In collaboration with J. B. Hunt of the National Physical Laboratory (NPL), we have concluded a major study of linearity, and response as a function of neutron energy, for several of these devices. Most of the data were taken at NPL, with additional low-energy data points taken at the NIST Reactor filtered beams. The "bubble dosimeter" (supplied by Bubble Technology, Inc. (BTI), Chalk River, Canada) has high sensitivity, a good dose equivalent response as a function of energy, and is linear up to the point where the bubbles can no longer be accurately counted. "Good . . . response . . ., " in this context, means within plus-or-minus a factor of two over the four decades of neutron

energy from 2 keV to 20 MeV. The "pen" dosimeter (Apfel Enterprises, New Haven, Conn.) is easier to read than the bubble dosimeter, but has intrinsically lower sensitivity and a useful response only between ~ 150 keV and 20 MeV. The performance of the Bubble Detector Spectrometer, from BTI, was disappointing. These devices are not reliable enough to be used as intended for neutron spectrum unfolding. The results of this study are to be published in Radiation Protection Dosimetry, under the title, "Measurement of the Energy Response of Superheated Drop Neutron Detectors".

A major drawback of all devices based on nucleation of superheated drops is the rather severe dependence of sensitivity on temperature - ~ 5%/°C. We have recently completed tests of prototype temperature compensated bubble dosimeters from BTI. While the performance of the devices was a bit erratic, they generally performed satisfactorily (within ± 10%) over the range from ~ 10 °C to 30 or 35 °C. The data for one of the tubes, in terms of bubbles per millirem as a function of temperature, are plotted on figure 1. The error bars (one standard deviation) are based solely on the number of bubbles. In most cases, we had ~ 100 bubbles (~ 40 mrem, from moderated
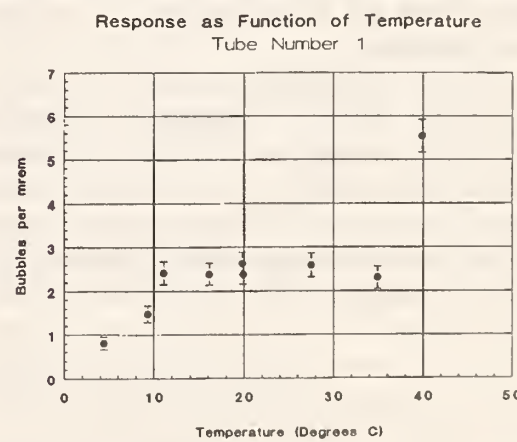
Figure 1. Response (bubbles/mrem) as a function of temperature for a temperature-compensated bubble dosimeter. The error bars (one standard division) are based on the number of bubbles.

californium), so the uncertainty is ~ 10%. (The point at 20 °C was run twice: as the initial datum point, and again near the end of the test, to check reproducibility.) This test serves as a

"proof of principle", and we will soon be testing the BTI production models.

We have also made preliminary tests of the Apfel Spectrometer. This device utilizes the fact that the threshold for nucleation is a function of pressure. It uses a single superheated drop detector, and a computer controlled system for stepping through a range of pressures, recording the count rate at each pressure, and then inverting the resultant data matrix to obtain the neutron spectrum. It is a very clever concept, but is not quite ready for prime time.

ICRU Publication on Practical Determination of Dose Equivalents. As was noted in last year's progress report, the International Commission on Radiation Units and Measurements (ICRU), in ICRU Report 39, recommended a new system for determining dose equivalents resulting from exposure to external radiation sources. These new "operational quantities" have several advantages, and our report committee is preparing the ICRU report on the practical use of these quantities; i.e., instrument design, calibration techniques, etc. Our report, entitled "Measurement of Dose Equivalents from External Photon and Electron Radiations," has been completed and submitted to the main ICRU commission for its approval. (For reasons which are totally unclear, neutron radiation has been split off and will be the subject of a separate, future, document.)

The main problem for our report committee has been the choice of a phantom for dosimeter calibration; the problem arises from the statement in ICRU 39 that ". . . a suitable phantom is the ICRU sphere.". In fact, the ICRU sphere is totally unsuitable, and much effort went into trying to determine a truly suitable phantom and calibration system which would not do violence to any of the ideas in ICRU 39. In the end, we decided to skate around that statement in ICRU 39 and recommend a simple lucite slab phantom (as is generally used anyway), together with a formulation which ties the results to the basic principles of ICRU 39. Unless this recommendation is shot down by diehards on the Commission, health physicists in the future will not have to wrestle with spherical phantoms.

ISO Document on Instrument Calibration. The (it-is-hoped) final version of ISO document CD 10647, "Procedures for Calibrating and Determining the Energy Response of Neutron Measuring Devices Used for Radiation Protection", has been submitted to the ISO secretariat, and from there gone to the member organizations (e.g., ANSI, for the US) for voting. A special meeting of the ISO working group responsible for this document is to be held at NIST during the first week in October, in order to consider the comments received as part of the voting procedure. Unless serious objections are raised by member organizations, this standard should finally be on the books

Data Acquisition System for AFRRI Dosimetry Group. NIST has provided a PC-based data acquisition system and software to replace the two HP-85 systems previously used for Ionization Chamber and Fission Chamber data acquisition by the Armed Forces Radiobiology Research Institute Dosimetry Group. The single PC system can acquire and display data from both the ionization chambers and fission chambers either together or singly. New set-up screens replace the former sequential set-up data entry so that default selections are clearly presented and easily selected or changed.

RESEARCH AND TECHNOLOGY

(all group members)

Research and technology assistance are strongly coupled in neutron dosimetry. A multiplicity of institutional involvements, drawn to the group by the availability of unique irradiation facilities and measurement capabilities, encourages a variety of attractive projects and unavoidable responsibilities.

Neutron Lifetime - Absolute Neutron Counting. The result of the first phase of the Univ. of Sussex/NIST/Geel collaboration to measure the free neutron lifetime was reported in Phys. Rev. Letters. The goal for this first phase of the project, as stated in our proposal to the DoE, was to achieve an overall uncertainty of $\pm$ 0.5% at this juncture; and the reported value of 893.6-$\pm$ 5.3s comes very close to this goal.

Two additional papers were presented documenting the work of the Central Bureau for Nuclear Measurements (Geel, Belgium), Univ. of Sussex, and NIST to make characterized deposits of B-10 and Li-6. These papers were presented at the International Nuclear Target Development Society meeting in Sante Fe (9/90) and will be published in a special issue of Nucl. Inst. Meth. in Phys. Res.

The NIST alpha-gamma coincidence apparatus has been tested with an isotopic alpha-gamma source and is ready for neutron beam runs as soon as a beam is available. This device is meant to achieve absolute neutron counting by means of the alpha-gamma coincidence method, without reference to isotopic target mass assay. Nevertheless, a continued collaboration with Geel in further refinement of B-10 deposits is planned, as well as continued collaboration with Harvard Univ. and Los Alamos National Laboratory in calorimetric neutron counting.

Benchmark Measurements for Criticality Counting. Two series of careful measurements of neutron leakage from a water-moderated Cf-252 source have been completed and compared with rigorous Monte Carlo calculations performed by the Computational Methods Development Group at Los Alamos Scientific Laboratory. The first results from this program were for the case of a 4-in diam sphere of water. For this case very detailed calculations by the Monte Carlo Neutron Photon (MCNP) code required about 50 h of supercomputer time. The comparisons of measured and calculated fission rates outside the sphere showed some interesting discrepancies. The thermalization was overpredicted in the calculations relative to the measurements. A number of auxiliary tests for unexpected absorption of thermal neutrons in the water, steel spherical shell, or fission chamber components failed to reveal any contamination that could explain the discrepancies. These

results will be reported in the American Nuclear Society Transactions, Winter, 1990. A second series of measurements with a 3-in diam sphere appear to show the same discrepancy in thermalization. The discrepancies for U-235 and Pu-239 fission rates are of the order of 4% to 7%, well beyond the combination of the overall uncertainty of the experiment and the statistical error of the calculation. However, the known errors in the cross section data and the thermalization model employed may be sufficient to explain the discrepancies. A complete uncertainty analysis is not yet available for the calculation, including the uncertainties of the cross sections and the $S(\alpha,\beta)$ thermalization model.

Neutron Fluence Rate Measurements at CNRF Guide Positions. Several measurements of both fast and thermal neutron fluence rates were made at various positions on cold neutron guide NG6. All of these measurements were made at a time when the cold source was not operational and filled with warm helium gas rather than heavy water ice.

On April 8, 1990, when NG-6 had been built only a few feet beyond the wall of the reactor building, a series of thermal and fast fluence rate measurements were made at the end of the guide as it stood at that date. These measurements were made at reactor power levels of 20 kW, 50 kW, 200 kW, 500 kW, and 1 MW. Since the average thermal neutron speed was not known, the thermal neutron results were reported as if the neutron speed were 2200 m/s. The fluence rate derived in this way is also known as the "capture flux." The energy spectrum of the fast neutrons was also unknown, and the fast neutron data was interpreted as if the fast spectrum were an unmoderated fission spectrum from the thermal neutron fission of U-235. The fluence rate determined in this way is termed the "fission-equivalent fluence rate." The guide was evacuated during these measurements.

On May 8, 1990, with the guide built to full length, the fast and thermal fluence rate measurements were repeated at 1 MW at the end of the guide. The guide was filled with helium, but somewhat contaminated with air during these measurements.

On May 17, 1990, the thermal fluence rate measurements were made once more with the guide filled with pure helium. These measurements were made at two positions: at the end of the guide, and inside the guide at an access point about 3 meters outside the reactor building wall.

Collaboration With U.S. Naval Academy. Monte Carlo calculations with the MCNP code have been used at NIST to determine the neutron spectrum from a 14-MeV neutron generator at the U.S. Naval Academy (USNA). Comparisons of dose equivalent with similar calculations by USNA showed a significant (40%) discrepancy. Further investigations revealed that the MCNP code at USNA did not duplicate sample problems distributed with the computer code package. It is not clear whether the discrepant values are due to the particular version of the code used at USNA or due to adaptation to their computer.

Collaboration With Institut de Protection et de Surete Nucleaire (IPSN). Because of our experience in calculations of anisotropic emission from small neutron sources NIST was asked to make calculations for a source used by IPSN. We checked their calculations of neutron spectra from a 14-MeV neutron source moderated by iron, uranium-238, and heavy water. This collaboration arose out of participation on ISO committee TC85, subcommittee 2, "Radiation Protection."

Neutron Penetration in Slabs of Finite Extent. Monte Carlo calculations of neutron transmission through slabs have been performed to help the U.S. Navy estimate shielding of personnel on submarines carrying nuclear missiles. These calculations demonstrate that neutron and gamma-ray penetration is insensitive to the position of a slab between a localized (point) source and detector. Furthermore, an angular parameter can be specified such that the relative contribution of neutrons or photons within that angle is also insensitive to the slab position. This is equivalent to quantifying the increase in scattered particles as one moves from a narrow-beam to a broad-beam configuration. A paper on the subject has been accepted for publication in Nuclear Science and Engineering. An oral paper has also been accepted for delivery at the Winter Meeting of the American Nuclear Society.

Radiation Shielding Calculations for the NIST Cold Neutron Facility (CNRF). Calculations of the necessary shielding for two shutters at the CNRF and for shielding around neutron guides were made. The latter calculations approximated the neutrons scattered from the walls of a guide as a line source. All calculations predicted dose equivalent rates which were conservative as determined by measurements with shielding in place.

Staff Member Elected to NCRP. C. Eisenhauer was elected to the National Commission on Radiation Protection and Units.

IRRADIATION AND CALIBRATION FACILITIES

J. A. Grundl, E. D. McGarry, E. Boswell, and D. M. Gilliam

Well-characterized neutron fields built and maintained as permanent irradiation facilities, provide certified fluences of pure fission neutrons, sub-MeV distributions, monoenergetic keV beams, and thermal neutrons. Passive and active detectors are exposed in these neutron fields for response calibrations, for cross section measurements, and for the investigation of new measurement techniques. A multi-purpose fission rate measurement capability is centered around the NIST "go anywhere" double fission chambers and the NIST set of fissionable isotope mass standards (FIMS). The Manganous Sulfate Bath is the primary neutron source strength calibration facility for the United States. Absolute neutron fluences for all fission-neutron-driven standard neutron fields at NIST are derived from source strength calibrations at this facility.

Neutron Source Strength Calibrations in FY-90. Fifteen neutron source-strength calibrations were accomplished this year by the $MnSO_4$ Bath

Facility. Eight of the calibrations were accomplished under Standards Publications (SP-250) contracts for the customers identified in Table 1. The remaining calibrations were for in-house neutron sources used with the Cf-252 Fission-Neutron Standard Field and the D$_2$O-moderated (and bare) Cf-252 source-range calibration of personnel monitoring equipment.

There was an on-site refurbishment of the manipulator arm by Sergeant Industries. This included some hands-on maintenance training of NIST personnel.

New Reference Neutron Field to Support NIST/NRC Dosimetry Contract Work. To supplement calibration and benchmarking

irradiations carried out in NIST standard fission spectrum facilities, there is a need for a higher fluence rate and larger volume irradiation facility to accept dosimeters in steel capsules. The University of Michigan Reactor has expressed an interest in cooperative research to develop such a facility in the water experimental area at their reactor.

Fission Neutron Irradiations Operations. The storage cave for radioactive sources, and standard neutron field assembly pieces is essentially complete. The extensive heavy-work required to build this facility was carried out entirely with staff personnel.

Table 1. Customers for FY90 neutron source emission rate calibrations

Laboratory/Company	No. of Sources	Type of Source
Oak Ridge National Laboratory	2	Cf-252
Battelle Pacific Northwest Laboratory	1	Cf-252
Sandia Laboratory	2	Pu-238 Be
NAVALEX Laboratory	1	Pu-239 Be
Naval Research Laboratory	1	Am-Be
Brookhaven National Laboratory	1	Cf-252

NUCLEAR METHODS GROUP: OVERVIEW

R. R. Greenberg (Center for Analytical Chemistry)

The development and application of nuclear analytical techniques for greater accuracy, higher sensitivity, and better selectivity are the goals of the Nuclear Methods Group. A high level of competence has been developed in both instrumental and radiochemical neutron activation analysis (INAA and RNAA). In addition, the group has the capability of using neutron beams as analytical probes for both prompt gamma activation analysis (PGAA) and neutron depth profiling (NDP). NDP determines concentrations of several important elements (isotopes) versus depth profiles within the first few micrometers of a surface by energy analysis of the prompt charged-particles emitted during neutron bombardment. PGAA, on the other hand, measures the total amount of an analyte present throughout a sample by the analysis of the prompt gamma-rays emitted during neutron capture. These techniques (INAA, RNAA, PGAA, and NDP) provide a powerful combination of complementary tools to address a wide variety of analytical problems of great importance in science and technology.

The use of a variety of nuclear methods has continued to contribute to the Standard Reference Material (SRM) certification effort; this year's efforts include multielement determinations performed on a number of SRMs including: Total Diet, Frozen Mussel Tissue, Apple Leaves, Peach Leaves, Bone Ash, Bone Meal, Water, Boron in Silicon, two Wear Metals in Oils, and three Soils. Group members are serving as Technical Champions for several of these new SRMs, and as such are responsible for scientific decisions made throughout the production and certification processes of these materials. RNAA measurements are currently under way to determine Hg in Bovine Serum. This will allow the certification of an additional, highly-important element in this existing SRM. In collaboration with members from other groups in the Inorganic Analytical Research Division, a dissolution study of the two new leaf materials has been completed which identifies problems potentially leading to analytical errors during the certification analyses. In addition, a study to determine the feasibility of preparing a dietary slurry SRM, instead of the traditional type of dried material, is under investigation. Members of the Nuclear Methods Group have also collaborated with researchers from the Microanalysis Group (553) in developing a boron depth-profiling SRM.

Recent applications of NAA in the life sciences by the group include nonclassical detection and determination of tags associated with biological macromolecules such as proteins, enzymes, and antibodies. In one application, an activatable tag has been attached to an antibody used in a medical diagnostic test. The INAA determination of the activatable tag is then used as the detection step of the diagnostic analysis. Research is continuing on the polyacrylamide gel electrophoresis neutron activation analysis technique (PAGE-NAA). The activation and subsequent determination of phosphorus in phosphoproteins has already been demonstrated, and research in this area was included as part of the Ph.D. requirements for one group member who has received her doctorate this past year. Research to extend this technique to the determination of other elements in specific macromolecules is under way. Such advanced uses of NAA in the life sciences may open a wide variety of applications for nuclear analytical chemistry.

The Biomonitoring Specimen Bank Research Project has continued its research support for other agencies' monitoring programs. These programs include the EPA human liver project, the NOAA National Status and Trends (NS&T) program, the NCI Micronutrient program, the IAEA/NIST/FDA/USDA Total Diet Study, the NOAA Alaska Marine Mammal Project, and the National Marine Mammal Tissue Bank. Research has centered on specimen banking protocols and improved analytical methodology. The group's participation in intercalibration exercises with the project participants and the development of QA materials for various marine analyses has helped to enhance the quality of the analytical results used in the assessment of the environmental health of the nation. Of major

importance this year has been the analysis of samples from the Alaska Marine Mammal Project. Both essential and pollutant elements have been studied to assess the effects of anthropogenic inputs to the environment.

The joint NIST/FDA/USDA study of trace elements in human diet, sponsored by the International Atomic Energy Agency, has completed its sixth year. A total of 200 diets from different countries have been analyzed to date for minor and trace elements. Ten diets from different regions of the United States have also been collected, and thus far, seven have been analyzed. The data obtained from the U.S. diet composites have confirmed daily intake results for some of the elements investigated by the FDA (based on individual food analysis), as well as established reliable daily dietary intakes for additional elements including B, Cr, Cs, Li, and Sn. In the case of Li, the observed intake values are considerably lower than earlier published results.

The collaboration with Brian Clarke of McMaster University on neutron activation-mass spectrometry has continued to provide valuable information on ultratrace levels of boron and lithium. A wide variety of materials was investigated this past year, and results were obtained for boron and lithium concentrations in several different protein components in blood, various individual foods, and a number of geological reference materials.

The group has taken an active role in the NIST program on high-temperature superconductivity research, both in the measurement of impurities in starting materials and final products, and in determination of the stoichiometry of metallic constituents. The effort this year has centered on the development of accurate, rapid measurements of these materials by both NAA and PGAA. An effort to establish an accurate, monitor activation analysis technique for further study of high-temperature superconductors at NIST is under way.

Nearly a decade ago, a systematic error for PGAA was observed in which elemental sensitivities (counts/μg-s) increased with increasing hydrogen concentration. Sensitivities in hydrogenous samples have been observed to increase by up to approximately 25% relative to samples with little H. Until now, this error has been handled by matching H concentrations in samples and standards without fundamental understanding of the problem. Substantial progress has recently been made in understanding the causes of this sensitivity enhancement, and in developing a method of analysis in which these effects are eliminated. Theoretical and experimental studies have shown that the elemental sensitivities in PGAA depend upon the scattering density (or hydrogen concentration), as well as the sample shape. Monte Carlo calculations have demonstrated that scattering can increase or decrease the neutron path length within the sample and thus may change the probability of neutron absorption. Thus the analytical signal is a function of the sample scattering density, the physical dimensions of the sample, and the sample orientation with respect to the beam. Theoretical studies have demonstrated that for spherical samples, neutron scattering only serves to mitigate the effects of neutron self shielding, and produces no additional enhancement. Experimental studies have shown that elemental sensitivities for disk-shaped samples with constant hydrogen concentration and constant diameter (12.7 mm) vary with thickness over the range of 2-12 mm. However, elemental sensitivities remain constant when spherical samples of the same materials (diameters 2-12 mm) are used.

Research on the recoil-nucleus time-of-flight NDP technique has focused on the problem of detecting (with good energy resolution) the low energy heavy nuclei which are emitted along with the light nuclei used in conventional NDP. These heavy nuclei can be used to provide very high resolution depth profiling capabilities in the sample region very close to the surface. Initial measurements appear to have validated this approach, and efforts are under way to determine how closely the actual depth resolution measured approaches the calculated values. This work is a continuing collaboration with Emile Schweikert at the Chemistry Department of Texas A & M University.

During the past year, a large part of the group's efforts has been directed at the exploitation of the analytical applications of cold neutrons. These efforts are needed to take full advantage of the guided cold neutron beams soon to be available at the new Cold Neutron Research Facility (CNRF). The group's involve-

ment includes the design and construction of state-of-the-art instruments for both PGAA and NDP using cold neutrons. The group's efforts have been aided substantially by the ability to use an existing cold neutron beam at the KFA Jülich facility. A new chamber for the cold neutron depth profiling (CNDP) instrument has been installed at the NIST Cold Tube West (CTW) location, and the new facility will be the closest instrument to the reactor cold source. The 60-cm diam chamber has ultra-high vacuum capability, and has been designed to be adaptable to many different types of experiments. The final configuration will allow remote scanning of 15 x 15 cm samples, and will also allow rotation of both sample and detector angles relative to the beam.

The cold neutron prompt gamma activation analysis (CNPGAA) instrument is currently under construction and will be ready for measurements this fall. Over the past year, several new mechanically-strong, radiation-stable, synthetic glasses containing Li-6 have been developed to efficiently absorb neutrons with minimal gamma-ray emission. These glasses will be used in the beam shutter and in the sample chamber. The conceptual design of the beam line is now complete, and it will include a cold beryllium/bismuth filter to make this the finest facility in the world for PGAA. In addition to greatly enhancing the sensitivities for all elements compared to existing thermal neutron PGAA instruments, collaborative measurements with Jülich have indicated that the cold neutron facility should allow the determination of a few micrograms of hydrogen in a wide variety of materials.

A novel technique of PGAA analysis of gas samples has been developed using both the currently available thermal neutron beam at the NBSR and the ELLA cold neutron facility at KFA, Jülich. Feasibility studies involving noble gases and gas mixtures indicate that sensitivities in the sub-ppm range for a number of elements should be achievable using the new NIST cold source PGAA instrument which will be operational later this year. The development of a nuclear technique for gas analysis will establish an independent analytical method for reference material certification.

A long-range program to explore and develop the analytical applications of focused beams of cold neutrons has been initiated within the group. The ultimate goal of this research is to produce beams of neutrons which have intensities several orders of magnitude greater than previously available. Such beams will greatly enhance the capabilities of both PGAA and NDP, and may ultimately lead to a neutron probe for microanalysis. The neutron microguide appears to be the most promising approach to achieve analytically useful focused neutrons. As a first approach, a device will be developed and tested using a stack of ultrathin, nickel-coated single-crystal silicon wafers as focusing elements. The silicon wafers act as the transmission medium for the neutrons, which reflect from the 1000 Å nickel surface coatings. The superposition of the individual outputs becomes the focal point. One hundred of these wafers have been obtained for tests of this first focusing element. Ultimately, this focusing element will be combined with a real-time, high-resolution neutron imaging detector to measure the neutron distribution and intensity. On the theoretical side of this project, the acceptance diagram technique has been adapted for both curved neutron guides and focusing elements, and this technique can be used for predicting the number of reflections within these neutron optical devices.

The strong interaction with industrial scientists using NDP, PGAA, and NAA has continued during the year with a growing number of guest workers, research associates, and joint publications. In collaboration with researchers at Eastman Kodak, NDP has been used to identify unambiguously, and to quantify the surface boron on "as received" single crystal silicon wafers. NDP requires no special sample preparation prior to analysis, in contrast to commonly used analytical techniques. By carefully controlling a variety of sample processing procedures prior to NDP analysis, the source of boron has been identified as ambient atmospheric boron compounds which react with the exposed surface of the silicon wafer and become incorporated into the native oxide layer.

The Nuclear Methods Group is also collaborating with scientists from the NIST Center for

Atomic Molecular and Optical Physics, the NIST Center for Radiation Research, and the University of Sussex in a new measurement of the neutron lifetime. The technique used involves detecting the protons which decay in a neutron beam passing through a superconducting-magnet proton trap. A measurement of the neutron lifetime has been made with a cold neutron beam at the Institut Laue-Langevin in Grenoble, France. A value of 893.6 ± 5.3 s was determined, and this has been reported in a paper in Physical Review Letters. Additional measurements will be made at the new NIST CNRF later this year.

During the coming year the group will continue to improve the accuracy, sensitivity and productivity of nuclear methods as applied to elemental measurements. Problems to be addressed include those inherent in sample preparation, irradiation, radiochemical separation, counting, and data reduction, with the goal of minimizing and quantifying various sources of random and systematic errors in analysis by nuclear methods. Maintaining full accuracy at high count rates using current generation data acquisition electronics is the goal of our count rate dependent studies. Accurate quantification of gamma-ray self-absorption and measurement of the shape of the efficiency curve are required for accuracy in monitor activation analysis (since matching of sample with primary standards is not done). The development of monitor activation analysis is part of the high-temperature superconductivity effort to achieve rapid sample turnaround with minimum sacrifice of accuracy; however, the approach also provides good quality control when used in parallel with tradiational primary standard NAA.

Robert R. Greenberg, Group Leader; Donald A. Becker, Maryanne S. Cassedy, M. James Blackman, Rabia Demiralp, R. Gregory Downing, Kathleen A. Fitzpatrick, Ronald F. Fleming, Karen Gilliland-Garrity, Brent L. Grazman, G. Venkatesh Iyengar, George P. Lamaze, John K. Langland, Richard M. Lindstrom, Elizabeth Mackey, David F. R. Mildner, J. Emlen Myers, Bruce R. Norman, Craig A. Stone, Susan F. Stone, Dana K. Weiss, and Rolf Zeisler.

DISSOLUTION PROBLEMS WITH BOTANICAL REFERENCE MATERIALS

R. R. Greenberg, H. M. Kingston, R. L. Watters, Jr., and K. W. Pratt
(Inorganic Analytical Research Division)

For many analytical techniques, the first step in analyzing solid samples is chemical dissolution or fusion. Losses in this stage of the analysis will affect the accuracy of the final results obtained. There are a number of possible loss mechanisms during sample decomposition including gaseous evolution, absorption or adsorption onto surfaces, precipitation and persistence of undissolved material. It is well known that botanical materials may contain various soil and/or mineral fractions, and thus may be difficult to dissolve [1-4]. Consequently, prior to analyzing the candidate Apple and Peach Leaves SRMs (SRMs 1515 and 1547) for certification, a dissolution study was undertaken to ensure that all elements of interest could be solubilized by the dissolution techniques intended to be used as part of the complete analytical procedure. The method chosen to study such losses involved irradiating the samples, performing the decomposition, filtering the clear solutions, and finally measuring residual radioactivity in the vessels and on the filters. Both botanical SRMs were irradiated in the NIST Research Reactor to form radioactive nuclides of a number of different elements. The irradiated samples were then decomposed using a variety of procedures. The sample decompositions were performed by four different chemists from NIST to minimize individual bias and to study the effects of minor differences in the dissolution procedures. The dissolution procedures produced clear solutions, which were then passed through filters to separate any residual particulate matter. The filters, solutions, and vessels used for decomposition, as

well as neutron-irradiated samples of unprocessed material, were then subjected to gamma-ray spectrometry to determine the fraction of each element remaining in undissolved, precipitated, or absorbed forms.

Various sample decomposition methods were investigated including: open-vessel dissolution with nitric, perchloric, and hydrofluoric acids, using several different types of dissolution vessels and procedures; closed-vessel microwave dissolution with nitric and hydrofluoric acids; closed-vessel microwave digestion with nitric and hydrofluoric acids followed by open-vessel dissolution with perchloric acid, and lithium metaborate fusion in platinum crucibles. It was originally expected that most, if not all, of the sample decomposition methods investigated would produce final solutions with negligible fractions of insoluble materials. In addition, it was believed that losses of metals to the walls of the Teflon and platinum vessels would be very small. The results of these studies, however, did not support these expectations.

Large fractions of some elements were observed on undissolved particles after some of the dissolutions, despite the fact that all solutions appeared clear prior to filtration. The microwave-only dissolutions produced very large fractions (i.e., 10% of the total amount present) of particulate Cr, Fe, Hf, Sc, and rare earths. Much of this material was probably a mixture of undissolved material and rare-earth fluorides that precipitated during the dissolution. Smaller amounts of most of these elements, with the exception of Cr, were observed on particulate material when perchloric acid was used after the initial decomposition with nitric and hydrofluoric acids. However, still significant amounts (i.e., percent level) of some elements were observed. In addition, sample-to-sample differences in the amount of material remaining on particles were observed, apparently due to minor differences in actual dissolution procedure followed. Two samples of the Peach Leaves, which were subjected to essentially the same dissolution procedure, contained very different (insoluble) fractions of some elements. It was noted during this study that one of these samples was processed on a slightly cooler area of the hot plate, and that the precipitated perchlorate salts were yellow at the end of dissolution instead of

white (as was observed for the other sample) indicating the presence of some residual organic material. Since the oxidizing power of perchloric acid is highly dependent on temperature, small differences in experimental conditions appear to have important effects on the amount of insoluble residue.

No acid dissolution procedure studied was adequate for Cr. The procedure that produced the smallest amounts of particulate Cr involved an extended reflux in $HClO_4$. Although this study was not designed to accurately determine losses due to volatility, a comparison of the combined amount of Cr remaining in the solution and on the filter for each material, with the amount present in the corresponding unprocessed material, indicated that approximately 60% of the Cr in both the Apple and Peach Leaves was volatilized during this dissolution. Significant fractions of Hf were also present in particulate form after all the acid dissolutions investigated, apparently indicating the presence of some Hf-containing mineral fraction or fractions, which were unaffected by the acid treatment.

Significant fractions of five elements (Au, Cr, Hf, Sb and Sc) remained in some of the Teflon dissolution vessels after the dissolved solutions were transferred and the vessels were washed (four times). Since bulk TFE Teflon is formed by pressing together small particles of material, it was expected that this type of Teflon would trap more material than the other two types of Teflon. Surprisingly, the FEP Teflon seemed to retain greater amounts of the four elements determined than did the PFA or TFE Teflons. Up to 6% of the Cr was found in the FEP vessels compared to ≤ 0.5% of the Cr in the other types of Teflon.

Very large fractions (i.e., 20%-60%) of the Co, Fe, Cu, Zn, As, and Sb present in the Leaves remained in the Pt crucibles used for the $LiBO_2$ fusions. These results, along with the amount remaining on undissolved particles, are listed in table 1. Although insoluble forms of Cr were small, and only 1-3% of the Cr was lost to the platinum crucibles, up to 30% was lost from the Apple Leaves by volatility.

The results of this study indicate the importance of fully testing sample decomposition methods to be used in the certification process of reference materials. No two analytical tech-

niques can truly be considered independent unless the possibility of common dissolution losses can be eliminated. It is possible that some analytical methods like Inductively Coupled Plasma spectrometry may effectively recover analytical signal from small particles suspended in sample solutions. However, accurate results can only be obtained if these particles do not stick to the walls of the containers used to store the samples during the period between dissolution and analysis, and if the particles are uniformly suspended at the time of sample introduction into the analytical instrument. This study further points to the value of using a nondestructive method of analysis as one of the analytical techniques used in the certification process of this type of botanical reference material.

Table 1. Percent loss from Apple and Peach Leaves during lithium metaborate fusion in platinum crucibles

	Peach Leaves		Apple Leaves	
	Crucible	Filter	Crucible	Filter
Br	3	0.05	4	1.8
Co	36	0.4	50	0.1
Cr	3	0.7*	~1	<0.1**
Fe	34	<0.09	49	0.05
Cu	29	<1	36	<1
Zn	21	0.03	18	<0.02
As	35	<1	27	<1
Sb	~40	<1	~60	<2

* Cr volatility losses ≤10%
** Cr volatility losses ~30%

References

[1] K. Heydo, Damsgaard and B. Rietz, Anal. Chem. 52, 1045-9 (1980).

[2] M. Ihnat, Comm. in Soil Sci. Plant Anal. 13, 11, 969-79 (1982).

[3] A. R. Byrne and L. Bendik, Talanta. 35, 161-6 (1985).

[4] National Bureau of Standards (U.S.), Certificates of Analysis, Standard Reference Materials 1570, 1571, 1572, 1573, 1575 (Spinach, Orchard Leaves, Citrus Leaves, Tomato Leaves, and Pine Needles).

MEASUREMENT OF BORON AT SILICON WAFER SURFACES BY NEUTRON DEPTH PROFILING

J. P. Lavine, T. Z. Hossain, J. B. Russell, and G. P. Zenner
(Eastman Kodak Company, Rochester, NY)
and
R. G. Downing and G. P. Lamaze (Inorganic Analytical Research Division)

Low levels of boron have been detected at the surface of high purity single crystal silicon wafers using spreading resistance [1] or by secondary-ion mass spectroscopy (SIMS) [2-6]. The presence of boron is observed after a vacuum anneal [1], after various types of wafer cleaning procedures [2,3] and after silicon molecular beam epitaxy [4]. A high temperature processing step is used to diffuse the boron into the silicon prior to analysis. Slusser and MacDowell [2] have deposited a polysilicon layer to permit the use of SIMS without a high temperature drive. However, even this introduces an additional processing step that may complicate the isolation of the true source of a surface contaminant such as boron. Neutron depth profiling (NDP) with the nuclear reaction $n + {}^{10}B \rightarrow {}^4He + {}^7Li$ provides a direct quantitative method to investigate the presence of boron at the surface of a silicon wafer without intermediate processing. Using NDP, measurements were performed on as-received Si wafers, on wafers with an oxide, on a polysilicon layer, and on an epitaxial silicon layer. The results indicate that a prime source of boron contamination is air, providing direct support for

the suggestions of Iyer, Delage, and Scilla [4] and of Kubiak et al. [5] that some boron contamination occurs upon air exposure of the wafers. Also these measurements support Casel et al. [6] experimental results that indicate air is a source of boron contamination.

Figure 1 displays the total front surface boron for 100-mm diam n-type Czochralski Si wafers from three different vendors. The wafers were removed from the plastic sealed as-received boxes at the time of measurement for vendors B and C. The wafer box from vendor A had been opened earlier. The measured ^{10}B concentration is converted to a total boron surface dose by assuming normal isotopic abundance. The highest boron concentration is seen for vendor C. The unpolished back surface of this wafer has nearly the same concentration of boron as the front side. The vendor-to-vendor variation seen from the figure indicates that wafer processing is probably responsible for some portion of the observed boron. Recent work supports this suggestion [6].
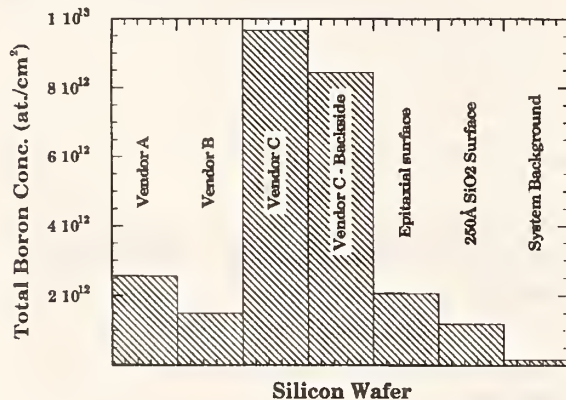
Figure 1. Total boron determinations by NDP for five-silicon wafers and nominal system background.

Boron was also found on the surface of a wafer which had been covered with a silicon epitaxial layer. The substrate underwent intrinsic getting before the deposition of a 10-μm arsenic-doped silicon layer. Figure 1 shows that the total surface boron is similar to that of the wafers from vendors A and B. Boron was also measured on the surface of and throughout a 250-Å oxide layer, grown during an intrinsic gathering procedure. As indicated in the figure the least amount of boron appears on this wafer.

NDP measurements indicate that boron appears at the surfaces of all wafers when the surface has been exposed to the atmosphere. While there is usually a low level of boron distributed throughout a silicon wafer, ordinary heat treatments cannot produce ~ 10^{12} atoms/cm^2 by up diffusion from the bulk of the wafer. Even if all the boron in an n-type wafer diffused to the surface during the heat treatments, only 2.5×10^{11} atoms/cm^2 would be at each surface for a bulk boron concentration of 1 $\times 10^{13}$ atoms/cm^3. The measured boron levels exceed this by about an order of magnitude. Thus, the simplest explanation is that there is a common external source for the observed boron.

Exposure to air is common to all the samples and thus can explain the surface peaks. The amount of surface boron is not correlated to the duration of exposure to air. Perhaps the native oxide that forms on silicon provides a limited number of sites for incorporation of boron atoms. Casel et al. [6] showed that the presence of the natives oxide is essential for boron to be found in the quantities seen by the NDP measurements of the native SiO$_2$ layer on the surface of the wafer. Since the formation of borated glass is well known, it is quite possible that a companion chemical reaction produces oxides of boron. This hypothesis is supported by the presence of boron in the air as both a gas phase and as an aerosol [7]. Gas-phase boron has a nominal concentration of 10-100 ng/m^3, and is probably in the chemical form B(OH)$_3$.

In summary, NDP was used to show the existence of surface boron contamination of processed silicon wafers. It is suggested that boron adsorbs or chemisorbs from air onto the wafer surface and likely is incorporated into the native oxide. As suggested by the data in the figure, the wafer preparation processes may also deposit boron during chemical or mechanical cleaning and polishing. However, the surface boron seen after polysilicon or epitaxial silicon deposition requires another boron source--the air itself. The present direct measurements of boron with thermal neutrons do not require heat treatment for sample preparation. Thus unequivocal support is provided for the earlier suggestion of Iyer, Delage, and Scilla [4] and Kubiak et al. [5] that the atmosphere is the source of some of the observed boron surface contamination of silicon surfaces.

We thank Dr. Gilbert Declerck, Interuniversitair Micro-Elektronica Centrum, Leuven, Belgium; Dr. David L. Anderson, the United States Food and Drug Administration; and Dr. Richard S. Hockett, Charles Evans and Associates for helpful discussions.

References

[1] M. Lieher, M. Reiner, R. A. Wachnik, and G. S. Scilla, J. Appl. Phys. 61, 4619,(1987).

[2] G. J. Slusser, and L. MacDowell, J. Vac. Sci. Technol. A5, 1649 (1987).

[3] H. T. Yang and P. M. Mooney, J. Appl. Phys. 58, 1854 (1985).

[4] S. S. Iyer, S. L. Delange, and G. Scilla, J. Appl. Phys. Lett. 52, 486 (1988).

[5] R. A. A. Kubiak, W. Y. Leong, M. G. Dowsett, D. S. McPhail, R. Houghton, and E. H. Parker, Cl J. Vac. Sci. Technol. A4, 1905 (1986).

[6] A. Casel, E. Kasper, H. Kibbel, and E. L. Sasse, J. Vac. Sci. Technol. B5, 1650 (1987).

[7] M. E. Kitto, Ph.D. dissertation, University of Maryland, 1987.

SOL PARTICLE IMMUNOASSAYS USING COLLOIDAL GOLD AND NEUTRON ACTIVATION

R. Zeisler and S. F. Stone (Inorganic Research Division)
R. P. Viscidi (Johns Hopkins University School of Medicine, Baltimore, MD)
and
E. H. Cerny (Fondation pour la Recherche Medicale, Geneva, Switzerland)

We are developing an ultrasensitive immunoassay using colloidal gold and neutron activation. The method is described in detail elsewhere [1] and is briefly summarized here. Individual wells of microtiter strips were coated with the specific samples to be measured, and the antibody reagent labeled with colloidal gold added and allowed to incubate. The excess unbound antigen was washed off and the gold labeled conjugate bound to the adsorbed analyte was measured via NAA. Samples for irradiation consisted of the individual wells of the microtiter strips containing the gold labeled reagent bound to the analyte and appropriate standards. Reactor irradiations were conducted in the NBSR pneumatic tube facilities at fluence rates of 2.0 and $7.7 \times 10^{17} n \times m^{-2} \times s^{-1}$ and length of irradiation ranged from 10 to 20 minutes per sample set (approximately 24 wells). Gamma counting utilized a sample changer with a germanium detector of about 4% absolute detector efficiency for the 411-keV line. The counting times per sample were between 300 to 1800 seconds. A comparison of the measured gamma activities of the ^{198}Au 411-keV peak from the standards and the samples was used to calculate the amounts of gold in the samples.

The initial studies were aimed at determining the sensitivity of immunoassays using colloidal gold labeled antibodies and neutron activation for detection of solid phase human immunoglobulin (IgG). Quadruplicate sample wells were prepared from logarithmic dilutions of purified human IgG. Sample wells containing bovine serum albumin (BSA) and uncoated wells served as controls to determine the gold blank due to the unspecific binding of the gold labeled antibodies and gold in the reagents and microtiter wells. Assays were performed with two concentrations of gold labeled antihuman IgG(1 μg/mL or 0.2 μg/mL) and with a 0.2-μg/mL antihuman IgG horseradish peroxidase conjugate.

The results from the gold labeled and enzyme labeled antibodies are compared in figure 1 for the 0.2-μg/mL antigen concentrations. Figure 1a depicts the amounts of gold determined in each well with its associated uncertainty due to the counting statistics. The line in figure 1a represents the mean value at each dilution point. The mean blank concentration (0.29 ± 0.12 ng) calculated from wells with

BSA was subtracted from the individual values. Similar results were obtained in assays with 1 µg/mL gold labeled antihuman IgG, although the amount of gold found ranges from 1.2 to 140 ng. The lowest concentration was again similar to the blank in this particular assay (0.8 ± 0.4 ng). Figure 1b depicts the optical density plotted with its uncertainty from three absorbance measurements. The sensitivities from each of the assays show similar linear ranges of between 0.001- and 0.033-µg/mL IgG. However, the relative change (between blank and saturation) in response to each dilution step is greater for the neutron activation assay than for the enzyme assay. Also, in the enzyme assay, the signal for the 0.0033-µg/mL dilution is not significantly different from the upper limit of the blank, while in the neutron activation assay, the signal remains discernible from the blank until the 0.00033 µg/mL dilution. These results demonstrate that an immunoassay for IgG using neutron activation of colloidal gold labeled antibody is at least comparable in performance, if not superior, to a conventional enzyme immunoassay.

This colloidal gold label and its detection is obviously adaptable to a number of standard immunoassay procedures that use absorbance measurements of conjugates or radioactive labels. The irradiation and measurement conditions in the preliminary studies were chosen to make the assay applicable to clinical investigations and could be modified to lower detection limits. Gamma counting in connection with a sample changer and well detector or autoradiography would provide the capability for high throughput. The method currently allows detection of 10^{-16} mol of analyte in routine operation with possible extension to 10^{-20} mol. For research applications, it would be desirable to approach the latter limit of detection. Currently, the limits caused either by the blank gold contained in substrates and reagents or by nonspecific binding of gold labeled reagent to the solid phase can certainly be reduced with technical improvements in the procedure.

1a)

1b)
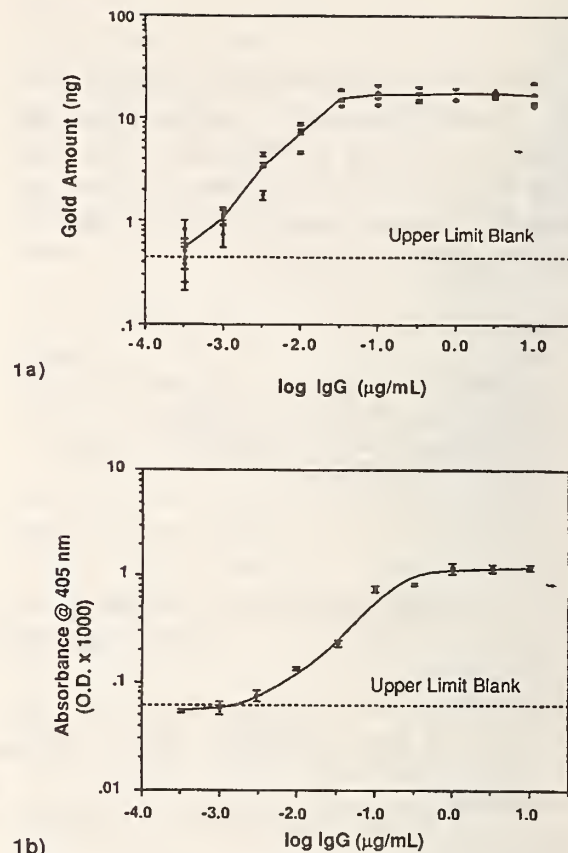
Figure 1. Immunoassay of human IgG. a) Assay with gold labeled antihuman IgG and subsequent NAA determination of gold. Plot depicts individual values of four replicates and their analytical uncertainty corrected for blank contribution. The solid line is a fit to the respective mean values. b) Assay with antihuman IgG horseradish peroxidase conjugate. The optical density (@ 405 nm) is plotted with its uncertainty from three measurements.

Reference

[1] R. Zeisler, S. F. Stone, R. P. Viscidi, E. H. Cerny, Clin. Chim. Acta (submitted for publication).

CHARACTERIZATION OF THE MINERAL FRACTION IN BOTANICAL REFERENCE MATERIALS AND ITS INFLUENCE ON HOMOGENEITY AND ANALYTICAL RESULTS

R. M. Lindstrom, D. A. Becker, and K. M. Garrity (Center for Analytical Chemistry)
and
A. R. Byrne and B. Smodis (Institut "Jozef Stefan," Ljubljana, Yugoslavia)

NIST has produced a series of natural-product leaf Standard Reference Materials (SRMs) which have proven valuable in developing and validating methods of analysis. Since these materials are prepared from field- grown leaves, some mineral matter (herein called grit) is generally present. The presence of this grit leads to two consequences that must be taken into account in the use of these materials. First, some trace constituents are present in a phase that may not be solubilized by the method used to decompose the bulk cellulose matrix. Incomplete dissolution may lead to error in any analytical method which requires the sample to be in solution. A second analytical consequence of the presence of a minor phase occurs when a trace constituent is present mostly in a small number of high-concentration grains. The statistics of sampling may lead to heterogeneity which cannot be resolved by any analytical method. Both of these effects have been reported in the literature to be observable in leaf SRMs.

To verify that these experimental difficulties are indeed related to the presence of a mineral phase, we performed heavy-liquid separations in carbon tetrachloride on all the available NIST leaf SRMs to concentrate the coarser, heavier particles from the material. The resulting grit was weighed, examined both optically and with an electron microscope, and analyzed by neutron activation. The weight fraction of grit from each of seven botanical SRMs is given in table 1.

Two new SRMs (to be issued in 1990), SRM 1515 Apple Leaves and SRM 1547 Peach Leaves, have been prepared with a jet mill which directs two high-velocity streams of the material in air against each other, resulting in a very finely ground leaf material. A cyclone classifier in this process discriminates against coarse grit, and therefore the content of minerals was expected to be less than in the first-generation materials. In fact, the expected improvement was observed. The CCl_4 separation showed very little heavy phase present in the jet-milled leaf materials, and that was of small particle size. Excellent homogeneity is observed in both by activation analysis, with at least six elements homogeneous to better than 1.5% (1s) at the 100-mg sample size [1].

Grit from four separations were analyzed by instrumental neutron activation analysis (INAA) for a number of elements. The contribution of the grit to the total content of each element is given in table 2. Duplicate analyses were made for the Apple Leaves grit, as indicated by pairs of numbers in the right column of the table. Gold, cobalt, zinc, and possibly uranium are significantly different in the two portions, which may indicate that these elements are contaminants. The rare earths (but not scandium or

Table 1. Quantity of Grit in SRMs

SRM		wt. % grit
1570	Spinach	1.5
1571	Orchard Leaves	0.6
1572	Citrus Leaves	0.6
1573	Tomato Leaves	0.9
1575	Pine Needles	0.2
1515	Apple Leaves	0.1
1547	Peach Leaves	0.1

thorium) appear to be 97%-98% concentrated in the leafy matrix. Sodium (but not potassium or rubidium) has a large contribution from the grit. Even though the amount of grit in this SRM is an order of magnitude less than in the older materials, the contribution of this fraction to the total trace element content is still 5% or greater for sixteen of the elements measured.

These results indicate that the two new botanical Standard Reference Materials, Peach Leaves and Apple Leaves, are substantially improved materials for evaluation of analytical methodology and confirmation of quality assessment procedures. As with all materials, however, the existence of resistant mineral phases must be taken into account. The analysis of any botanical samples by solution-based analytical techniques must ensure that the mineral is dissolved as well as the bulk matrix. Commonly, a small amount of HF is added to complete the solution, but Greenberg et al. [2] have shown that incomplete solubilization can occur even when well-accepted, vigorous regimens are used. Whenever a new technique is applied to real samples, even if it has been shown to be reliable for the analysis of these SRMs, caution must be observed that any sampling inhomogeneities be considered and appropriately dealt with.

Table 2. Percentage of total element in grit phase

| Element | SRM | | |
| | 1572 | 1570 | 1515 |
	Citrus Leaves	Spinach	Apple Leaves
Ag			4.5
Al		39	8.3
As	34	>40	6.7
Au			44, 5.2
Br	26	0.2	
Ca	3		17, 17
Ce	3		1.7, 1.4
Co	33	2.0	11, 6
Cr	30	12	13, 12
Eu	>2		1.7, 1.0
Fe	22	11	7.8,8.6
Hf			8,5
K	<0.1		0.9,0.7
La	3	16	1.7,1.3
Lu			2.1,1.3
Mg		0.3	0.1
Mn		15	1.9
Na			9, 8
Nd			1.5, 1.1
Rb	>1	>5	0.5,1.0
Sb	>5	>40	14
Sc	22	10	6.6, 6.6
Sm	2		1.4, 1.0
Sr	2		10, 8
Si		99	
Tb			1.0, 1.0
Th	110		5.7, 5.1
Ti		140	
U			5, 3
V		25	12
Yb			3.6, 1.1
Zn			40, 1.4

References

[1] D. A. Becker, NIST Tech. Note 1272, 238 (1989); D. A. Becker. Biolog. Trace Elem. Res. (in press).

[2] R. R. Greenberg, H. M. Kingston, R. L. Watters, Jr; and K. W. Pratt, Fresenius Z. Anal. Chem. (in press).

ATMOSPHERIC AND ENVIRONMENTAL STUDIES BY INSTRUMENTAL AND NEUTRON-CAPTURE PROMPT γ-RAY ACTIVATION ANALYSIS

G. E. Gordon, J. M. Ondov, and W. B. Walters (University of Maryland, College Park, MD)

We have made rather little use of the reactor this year because of the long shutdown. The major new work involved studies of the effects of target shape and neutron scattering by hydrogen on sensitivities for various elements by neutron-capture prompt γ-ray activation analysis (PGAA), as discussed by Mackey et al. in the following section. This work is being done in preparation for the use of cold neutrons in PGAA. Also, we briefly note projects in which we have collected large numbers of samples, which will be irradiated soon. It had been several years since we had upgraded our γ-ray spectrometry facilities, so we have been doing that in preparation for the new round of projects.

EFFECTS OF TARGET SHAPE AND NEUTRON SCATTERING BY HYDROGEN ON NEUTRON-CAPTURE PROMPT γ-RAY ACTIVATION ANALYSIS (PGAA)

E. A. Mackey and G. E. Gordon (University of Maryland, College Park, MD)
and
R. A. Lindstrom (Center for Analytical Chemistry)

We are studying the effects of neutron scattering by H on analytical sensitivities (cps/mg) of neutron capture prompt γ-ray activation analysis (PGAA). Hydrogen is a particular problem because of its large free-atom scattering cross-section, $\sigma_{scat} = 20.5$ b. For 11 elements in liquid matrices of constant shape, sensitivities increase linearly with increasing H concentration over the range of 0 to 11% H. Also, for hydrogenous samples, sensitivities vary with sample shape [1]. The magnitude of these effects can be as large as 25%. If H concentration were the only parameter influencing sensitivities, accurate data interpretation could be achieved through a simple calibration of sensitivity vs. H concentration. Because both sample shape and the amount of H affect sensitivities, further studies were performed to determine a method of analysis which would allow accurate data interpretation with minimum uncertainty.

Theoretical work by R. F. Fleming [2] indicates that the use of spherical samples will greatly reduce the magnitude of the effects of scattering on analytical sensitivities. He argues that for a spherical sample, neutron scattering will only serve to mitigate the effects of neutron self-shielding, so that no enhancement would be observed. According to this work, the correction factor, defined as the ratio of the observed reaction rate to the reaction rate which would be observed in the absence of scattering, is bounded by the self-absorption correction factor [3] and unity. PGAA was performed on a series of spheres and disks for each of several hydrogenous materials to test this theory.

A series of disks, 12.7-mm diam, ranging in thickness from 1 to 13 mm and a series of spheres ranging in diam from 5 to 13 mm were prepared from each of the following substances: urea, tris-(hydroxymethyl)-aminomethane (THAM), paraffin, SRM 371g Sulfur; and SRM 1632a Bituminous Coal. Disks were formed using a standard 12.7-mm diam die and hydraulic press; spheres were formed using dies designed and fabricated by instrument maker, Dick Turner. Hydrogen sensitivities were measured in all samples except SRM 371g. Sensitivities for B, Si and S, were measured in SRM 1632a, and sulfur sensitivity was measured in SRM 371g. All data were corrected for neutron self-shielding, temporal variations in the neutron fluence rate, the effects of pulse pile-up, and for the presence of H and B in the background.

Results for H sensitivities in paraffin disks and spheres are shown in figure 1. For spherical samples, H sensitivities remain constant within the errors shown. These errors include uncertainties associated with counting statistics and correction factors. Sensitivities measured in disks showed increasing sensitivities with decreasing thickness from the thickest disks down to thicknesses of about 2 mm. Sensitivities for thinner disks showed decreases with decreasing thickness. Similar results were obtained for H sensitivities in urea, THAM, and SRM 1632a (not shown).

Boron sensitivities measured in SRM 1632a disks and spheres are shown in figure 2. These data show the same qualitative trends as those of the H data.

Sensitivities from disks and spheres of SRM 371g, pure sulfur, are identical within the uncertainties associated with counting statistics. This was expected since these samples contain no H and should scatter fewer neutrons (σ_{scat} = 0.975 b for S).

These findings are consistent with the theoretical work of R. F. Fleming [2], and the Monte Carlo calculations of Copley and Stone [4]. Copley and Stone have shown that neutron scattering by H can alter the distance traveled by neutrons within the sample and that, depending upon the size and shape of the sample, can cause either an increase or a decrease in the probability for neutron absorption. For the types of samples routinely analyzed at this facility, i.e., samples which are smaller than the neutron beam and which are thinner than they are long, sensitivity increases (rather than decreases) are commonly observed. Accuracy in the analysis of hydrogenous materials has been achieved by carefully matching standards to samples or by calibration techniques [5]. These experiments demonstrate that scattering effects will be successfully eliminated through the use of spherically shaped samples.

Results of this study were presented at the 1989 winter meeting of the American Nuclear Society. A manuscript describing this work has been submitted to *Analytical Chemistry*.
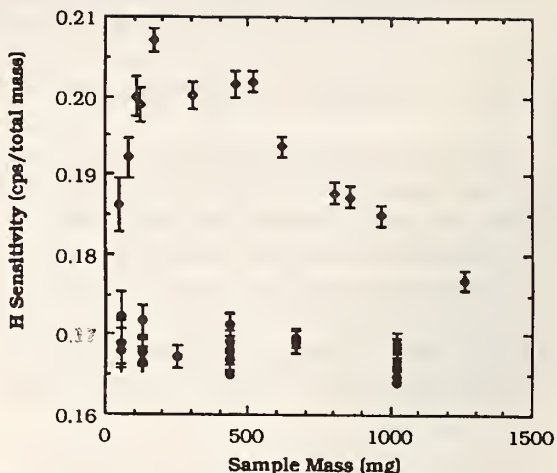
Figure 1. Hydrogen sensitivities (cps/mass) in paraffin disks (◊) and spheres (•).
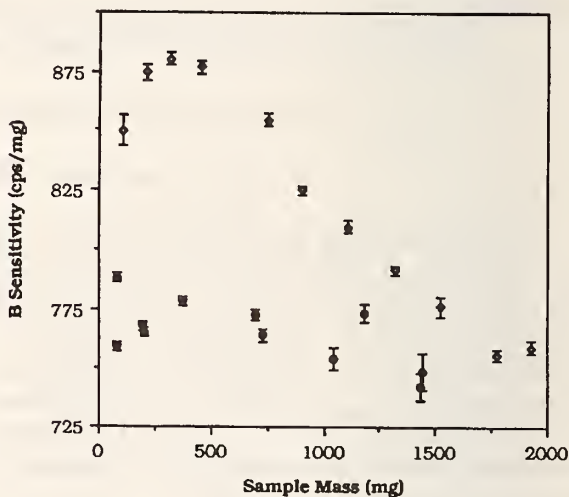
Figure 2. Boron sensitivities (cps/mg) in SRM 1632a, Bituminous Coal, disks (◊) and spheres (•).

References

[1] E. A. Mackey, D. L. Anderson, R. M. Lindstrom, G. E. Gordon, American Nuclear Society Transactions, 60, 14, 1989; E. A. Mackey, G. E. Gordon, R. M. Lindstrom, D. L. Anderson. Anal. Chem. (submitted for publication).

[2] R. F. Fleming, unpublished work.

[3] R. F. Fleming, J. Appl. Radiat. Isot. 33, 1263, (1982).

[4] J. R. D. Copley and C. A. Stone, Nucl. Instrum. Meth. Phys. Res. A281, 593, (1989).

[5] D. L. Anderson, W. C. Cunningham, E. A. Mackey, Biol. Trace Element Research (in press).

SUBMICROMETER SIZE DISTRIBUTIONS OF AIRBORNE PARTICLES BEARING VARIOUS TRACE ELEMENTS

J. M. Ondov, F. Divita, and A. Cargill (University of Maryland, College Park, MD)

Knowledge of the composition and size distributions of atmospheric fine particles is important because these parameters govern respirability, deposition, nucleation of water vapor and light scattering. Submicrometer particles are of special interest, as they are respirable, have long atmospheric residence times, and are frequently enriched in potentially toxic species. Trace elements borne by these particles are also useful for apportioning sources and tracking air masses over long distances.

Despite the importance of this information, reliable measurements of the distributions of major, minor and trace constituents of the submicrometer aerosol have been limited because of limitations of the equipment available for reliable collection and analysis of particles in size cuts ranging far below 1-μm diam. As described in last years' Progress Report, in 1981, Kuhlmey et al. developed an impactor capable of sizing submicrometer particles at modest pressure drops (i.e., about 250 torr for 0.06-μm minimum size cut) and modest jet velocities (127 m/sec for 0.09-μm cut) using micro-orifice technology [1]. The impactor's low-pressure drop and 28-L/min flow rate permit collection of samples suitable for trace analysis with a standard air-sampling pump.

We tested the micro-orifice impactor (MOI) by field collections of particles at a rural site in western Maryland near Deep Creek Lake. Most samples were collected between August 1 and 31, 1983, with sampling periods ranging from 6 to 24 h. Cutoff diameters for the stages ranged from about 1.0 to 0.08 μm and the cyclone removed particles down to 3-μm diam.

Impactor collection surfaces and the afterfilters from seven out of the 60 sample sets were analyzed by INAA at the reactor using a combination of 10 min followed by 3-h irradiations. At least 26 elements, including Al, As, Br, Ca, Ce, Cl, Co, Cr, Fe, K, La, Mg, Mn, Na, Se, Sb, V, Ti, and Zn, could be detected on at least three or the five submicrometer stages. Only because of the high sensitivity of INAA with the large flux of the reactor was it possible to observe so many elements with a total fine particle loading of only 180 μg. Detection on more stages was generally achieved with loadings of 240 to 400 μg.

A paper describing the experimental work was published during the past year [2]. We have applied a deconvolution procedure to the raw size spectra to remove the effects of the non-sharp collection-efficiency curves to obtain the inherent size distributions and will soon publish the results.

Recently, the EPA Extramural Grant Program awarded us a grant for more extensive studies of detailed size distributions in a variety of settings. Field collections with three MOIs are being done now at Washington suburban sites on the University campus, at Andrews Air Force Base, and at Vienna, VA. Plans are being made to collect samples in the Ft. McHenry motor-vehicle tunnel in Baltimore, among other things to seek a motor-vehicle tracer to replace the Pb and Br, which are nearly phased out. Urban sites in Philadelphia previously used in studies by this group [3] will also be studied. From the previous work, we know that the sites are influenced by several types of industrial sources (e.g., Sb roaster, pigment plant, oil refineries) as well as common urban sources such as motor vehicles, oil-fired power plants and municipal refuse incinerators. We know the chemical signatures for most of these sources, but will be interested here in finding out the detailed size distributions.

References

[1] G. A. Kuhlmey, B. Y. H. Liu, and V. A. Marple, Amer. Indust. Hyg. Assn. J. 42, 790 (1981).

[2] J. M. Ondov, J. A. Dodd, and G. Tuncel, Aerosol Sci. Technol. 13, 229 (1990).

[3] T. G. Dzubay, R. K. Stevens, G. E. Gordon, I. Olmez, A. E. Sheffield, and W. J. Courtney, Environ. Sci. Technol. 22, 46-52 (1988).

SOURCES OF AIRBORNE PARTICLES IN AND NEAR MARYLAND AND THEIR WET DEPOSITION

M. Han and G. E. Gordon (University of Maryland, College Park, MD)

For several years, first with EPA support and presently with support of the Maryland Power Plant Research Project, we have been determining the concentrations of many elements on airborne particles at various sites in and near Maryland. We resolve the detailed composition patterns of the airborne particles into contributions originating from various anthropogenic and natural sources, relying heavily on concentrations of certain "marker" elements for certain sources, e.g., V and Ni for oil-fired power plants, As and Se from coal-fired plants, Zn, Sb and Cd from refuse incinerators, etc., a technique called "receptor modeling" [1]. Most of the analyses of these samples have been performed by INAA at the NIST reactor.

Results of a study conducted at Deep Creek Lake in western Maryland, performed in cooperation with EPA have been published [2]. Recently we have performed more detailed studies in cooperation with Prof. T. E. Church and J. Scudlark, of the University of Delaware, who have long operated a station in Lewes, DE as part of the DOE and, later, EPA network (MAP3S) of about ten wet deposition stations. Our group collected particulate and gas samples in a filter pack in which the first filter collected particles, followed by three filters impregnated with KOH and glycerol to collect acidic gases. This work was done in two phases. In the first phase, samples were collected every 12 hours without regard to rain events. However, the sampler was located close to the Lewes precipitation collector so that results from the two kinds of samples can be correlated later to obtain information about wet deposition efficiencies. In the second phase, an attempt was made to collect air-filter samples for several hours prior to passage of large frontal systems associated with precipitation. When precipitation started, the first sampler was shut off and a second one started. If the precipitation lasted long enough to collect sufficient material for analysis, the second sampler was left on until the rain ended, and a third sample was taken for several hours following the event. We will soon begin a sampling similar to Phase 2 on the grounds of the USDA Beltsville Agricultural Research Center, where there is already a station that is part of EPA's Dry Deposition Network. The base-loaded filters from Lewes have been analyzed by ion chromatography (IC) and we will shortly begin to analyze the one hundred particle filters by INAA at the NIST reactor. We expect to collect and analyze another 40 to 50 from the Beltsville experiment.

References

[1] G. E. Gordon, Receptor Models, Environ. Sci. Technol. 22, 1132-1142 (1988).

[2] T. L. Vossler, C. W. Lewis, R. K. Stevens, T. G. Dzubay, G. E. Gordon, S. G. Tuncel, G. M. Russwurm, and G. J. Keeler, Composition and Origin of Summertime Air Pollutants at Deep Creek Lake, McHenry, MD, Atmos. Environ. 23, 1535-1547 (1989).

[3] M. E. Kitto, Ph.D. thesis, Department of Chemistry and Biochemistry, University of Maryland, College Park, MD, 1988.

[4] L. E. McCarthy, M. S. thesis, Department of Chemistry and Biochemistry, University of Maryland, College Park, MD, 1988.

SOURCES OF BACKGROUND IN Ge GAMMA DETECTORS

R. M. Lindstrom and J. K. Langland (Center for Analytical Chemistry)
D. J. Lindstrom (NASA Johnson Space Center, Houston, TX)
and
L. A. Slaback (Occupational Health and Safety Division)

Three sources of gamma radiation contribute to the background of a shielded gamma-ray detector: natural radioactivity of the detector and its surroundings, man-made contamination, and cosmic radiation. As discussed in last year's report, a detector system is in use which shows no detectable contribution from long-lived radioactivity in the detector itself and very little from contamination. The cosmic contribution was shown to be dominant and evaluated quantitatively in the present work.

Two broad peaks in the background result from inelastic scattering of cosmic-ray neutrons $(0.02 \text{ cm}^{-2}\text{s}^{-1})$ in germanium. The counting rate of the fast-neutron and positron peaks did not change when heavy neutron shielding (7.5% lithium in polyethylene, 20-cm thick by 120-cm square) was laid on top of the shield, from which we conclude that the neutrons were generated in the lead itself. Fast neutrons also excite the lower nuclear levels of lead and structural iron to produce additional gamma-ray peaks in the spectrum.

The shield for the low-background "Ty" detector was at first lined with material of lower atomic number to absorb the lead fluorescent x-rays excited by background radiation. Neither cadmium, tin, copper, nor plastic (hydrocarbon or fluorocarbon) was desirable in the end as a shield liner, since all these increased the background continuum or introduced characteristic peaks into the background spectrum; in consequence no x-ray absorber was used. The shield was finally lined with sheets of 1.6-mm Teflon TFE to provide an easily cleanable surface. Excitation peaks from ^{19}F make even this amount of lining material undesirable.

The background of the Ty detector in the final shield configuration showed only 511-keV positron annihilation radiation, products of cosmic-ray neutron interactions with the germanium of the detector itself, excitation peaks of ^{19}F and ^{206,207}Pb, radon daughters, ^{60}Co, thorium daughters, and ^{40}K, in that order of importance (Table 1). All peaks in the background were identified. Only the positron peak was higher than 5 c/hr. Except for ^{60}Co gamma rays, no peaks are detected which can be attributed with certainty to long-lived radioactivity in the materials of which the detector or the shield are constructed.

A comparison among four detector:shield combinations helped to elucidate the sources of the background observed. The four counting systems are the Ty detector in the low-background shield in the Reactor Building; the same detector in a lead shield in the underground Radiation Counting Laboratory at the Johnson Space Center; a second low-background detector, named RCL5, with a J-shaped cryostat in the same shield (now with a shadow shield beneath and a graded liner to absorb x-rays) in the RCL; and a third large, standard detector called HP2 in a commercial cylindrical shield in the low-level laboratory at NIST. All the detectors were comparable in efficiency

The results of the comparison are given in table 2; since the detectors are of similar efficiency, the ratios of count rates are quantitative measures of the effects of the different materials and the laboratory environments. The Cd-Cu liners in the RCL5 and HP2 shields suppress the Pb x-rays by a factor of five. The importance of the cosmic-ray contributions are most clearly shown in the relative intensity of the positron annihilation peak, the ^{206,207}Pb excitation peaks, and the level of the background continuum at 1 MeV. These three components were reduced fivefold in both detectors in the underground laboratory. The lower levels of positron and lead peaks in the HP2 background compared to the Ty detector above ground may be due to the lesser buildup of the cosmic cascade in the HP2 shield, which was only a third as massive as the other. The benefits of low-background construction and selected lead were clearly evident in the much greater intensity of radon (and uranium), thorium, and potassium peaks in background of

the HP2 detector. The continuum background, however, was not greatly different from the low-background Ty detector.

Achieving a low background in close proximity to a reactor, or to laboratories in which substantial quantities of radioactivity are handled, might appear to have small chance of success. However, we have found that, with care in selecting materials and in locating the

laboratory, the achievable background can be remarkably good. Since these experiments have shown that the most important source of residual background in the low-background detector described is cosmic radiation, we conclude that the greatest additional improvement will require either burial of the counting room 10 meters or more deep to reduce the cosmic-ray flux, or active (anticoincidence) shielding.

Table 1. Gamma-ray peaks in residual background. The number of significant figures given reflects the uncertainty of counting statistics

Energy, keV	Nuclide	Count rate, c/s	Energy keV	Nuclide	Count rate, c/s
53.4	^{73*}Ge	0.0004	511.0	β^+ annihilation	0.029
66.7	^{73*}Ge	0.003	569.7	^{207*}Pb	0.0008
72.8	Pb Kα2	0.009	583.1	^{208}Tl	0.0003
75.0	Pb Kα1	0.015	596.1	^{74}Ge(n,n')	0.010
84.8	Pb Kβ1'	0.011	609.3	^{214}Bi	0.001
87.3	Pb Kβ2'	0.003	693.4	^{72}Ge(n,n')	0.007
109.9	^{19*}F	0.002	803.3	^{206*}Pb	0.001
122.1	^{57*}Fe	0.0003	846.8	^{56*}Fe	0.0006
139.7	^{75m}Ge	0.002	911.2	^{228}Ac	0.0003
159.7	^{77m}Ge	0.001	1063.6	^{207*}Pb	0.0003
174.9	^{71*}Ge	0.0003	1120.3	^{214}Bi	0.0003
197	^{71*}Ge +^{19*}F	0.006	1173.2	^{60}Co	0.0006
238.6	^{212}Pb	0.0005	1332.5	^{60}Co	0.0006
295.2	^{214}Pb	0.0004	1460.8	^{40}K	0.0003
352.0	^{214}Pb	0.001			

Table 2. Comparison of backgrounds of different detectors and locations. Uncertainties are given as $\pm$ 1 s. d.

Detector identification	Ty	Ty	RCL5	HP2
Location	NIST	RCL	RCL	NIST
Cryostat configuration	Upright		J-shape	Upright
Background counting rates:				
Lead x-ray	=1	0.83 $\pm$ 0.02	<0.2	0.16 $\pm$ 0.03
β^+ annihilation	=1	0.23 $\pm$ 0.01	0.23 $\pm$ 0.01	0.57 $\pm$ 0.01
Lead excitation	=1	0.18 $\pm$ 0.09	0.18 $\pm$ 0.05	0.63 $\pm$ 0.10
1-MeV continuum	=1	0.20 $\pm$ 0.01	0.22 $\pm$ 0.02	1.16 $\pm$ 0.03
Radon	=1	1.5 $\pm$ 0.6	0.8 $\pm$ 0.3	3.5 $\pm$ 0.7
Thorium	=1	0.8 $\pm$ 0.3	0.5 $\pm$ 0.2	5. $\pm$ 2
^{40}K	=1	1.6 $\pm$ 0.5	0.7 $\pm$ 0.2	9.9 $\pm$ 1.6

CHEBYSHEV EXPANSION OF ATTENUATION CORRECTION FACTORS
FOR CYLINDRICAL SAMPLES

D. F. R. Mildner (Center for Analytical Chemistry)
and
J. M. Carpenter (Argonne National Laboratory, Argonne, IL)

The attenuation correction factor $A(\theta)$ for cylindrical samples for all scattering angles θ can be expressed in terms of a cosine series of functions $Z_{mn}(\theta)$, which are independent of the scattering angle for m or n equal to zero, using Chebyshev expansion coefficients $c_s(m,n)$ [1]. The accuracy of these expansion coefficients has been improved [2]. An increased order of expansion allows the method to be useful over a greater range of attenuation. It is shown that many of these coefficients are exactly zero, others are rational numbers, and others are rational fractional fractions of π^{-1}.

The attenuation factor for scattering of x-rays and neutrons in cylindrical samples can be expressed for all scattering angles in terms of a Fourier cosine series. The factors may be calculated by numerical integration [3], and tables are available of values with an accuracy of 10^{-4} [4]. With more accurate values for the expansion coefficients, the limited range of applicability of the Chebyshev expansion method can be extended to greater values of attenuation and with increased accuracy.

The attenuation correction factor is given by

$$A(\theta) = \frac{1}{\pi R^2} \int_0^R \int_0^{2\pi} \exp(-\mu \ell) \exp(-\mu' \ell') \rho \, d\rho \, d\phi = \sum_{m=0}^{\infty} \sum_{n=0}^{\infty} \frac{(-\mu R)^m (-\mu' R')^n}{m! n!} \sum_{s=0}^{\infty} c_s(m,n) \cos(s\theta)$$

with the summations extending over a range dependent on the required accuracy. This expansion is an absolutely convergent series, and in practice we may compute all terms up to

$(m + n) = N$ for the determination of A. The error (precision) is less than the $(N + 1)$th order term, so that for all θ the error is less than $(2\mu R)^{N+1} Z_{0,N+1}/(N+1)!$

For $s > 0$, the Chebyshev expansion coefficients are given by

$c_s(m,n) =$

$$\pi^{-2} \int_0^1 \rho \, d\rho \int_0^{2\pi} d\xi \cos s\xi [\rho \cos \xi + (1-\rho^2 \sin^2 \xi)^{1/2}]^m \int_0^{2\pi} d\psi \cos s\psi [-\rho \cos \psi + (1-\rho^2 \sin^2 \psi)^{1/2}]^n$$

Integrals for the coefficients $c_s(m,n)$ may be evaluated using a power series expansion for the complete elliptical integrals, which for lower-order coefficients are expressed as ρ moments of combinations of complete integrals of the first and second kinds. When s has the same parity as

m (or n), the ξ (or ψ) integral gives an expression involving π multiplied by a polynomial in ρ.

We have computed values of the coefficients $c_s(m,n)$ for $s \leq 9$ and for $(m + n) \leq 10$ to six decimal places with an accuracy of at least 10^{-4},

and have shown that many of these coefficients are identically equal to zero. We have also found some interesting properties of these expansion coefficients. The summation of coefficients $c_s(m,n)$ may be expressed in terms of specific fractions of $Z_{0,m+n}$. Also the difference between the summation of the coefficients $c_s(m,n)$ for even s and the summation of $c_s(m,n)$ for odd s is exactly $Z_{0,m+n}$. These sum laws provide a check on the accuracy of the computation of the coefficients. Various general properties have been found for these coefficients. When both m and n are even (odd), these summations are rational numbers, and the coefficients themselves are rational numbers for even (odd) s. When m and n are mixed indices, these summations are rational fractions of π^{-1}, and the coefficients

themselves are also rational fractions of π^{-1} for all s.

These values are sufficiently accurate for $\mu R < 1.0$, which is the usual range for neutron diffraction. Extra precision may be obtained by using the Chebyshev expansion as a correction to an approximation $\exp(-2\mu\overline{\ell})$ to A. For example, if $\overline{\ell}/R$ is set to unity, the results are reasonable for $\mu R < 2.5$. An approximate analytic expression for the correction factor which is adequate in most cases of neutron diffraction and inelastic scattering can be expressed in terms of the first two Chebyshev expansion coefficients [3]. An analytic expression for $A(\theta)$ given by Rouse et al. [5] can use asymptotic values determined from these two coefficients. We show that this is equivalent to taking $\overline{\ell}/R = 0.8488$.

References

[1] J. M. Carpenter, Rev. Sci. Instrum. <u>40</u>, 555-556 (1969).

[2] D. F. R. Mildner and J. M. Carpenter, J. Appl. Cryst. <u>23</u>, 378-386 (1990).

[3] V. F. Sears, J. Appl. Cryst. <u>17</u>, 226-230 (1984).

[4] V. F. Sears, Atomic Energy of Canada Report AECL-8176 (1983).

[5] K. D. Rouse, M. J. Cooper, E. J. York, and A. Chakera, Acta Cryst. <u>A26</u>, 682-691 (1970).

MEASUREMENT OF THE ^{93}Nb(n,2n)^{92m}Nb CROSS SECTION IN A ^{235}U FISSION SPECTRUM

G. P. Lamaze (Inorganic Analytical Research Division)
and
T. G. Williamson (University of Virginia, Charlottesville, VA)

When niobium is used as a fast neutron monitor, the isotopes ^{93m}Nb and ^{92m}Nb are produced. The reaction ^{93}Nb(n,2n)^{92m}Nb produces an isotope with a 10.15 day half life, and has a threshold energy of about 9 MeV. This reaction is of interest as a monitor for fusion studies. In the course of measurements of the ^{93}Nb(n,n')^{93m}Nb reaction rate, spectrum-averaged cross sections for the ^{93}Nb(n,2n)^{92m}Nb reaction in a ^{235}U fission spectrum have been determined.

Five niobium foils (1.27-mm diam and ranging in thickness from .004-mm to .125-mm thick) from two commercial suppliers were irradiated in the cavity fission source [1] of the

NIST reactor. Calibration of this facility has been described by McGarry et al [2].. In this facility, two ^{235}U metal fission source disks are placed outside a cadmium box coaxial with the detector stack. This assembly is placed in the center of a 0.3-m diam cavity in the graphite thermal column. Three of the foils were irradiated at one time and the other two included in separate irradiations. Each foil was exposed for ~ 100 h. The neutron fluences were determined by fluence transfer with nickel foil irradiations [3]. In the fluence transfer method, the fluence is, by a series of ratio measurements, traceable to NBS-1, the national standard Ra-Be neutron source, which has been absolutely calibrated

with the manganous sulfate bath technique. No cross sections enter directly into the fluence determination. Corrections have been made for deviations from a pure fission field due to scattering. These corrections were made with a Monte Carlo technique and the correction varies from 1.7 ± 1.0 to $2.9 \pm 1.0\%$ depending on the number and thickness of other foils irradiated with the niobium. The one standard deviation uncertainty in the fluence measurement is 2.1%.

The foils were counted with germanium detectors and the analysis done with the 934-keV gamma ray. The detectors were calibrated with standard point sources and have an uncertainty in the detector response efficiency of 3% at this energy. A gamma-ray abundance of 0.9915 and half life of 10.15 days was used in the analysis. The activity of each foil was measured several times over a 2 week decay period. All uncertainties were combined in quadrature to give an uncertainty of 4% for each individual determination of the cross section.

The average determination of the spectrum-averaged cross section from the five foils is 0.433 mb with a one standard deviation from the average of 2.6%. Combining all uncertainties gives a final result of 0.433 ± 0.017. Using the calculated cross section of Strohmaier [4], ENDF/B-V [5], and NIST [1] evaluated fission spectra, a calculated value of the $^{93}Nb(n,2n)^{92m}Nb$ spectrum-averaged cross section has been obtained. Table 1 lists the present results compared with some previous results and the calculated cross section.

In summary, a spectrum-averaged cross section of 0.433 ± 0.017 mb has been measured for the reaction $^{93}Nb(n,2n)^{92m}Nb$ in a ^{235}U fission spectrum. The measurement compares favorably with a calculated value using the Strohmaier calculation and either ENDF/B-V or the NIST evaluated ^{235}U fission neutron spectrum. The uncertainty is about half that of previously reported measurements.

Table 1. $^{93}Nb(n,2n)^{92m}Nb$ spectrum averaged cross section

Value (mb)	Reference	Comments
0.433 ± 0.017	This work	^{235}U fiss. spec.
0.432 ± 0.033	Ref. 6	Reactor Spec.
0.402 ± 0.034	Ref. 6	Fission Plate
0.47 ± 0.03	Ref. 7	^{235}U fiss. spec.
0.44	Ref. 4 and 5	Calculated
0.43	Ref. 4 and 1	Calculated

References

[1] J. A. Grundl and C. M. Eisenhauer, "Compendium of benchmark neutron fields for reactor dosimetry," NBSIR 85-3151, Jan. 1986.

[2] E. D. McGarry, C. M. Eisenhauer, D. M. Gilliam, J. Grundl, and G. P. Lamaze, "The U.S. U-235 fission spectrum standard neutron field revisited," in Proceedings of the Fifth ASTM-Euratom Symposium on Reactor Dosimetry, Geesthact, West Germany, Sept. 1984.

[3] G. P. Lamaze, E. D. McGarry, and F. J. Schima, in Proceedings of the Intn'l. Conf. on Nuclear Data for Science and Technology, Antwerp, Belgium, Sept. 1982.

[4] B. Strohmaier, Ann. Nucl. Energy, 16 (1989) p. 461.

[5] B. A. Magurno, R. R. Kinsey, and F. M. Scheffel, Guidebook for the ENDF/B-V Nuclear Data Files, EPRI NP-2510 (1982).

[6] H. Kimura, K. Kobayashi, and T. Shibata, J. Nucl. Sc. and Tech. 8(2) 59-69 (1971).

[7] A. Fabry, Rep. BLG-465 (1972).

REACTOR OPERATIONS AND ENGINEERING

T. M. Raby, J. F. Torrence, J. H. Ring, and N. A. Bickford (Reactor Operations and Services)
and
J. H. Nicklas and R. S. Conway (Reactor Engineering)

Installation of the first three of seven guide tubes for the cold neutron research facility allowed time for only two operating cycles during the past year. The reactor was on-line the entire available operating time of slightly more than 2 months and was heavily utilized for both neutron beam and irradiation programs. The shutdown period was used by both reactor operations and engineering to perform design modifications and improvements, major maintenance, and equipment repair. Highlights of significant activities are listed below, all of which were performed in-house by the operating and engineering staffs.

Confinement Building and Penetrations. Seven penetrations through 24-ft thick confinement building walls were drilled to accommodate the new guide tubes. Four penetrations were temporarily resealed for future tubes. Confinement isolation valves were installed in the remaining three penetrations currently in use. A complete control system for the operation of these valves was designed and installed. This included connection to the reactor safety system that would cause automatic closure and isolation of the confinement building upon a major scram signal. Both the operation and safety function of these valves, as well as their effect on confinement leak rate, were tested and the valves met all aspects of the technical specifications requirements on the first try. This is a significant milestone because of the complex design and the stringent requirements.

The confinement building was completely refurbished. The experimental and operating floors were repainted with special sealant type paint. The building roof was replaced. Most of the asbestos used as insulation was removed and replaced with nonasbestos insulation.

Heavy Water, Fuel, and Shim Arms. Both heavy water and enriched fuel are in extremely short supply in the United States. Because fuel utilization, which is already the best in the country, continues to improve further through innovative management and design, there is enough fuel on hand to last to the end of the decade. Negotiations with the Department of Energy resulted in a commitment of 36 tons of heavy water for future use. Three sets of shim arm blades, which are unique to the facility, are currently being assembled and should provide replacement for the next 15 years.

Extensive maintenance was performed on all four shim arm drives. A test stand was designed and built to test the drives prior to installation. The stand provides for rapid and superior testing compared to that done in-place, which is cumbersome and time consuming. For some time, shim No. 2 would not return to the same position following a scram. After months of testing, the problem was traced to the inner bearing of the shim arm shaft. Finding the actual cause was in itself a significant accomplishment because the problem was elusive and nonrepetitive. Both the bearing and the heavy water seal were replaced with the core in place. This is the first time in the history of the facility that something of this critical nature was done and it could not have been performed better with minimal exposure and flawless operation.

Main Heat Exchangers. The extended shutdown was used to locate a very small leak (on the order of 0.0001 gpm) in one of the main heat exchangers. After extensive searching and testing, several tubes were plugged. Two new leaks subsequently developed and additional tubes were plugged. This heat exchanger has been in service for more than 15 years and every effort is being made to extend its use until replacement heat exchangers are obtained. Comprehensive specifications for new heat

exchangers were completed and a request for bids has gone out.

Thermal Shield Cooling System.   An improved cooling system which incorporates a new high efficiency heat exchanger and an automatic temperature control system was designed and installed. This system minimizes temperature variations under both operating and shutdown conditions, and should help to reduce leaks caused by sudden temperature changes. Our program of leak sealing using a method developed by the National Nuclear Corporation of England is now well established, and will continue to be followed.

Cooling Tower. A major overhaul of the cooling tower was initiated and is near completion. This work included the replacement of nearly 1000 carbon steel bolts with stainless steel bolts.

Staffing. Extensive training was provided to the staff of 16 licensed senior operators in many technical areas as part of the new Nuclear Regulatory Commission (NRC) required requalification program. Two new operators will take their senior licensing examination scheduled for the end of the year by the NRC. One senior operator, who is a graduate electrical engineer, will then be transferred to Engineering to augment the small staff.   The efforts and performance of the operating staff over the years received high recognition from the Department of Commerce with the unprecedented award of the Silver Medal to the entire group.

NEUTRON ACTIVATION ANALYSIS AT THE FOOD AND DRUG ADMINISTRATION

D. L. Anderson and W. C. Cunningham
(U. S. Food and Drug Administration, Washington, DC)

The Food and Drug Administration (FDA) maintains a neutron activation analysis (NAA) facility in the reactor building of NIST. This facility is directed by FDA's Center for Food Safety and Applied Nutrition and provides agencywide analytical support for special investigations and applications research. NAA complements other analytical techniques used at FDA and serves as a reference technique and confirmatory quality assurance (QA) tool. Instrumental, neutron-capture prompt-γ, and radiochemical NAA procedures (INAA, PGAA, and RNAA, respectively) continue as the prime analytical approaches.   In addition, a radioisotope-induced x-ray emission (RIXE) spectrometer was assembled this year to provide support for FDA programs which monitor toxic elements in housewares, and the low-level γ-ray counting facility developed by the Nuclear Methods Group of the NIST's Center for Analytical Chemistry was used to determine the radionuclide content in various matrices. This combination of nuclear techniques enables diverse multielement and radiological information to be obtained for foods and related materials.

A variety of quality control-related NAA studies were undertaken in 1989-90. Foods collected as part of FDA's Total Diet Study and IUPAC (International Union of Pure and Applied Chemistry) check samples were analyzed for aluminum.   Multielement analysis of 13 proposed food reference materials prepared by Agriculture Canada was completed, and work continued on the development of methodology for sodium determination by INAA.   The method for sodium will be collaboratively studied for adoption as an official AOAC (Association of Official Analytical Chemists) method. Preliminary work has also begun on the development of an in-house FDA infant formula reference material.

PGAA efforts during the past year were primarily devoted to the optimization of boron determination in foods and biological materials. Matrix effects resulting from the scattering of

thermal neutrons by the analytical portion were accurately determined. These scattering phenomena and the resulting enhancements of element sensitivity and background count rate are detailed elsewhere [1-3]. Boron concentrations in 31 reference materials were determined and reported at the Fourth International Symposium on Biological and Environmental Reference Materials [2]. Among the findings are boron concentrations of three proposed NIST Reference Materials, SRM 1548 Total Diet (2.61 $\pm$ 0.25 µg/g), SRM 1515 Apple Leaves (28.8 $\pm$ 0.6 µg/g), and SRM 1547 Peach Leaves (28.6 $\pm$ 0.6 µg/g). In other boron studies, PGAA and inductively coupled plasma atomic emission spectrometry (ICP-AES) results were compared from analyses of Total Diet food composites (in conjunction with the United States Department of Agriculture and NIST) and orange juices. These studies showed that an average boron loss of approximately 20% occurs during the digestion step in analysis by ICP-AES. Previous experiments [1] had shown that large boron losses may also occur during freeze-drying, especially for wet, low-pH samples.

The availability of specialized nuclear counting facilities had made possible the initiation of preliminary RIXE experiments designed to identify lead (Pb) in ceramic glazes. Using a ^{109}Cd excitation source, Pb- and non-Pb-glazed ceramics may be distinguished from one another. The possibility of implementing field use of such a unit is being explored. Other excitation sources (e.g., ^{55}Fe and ^{241}Am) are being considered for the identification of other potentially toxic elements such as Cd.

References

[1] D. L. Anderson, W. C. Cunningham, and E. A. Mackey, Biol. Trace Elem. Res. (1990) (in press).

[2] D. L. Anderson, W. C. Cunningham, and E. A. Mackey, Fresenius J. Anal. Chem. 338, 554-558 (1990).

[3] E. A. Mackey, G. E. Gordon, R. M. Lindstrom, and D. L. Anderson, Anal. Chem. (1990) (in press).

D. PERSONNEL ROSTER

```
                    ┌─────────────────────────────────────┐
                    │       REACTOR RADIATION DIVISION     │
                    │                                      │
                    │         J. M. Rowe, Chief            │
                    │         T. M. Raby, Deputy           │
                    │         H. J. Prask, Sci. Asst.      │
                    │       E. C. Maxwell, Admin. Officer  │
                    │        S. L. Neal, Admin. Asst.      │
                    └─────────────────────────────────────┘
```

REACTOR OPERATIONS & ENGINEERING	COLD NEUTRON PROJECT	NEUTRON CONDENSED MATTER SCIENCE
T. M. Raby, Chief	J. M. Rowe, Manager	J. J. Rush, Leader
J. F. Torrence, Deputy	I. G. Schröder, Tech. Leader	J. K. Spillman, Sec'y
J. H. Nicklas, Chief Eng.	C. O'Connor, User Coord.	L. K. Clutter, Sec'y
A. Wise, Sec'y	L. M. Thomas, Sec'y	
C. M. Sweeney, Sec'y		

RESEARCH AND ENGINEERING STAFF

J. F. Ankner
- o Condensed matter physics
- o Neutron reflectometry and grazing-angle diffraction
- o Instrument development

N. F. Berk
- o Condensed matter theory
- o SANS theory for microstructure analysis
- o Computer software for graphics and data analysis

J. A. Borchers
- o Thin-film analysis
- o Artificially modulated materials
- o Magnetism

R. C. Casella
- o Theory of neutron scattering from light-atom defects in metals
- o Group theory analyses of neutron scattering from condensed matter
- o Elementary particle theory, especially as related to reactor generated experiments

R. S. Conway
- o Electronic engineering
- o Nuclear instrumentation

J. R. D. Copley
- o Time-of-flight spectrometer development
- o Neutron instrumentation conceptual design
- o Condensed matter physics

W. E. Dickerson
- o Neutron scattering instrumentation
- o Microcomputer interfacing
- o Nuclear and engineering physics

R. W. Erwin
- o Magnetic materials
- o Phase transformations
- o Spin echo techniques
- o Cryogenics

C. J. Glinka
- o SANS microstructure of metals and porous media
- o Magnetic materials
- o Cold neutron instrument development

J. A. Gotaas
- o Magnetism and phase transformations
- o Cold neutron sources
- o SANS instrumentation and research

P. H. Graham
- o Engineering design

G. C. Greene
- o System and user software for cold neutron instrumentation
- o Spectrometer and data acquisition systems interfaces

B. Hammouda
- o SANS from polymer systems
- o Quasielastic scattering from polymer solutions
- o SANS instrument development

V. L. Himes
- o Crystal database development
- o X-ray crystallography

P. A. Kopetka
- o Mechanical engineering
- o Cold source design
- o Electro-mechanical systems

S. Krueger
- o Small angle neutron scattering instrumentation
- o Microstructure of materials
- o Biological problems

J. G. LaRock
- o Mechanical engineering
- o Neutron instrumentation design

H. P. Layer
- o Electronics and data processing
- o Advanced instrumentation
- o Fundamental physics

J. W. Lynn
- o Condensed matter physics
- o Magnetic materials
- o Neutron scattering methods

C. F. Majkrzak
- o Condensed matter physics
- o Polarized neutron scattering
- o Polarizing and monochromating devices

A. D. Mighell
- o Crystallographic database development
- o Single crystal diffraction
- o Theory of crystal lattices

B. Mozer
- o Structure and microstructure of metallic glasses
- o Dynamics of liquids
- o NDE of alloys

D. A. Neumann
- o Condensed matter physics
- o Two-dimensional materials
- o Neutron and x-ray scattering instrumentation

J. H. Nicklas
- o Mechanical engineering
- o Reactor fuel design
- o Reactor engineering support

D. J. Pierce
- o Mechanical engineering
- o Neutron instrumentation design

H. J. Prask
- o Residual stress measurement
- o Neutron NDE of hardware
- o Neutron NDE instrumentation

E. Prince
- o Structural properties of alloys, catalysts and minerals
- o Advanced crystallographic refinement methods
- o Software for materials structure analyses

T. M. Raby
- o Reactor operations
- o Nuclear engineering
- o Reactor standards

J. J. Rhyne
- o Properties and transformations of high technology magnetic materials
- o Structure of amorphous solids
- o Data acquisition and analysis systems

J. M. Rowe
- o Orientationally disordered solids
- o Hydrogen in metals
- o Cold neutron research and instrumentation

J. J. Rush
- o Catalysts and molecular materials
- o Hydrogen in metals
- o Two-dimensional systems
- o Inelastic scattering methods

A. Santoro
- o Structure of electronic and structured ceramics
- o Theory of crystal lattices
- o Powder diffraction methods

S. K. Satija
- o Low-dimensional molecular systems
- o Fractal aspects of microporous media
- o Neutron reflectometry

I. G. Schröder
- o Cold neutron instrumentation development
- o Nuclear and engineering physics
- o Optical devices for neutron transport

J. K. Stalick
- o Neutron and x-ray diffraction
- o Inorganic chemistry
- o Crystal database development

J. B. Sturrock
- o Design engineering
- o Nuclear systems and components

M. Suthar
- o Design engineering
- o Nuclear systems and components

J. F. Torrence
- o Reactor supervision
- o Reactor maintenance
- o Nuclear engineering

T. J. Udovic
- o Neutron time-of-flight instrumentation
- o Properties of catalysts
- o Spectroscopy of surfaces

R. E. Williams   o Cold neutron source development
                  o Nuclear engineering

TECHNICAL STAFF

Reactor Operations

Richard D. Beasley   Michael J. McDonald
Myron H. Bell   William W. Mueller
Nathan A. Bickford   Thomas J. Myers
Mark G. Cassells   John H. Ring
Forrest C. Clark   Ricky P. Sprow
Howard W. Dilks   Robert F. Stiber
Daniel J. Flynn   Attila L. Toth
Larry T. Lindstrom   Daniel P. Wilkison
                            Kevin I. Wright

Neutron Research

George M. Baltic   David Roeseler
David Clem   William H. Rymes
Donald H. Fravel   Dan Swearingen
Thomas Green   Thuan Thai
Wayne C. Knill   Robert H. Williams
Michael J. Rinehart

Reactor Engineering

James A. Beatty
Richard P. Hayes

NON-RRD NIST STAFF LOCATED AT REACTOR

Occupational Health
and Safety Division (354)
  D. Brown
  C. Campbell
  J. Clark
  G. Deardorff
  I. Jensen
  T. Mengers
  F. Moore
  J. Shubiak
  L. Slaback

Ionizing Radiation
Division (536)
  E. Boswell
  C. Eisenhauer
  D. Gilliam
  J. Grundl
  E. McGarry
  R. Schwartz

Inorganic Analytical
Research Division (551)
  D. Becker
  G. Downing
  K. Fitzpatrick
  K. Garrity
  R. Greenberg
  G. Iyengar
  H. Kingston
  G. Lamaze
  J. Langland
  R. Lindstrom
  K. Littrell
  D. Mildner
  B. Norman
  K. Pratt
  C. Stone
  S. Stone
  R. Watters, Jr.
  R. Zeisler

GUEST WORKERS AND COLLABORATORS

MATERIALS SCIENCE AND ENGINEERING
LABORATORY (400)
  J. Cahn

Ceramics Division (420)
  D. Black
  D. Blackburn
  D. Cranmer
  E. Fuller
  W. Haller
  D. Kauffman
  R. Krause
  G. Long
  S. Malghan
  R. Roth
  W. Wong-Ng

Polymers Division (440)
  B. Bauer
  R. Briber
  F. Brinkman
  L. Coyne
  T. Davis
  C. Han
  A. Nakatani
  W. Wu

Metallurgy Division (450)
  L. Bendersky
  F. Biancaniello
  W. Boettinger
  R. Fields
  F. Gayle
  C. Johnson
  D. Lashmore
  R. Schaefer

Surface Science Division (541)
  R. Cavanagh

Organic Analytical
Division (552)
  B. Koster
  L. Sander
  S. Wise

Gas and Particulate
Science Division (553)
  W. Dorko
  C. Poston
  D. Simmons
  J. Small
  S. Wight

Center for Advanced Research
Biotech. (581)
  G. Gilliland
  L. Svensson

Center for Atomic, Molecular,
and Optical Physics (570)
  M. Arif
  R. Deslattes
  S. Dewey
  G. Greene

Semiconductor Electronics
Division (727)
  J. Ehrstein
  J. Suehle

Thermophysics Division (774)
  H. Hanley
  J. Straty

Armed Forces Institute of Pathology
  D. Nagarajan

Army Armament Research, Development,
and Engineering Center
  C. Choi
  S. Trevino

Army Ballistics Research Lab
  B. Rice
  L. Vande Kieft

Federal Bureau of Investigation
  R. Aaron
  R. Bilko
  R. Halberstam
  J. Havekost
  K. Lundy
  E. Peele
  R. Rebbert
  J. Riley
  P. Sanderson

Food and Drug Administration
  D. Anderson
  W. Cunningham
  J. Tanner

Geological Survey
  M. Mrose

NASA
  D. Lindstrom

National Institutes of Health
  M. Gellert
  R. Nossal

National Oceanic and
Atmospheric Administration
  G. Lauenstein

Naval Research Laboratory
  D. Collins
  K. Grabowski
  P. Skeath
  C. Roland

Naval Surface Weapons Center
  G. Riel
  M. Spano

Pittsburgh Energy Tech. Ctr. (DOE)
  G. Olsen

Smithsonian Institution
  R. Bishop
  M. Blackman
  Y. Cheng
  R. Cunningham
  E. Myers
  J. Olin
  G. Stein

Argonne National Laboratory
 T. Brun
 J. Carpenter
 G. Felcher
 Y. Huang
 J. Liu
 J. Richardson
 P. Thiyagarajan
 K. Vandervoort

Atom. Inst. (Vienna)
 G. Westphal

Boris Kidric Inst.,
Belgrade, Yugoslavia
 M. Davidovic
 D. Djordjevic

Brookhaven National Laboratory
 H. Chou
 R. DiNardo
 L. Passell
 A. Saxena
 M. Sanyal
 G. Shirane
 S. Sinha

CECM/CNRS Grenoble, France
 M. Bessiere
 Y. Calvayrac
 J. Capponi
 M. Cornier-Quiquandon
 D. Gratias
 E. Hewat
 S. Lefebvre
 M. Marezio
 A. Quivy

CEN - Saclay, France
 R. Bellissent

Central Bur. Nucl. Meas. (Belgium)
 J. Pauwels

Energy Research Foundation
(The Netherlands)
 J. Woittiez

Foundation pour la Recherche
Medicale (Geneva, Switzerland)
 E. H. Cerny

Hahn-Meitner Institute
(Berlin)
 D. Behne

Harwell Lab (U.K.)
 A. Allen

Institut Laue-Langevin
Grenoble, France
 A. Magerl
 M. Thomas
 C. Vettier
 G. Zaccai

Institut "Jozef Stefan" (Yugoslavia)
 A. Byrne
 B. Smodis

Instituto se Pesquisas
Energeticas Nucleares (Sao Paulo, Brazil)
 M. Saiki

International Centre for Diffraction Data
 M. Morris
 H. McMurdie

KFA Jülich, Germany
 H. Grimm
 R. Hempelmann
 D. Richter
 M. Rossbach
 M. Stoepler

Korea Atomic Energy Research Institute
 C.-H. Lee

Korean Inst. of Sci. & Tech.
 H. Kim

Korean Standards Research Inst.
 S.-T. Hwang

Paul Scherrer Inst. (Switzerland)
 I. Anderson
 O. Elsenhans

National Research Council (Canada)
 J. Rodgers
 W. McKinnon

Lawrence Berkeley Lab.
D. Morris
R. Sid

Los Alamos National Laboratory
T. Bowles
S. W. Cheong
J. Eckert
Z. Fisk
W. Hamilton
H. Robertson
R. Robinson
G. Smith
T. Sosnick
J. Trewhella
J. Wilkerson
M. Yethiraj

Oak Ridge National Laboratory
J. Cable
J. Fernandez-Baca
J. Hayter
H. Mook
R. Nicklow
B. Sales
H. Smith

Risø National Laboratory
J. Bohr

Sandia National Laboratory
B. J. Olivier

Alfred University
R. Snyder
R. Zhow

Auburn University
B. Taterchuck

Chalmers University of Technology
L. Sjölin

City University of New York
M. An
C. Lu

City University of New York (Brooklyn)
H. Homma

Chinese Academy of Sciences
Q. Lin

College of William and Mary
E. Schoe
R. Wright

Colorado School of Mines
N. Wada

Columbia University
G. Luke
Y. Uremura

Florida International U.
W. Jones

Georgetown University
W. Clinton

Goethe University
W. Baur
A. Bieniok

Harvard University
T. Chupp
J. Richardson
E. Wasserman

Iowa State University
A. Goldman
R. Barnes

Istanbul Tech. University
R. Demiralp

John Carroll University
J. Trivisonno

Johns Hopkins University
C. L. Chien
M. Cieplak
D. Musser
F. Streitz
R. Viscidi
T. Wilson
G. Xiao

Kyoto Institute of Technology
H. Kurokawa
M. Shibayama
Q. Tran-Cong

Kyoto University (Japan)
H. Hasegawa
T. Hashimoto
H. Jinnai
S. Sakurai

Lehigh University
A. Klein
L. Sperling
S. Yang
J. Yoo

M.I.T.
R. Birgeneau
M. Dresselhaus
S. Haile
J. Speck
B. Wuensch

McMaster University
W. Clarke
R. Barr

Miami University (Ohio)
J. Cantrell

Michigan State University
T. Pinnavaia
S. Solin

Nagoya University
Y. Matsushita
Y. Mogi
K. Mori
Y. Muroga
M. Nagasawa
I. Nodo
R. Saguchi
Y. Takahashi

Northwestern University
J. Barker
P. Jemian
J. Weertman

Oklahoma State University
B. Ackerson

Penn State University
L. Pilione
J. Yehoda

Princeton University
W. Graessley

Purdue University
A. Overhauser

Rochester Institute of Technology
M. Kotlarchyk

Rutgers University
R. Gerhardt

San Jose State University
P. Englert

Scottish Universities Research Reactors
R. Scott

Temple University
J. Crow
C.-S. Jee
A. Kebede
T. Mihalisin

Texas A&M University
B. Grazman
E. Schweikert

University of Antwerp (Belgium)
K. Michel
C. Bostoen

University of California (Davis)
P. Klavins
J. Liu
R. Shelton

University of California (Irvine)
V. Guinn

University of California
(Santa Barbara)
  S. Cox
  D. Klingensmith
  E. Mader
  R. Odette
  G. Stucky

University of California (San Diego)
  J. Arnold
  A. Berkowitz
  J. Ferreira
  B. Lee
  B. Maple
  J. Neumeier
  K. Nishiizumi
  K. Yang

University College (London)
  F. Beech

University of Delaware
  J. Beamish
  W. Dubner

University of Exeter (U.K.)
  R. Slade

University of Florida
  S. Nagler

University of Guelph (Canada)
  F. Hallett

University of Houston
  W.-K. Chu
  S. Moss
  L. Reinhard
  J. Robertson

University of Illinois (Urbana)
  R. Beach
  R. Du
  J. Dura
  C. Flynn
  J. Kordas
  A. Matheny
  G. Moore
  H. Morkoç
  P. Reimer
  M. Salamon

A. Salvador
F. Tsui
H. Zabel

University of Illinois (Chicago)
  M. Said
  J. Kouvel

University of Maryland
  H. Ammon
  A. Cargill
  C.-H. Chen
  O. Chitale
  T. Clinton
  F. Divita
  G. Gordon
  D. Gretz
  M. Han
  W. Li
  Z. Li
  J. Lynn
  E. Mackey
  J. Nicol
  J. Ondov
  J. Peng
  T. Quinn
  B. Schmid
  S. Skanthakumar
  W. Sumarlin
  J. Valette-Silver
  W. Walters
  J. Weber
  H. Zhang

University of Massachusetts
  A. Hanyu
  L. Jong
  R. Stein

University of Milan (Italy)
  M. Zocchi

University of Michigan
  D. Vincent
  R. Fleming

University of Minnesota
  F. Bates
  M. Foster
  M. Sikka

University of Missouri (Columbia)
R. Berliner
H. Kaiser
A. Krawitz
G. Schupp
S. Werner
D. Worcester

University of Missouri (Rolla)
P. Lindemuth
R. Venable

University of NSW (Australia)
B. Hunter

University of Nancy (France)
C. Du Four
P. Mangin
G. Marchal
M. Vergnat

University of New Hampshire
N. Blakemore
R. Blakemore
Y. Gorby

University of North Carolina
N. Parikh
M. Swanson

University of Notre Dame
J. Furdyna
T. Giebultowicz
P. Klosowski
H. Luo
N. Samarth

University of Pennsylvania
P. Davis
R. Egami

University of Pittsburg
W. Goldberg

Universite Pierre et Marie Curie (France)
Ph. Depondt

University of Sussex (U.K.)
J. Byrne
P. Dawber
J. Spain

University of Vermont
T. Flanagan

University of Virginia
T. Williamson

University of Washington
J. Billman
B. Heckel
E. Kaler
W. Zoller

University of West Virginia
R. Kannan
M. Seehra

Utah State University
T. Isenhour

Yale University
J. Flanagan

AT&T Bell Laboratories
R. Cava
S. Cheong
G. Fredrickson
J. Krajewski
P. Marsh
J. Mitchell
D. Murphy
W. Peck
W. Rhodes
J. Riley
J. Rosedale
L. Schneemeyer
S. Sunshine
J. Waszazak
S. Yegnasubramanian

Aeroject Electrosystems
R. Bowman

Aerospace Corporation
J. Knudsen

Allied Signal Corporation
T. Barden
G. Fish
C. Parker

Atomic Energy of Canada, LTD
  W. Lennard

Battelle Pacific Northwest
Laboratories
  F. Brauer
  G. Dudder
  G. Endres
  M. Failey

Bellcore
  S. Allen
  G. Hull
  P. Miceli
  C. Palmstrøm
  K. Remschnig
  J. Tarascon

Charles Evans & Assoc.
  R. Fleming

CIDTECH
  J. Carbone
  M. Wadsworth

John Deere Product Eng. Ctr.
  T. Cordes

Directed Technologies, Inc.
  N. Chesser

Dow Chemical
  R. Bubeck

E. I. DuPont de Nemours Co.
  J. Parise
  M. Subramanian

Eastman Kodak
  M. Landry
  J. Lavine
  J. O'Reilly
  J. Russell
  C. Swanson
  J. Tritten
  H. Yang
  G. Zenner

Exxon
  B. Abeles
  L. Fetters
  J. Huang
  G. Hughes
  M. Kim
  K. Liang
  M. Lin
  D. Lohse
  R. Overfield
  E. Sirota

GE Corporate R&D
  R. Rowe

GE Plastics
  J. Schroeder

GEN Corp.
  I. Hargis

GTE Laboratories
  G. Hamill

W. R. Grace
  R. Wormsbecker

Hughes, Malibu
  R. Wilson

IBM (San Jose)
  S. Anastasiadis
  G. Hadziioannou
  A. Menelle
  T. P. Russell

Imperial Chemical Industries
  J. Howard
  H. Stanley

Intel Corporation
  J. Cox

Mobil Oil
  A. Moini

Optoline Corp.
  J. Bradshaw

Polaroid Corp.
  S. Roy

Southwest Research Inst.
  R. Page

SRI, Inc.
  S. Johnson

Texaco Research Center
  E. Sheu

Texas Instrument
  T. Hossain

E. PUBLICATIONS

Anastasiadis, S. H.; Russell, T. P.; Satija, S. K.; Majkrzak, C. F, "The Morphology of Symmetric Diblock Copolymers as Revealed by Neutron Reflectivity," J. Chem. Phys. $\underline{92}$, 5677 (1990).

Anderson, I. S.; Berk, N. F.; Rush, J. J.; Udovic, T. J.; Barnes, R. G.; Richter, D.; Magerl, A., "Rapid Low Temperature 'Hopping' of Hydrogen in a Pure Metal: The ScH_x System," Phys. Rev. Lett. $\underline{65}$, 1439 (1990).

Ammon, H.; Choi, L.; Damvarapu, C. S.; Iyer, R. S.; Alster, S., "Stucture of Cubane-1, 4-diammonium Bis-(trinitromethide)," Acta Crystallogr. C $\underline{46}$, 295 (1990).

Ankner, J. F.; Zabel, H.; Neumann, D. A.; Majkrzak, C. F.; Matheny, A.; Dura, J. A.; Flynn. C. P., "Neutron Reflectivity Study of Gd-Y Interface," in Neutron Scattering for Material Science, edited by S. M. Shapiro, S. C. Moss, and J. D. Jorgensen, Mater. Res. Soc. Symp. Proc., Vol. 166 (Materials Research Society, Pittsburgh, 1990), p. 109.

Ankner, J. F.; Zabel, H.; Neumann, D. A.; Majkrzak, C. F.; Dura, J. A.; Flynn, C. P., "Grazing-Angle Neutron Diffraction," J. Phys. (Paris) $\underline{50}$, C7-189 (1989).

Bashir-Hashemi, A.; Ammon, H. L.; Choi, C. S., "Chemistry and Structure of Phenylcubanes," J. Org. Chem. $\underline{55}$, 416 (1990).

Baur, W. H.; Bieniok, A.; Shaaon, R. D.; Prince, E., "Neutron Powder Diffraction Study and Thermogravimetry of Sodium Cesium Zeolite Rho," Z. Kristallogr. $\underline{187}$, 253 (1989).

Beach, R. S.; Borchers, J.; Salamon, M. B.; Du, R.; Flynn, C. P., "Observation of Intermediate Spin States in Er/Y Superlattices," J. Appl. Phys. $\underline{67}$, 5710 (1990).

Berk, N. F.; Glinka, C. J.; Haller, W.; Sander, L. C., "Analysis of SANS from Controlled Pore Glasses" in Neutron Scattering for Materials Science, edited by S. M. Shapiro, S. C. Moss, and J. D. Jorgensen, Mater. Res. Soc. Symp. Proc., Vol. 166 (Materials Research Society, Pittsburgh, 1990), p. 409.

Berk, N. F.; Rush, J. J.; Udovic, T. J.; Anderson, I. S., "Anomalous Hydrogen Dynamics in Rare Earth Metals," J. Less-Common Met. (in press).

Biswas, R.; Bouchard, A. M.; Kamitakahara, W. A.; Grest, G. S.; Soukoulis, C. M., "Vibrational Localization and Vibrational Spectra in Amorphous Silicon," in Atomic Scale Calculations in Materials Science, edited by J. Tersoff, D. Vanderbilt, and V. Vitek, Mater. Res. Soc. Symp. Proc., Vol. 141 (Materials Research Society, Pittsburgh, 1989), p. 213.

Boolchand, P.; Enzweiler, R. N.; Cappelletti, R. L.; Kamitakahara, W. A.; Cai, Y.; Thorpe, M. F., "Vibrational Thresholds in Covalent Networks," Solid State Ionics $\underline{39}$, 81 (1990).

Bowman, R. C.; Maeland, A. J.; Venturini, E. L.; Rush, J. J.; Cantrell, J. S., "Studies of the Structure and Properties of Amorphous $a\text{-}Zr_{76}Fe_{24}H_x$," Z. Phys. Chem. $\underline{163}$, 373 (1989).

PUBLICATIONS

Bowman, R. C.; Torgeson, D. R.; Barnes, R. G.; Maeland, A. J.; Rush, J. J., "Relationship of Hydrogen Site Occupancy to Diffusion Behavior in Crystalline and Amorphous Zr_2PdH_x," Z. Phys. Chem. <u>163</u>, 203 (1989).

Bradford, D.; Hammouda, B.; Bubeck, R. A.; Schroeder, J. R.; Glinka, C. J.; Thiyagarajan, P., "Deformations of Polystyrene Chains Upon Hot Stretching," J. Appl. Crystallogr. <u>23</u>, 1 (1990).

Carstanjen, H.-D.; Huang, X. Y.; Kieninger, W.; Kirchheim, R.; Rush, J. J.; Udovic, T. J.; Glinka, C., "A Neutron Scattering Study of Deuterium Trapping by Dislocations," Z. Phys. Chem. Neue Folge <u>163</u>, 203 (1989).

Cava, R. J.; Marezio, M.; Krajewski, J. J.; Peck, W. F.; Santoro, A.; Beech, F., "Neutron Powder Diffraction Study of $Pb_2Sr_2YCu_3O_8$, the Prototype of a New Family of Superconductors," Physica C <u>157</u>, 272 (1989).

Cava, R. J.; Santoro, A.; Krajewski, J. J.; Fleming, R. M.; Waszczak, J. V.; Peck, W. F.; Marsh, P., "The Crystal Structure of the 60K Superconductor $La_{1.6}Sr_{0.4}CaCu_2O_{6\pm d}$," Physica C (in press).

Casella, R. C., "Comparison of Interplanar-Boson-Exchange Models of High-Temperature Superconductivity--Possible Experimental Tests," Appl. Phys. Lett. <u>55</u> (9), 908 (1989).

Chaiken, A.; Dresselhaus, M. S.; Orlando, T. P.; Dresselhaus, G.; Tedrow, P. M., Neumann, D. A.; Kamitakahara, W. A., "Anisotropic Superconductivity in C_4KHg," Phys. Rev. B <u>41</u>, 71 (1990).

Choi, C. S.; Prask, H. J.; Ostertag, C. P., "Texture Study of Magnetically Aligned $YBa_2Cu_3O_7$ - Type Materials by Neutron Diffraction," J. Appl. Crystallogr. <u>22</u>, 465 (1989).

Cieplak, M. Z.; Xiao, G.; Chien, C. L., Stalick, J. K.; Rhyne, J. J., "Unexpected Effects of Gold on the Structure, Superconductivity, and Normal-State of $YBa_2Cu_3O_7$," Appl. Phys. Lett. <u>57</u>, 934 (1990).

Cieplak, M. Z.; Xiao, G.; Bakhshai, A.; Artymowicz, D.; Bryden, W.; Chien, C. L.; Stalick, J. K.; Rhyne, J. J., "Incorporation of Gold Into YBa Cu O: Structure and T Enhancement," Phys. Rev. B (in press).

Clinton, T. W.; Lynn, J. W., "Magnetic Ordering of Er in Powder and Single Crystals of $ErBa_2Cu_3O_7$," Physica C (in press).

Collins, D. M.; Prince, E., "Exponential Density: Exact Fitting of Structure Moduli by Entropy Maximization," Proc. of the International School on Crystallogr. Computing (in press).

Copley, J. R. D., "The Effects of Chopper Jitter on the Time-Dependent Intensity Transmitted by Multiple-Slot Multiple Disk Chopper Systems," in <u>Advanced Neutron Sources 1988</u>, edited by D. K. Hyer, The Inst. Phys. Conf. Series, Vol. 97 (Institute of Physics, Bristol and New York, 1989), p. 327-339.

Copley, J. R. D.; Mildner, D. F. R., "Production of Intense Clean Neutron Beams for Neutron Absorption Experiments," Trans. Am. Nucl. Soc. <u>61</u>, 105 (1990).

Copley, J. R. D., "An Analytical Method to Characterize the Performance of Multiple Section Straight-Sided Neutron Guide Systems," Nucl. Instrum. & Methods in Phys. Res. A <u>287</u>, 363-373 (1990).

Copley, J. R. D., "On the Use of Acceptance Diagrams to Calculate the Performance of Multiple Section Straight-Sided Neutron Guide Systems," in Advanced Neutron Sources 1988, edited by D. K. Hyer, The Inst. Phys. Conf. Series, Vol. 97 (Inst. of Physics, Bristol and New York, 1989), p. 821-828.

Copley, J. R. D., "Acceptance Diagram Analysis of the Performance of Vertically Curved Neutron Monochromators," Nucl. Instrum. & Methods in Phys. Res. A (in press).

Copley, J. R. D., "Optimized Design of the Chopper Disks and the Neutron Guide in a Disk Chopper Neutron Time-of-Flight Spectrometer," Nuclear Instruments & Methods in Phys. Res. A 291, 519-532 (1990).

Erwin, R. W., "Domain Size and Spin Waves in a Rentrant Spin Glass," J. Appl. Phys. 67, 5229 (1990).

Erwin, R. W.; Rhyne, J. J.; Borchers, J. A.; Salamon, M. B.; Du, R.; Flynn, C. P., "Magnetoelasticity in Rare-Earth Multilayers and Films," in Neutron Scattering for Material Science, edited by S. M. Shapiro, S. C. Moss, and J. D. Jorgensen, Mater. Res. Soc. Symp. Proc., Vol. 166, (Materials Research Society, Pittsburgh, 1990), p. 133.

Erwin, R.; Rhyne, J. J.; Borchers, J.; Du, R.; Salamon, M.; Flynn, C. P., "Magnetoelasticity in Rare-Earth Superlattices and Films," Physica B 159, 111 (1989).

Fan, Y.; Neumann, D. A.; Solin, S. A.; Kim, H.; Pinnavaia, T.J., "Elastic and Inelastic Neutron Scattering Study of Hydrogenated and Deuterated Trimethylammonium Pillared Vermiculite Clays," J. Chem. Phys. (in press).

Felcher, G.P.; Schneider, D.; Farnoux, B.; Majkrzak, C.; Spooner, S.; Timmins, P.; White J.; Wignall, G., "Small-Angle Scattering and Reflectometry," in Proceedings of the Oak Ridge National Laboratory/ Brookhaven National Laboratory Workshop on Neutron Scattering Instrumentation at High-Flux Reactors, Report CONF-8906311, (1990), p. 39-47.

Fernandez-Baca, J. A.; Nicklow, R. M.; Tun, Z.; Rhyne, J. J., "Magnetic Excitations in Thulium Metals," J. Appl. Phys. 67, 5283 (1990).

Fernandez-Baca, J. A.; Hennion, M.; Hennion, B.; Rhyne, J. J.; Fish, G. E., "Spin Dynamics of Amorphous $Fe_{90-x}Ni_xZr_{10}$," J. Appl. Phys. 67, 5223 (1990).

Fischer, R.; Baur, W.; Shannon, R.; Parise, J.; Faber, J.; Prince, E., "New, Different Forms of Ammonium Loaded, and Partly Deammoniated Zeolite Rho Studied by Neutron Powder Diffraction," Acta Crystallogr. C 45, 983 (1989).

Flynn, C. P.; Borchers, J. A.; Demers, R. T.; Du, R.-R.; Dura, J. A.; Klein, M. V.; Kong, S. H.; Salamon, M. B.; Tsui, T.F.; Yadavalli, S.; Zhu, X.; Zabel, H.; Cunningham, J. E.; Erwin, R. W.; and Rhyne, J. J.; in Proceedings of the MRS Conference on Advanced Materials, Tokyo, 1988 edited by Yamamoto Ryoichi, J. Phys. (Paris) Collog. (in press).

Forano, C.; Slade, R. C.; Krogh, E.; Andersen, I. G.; Prince, E., "Neutron Diffraction Determination of Full Structures of Anhydrous Li-X and Li-Y Zeolytes," J. Solid State Chem. 82, 95 (1989).

Giebultowicz, T. M.; Klosowski, P.; Rhyne, J. J.; Udovic, T. J.; Furdyna, J. K.; Giriat, W., "Magnetic Exchange Interactions in Co-Based II-VI Diluted Magnetic Semiconductors: $Zn_{1-x}Co_xS$," Phys. Rev. B $\underline{41}$, 504 (1990).

Giebultowicz, T. M.; Klosowski, P.; Rhyne, J. J.; Samarth, N.; Luo, H.; Furdyna, J. K., "Neutron Diffraction Studies of $Cd_{1-x}Mn_xSe$ Epilayers and ZSe/MnSe Multilayers," in <u>Neutron Scattering for Material Science</u>, edited by S. M. Shapiro, S. C. Moss, and J. D. Jorgensen, Mater. Res. Soc. Symp. Proc., Vol. 166 (Materials Research Society, Pittsburgh, 1990), p. 115.

Giebultowicz, T. M.; Klosowski, P.; Samarth, N.; Luo, H.; Rhyne, J. J.; Furdyna, J. K., "Antiferromagnetic Phase Transition in $Cd_{1-x}Mn_xSe_x$ Epilayers," Phys. Rev. B $\underline{42}$, 2582 (1990).

Giebultowicz, T. M.; Rhyne, J. J.; Furdyna, J. K.; Klosowski, P., "Inelastic Neutron Scattering Studies of II-VI Diluted Magnetic Semiconductors," J. Appl. Phys. $\underline{67}$, 5096 (1990).

Glinka, C. J.; Sander, L. C.; Wise, S. A.; Berk, N. F., "Characterization of Chemically Modified Pore Surfaces by Small Angle Neutron Scattering," in <u>Neutron Scattering for Materials Science</u>, edited by S. M. Shapiro, S. C. Moss, and J. D. Jorgensen, Mater. Res. Soc. Symp., Vol. 166 (Materials Research Society, Pittsburgh, 1990), p. 415.

Hammouda, B.; Schupp G.; Maglic, S., "QEGS from Polydimethylsiloxane in Benzene Solutions," J. Chem. Phys. $\underline{93}$, 5473 (1990).

Hammouda, B., "Treatment of Asymmetric SANS Data," J. Polym. Sci., Polym. Phys. Ed. B $\underline{27}$, 1971 (1989).

Hammouda, B.; Yelon, W. B.; Lind, A. C.; Hansen, F., "SANS From a BPAC/DMS Block Copolymer Under Uniaxial External Stretch," Macromol. $\underline{22}$, 418 (1989).

Hempelmann, R.; Richter, D.; Rush, J. J.; Rowe, J. M., "Hydrogen Site Distribution in the Alloy System $Nb_{100x}V_xH_y$ Studied by Means of Neutron Vibrational Spectroscopy," J. Less-Common Met. (in press).

Himes, V. L.; Mighell, A. D.; Stalick, J. K.; Young, S. L.; Carr, M. J.; Lyman, C. E.; Anderson, R.; Holomany, M. A.; Jenkins, R., Elemental and Interplanar Spacing Index for Phase Identification by Electron or X-Ray Diffraction, (U.S. Dept. of Commerce, NIST and the International Centre for Diffraction Data, 1989), 880 pages.

Kamitakahara, W. A., "Low Frequency Vibratonal Spectra of Amorphous Solids," in <u>Phonons 89</u>, edited by S. Hunklinger, W. Ludwig, and G. Weiss, (World Scientific, New Jersey, 1990), p. 387.

Kamitakahara, W. A.; Biswas, R.; Bouchard, A. M.; Gompf, F.; Suck, J. B., "Vibrational Spectra for Hydrogenated Amorphous Semiconductors," in <u>Neutron Scattering for Material Science</u>, edited by S. M. Shapiro, S. C. Moss, and J. D. Jorgensen, Mater. Res. Soc. Symp. Proc., Vol. 166 (Materials Research Society, Pittsburgh, 1990), p. 361.

Kirchheim, R.; Kieninger, W.; Huang, X.Y.; Filipek, S. M.; Rush, J. J.; Udovic, T. J., "Hydrogen in Amorphous Ni-Zr and Ni-Ti Alloys," J. Less- Common Met. (in press).

Krueger, S.; Chen, S.-H.; Hofrichter, J.; Nossal R., "Small Angle Neutron Scattering Studies of HbA in Concentrated Solutions," Biophys. J. (in press).

Krueger, S.; Lynn, J. W.; Russell, J. T.; Nossal, R., "Small-Angle Neutron Scattering Method for In Situ Studies of the Dense Cores of Biological Cells and Vesicles: Application to Isolated Neurosecretory Vesicles," J. Appl. Crystallogr. 22, 546 (1989).

Krueger, S.; Long, G. G.; Page, R. A., "Multiple Small Angle Neutron Scattering Characterization of the Densification of Alumina," in Neutron Scattering for Materials Science, edited by S. M. Shapiro, S. C. Moss, and J. D. Jorgensen, Mater. Res. Soc. Symp. Proc., Vol. 166 (Materials Research Society, Pittsburgh, 1990), p. 61.

Krueger, S.; Olson, G. J.; Rhyne, J. J.; Blakemore, R. P.; Gorby, Y. A.; Blakemore, N., "Small Angle Neutron and X-Ray Scattering From Magnetite Crystals in Magnetoactic Bacteria," J. Magn. Magn. Mater. 82, 17 (1989).

Krueger, S.; Olson, G. J.; Rhyne, J. J.; Blakemore, R. P.; Gorby, Y. A.; Blakemore, N., "Small Angle Neutron Scattering From Bacterial Magnetite," J. Appl. Phys. 67, 4475 (1990).

Krueger, S.; Zaccai, G.; Wlodawer, A.; Langowski, J.; O'Dea, M.; Maxwell, A., Gellert, M., "Neutron and Light-Scattering Studies of DNA Gyrase and Its Complex With DNA," J. Mol. Biol. 211, 211 (1990).

Lewicki, A.; Schindler, A. I.; Furdyna, J. K.; Giebultowicz, T. M., "Magnetic Properties of Co-Based Diluted Magnetic Semiconductors," in Diluted Magnetic Semiconductors, edited by M. Jain, World Scientific (in press).

Li, W. H.; Lynn J. W.; Skanthakumar, S.; Clinton, T. W.; Kebede, A.; Jee, C. S.; Crow, J. E.; Mihalisin, T., "Magnetic Order of Pr in $PrBa_2Cu_3O_7$," Phys. Rev. B 40, 5300 (1989).

Li, W. H.; Lynn, J. W.; Stanley, H. B., Udovic, T. J.; Shelton, R. N.; Klavins, P., "Crystal Field Splittings in the Cubic Magnetic Superconductors $HoPd_2Sn$ and $ErPd_2Sn$," Phys. Rev. B 39, 4119 (1989).

Li, W. H.; Lynn, J. W.; Fish, Z., "Magnetic Order of the Cu Planes and Chains in $NdBa_2Cu_3O_{6+x}$," Phys. Rev. B 41, 4098 (1990).

Lin, M.; Sinha, S. K.; Huang, J. S.; Abeles, B.; Johnson, J. K.; Drake, J. M.; Glinka, C. J., "A SANS Study of Capillary Condensation in Porous Media," in Neutron Scattering for Materials Science, edited by S. M. Shapiro, S. C. Moss, and J. D. Jorgensen, Mater. Res. Soc. Symp. Proc., Vol. 166 (Materials Research Society, Pittsburgh, 1990), p. 449.

Lindemuth, P.; Hammouda, B.; Duck, J. R.; Blum, F.; Venable, R., "PGSE-NMR and SANS From TPB Based Microemulsions," in Macromolecular Liquids, edited by C. R. Safinya, S. Safran, and P. A. Pincus, Mater. Res. Soc. Symp. Proc., Vol. 177 (Materials Research Society, Pittsburgh, 1990), p. 117.

Lindemuth, P.; Hammouda, B.: Venable, R., "SANS from TPB based Microemulsions," J. Phys. Chem. J. Phys. Chem. 94, 8247 (1990).

Long, G. G.; Krueger, S., "Multiple Small Angle Neutron Scattering Characterization of the Densification of Ceramics: Application to Microporous Silica," J. Appl. Crystallogr. 22, 539 (1989).

Long, G. G.; Krueger, S.; Black, D. R.; Cline, J. P.; Jemian; P. R. Gerhardt, R. A., "Small Angle Neutron Scattering and Small Angle X-Ray Scattering From Bulk Microporous Silica," in <u>Neutron Scattering for Materials Science</u>, edited by S. M. Shapiro, S. C. Moss, and J. D. Jorgensen, Mater. Res. Soc. Symp. Proc., Vol. 166 (Materials Research Society Pittsburgh, 1990 p. 421.

Long, G. G.; Krueger, S.; Jemian, P. R.; Black, D. R.; Burdette, H. E.;Cline, J. P.; Gerhardt; R. A., "Small Angle Scattering Determination of the Microstructure of Porous Silica Precursor Bodies," J. Appl. Crystallogr. (in press).

Lynn, J. W., "Magnetic Order and Spin Fluctuations in Oxide Superconductors," Physica B <u>163</u>, 69 (1990).

Lynn, J. W.; Clinton, T. W.; Li, W. H.; Erwin, R. W.; Liu, J. Z.; Vandervoort, D.; Shelton, R. N., "2D and 3D Magnetic Behavior of Er in $ErBa_2Cu_3O_7$," Phys. Rev. Lett. <u>63</u>, 2606 (1990).

Lynn, J. W.; Clinton, T. W.; Li, W. H.; Erwin, R. W.; Liu, J. Z.; Shelton, R. N.; Klavins, P., "Two-Dimensional Magnetic Order of Er in $ErBa_2Cu_3O_7$," J. Appl. Phys. <u>67</u>, 4533 (1990).

Lynn, J. W.; Li, W. H.; Trevino, S. F.; Fish, Z., "Pressure Dependence of the Cu Magnetic Order in $RBa_2Cu_3O_{6+x}$," Phys. Rev. B <u>40</u>, 5172 (1989).

Lynn, J. W.; Sumarlin, I. W.; Skanthakumar, S.; Li, W. H.; Shelton, R. N.; Peng, J. L.; Fisk, Z.; Cheong, S. W., "Magnetic Ordering of Nd in $(Nd,Ce)_2CuO_4$," Phys. Rev. B <u>41</u>, 2569 (1990).

Majkrzak, C. F.; Kwo, J.; Hong, M.; Yafet, Y.; Gibbs, Doon; Chien, C. L.; Bohr, J., "Magnetic Rare Earth Superlattices," Adv. Phys. (in press).

Majkrzak, C. F.; Felcher, G. P., "Neutron Scattering Studies of Surfacers and Interfaces," MRS Bulletin (in press).

Majkrzak, C. F.; Satija, S.; Neumann, D. A.; Rush, J. J.; Lashmore, D.; Johnson, C.; Bradshaw, J; Passell, L.; Dinardo, R., "Determination of Hydrogen Density Profiles in Thin Films and Multilayers by Neutron Reflection," in <u>Neutron Scattering for Materials Science</u>, edited by S. M. Shapiro, S. C. Moss, and J. D. Jorgensen, Mater. Res. Soc. Symp., Vol. 166, (Materials Research Society, Pittsburgh, 1990), p. 127.

Mangin, P.; Boumazouza, D.; George, B.; Rhyne, J. J.; Erwin, R. W., "Static and Dynamic Properties of the $(Fe_xCr_{1-x})_{75}P_{15}C_{10}$ Reentrant Spin Glass Amorphous Alloy," Phys. Rev. B <u>40</u>, 11123 (1989).

Marezio, M.; Santoro, A.; Capponi, J. J.; Hewat, E. A.; Cava, R. J.; Beech, F., "Crystal Structure, Atomic Ordering and Charge Localization in $Pb_2Sr_2YCu_3O_{8+Z}$(M=1.47)," Physica C <u>169</u>, 401 (1990).

McKinnon, W. R.; Tselepis, E.; LaPage, Y.; McAlister, S. P.; Pleziter, C.; Tarascon, J. M.; Miceli, P. F.; Ramesh, R.; Hull, G. W.; Waszczak, J. V.; Rhyne, J. J.; Neumann, D. A., "Structure and Magnetism of $Bi_2(Sr,Ca)_2MnO_{6+y}$," Phys. Rev. B <u>41</u>, 4489 (1990).

Miceli, P. F.; Tarascon, J. M.; Bagley, B. G.; Greene L. H.; Barboux, P.; Hull, G. W.; Giroud, M.; Rhyne, J. J.; Neumann, D. A., "Magnetic Properties of Some High T_c Superconducting Compounds," in High Temperature Superconductors, edited by T. Akachi, J. A. Cogordan, and A. A. Valladares, Prog. in High Temp. Superconductivity, Vol. 20, (World Scientific Publishing, Singapore, 1989), p. 89.

Miceli, P. F.; Tarascon, J. M.; Greene, L. H.; Rhyne, J. J.; Neumann, D. A., "Magnetic Ordering In $YBa_2Cu_{3-x}M_xO_{6+y}$," Physica C 162, 1267 (1989).

Mighell, A. D.; Himes, V. L., "A New Method for Phase Identification for Electron Microscopists," J. Electron Microscopy Technique. 16, 155 (1990).

Moon, R.M.; Fernandez-Baca, J.A.; Hewat A.; Jorgensen, J.D.; Kamitakahara, W.; Powell, B.M.; Yelon, W.B., "Powder/Liquids Diffraction," in Proceedings of the Oak Ridge National Laboratory/ Brookhaven National Laboratory Workshop on Neutron Scattering Instrumentation at High-Flux Reactors, Report CONF-8906311, (1990), p. 31-37.

Mozer, B.; Bendersky, L. A.; Boettinger, W. J.; Rowe, R. G.; "Neutron Powder Diffraction Study of the Orthorhombic Ti_2AlNb Phase," Scripta Metallurgia (to be published).

Neumann, D. A.; Nicol, J. M.; Rush, J. J.; Wada, N.; Fan, Y.; Kim, H.; Solin, S. A.; Pinnavaia, T. J.; Trevino, S. F., "Neutron Scattering Study of Layered Silicates Pillared With Alkylammonium Ions," in Neutron Scattering for Materials Science, edited by S. M. Shapiro, S. C. Moss, and J. D. Jorgensen, Mater. Res. Soc. Symp. Proc., Vol. 166 (Materials Research Society, Pittsburgh, 1990), p. 397.

Neumeier, J . J.; Bjornholm, T.; Maple, M. B.; Rhyne, J. J.; Gotaas, J. A., "Neutron Diffraction Study of Pr Valence and Oxygen Ordering in the $Y_{1-x}Pr_xBa_2Cu_3O_{7-d}$ System," Physica C 166, 191 (1990).

Nicol, J. M.; Udovic, T. J.; Rush, J. J.; Cox, S. D.; Stuckey, G. D., "Inelastic Neutron Scattering Studies of Nonlinear Optical Materials: p- Nitroaniline Adsorbed in ALPO-5," in Neutron Scattering for Materials Science, edited by S. M. Shapiro, S. C. Moss, and J. D. Jorgensen, Mater. Res. Soc. Symp. Proc., Vol. 166 (Materials Research Society, Pittsburgh, 1990), p. 367.

O'Connor, C. L., editor, "NIST Reactor: Summary of Activities July 1988 Through June 1989," National Institute of Standards and Technology Tech. Note 1272, Dec. 1989.

Passell, L.; Carpenter, J. M.; Copley, J. R. D.; Dorner, B.; Ito, Y., "Time-of-Flight," in Proceedings of the Oak Ridge National Laboratory/ Brookhaven National Laboratory Workshop on Neutron Scattering Instrumentation at High- Flux Reactors, Report CONF-8906311, (1990), p. 15-23.

Parise, J. B.; Torardi, C. C.; Subramanian, M. A.; Gopalakrishnan, J.; Sleight, A. W.; Prince, E., "Superconducting $Tl_{2.0}Ba_{2.0}CuO_{6+d}$: A High Resolution Neutron Powder and Single Crystal X-Ray Diffraction Investigation," Physics C 159, 239 (1989).

Prask, H. J. "The Reactor and Cold Neutron Facility at NIST," Neutron News 1 (1), 9 (1990).

Prask, H.; Choi, C. S., "Residual Stress Measurements by Means of Neutron Diffraction," in Neutron Scattering for Materials Science, edited by S. M. Shapiro, S. C. Moss, and J. D. Jorgensen, Mater. Res. Soc. Symp. Proc., Vol. 166 (Materials Research Society, Pittsburgh, 1990), p. 293.

Prince, E., "Mathematical Aspects of Rietveld Refinement," Proceedings of the International Workshop on the Rietveld Method, Petten, The Netherland, Oxford University Press (in press).

Prince, E.; Evans, H. T., "The Crystal Structure of Ammonium Paradodecatunstat Tetrahydte by Neutron Diffraction," Acta Crystallogr. C (in press).

Prince, E.; Sjölin, L., "Maximum Entropy as a Phasing Tool in Macromolecular Crystallography," Chemometrics and Intelligent Laboratory Systems (in press).

Rhyne, J. J.; Erwin, R. W.; Borchers, J.; Salamon, M. B.; Du, R.; Flynn, C. P.; "Magentic Multilayers," Phys. Scr. T29, 31 (1989).

Rhyne, J. J.; Majkrzak, C. F., "The NIST Cold Neutron Research Facility and Magnetic Neutron Scattering," J. Appl. Phys. 67, 5693 (1990).

Rowe, J. M.; Rorer, D. C., "Existing Cold Sources at U. S. Reactors." Proceedings of International Workshop on Cold Neutron Research Sources (in press).

Rush, J. J.; Flanagan, T. B.; Craft, A. P.; Clewley, J. D.; Sakamoto, Y., "The Optic Mode Frequencies and Solubilities of Hydrogen in Ordered and Disordered Pd_3Mn," J. Phys.: Condens. Matter 1, 5095 (1989).

Russell, T.P.; Anastasiadis, S. H.; Satija, S. K.; Majkrzak, C. F., "Temperature Dependence of the Morphology of Thin Diblock Copolymer Films as Revealed by Neutron Reflectivity," in Neutron Scattering for Materials Science, edited by S. M. Shapiro, S. C. Moss, and J. D. Jorgensen, Mater. Res. Soc. Symp. Proc., Vol. 166 (Materials Research Society, Pittsburgh, 1990), p. 145.

Salamon, M. B.; Borchers, J.; Du, R.; Flynn, C. P.; Tsui, F.; Beach, R. S.; Erwin, R. W.; Rhyne, J. J., "Magnetic Properties of Epitaxial Metallic Superlattice," Phy. Scr. (in press).

Santoro, A., "Crystal Chemistry of Superconductors and Related Compounds," in Chemistry of Superconducting Materials, edited by T. A. Vanderah, Noyes publications (in press).

Santoro, A., "Models for Oxygen Ordering and Diffusion in $Ba_2YCu_3O_x$ and $Ba_2YCu_{3-x}M_xO_y$ [M=Fe, Co, Al, Ga]," Proc. 7th CIMTEC Meeting on Superconductors (in press).

Santoro, A., "Defective Structures of $Ba_2YCu_3O_x$ and $Ba_2YCu_{3-y}M_yO_z$, (M = Fe, Co, Al, Ga,...)," in Chemistry of Superconducting Materials, edited by T. A. Vanderah, Noyes publications (in press).

Santoro, A.; Beech, F.; Cava, R. J., "Neutron Powder Diffraction Study of the Structures of $La_{1.9}Ca_{1.1}Cu_2O_6$ and $La_{1.9}Sr_{1.1}Cu_2O_{6+w}$," in Neutron Scattering for Materials Science, edited by S. M. Shapiro, S. C. Moss, and J. D. Jorgensen, Mater. Res. Soc. Symp. Proc., Vol. 166 (Materials Research Society, Pittsburgh, 1990), p. 187.

Santoro, A., "Crystallography" in High Temperature Superconductivity, edited by J. W. Lynn, (Springer-Verlag, New York, 1990), p. 84.

Satija, S. K.; Majkrzak, C. F.; Anastasiadis, S. H.; Russell, T. P., "The Morphology of Symmetric Dieblock Copolymers as Revealed by Neutron Reflectivity" in <u>Neutron Scattering for Materials Science</u>, edited by S. M. Shapiro, S. C. Moss, and J. D. Jorgensen, Mater. Res. Soc. Symp. Proc., Vol. 166 (Materials Research Society, Pittsburgh, 1990), p. 139.

Satija, S. K.; Majkrzak, C. F.; Russell, T. P.; Sinha, S. K.; Sirota, E. B.; Hughes, C. J., "Neutron Reflectivity Study of Block Copolymers Adsorbed From Solution," Macromol. <u>23</u>, 3860 (1990).

Schupp, G.; Hammouda, B.; Hsueh, C. M., "QEGS From Pentadecane," Phys. Rev. A <u>41</u>, 5610 (1990).

Sjölin, L.; Svensson, L.; Prince, E.; Sundell, S., "Phase Inprovement in the Structure Interpretation of Fragment TR_2C From Bull Testis Calmodulin Using Combined Entropy Maximization and Solvent Flattening," Acta Crystallogr. B <u>46</u>, 209 (1990).

Sjölin, L.; Prince, E.; Svensson, L. A.; Gilliland, G. L., "Maximum Entropy Phase Determination for X-Ray Diffraction Data From Crystals of Native Proteins," Science (in press).

Skanthakumar, S.; Li, W. H.; Lynn, J. W.; Kebede, A.; Crow, J. E.; Mihalisin T., "Magnetic Properties of Pr in $PrBa_2Cu_3O_7$," Physica B <u>163</u>, 239 (1990).

Skanthankumar, S; Lynn, J. W., "On the Nature of the Magentic Order and Structure of Nd_2CuO_4," Physica C (to be published).

Skanthakumar, S.; Zhang, H.; Clinton, T. W.; Li, W. H.; Lynn, J. W.; Fisk, Z.; Cheong, S-W., "Magnetic Phase Transitions and Structural Distortion in Nd_2CuO_4," Physica C <u>160</u>, 124 (1989).

Skanthakumar, S.; Zhang, H.; Clinton, T. W.; Sumarlin, I. W.; Li, W. H.; Lynn, J. W.; Fisk, Z.; Cheong, S. W., "Magnetic Phase Transitions in Nd_2CuO_4," J. Appl. Phys. <u>67</u> 4530 (1990).

Slade, R. C. T.; Ramanan, A.; West, B. C.; Prince, E., "The Structure of $V_9Mo_6O_{40}$ Determined by Powder Neutron Diffraction," J. of Solid State Chem. <u>82</u>, 65 (1989).

Stalick, J. K.; Wong-Ng, W., "Neutron Diffraction Study of the "Brown Phase" $BaNd_2CuO_5$," Mater. Lett. <u>9</u>, 401 (1990).

Straty, G. C.; Hanley, H. J. M.; Glinka, C. J., "Shearing Apparatus for Neutron Scattering Studies on Fluids: Preliminary Results for Colloidal Suspensions," J. Stat. Phys. (in press).

Trevino, S. F., "Inelastic Neutron Scattering in Molecular Crystals" in <u>Phonons 89</u>, edited by S. Hunklinger, W. Ludwig, and G. Weiss, (World Scientific, New Jersey, 1990), p. 7.

Tsai, D. H.; Trevino, S. F., "Investigation of Energy Transport in the Detonation Wave and Energy Sharing in Rapid Chemical Reactions," in <u>Chemistry and Physics of Energetic Materials</u>, edited by Surya N. Bulusu, Mathematica and Physical Sciences, Vol. 309 (1989), p. 228.

Udovic, T. J.; Rush, J. J.; Anderson, I. S.; Barnes, R. G., "Hydrogen Vibrational Modes and Anisotropic Potential in α-ScH_x," Phys. Rev. B <u>41</u>, 3460 (1990).

Vergnat, M.; Houssaini, S.; DuFour, C.; Brunson, A.; Marchal, G.; Mangin, Ph.; Erwin, R. W.; Rhyne, J. J.; Vettier, C., "Evidence of Hydrogen Modulation in Si/Si:H Amorphous Multilayers," Phys. Rev. B <u>40</u>, 1418 (1989).

Vergnat, M.; DuFour, C.; Brunson, A.; Houssaini, S.; Marchal, G.; Mangin, P.; Rhyne, J. J.; Erwin, R. W.; Vettier, C., "Multilayers and Low Angle Neutron Scattering," J. Phys. (Paris) $\underline{50}$, C7-202 (1989).

Wada, N.; Kamitakahara, W. A., "Inelastic Neutron and Raman Scattering Studies of Muscovite and Vermiculite Layered Silicates," Phys. Rev. B (in press).

Werner, S. A.; Overhauser, A. W.; Giebultowicz, T. M., "Neutron Diffraction Structure in Potassium Near the [011] and [022] Bragg Points," Phys. Rev. B $\underline{41}$, 12535 (1990)

Yang, K. N.; Ferreira, J. M.; Lee, B. W.; Maple, M. B.; Li, W. H.; Lynn, J. W.; Erwin, R. W., "Antiferromagnetic Ordering in Superconducting and Oxygen-Deficient Non-Superconducting $RBa_2Cu_3O_{7-d}$ Compounds (R = Nd and Sm)," Phys. Rev. B $\underline{40}$, 10963 (1989).

Yethiraj, M.; Robinson, R. A.; Rhyne, J. J.; Gotaas, J. A.; Buschow, K. H. J., "Magnetic and Crystallographic Properties of UNiSn," J. Magn. Magn. Mater. $\underline{79}$, 355 (1989).

Yoo, J. N.; Sperling, L. H.; Glinka, C. J.; Klein A., "Characterization of Film Formation From Polystyrene Latex Particles Via SANS," Macromol. $\underline{23}$, 3962 (1990).

Yu, S. C.; Lynn, J. W., "X-Ray Diffraction Studies of Ni-Cr-Based Amorphous Alloys," Jpn. J. Appl. Phys. $\underline{29}$, 902 (1990).

Zabel, H.; Magerl, A.; Rush, J. J.; Misenheimer, M. E., "Diffusion and Melting in Two Dimensions: A Quasi-Elastic Neutron Scattering Study of Alkali--Metals in Graphite," Phys. Rev. B $\underline{40}$, 7616 (1989).

Zhang, H.; Lynn, J. W.; Li, W. H.; Clinton, T. W.; Morris, D. E., "Two- and Three-Dimensional Magnetic Order of the Rare-Earth Ions in $RBa_2Cu_4O_8$," Phys. Rev. B $\underline{41}$, 11229 (1990).

INDEPENDENT PROGRAMS

Abderrahim H. A., McGarry, E. D., Spiegel, V., "Assessment of the Fast Neutron Sensitivity of Thermoluminescent Gamma Dosimeters," 7th ASTM/Euratom Symposium on Reactor Dosimetry, Strasbourg, France, 27-31 August, 1990.

Bartko, J., Ruddy, F. H., Schoch, K. F., Congedo, T. V., McGarry, E. D., "A Novel On-Line Neutron Dosimeter Based on a Conducting Polymer," 7th ASTM/Euratom Symposium on Reactor Dosimetry, Strasbourg, France, 27-30 August, 1990.

Becker, D. A., "INAA Homogeneity Measurements on the New NIST Leaf Reference Materials," National Institute of Standards and Technology Tech. Note 1272, U.S. Dept. of Commerce, Washington, D.C. pp. 238 (1989).

Becker, P. R., Wise, S. A., Zeisler, R., Alaskan Marine Mammal Tissue Archival Project: "Acquisition and Curation of Alaskan Marine Mammal Tissues for Determining Levels of Contaminants Associated With Offshore Oil and Gas Development," National Atmospheric and Oceanic Administration, Oceans Assessment Division, Report (1989), p. 98.

Becker, P.R., Koster, B.J., Wise, S.A., and Zeisler, R., "Alaskan Marine Mammal Tissue Archival Project," Biol. Trace Elem. Res. 26, 329 (1990).

Becker, D. A., "Standards and Reference Materials for Mercury Analysis by NAA," Trans. Am. Nucl. Soc. 60, 48 (1989).

Blackman, M.J., Vidale, M., "Defining the Inter-Site Variability of Stoneware Bangles at Mohenjo-Daro and Harappa by Neutron Activation Analysis," Proceedings of the South Asian Archaeological Conference, Paris (in press).

Bode, P., Hoffmann, E. L., Lindstrom, R. M., Parry, S. J., Rosenberg, R. J., Practical Aspects of Operating a Neutron Activation Analysis Laboratory (TECDOC-564), Internat. Atomic Energy Agency, Vienna (in press).

Byrne, J., Dawber, P. G., Spain,J. A., Williams, A. P.,Dewey, M. S., Gilliam, D. M., Greene, G. L., Lamaze, G. L., Scott, R. D., Pauwels, J., Eykens, R., Lamberty, A., "Measurement of the Neutron Lifetime by Counting Trapped Protons," Phys. Rev. Lett. 65, 289 (1990).

Byrne, J., Dawber, P. G., Spain, J. A., Dewey, M. S., Gilliam, D. M., Greene, G. L., Lamaze, G. L., Williams, A. P., Pauwels, J., Eykens, R., VanGestel, J., Lamberty, A., Scott, R. D., "Determination of the Neutron Lifetime by Counting Trapped Protons," Nucl. Instrum. & Meth. A 284, 116 (1989).

Carew, J. F., Todosow, M., McGarry, E. D., Grundl, J. A., Kam, F.B.K., Maerker, R. E., Stallmann, F. W., "Status of a New Regulatory Guide on Methods and Assumptions for Determining Pressure Vessel Fluence," 7th ASTM/Euratom Symposium, and presented oral paper on the status of the new draft regulatory guide.

Caroli, S., Iyengar, G. V., Muntau, H., (Eds). Bioelements: Health Aspects, Annali dell'Istituto Superiore di Sanita, 25, (1989).

Cohen, A., White, E., Coxon, V. B., Christensen, R. G., Welsh, M. J., Paule, R. C., Becker, D. A., "Certification of Bilirubin SRM 916a," Fres. Z. Anal. Chem. (in press).

Copley, J.R.D., Stone, C.A., "Neutron Scattering and Its Effect on Reaction Rates in Neutron Absorption Measurements," Nucl. Instr. Meth., A 281, 593 (1989).

Eisenhauer, C. M., "Study of Slab Transmission and Reflection," publication in Nuclear Science and Engineering.

Eisenhauer, C. M., Review of Scattering Corrections for Calibration of Neutron Instruments, Radiation Protection Dosimetry 4, 253, (1989).

Eykens, R., Lamberty, A., "Measurements of the Neutron Lifetime by Counting Trapped Protons," Phys. Rev. Lett. 65, 282 (1990).

Gilliam, D. M., Greene, G. L., Lamaze, G. P., "Absolute Neutron Counting Basedon B-10 Alpha-Gamma Coincidence Methods," Nucl. Instr. and Meth. in Physics Research, A 284, 220 (1989).

Greenberg, R. R., "Recent Advances in Radiochemical Neutron Activation Analysis," Trans. Am. Nucl. Soc. <u>60</u>, 9 (1989).

Greenberg, R.R., Kingston, H.M., Zeisler, R., Woittiez, J.R.W., "Neutron Activation Analysis of Biological Samples With a Pre–Irradiation Separation," Biol. Trace Elem. Res. <u>26</u>, 17 (1989).

Greenberg, R. R., "Determination of Mercury in Biological Materials by Radiochemical Neutron Activation Analysis," Trans. Am. Nucl. Soc. <u>60</u>, 47 (1989).

Greenberg, R. R., Kingston, H. M., Watters, R. L., Jr., Pratt, K. W., "Dissolution Problems With Botanical Reference Materials," Fresenius Z. Anal. Chem. (in press).

Greenberg, R. R., "Analysis of Atmospheric Particulate Samples Via Instrumental Neutron Activation Analysis, "<u>Monitoring Methods for Toxics in the Atmosphere</u> , in Zielinski and Dorko, edited by, ASTM STP 1052, 175 (1990).

Iyengar, G. V., "Multidisciplinary Approaches in Biological Trace Element Research," ACS Symposium Series, No. 445, (in press).

Iyengar, G. V., "Milestones in Biological Trace Element Research," Sci. Total Environ. (in press).

Iyengar, G. V., Kumpulainen, J., Okamoto, K., Morita, M., Hirai, S., and Nomoto, S., "Recent Trends in Analytical Approaches for Trace Element Determinations in Biomedical Investigations," in Essential and Toxic Trace Elements in Health and Disease, A. S. Prasad, edited by, Alan R. Liss, New York, 1990 (in press).

Iyengar, G. V., "Analytical Methodology, Chapter 3 in FAO/WHO/IAEA Report on Trace Elements in Human Nutrition, Geneva/Rome, (in press).

King, S. Q., Gilliam, D. M., Comparison of the Calculated to Measured Values of the Integrated Gamma Dose in the Cavity of a Full-Scale Operating Power Reactor, ASTM-STP (in press).

Lindstrom, R. M., "Analytical Standards and Silicon Analysis," in Analytical Chemistry in Semiconductor Manufacturing: Techniques, Role of Nuclear Methods and Need for Quality Control" (IAEA-TECDOC-512), Internat. Atomic Energy Agency, Vienna, (1989), p. 35.

Lindstrom, R. M., Greenberg, R. R., "Quality Control," in Bode, P., Hoffmann, E. L., Lindstrom, R. M., Parry, S. J., and Rosenberg, R. J., Practical Aspects of Operating a Neutron Activation Analysis Laboratory (TECDOC-564), Internat. Atomic Energy Agency, Vienna (in press).

Lindstrom, R. M., Lutz, G. J., Norman, B. R., "High-Sensitivity Determination of Iodine Isotopic Ratios by Thermal and Fast Neutron Activation," J. Trace Microprobe Tech. <u>8</u> (in press).

Lindstrom, R. M., Byrne, A. R., Becker, D. A., Smodis, B., Garrity, K. M., "Characterization of the Mineral Fraction in Botanical Reference Materials and Its Influence on Homogeneity and Analytical Results," Fresenius Z. Anal. Chem. (in press).

Lindstrom, D. J., Zolensky, M. E., Lindstrom, R. M., "Procedures for Instrumental Neutron Activation Analysis of Individual Cosmic Dust Particles," Lunar and Planetary Science XX, Lunar and Planet. Inst., Houston (1989), p. 574.

PUBLICATIONS

Lindstrom, R. M., "Neutron Beams in Analytical Chemistry," Trans. Am. Nucl. Soc. 61, 132 (1990).

Lindstrom, R. M., Lindstrom, D. J., Slaback, L. A., Langland, J. K., "A Low-Background Gamma Ray Assay Laboratory for Activation Analysis," Nucl. Inst. Methods, (in press).

Mackey, E. A., Anderson, D. L., Gordon, G. E., Lindstrom, R. M., "Effects of Neutron Scattering by Hydrogen on Prompt Gamma Activation Analysis," Trans. Am. Nucl. Soc. 60, 14 (1989).

McGarry, E. D., Grundl, J. A., Carew, J. R., Todosow, M. Kam, F. B. K., Stallmann, F. W., Status of New Regulatory Guide on Methods and Assumptions for Determining Pressure Vessel Fluence, 7th ASTM/Euratom Symposium on Reactor Dosimetry, Strasbourg, France, 27-30 August, 1990.

McGarry, E. D., Grundl, J. A., Carew, J. R., M. Todosow, Kam, F.B.K., Stallmann, Becker, D. A., "Homogeneity and Evaluation of the New NIST Leaf SRMs," J. Micro. Tech. (in press).

Mildner, D. F. R., Carpenter, J. M. "Improvements to the Chebyshev Expansion of Attenuation Correction Factors for Cylindrical Samples," J. Appl. Cryst. 23, (in press).

Mildner, D. F. R., "Comments on 'Design Optimization of a Small-Angle Neutron Scattering Spectrometer," Nucl. Instrum. & Meth. A 290, 259 (1990).

Mildner, D. F. R., "The Neutron Microguide as a Probe for Materials Analysis," Nucl. Instrum. & Meth. (in press).

Mildner, D. F. R., "Neutron Focusing Using Microguides," Nucl. Instrum. & Meth. (in press).

Mildner, D. F. R., "Multiple Reflections Within Neutron Optical Devices," Nucl. Instrum. & Meth. A 292, 693 (1990).

Mildner, D. F. R., "Acceptance Diagrams for Curved Neutron Guides," Nucl. Instrum. & Meth. A 290, 189 (1990).

Myers, J. E., Boone, J. L., Redman, C. L., "Archaeological and Historical Approaches to Complex Societies: The Islamic States of Medieval Morocco,"American Anthropologist, 92 (1) 47-63 (1990).

Myers, J. E., "Book review of The Collapse of Complex Societies, by Joseph Tainter and The Collapse of Ancient States and Civilizations by Norman Yoffee and George L. Cowgill," American Anthropologist, 91 (4) 1065-66 (1989).

Parr, R. M., DeMaeyer, E. M., Iyengar, G. V. et al. "Minor and Trace Elements in Human Milk From Guatemala, Hungary, Nigeria, Philippines, Sweden and Zaire: Results from a WHO/IAEA Joint Project," Biol. Trace Elem. Res. (in press).

Pauwels, J., Eykens, R., Lamberty, A., Gestel, J. Van, Tagziria, H., Scott, R. D., Byrne, J., Dawber, P. G., Gilliam, D. M., "The Preparation and Characterization of ^{6}Li and ^{10}B Reference Deposits for the Measurement of the Neutron Lifetime," Nucl. Inst. and Meth. in Physics Research, (in press).

Rossbach, M., Zeisler, R., Woittiez, J.R.W., "The Use of Compton Suppression Spectrometers for Trace Element Studies in Biological Materials," Biol. Trace Elem. Res. 26, 63 (1990).

Rothman, M.J., Blackman, M. J., "Instrumental Neutron Activation Analysis of Sealing Clays From Tepe Gawra, Nineveh, Arpachiyah, and Tell Brak, Northern Mesopotamia," MASCA Journal, (in press).

Ruddy, F. H., McGarry, E. D., Benchmark Referencing of Solid State Track Recorder Neutron Dosimeters in Standard Neutron Fields, 7th ASTM/Euratom Symposium on Reactor Dosimetry, Strasbourg, France, 27-30 August, 1990.

Schantz, M. M., Benner, B. A., Chesler, S. N., Koster, B. J., Hehn, K., E., Stone, S. F., Kelly, W. R., Zeisler, R., Wise, S. A., "Preparation and Analysis of a Marine Sediment Reference Material for the Determination of Trace Organic Constituents," Fresenius Z. Anal. Chem. (in press).

Scholfield, D. J., Iyengar, G. V. and Reiser, S., "Long Term Stability of Mitochondrial Superoxide Dismutase activity in USDIETS I-V," Fres. J. Anal. Chem. (in press).

Schwartz, R. B., Hunt, J. B., "Measurement of the Energy Response of Superheated Drop Neutron Detectors," in Radiation Protection Dosimetry, (in press).

Stone, S. F., Zeisler, R., Gordon, G. E., "Application of Polyacrylamide Gel Electrophoresis/Neutron Activation Analysis for Protein Determination," Biol. Trace Elem. Res., 26-27, 85 (1990).

Stone, S. F., Zeisler, R., Gordon, G.E., Viscidi, R.P., Cerny, E.H., "Neutron Activation Analysis Combined With Biological Isolation Techniques for Protein Determination," ACS Symposium Series, No. 445, Biological Trace Element Research: Multidisciplinary Perspectives, (in press).

Stone, S. F., Koster, B. J., Zeisler, R., "Instrumental Neutron Activation Analysis of SRM 1941 Organics in Marine Sediment, Element Content and Homogeneity," Biol. Trace Elem. Res., 26-27, 579 (1990).

Stone, S. F., "Quantitative Analysis With Autoradiography" Trans. Am. Nucl. Soc. (in press).

Stone, C. A., "Neutron Scattering and Its Effect on Reaction Rates in Neutron Absorption Experiments," Trans. Am. Nucl. Soc. 60, (1989).

Tagziria, H., Pauwels, J., Verdonk, J., Gestel, J. Van, Eykens, R., Gilliam, D. M., Scott, R. D., Byrne, J., Dawber, P. G., "Problems Related to the Determination of Mass Densities of Evaporated Reference Deposits, Nucl. Instr. and Meth. in Physics Research, (in press).

Tanner, J. T., Iyengar, G. V., Wolf, W. R., "Organic Nutrient Content of U.S. Food and Drug Administration's Total Diet and Its Possible Use as a Standard Reference Material," Fres. J. Anal. Chem. (in press).

Williamson, T. G., Lamaze, G. L., "Measurement of the ^{93}Nb(n,2n)^{92}Nb Cross Section in a ^{235}U Fission Spectrum," Proceedings of the 7th ASTM–Euratom Symposium on Reactor Dosimetry (Strasbourg, France, Aug.26–31, 1990) (in press).

Wise, S. A., Koster, B. J., Parris, R. M., Schantz, M. M., Stone, S. F., Zeisler, R., "Experiences in Environmental Specimen Banking," Intern. J. Environ. Anal. Chem. 37, 91 (1989).

Wolf, W. R., Iyengar, G. V., Tanner, J. T., "Mixed Diet Reference Materials for Nutrient Analysis of Foods: Preparation of SRM 1548 Total Diet," Fres. J. Anal. Chem. (in press).

Zeisler, R., "Recent Advances in Instrumental Neutron Activation Analysis in the Life Sciences," Trans. Am. Nucl. Soc. 60, 5 (1989).

Zoetelief, J., Eisenhauer, C. M., and Coyne, J. J., "Calculations on Displacement Corrections for In-Phantom Measurements with Ionization Chambers for Mammography," Phys. Med. Biol. (in press).

Zolensky, M. E., Lindstrom, D. J., Thomas, K. L., Lindstrom, R. M., Lindstrom, M. M., "Trace Element Compositions of Six 'Chondritic' Stratospheric Dust Particles," Lunar and Planetary Science XX, Lunar and Planet. Inst., Houston (1989), p. 1255.

U.S. DEPT. OF COMM. **BIBLIOGRAPHIC DATA SHEET** *(See instructions)*	1. PUBLICATION OR REPORT NO. NIST/TN 1285	2. Performing Organ. Report No.	3. Publication Date December 1990

4. TITLE AND SUBTITLE

NIST Reactor: Summary of Activities July 1989 Through June 1990

5. AUTHOR(S)

C. O'Connor, editor

6. PERFORMING ORGANIZATION *(If joint or other than NBS, see instructions)*

NATIONAL INSTITUTE OF STANDARDS AND TECHNOLOGY
(formerly NATIONAL BUREAU OF STANDARDS)
U.S. DEPARTMENT OF COMMERCE
GAITHERSBURG, MD 20899

7. Contract/Grant No.

8. Type of Report & Period Covered

Tech Note, 7/89 - 6/90

9. SPONSORING ORGANIZATION NAME AND COMPLETE ADDRESS *(Street, City, State, ZIP)*

Same as item #6 above.

10. SUPPLEMENTARY NOTES

☐ Document describes a computer program; SF-185, FIPS Software Summary, is attached.

11. ABSTRACT *(A 200-word or less factual summary of most significant information. If document includes a significant bibliography or literature survey, mention it here)*

This report summarizes all those programs which use the NIST reactor. It covers the period for July 1989 through June 1990. The programs range from the use of neutron beams to study the structure and dynamics of materials through nuclear physics and neutron standards to sample irradiations for activation analysis, isotope production, neutron radiography, and nondestructive evaluation.

12. KEY WORDS *(Six to twelve entries; alphabetical order; capitalize only proper names; and separate key words by semicolons)*

activation analysis; cold neutrons; crystal structure; diffraction; isotopes; molecular dynamics; neutron; neutron radiography; nondestructive evaluation; nuclear reactor; radiation.

13. AVAILABILITY

☒ Unlimited
☐ For Official Distribution. Do Not Release to NTIS
☒ Order From Superintendent of Documents, U.S. Government Printing Office, Washington, D.C. 20402.
☒ Order From National Technical Information Service (NTIS), Springfield, VA. 22161

14. NO. OF PRINTED PAGES

186

15. Price

NIST *Technical Publications*

Periodical

Journal of Research of the National Institute of Standards and Technology—Reports NIST research and development in those disciplines of the physical and engineering sciences in which the Institute is active. These include physics, chemistry, engineering, mathematics, and computer sciences. Papers cover a broad range of subjects, with major emphasis on measurement methodology and the basic technology underlying standardization. Also included from time to time are survey articles on topics closely related to the Institute's technical and scientific programs. Issued six times a year.

Nonperiodicals

Monographs—Major contributions to the technical literature on various subjects related to the Institute's scientific and technical activities.

Handbooks—Recommended codes of engineering and industrial practice (including safety codes) developed in cooperation with interested industries, professional organizations, and regulatory bodies.

Special Publications—Include proceedings of conferences sponsored by NIST, NIST annual reports, and other special publications appropriate to this grouping such as wall charts, pocket cards, and bibliographies.

Applied Mathematics Series—Mathematical tables, manuals, and studies of special interest to physicists, engineers, chemists, biologists, mathematicians, computer programmers, and others engaged in scientific and technical work.

National Standard Reference Data Series—Provides quantitative data on the physical and chemical properties of materials, compiled from the world's literature and critically evaluated. Developed under a worldwide program coordinated by NIST under the authority of the National Standard Data Act (Public Law 90-396). NOTE: The Journal of Physical and Chemical Reference Data (JPCRD) is published quarterly for NIST by the American Chemical Society (ACS) and the American Institute of Physics (AIP). Subscriptions, reprints, and supplements are available from ACS, 1155 Sixteenth St., NW., Washington, DC 20056.

Building Science Series—Disseminates technical information developed at the Institute on building materials, components, systems, and whole structures. The series presents research results, test methods, and performance criteria related to the structural and environmental functions and the durability and safety characteristics of building elements and systems.

Technical Notes—Studies or reports which are complete in themselves but restrictive in their treatment of a subject. Analogous to monographs but not so comprehensive in scope or definitive in treatment of the subject area. Often serve as a vehicle for final reports of work performed at NIST under the sponsorship of other government agencies.

Voluntary Product Standards—Developed under procedures published by the Department of Commerce in Part 10, Title 15, of the Code of Federal Regulations. The standards establish nationally recognized requirements for products, and provide all concerned interests with a basis for common understanding of the characteristics of the products. NIST administers this program as a supplement to the activities of the private sector standardizing organizations.

Consumer Information Series—Practical information, based on NIST research and experience, covering areas of interest to the consumer. Easily understandable language and illustrations provide useful background knowledge for shopping in today's technological marketplace.
Order the above NIST publications from: Superintendent of Documents, Government Printing Office, Washington, DC 20402.
Order the following NIST publications—FIPS and NISTIRs—from the National Technical Information Service, Springfield, VA 22161.

Federal Information Processing Standards Publications (FIPS PUB)—Publications in this series collectively constitute the Federal Information Processing Standards Register. The Register serves as the official source of information in the Federal Government regarding standards issued by NIST pursuant to the Federal Property and Administrative Services Act of 1949 as amended, Public Law 89-306 (79 Stat. 1127), and as implemented by Executive Order 11717 (38 FR 12315, dated May 11, 1973) and Part 6 of Title 15 CFR (Code of Federal Regulations).

NIST Interagency Reports (NISTIR)—A special series of interim or final reports on work performed by NIST for outside sponsors (both government and non-government). In general, initial distribution is handled by the sponsor; public distribution is by the National Technical Information Service, Springfield, VA 22161, in paper copy or microfiche form.